DEPARTMENT OF CHEMISTRY
UNIVERSITÀ DEGLI STUDI DI MILANO

Ph.D. course in INDUSTRIAL CHEMISTRY (XXXII cycle)
- CHIM/02 -

DEVELOPMENT OF FUNCTIONAL NANOCOMPOSITE MATERIALS TOWARDS BIODEGRADABLE SOFT ROBOTICS AND FLEXIBLE ELECTRONICS

Supervisor: Prof. Sandra Rondinini
Ph.D. coordinator: Prof. Dominique Marie Roberto

Ph.D. thesis of
Lorenzo MIGLIORINI

Academic Year: 2018-2019

EXTERNAL REFEREEES:

Prof. Peer Fischer
Chemistry, Max Planck Institute for Intelligent Systems, Stuttgart University, Germany.

Prof. Francesco Greco
Institute of Solid Phase Physics, Graz University of Technology, Austria.

EXAM BOARD:

Prof. Patrizia R. Mussini
Chemistry Department, University of Milan, Italy.

Prof. Alvo Aabloo
Institute of technology, University of Tartu, Estonia.

Prof. Massimo Innocenti
Chemistry Department, University of Florence, Italy.

FINAL EXAMINATION:

January 30th, 2020
Department of Chemistry, University of Milan, Italy

“An expert is a person who has made
all the mistakes that can be made
in a very narrow field”.

- Niels Bohr -

DEVELOPMENT OF FUNCTIONAL NANOCOMPOSITE MATERIALS TOWARDS BIODEGRADABLE SOFT ROBOTICS AND FLEXIBLE ELECTRONICS

- Ph.D. in INDUSTRIAL CHEMISTRY -

ABSTRACT

Candidate: Lorenzo Migliorini **Supervisor**: Prof.ssa Sandra Rondinini

World population is continuously growing, as well as the influence we have on the ecosystem's natural equilibrium. Moreover, such growth is not homogeneous and it results in an overall increase of older people. Humanity's activity, growth and aging leads to many challenging issues to address: among them, there are the spread of suddenly and/or chronic diseases, malnutrition, resource pressure and environmental pollution. Research in the novel field of biodegradable soft robotics and electronics can help dealing with these issues.

In fact, to face the aging of the population, it is necessary an improvement in rehabilitation technologies, physiological and continuous monitoring, as well as personalized care and therapy. Also in the agricultural sector, an accurate and efficient direct measure of the plants health conditions would be of help especially in the less-developed countries. But since living beings, such as humans and plants, are constituted by soft tissues that continuously change their size and shapes, today's traditional technologies, based on rigid materials, may not be able to provide an efficient interaction necessary to satisfy these needs: the mechanical mismatch is too prohibitive. Instead, soft robotic systems and devices can be designed to combine active functionalities with soft mechanical properties that can allow them to efficiently and safely interact with soft living tissues. Soft implantable biomedical devices, smart rehabilitation devices and compliant sensors for plants are all applications that can be achieved with soft technologies. The development of sophisticated autonomous soft systems needs the integration on a unique soft body or platform of many functionalities (such as mechanical actuation, energy harvesting, storage and delivery, sensing capabilities). A great research interest is recently arising on this topic, but yet not so many groups are focusing their efforts in the use of natural-derived and biodegradable raw materials. In fact, resource pressure and environmental pollution are becoming

more and more critical problems. It should be completely avoided the use of in exhaustion, pollutant, toxic and non-degradable resources, such as lithium, petroleum derivatives, halogenated compounds and organic solvents. So-obtained biodegradable soft systems and devices could then be manufactured in high number and deployed in the environment to fulfil their duties without the need to recover them, since they can safely degrade in the environment.

The aim of the current Ph.D. project is the use of natural-derived and biodegradable polymers and substances as building blocks for the development of smart composite materials that could operate as functional elements in a soft robotic system or device. Soft mechanical properties and electronic/ionic conductive properties are here combined together within smart nanocomposite materials. The use of supersonic cluster beam deposition (SCBD) technique enabled the fabrication of cluster-assembled Au electrodes that can partially penetrate into the surface of soft materials, providing an efficient solution to the challenge of coupling conductive metallic layers and soft deformable polymeric substrates. In this work, cellulose derivatives and poly(3-hydroxybutyrate) bioplastic are used as building blocks for the development of both underwater and in-air soft electromechanical actuators that are characterized and tested. A cellulosic matrix is blended with natural-derived ionic liquids to design and manufacture completely biodegradable supercapacitors, extremely interesting energy storage devices. Lastly, ultrathin Au electrodes are here deposited on biodegradable cellulose acetate sheets, in order to develop transparent flexible electronics as well as bidirectional resistive-type strain sensors. The results obtained in this work can be regarded as a preliminary study towards the realization of full natural-derived and biodegradable soft robotic and electronic systems and devices.

CONTENTS

1.

INTRODUCTION

1.1 SOFT TECHNOLOGIES FOR HUMANS AND CROPS HEALTH CARE

1.1.1 Soft robotics for rehabilitation and restoration

The world population continues to grow older rapidly as fertility rates have fallen to very low levels in most world regions and people tend to live longer [1]. Such aging of the population led to the spread of non-communicable and/or sudden diseases, as well as chronic diseases and strokes. **It is therefore necessary an improvement in rehabilitation technologies, physiological and continuous monitoring, as well as personalized care and therapy**. A functional and efficient solution to address these issues can be provided by **soft robotics**, a novel branch of robotics that can trigger the development of rehabilitation and implantable devices, characterized by biocompatibility, safeness, ease of control and adaptability to the personal needs of a patient.

In recent years, great attention and efforts are being attempted to the development of integrated robotic systems whose design, features and behavior are inspired by those of biological species. Traditional robots are usually made of rigid materials such as steel and aluminum (elastic modulus of the order of 10^9–10^{12} Pa), while biological systems are rarely composed of rigid mechanical components, but they generally make use of soft, elastic, and flexible materials (elastic modulus of the order of 10^3–10^8 Pa) in order to survive in complex unstructured environments. Animals' bodies are composed of soft skins and hairs, elastic muscles and tendons, and various soft organs. *Figure 1.1.1(a)* shows few examples of soft-bodied living organisms able to change their size and shape as a reaction to external stimuli or to adapt to the surrounding environment. While the conventional robotic systems usually rely on the pre-programmed motion patterns, biological systems update their neural circuitry continuously to adapt to the dramatic changes of body structures. As a consequence, while traditional robotic arms can display a still complex but joint-dependent mobility, **bio-inspired robotic arms based on soft active materials** could exploit a much higher degrees of freedom in their motion (a graphic example is reported in *Figure 1.1.1(b)*).

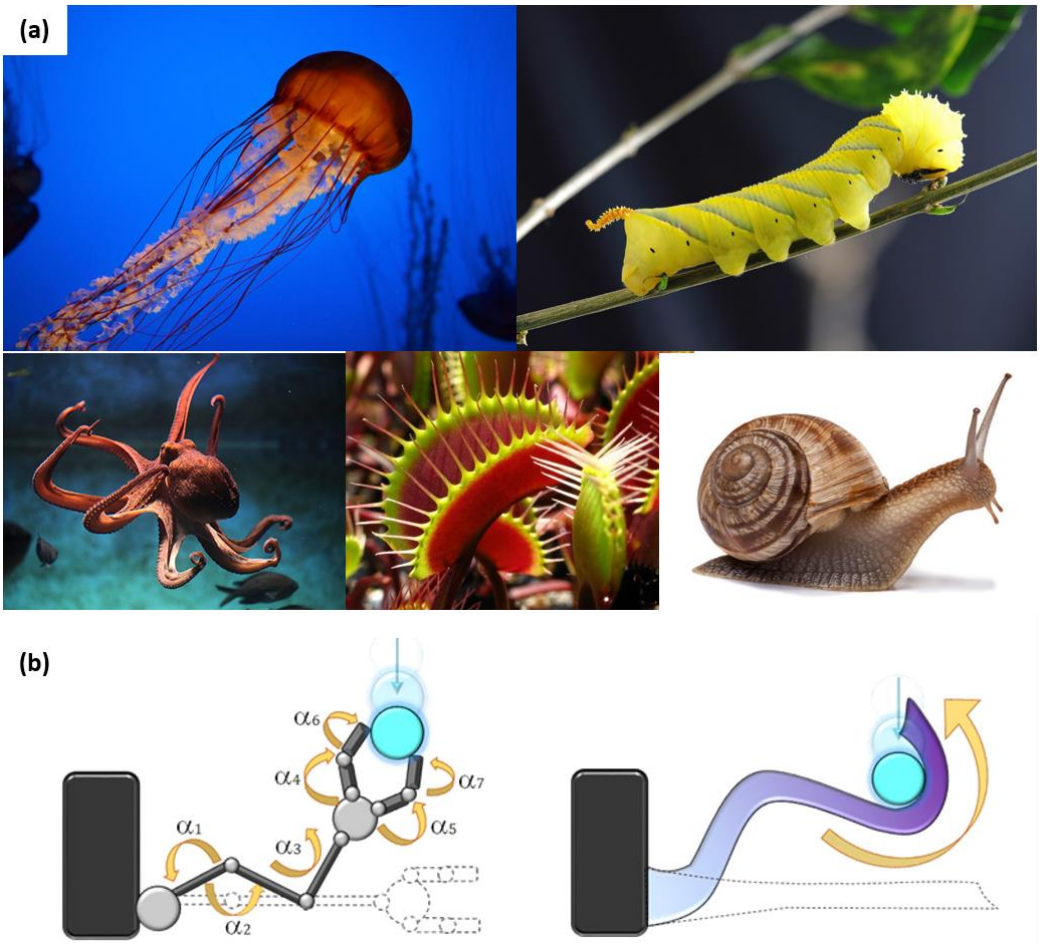

Figure 1.1.1. (a) *Examples of soft-bodied animals and plants that live both on the land and underwater. Starting from the upper left corner, an octopus, a caterpillar, a jellyfish, a carnivorous plant and a snail are shown (generic pictures obtained from google search).* ***(b)*** *Schematic of robotic arms composed by a stiff body provided with rigid joints (on the left) and a fully soft body (on the right) with a higher mobility degrees of freedom* [2].

Given such salient differences in constituent materials of artificial and natural autonomous systems, there has been an increasing interest in the studies of “softness” in the context of embodied intelligence research, for which the field of soft robotics is emerging. For example, a number of researchers have been investigating unconventional materials for robotic systems, in which soft matter such as polymer-based materials are examined for integration as novel sensory devices and actuators [3,4]. *Figure 1.1.2* shows the elastic moduli of several soft materials and biological

tissues. The raising interest in this field is driven not only by new scientific paradigms (biomimetics, morphological computation, and others) but also by many application requirements (in the fields of biomedical, service, rescue robots, and many more), because of the expected capability of soft robots to interact more easily and effectively with real-world environments [5,6]. Indeed, the use of soft deformable and variable stiffness technologies in robotics represents an emerging approach to build new classes of robotic systems that are expected to interact more safely with the natural, unstructured environment and with humans, and to better deal with uncertain and dynamic tasks (i.e., grasping and manipulation of unknown objects [7], locomotion in rough terrains [8], physical contacts with human bodies, etc.).

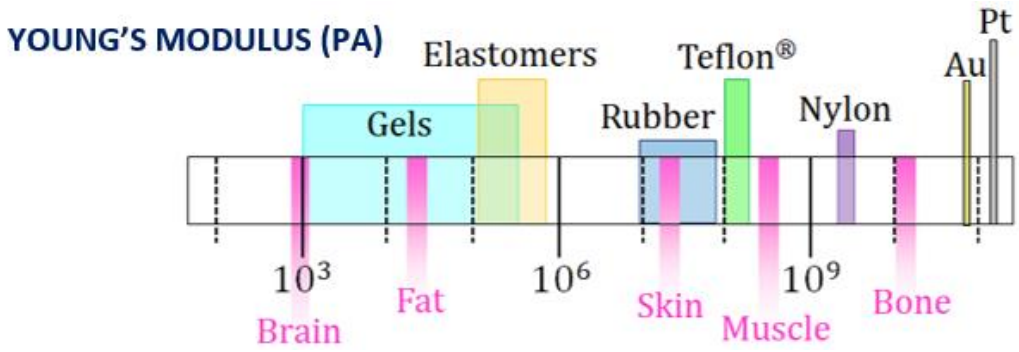

Figure 1.1.2. *Elastic (or Young's) modulus values of biological tissues compared with those of soft polymeric materials as well as hard metals. It is possible to mimic and replicate the mechanical properties of a specific tissue by identifying and tuning the most suitable polymer* [2].

Soft robots have potential of being able to bend and twist with high curvatures and thus can be used in confined spaces [9]; to deform their bodies in a continuous way and thus achieve motions that emulate biology [10]; to adapt their shape to the environment, employing compliant motion and thus manipulate objects [5], or move on rough terrain and exhibit resilience [11]; or to execute rapid, agile maneuvers, such as the escape maneuver in fish [12]. The key challenge for creating soft machines that achieve their full potential is the development of controllable soft bodies using materials that integrate sensors, actuators and computation, and that together enable the body to deliver the desired behavior. A soft robot of this kind, for instance, was developed and described in the work of Must et al. (*Figure 1.2.3(i)*) [13]. This and some other examples of soft robotic systems inspired by living organisms are shown in *Figure 1.1.3*.

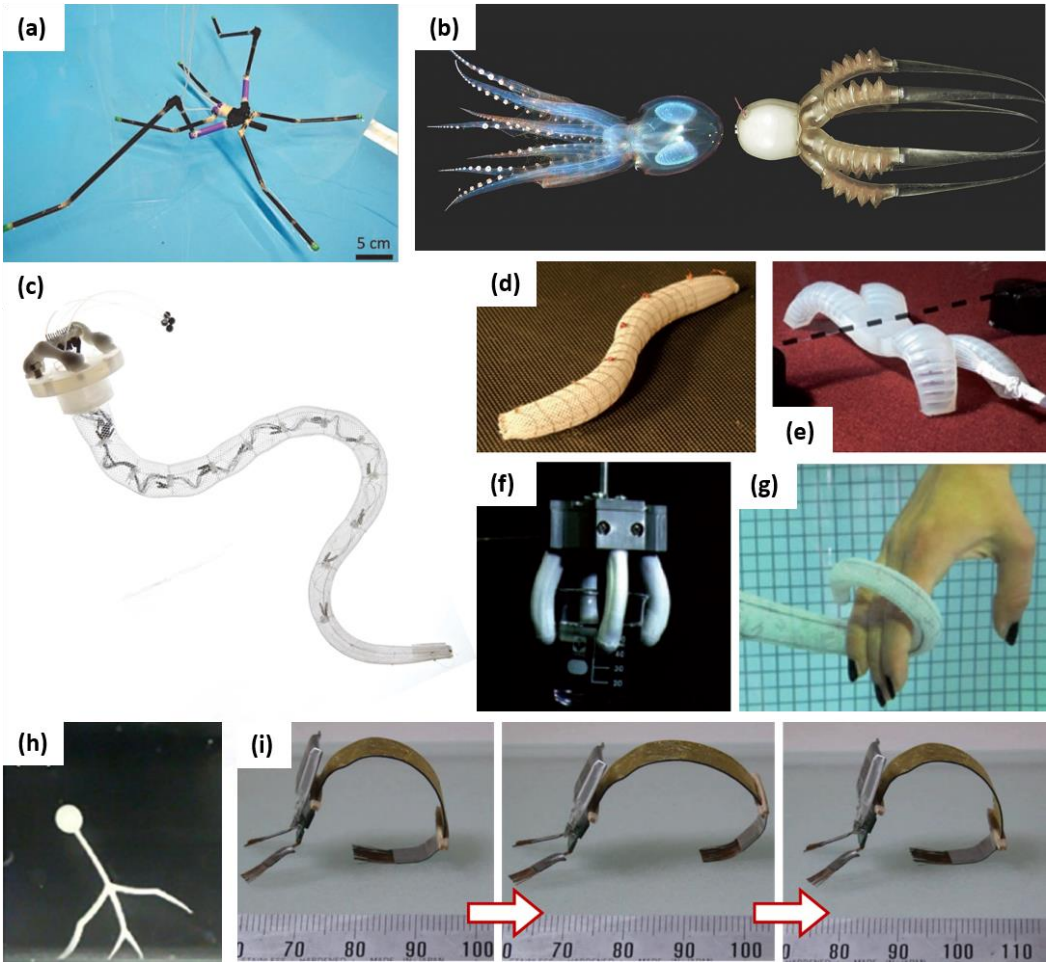

Figure 1.1.3. *Examples of bio-inspired soft robots, engineered with different locomotion and actuation features:* ***(a)*** *a rowing arthrobot* [26]*;* ***(b)*** *an octopus-like swimming soft robot* [27]*;* ***(c)*** *flexible octopus-like robotic arm* [28]*;* ***(d)*** *worm-inspired soft walker* [29]*;* ***(e)*** *multi-gait quadruped robot* [30]*;* ***(f)*** *soft micro-manipulator* [31]*;* ***(g)*** *octopus-inspired soft manipulator* [32]*;* ***(h)*** *underwater walking soft robot* [33]*;* ***(i)*** *Inchworm-inspired biomimetic soft robot* [13].

Soft robotics approach provides opportunities to develop robots that are well suited for intimate interactions with humans and with tuneable chemical-physical properties. Furthermore, by combining a suitable design with a simple control, these soft robots can be programmed to mimic the complex motions of tissues in the human body [14–16] using specifically designed contractile elements or actuators [17–21]. Thanks to

this, it becomes appealing the creation of **external and/or implantable soft robotic systems** whose objective is the restoration of physiological functions in patients with chronic diseases or strokes. For example, different research groups [22], used soft robotic techniques to develop a tethered implantable sleeve that can provide circulatory support for patients with compromised heart function (see *Figure 1.1.4(a-b)*). Other groups, instead, worked on soft robotic gloves designed to assist individuals with functional grasp pathologies in performing activities of daily living, by supporting fingers and thumb motions during hand closure (*Figure 1.1.4(c)*) [23–25].

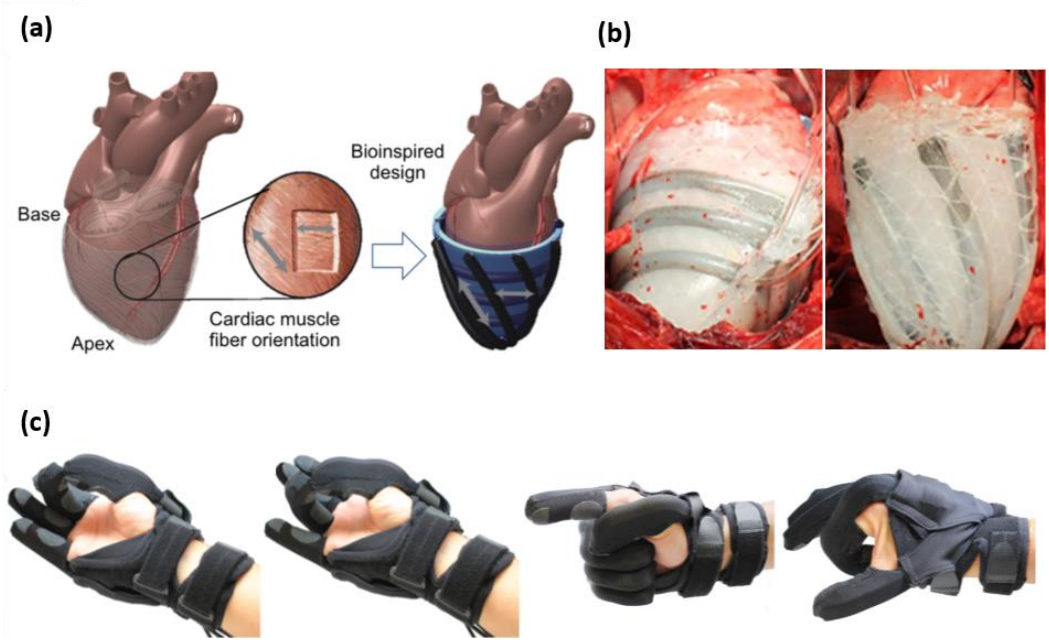

Figure 1.1.4. (a) *Modeling of tethered implantable sleeve meant to work as a ventricular assist soft device and* ***(b)*** *the real device tested by circumferential (on the left) and twisting (on the right) actuation around a porcine heart* [22]*;* ***(c)*** *Soft robotic glove helping the motion of hand and fingers* [25]*.*

Elastic inflatable actuators represent one of the most diffuse choice to achieve soft actuation, thanks to their easy fabrication, formulation and control, even if they need to be continuously connected to a pressure supply and their miniaturization involves many critical tasks [34]. Alternatively, **Shape memory alloys** can be used as actuators thanks to their ability to be deformed at low temperature and to recover their original shape by heating [35]. But soft robotics also needs the development of novel **smart stimuli-responsive materials** characterized by soft mechanical properties and

stimuli-responsive behaviour. They need to be flexible, with an elastic modulus usually between 10^3 and 10^8 Pa, able to be stretched and bent seamlessly and without sharp edges and peaks in order to safely interact with biological entities and/or fragile objects. Stimuli-responsive properties allow these materials to feel physical or chemical stimuli in the surrounding environment and to change their shape accordingly, generating a net mechanical force, even without the presence of physical rigid joints in their structure. The key to understand and to exploit the properties of these class of materials is the relationship between the type and entity of the applied stimuli, the actuators shape and geometry, the surrounding environment and the consequent mechanical actuation [36]. The working ambient is itself an important information to be taken into account: usually, the main distinction regards actuators able to operate in underwater environments and those meant to operate in plain air. Among many kinds of stimuli-responsive materials, **electro-responsive** ones are extremely interesting to be used as **electromechanical actuation**, since nowadays electric signals can be easily generated and controlled with extreme precision [37]. Apart from actuation, another critical issue to be faced towards the realization of an autonomous soft robotic system is the integration on the same platform or body of other necessary functions: power supply sources, electrical connections, sensors able to detect the surrounding environments and remote communication elements.

1.1.2 Soft electronic devices for health monitoring

Besides the personalized treatment of a disease or a stroke, many efforts should be evenly or mostly put in finding an efficient, safe and non-invasive way to continuously monitor the physiological conditions of subjects at risk, in order to anticipate and prevent the arising of diseases.

Skin is the largest organ of the human body, and it offers diagnostic interface rich with vital biological signals from the inner organs, blood vessels, muscles, and dermis/epidermis. It can both generate and transmit biological signals that provide important health metrics of an individual [38–43]. Soft, flexible, and stretchable electronic devices can provide a novel platform to interface with soft tissues for robotic feedback and control, regenerative medicine, and continuous health monitoring. Many examples of branches of medicine can be found where the use of monitoring electronic devices compliant with the skin could bring great advantages. **Cardiology** is a branch of medicine related to disorders of the heart and circulatory system. Key vital signals like heart sounds, blood pressure (BP), temperature, pulse rate and respiration rate are

studied and monitored to assess the health of the cardiovascular system [44]. None of actual standard diagnostic tools is well suited for continuous measurement, neither for detect all of these signals at the same time. Through wearable sensing and miniaturization, soft autonomous devices may be developed in order to enable a high-quality, simultaneous, continuous, real-time and non-invasive monitoring, that could allow for an immediate feedback to the patient. **Dermatological diseases**, instead, can be detected by checking the mechanical and thermal properties of the skin, while the dose of UV exposure can be measured by UV sensors. The integration of these functionalities in a single compliant device would be extremely appealing [45–48]. Such systems could even be used to induce a local heating of the tissues. Moreover, by studying and measuring the electrical properties of biological cells and tissues (**electrophysiology**) [49], many physiological parameters can be checked: it is possible to obtain information on the ventricles and atria for cardiac diseases [50], or to measures electrical activities in the brain for studies of sleep apnoea [51], epilepsy [52] and other neural disorders, as well as to provide information on nerve and muscle health [50,53]. *Figure 1.1.5* reports examples of soft biosensors for the monitoring of the aforementioned parameters.

The final purpose is to **complement or even replace current diagnostic tools**, allowing for higher levels of comfort and mobility of the patients without compromising accuracy, reliability, or functionality. Commercially established classes of **wearable medical electronics** are fundamentally based on rigid materials and designs [55,56]. Despite the reliable functionalities they display for clinical applications, their unwieldy wiring and not efficient integration with the skin does not allow to achieve a mobile, comfortable and continuous long-term precision monitoring [57]. More specifically, the greatest challenge is represented by the overcoming of the mismatch in physical properties [58,59] at the electronic-skin interface, preventing the development of integrated wearable systems with applications from basic healthcare monitoring to clinical evaluation of disease states [60–62]. Polymeric materials can represent a promising solution to this problem. Due to their tuneable mechanical properties they can constitute soft platforms for wearable technologies. Indeed, numerous soft, flexible, and stretchable electronic devices integrated with polymeric substrates have emerged as platforms capable of digitizing biological signals for healthcare monitoring [63], allowing the development of mechanically invisible electronic interfaces with embedded sensors, power supplies, processing, memory, and communication components [64–69].

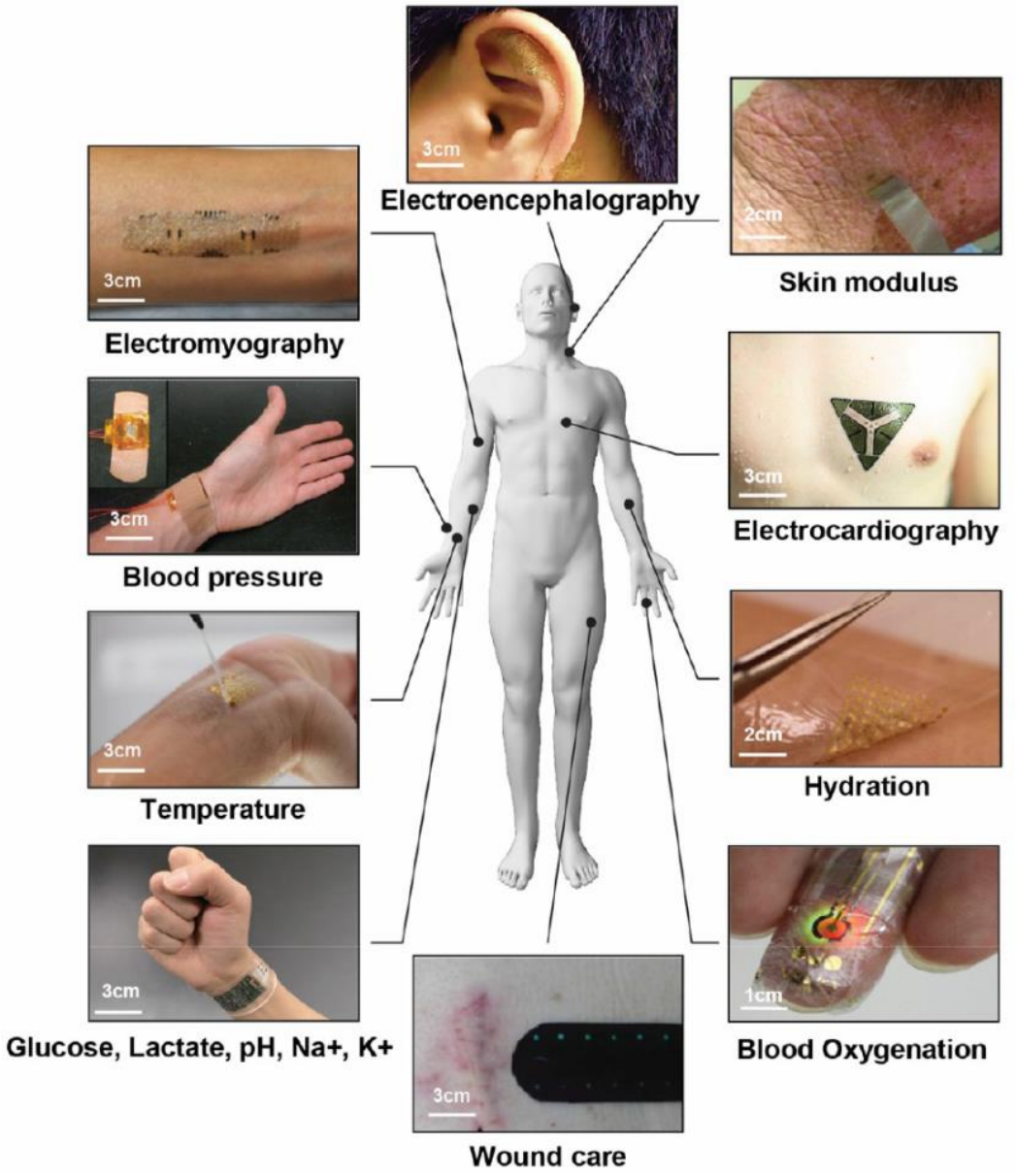

Figure 1.1.5. *Soft electronic devices as biosensors for measuring (clockwise from top right) skin modulus, electrocardiology, hydration, blood oxygen, wound-healing rate, sweat content, skin surface temperature, blood pressure, electromyography, and electroencephalography* [54].

The largest mismatch in mechanical properties usually occurs between biological tissues (brain, skin, cartilage) and the materials used as the active functional layers in the electronic devices (silicon, gold, etc.). Then the supporting and encapsulating polymeric should have mechanical properties much closer to those of the biological tissues. In particular, integrating **high-performance inorganic semiconductors and conductive metals with soft substrates** has produced classes of electronic devices that can stretch, twist, and bend without permanent mechanical damage [42,63,70–73] (*Figure 1.1.6(a)*). Besides the mechanical properties, **electronic properties** also play a major role in the development of these kind of devices. Organic materials can be commercially printed at large scales, but the poor electrical mobility and the chemical instability of organic semiconductors have hampered the realization of fast circuitry and stable operation. Instead, inorganic materials including semiconductors, dielectrics, and conductors can be employed to form high-performance functional active devices. For example, silicon nanomembranes (NMs) have been used to build flexible transistors, diodes, and circuits [57], even if they present complicated and long fabrication processes, difficult to implement on large scales. One-dimensional and two-dimensional inorganic materials, such as carbon nanotubes (CNTs), graphene (*Figure 1.1.6(d)*) and their derivatives, show promising electrical and mechanical properties [60] but they remain in an early stage of development [74–76]. Ferroelectric and piezoelectric layers have also been exploited for the production of flexible non-volatile memory [77–79], pressure sensing [80], and energy scavenging [81,82]. Among metals, gold and platinum are widely used for electrodes that interface with the skin thanks to their chemical inertness and low contact impedance [57,66], (*Figure 1.1.6(b, c)*). Copper is the metal of choice for most interconnects and antennas due to its low electrical resistivity [83]. For example, composite conductors [84], obtained by the dispersion of conductive nanoparticles into soft polymeric matrices, can provide the opportunity to tune the electrical and mechanical properties depending on the specific application. The same can be done with metallic (e.g. silver) nanowires (*Figure 1.1.6(e)*).

A critical task for the realization of wearable health monitoring systems is represented by energy autonomy, that is the capability of remote sensing and communicating in a continuous mode without a physical connection to a physical network. To do this, many efforts have been spent on using the human body itself as a power supply or harvesting energy from the surrounding environment [85–89]. **Many low-power energy sources are available directly from the body** and can be transduced to exploitable forms of energy, such as mechanical (vibrational) to electrical transduction [90–92], thermal to electrical [93] and chemical to electrical. Considering instead **the surrounding environment, the available sources** include energy from sunlight [94,95] and radio frequency (RF) electromagnetic sources [87,88,96]. Anyway, conversion and conditioning of the energy will always involve a loss of part of the harvested ambient energy.

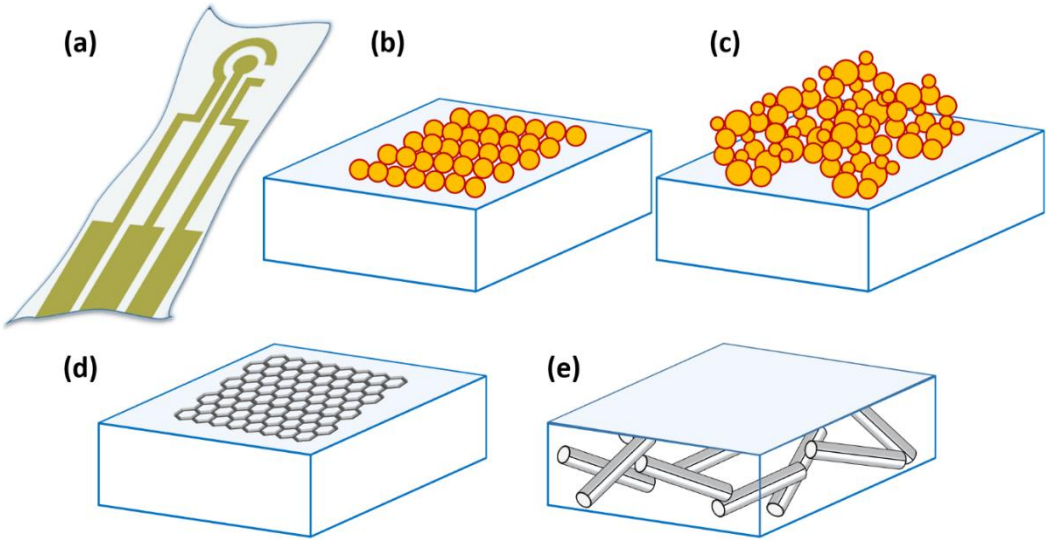

Figure 1.1.6. *Different examples of deformable and conductive composite films.* ***(a)*** *Example of a thin conductive three-electrodes chip on a soft deformable substrate.* ***(b)*** *A tight monolayer of a metallic specie on the surface of a soft polymer, usually characterized by low porosity and high conductivity.* ***(c)*** *A metallic nanoparticle-based assembly, usually characterized by a higher porosity but a lower conductivity.* ***(d)*** *Example of a graphene nanosheet compliant with the polymer's surface.* ***(e)*** *Example of silver nanowires physically embedded as nanofillers inside a polymeric matrix; they can form an interconnected conductive lattice able to bend and stretch together with the polymer.*

Moreover, many factors can strongly affect the power densities of transducer devices, such as the body part on which the device is placed, the frequency and entity of the mechanical movements as well as the behaviour and the habits of the people (for example a device on a person spending many daily hours indoor can exploit a lower amount of solar energy rather than the same device on a person spending many daily hours outdoor). As a result, it is almost mandatory to endow the soft devices with the ability to store energy, for example with the introduction of soft and flexible supercapacitors or batteries. Mechanics plays a key role in the design and fabrication of **flexible and stretchable batteries** [97–100]. To construct flexible systems, batteries should be thin, even if this will reduce their overall capacities and consequently printed batteries reported in literature possess an aerial densities lower than traditional ones [101]. Also, the current collectors must be chemically compatible with the active layers

while providing strong adhesion to surrounding materials in order to avoid mechanical damage during operation. Concerning the electrolyte, many polymer-based electrolytes [102,103] have replaced conventional liquid ones due to health and safety benefits. Parallel coplanar architectures are usually preferred due to their simplified fabrication processes and reduced risks of shorting when they are subjected to a mechanical deformation. **Supercapacitors** represent an alternative solution to batteries for energy storage: they can charge and discharge faster, they have a longer cycle-life but they can store a lower amount of energy. Electrode materials with high surface areas and mechanical flexibility are needed to fabricate flexible supercapacitors. Thus, the electrodes are usually based on the use of nanostructures in the form of one-dimensional (nanowires, nanofibers, nanotubes, etc.), two-dimensional (graphene, inorganic ultrathin nanosheets, etc.), and three-dimensional structures (graphene networks or foam structures) [104]. In particular, graphene has been widely employed thanks to its high theoretical specific surface area (2630 m^2g^{-1}) [105]. However, for the majority of graphene-based supercapacitors, the values of specific capacitance, energy density and power density have remained lower than expected due to restacking of graphene sheets [106].

Concerning the energy **transduction mechanisms**, many transducers are currently studied that exploits different energy sources. Mechanical vibrations can be exploited as a source of power for wearable devices [90–92]: they are based on piezoelectric [107] and triboelectric [91] mechanisms and they have been recently investigated for both wearable and implantable applications. In this case, one of the major problem is the difficulty of harvesting energy at different frequencies. To do this, supercapacitors may represent a good solution to store such a discontinuous energy. Approaches in scavenging energy from the body involve exploiting bioelectrocatalytic reactions of common chemicals and metabolites. Implantable glucose and lactate biofuel cells have been developed [108,109] and, even if their stabilities are limited to few hours, experimental results proved that the fuel cells, when mounted on skin, can power a low power Bluetooth module [110]. Besides these, flexible and stretchable solar cells represent the source capable of providing the most power [94–96,111], despite the lower efficiency with respect to traditional rigid ones. For the development of such devices, it is of mandatory importance the employment of not only soft but also transparent electronics.

The integration of all these functionalities on light, flexible soft platform, able to operate for long time in an efficient and safe way, is still a complex challenge that requires the cooperation of expert scientists and researchers with knowledge and experience coming from different scientific fields. But it could be the only way to really spread all over the population a steady and reliable system of health monitoring.

1.1.3 Soft technologies in precision agriculture

The **global food chain cannot be taken for granted**: it is under pressure from global population growth and needs to drive productivity, climate change, inescapable political impacts of migration, population drift from rural to urban regions, and the demographics of an aging global population in advanced economies including China. Agricultural scientists, farmers, and growers are facing the challenge of producing more food from less land in a sustainable way to meet the demands of the predicted 9.8 billion populations in 2050 [112]. In addition, jobs in the Agri-Food sector can be physically demanding, repetitive in nature, conducted in adverse environments and relatively unrewarding. Malnutrition is one of the most serious problems for a big part of humanity. Then there is the need to improve the agricultural yield in a strategic yet sustainable way.

Also known as 'smart farming', **precision agriculture** is a paradigm that can help to address this issue. It has its origins in developments first applied in industrial manufacturing as far back as the 1970s and 80s. It concerns the use of monitoring and intervention techniques to improve efficiency, realised in application through the deployment of interconnected sensing technologies and automation [113]. *Figure 1.1.7* conveys the idea of many wireless interconnected sensoristic platforms that can collect and deliver data and analysis results. One approach is to utilise more intelligent machines to reduce and target inputs in more effective ways. The advent of autonomous system architectures creates the opportunity to develop a new range of flexible agricultural equipment based on small, smart machines that reduces waste, improves economic viability, reduces environmental impact and increases food sustainability. There is also considerable potential for robotics technologies to increase the window of opportunity for intervention, for example, being able to travel on wet soils, work at night, etc.

Sensory data collected by robotic platforms in the field can further provide a wealth of information about soil, seeds, livestock, crops, costs, farm equipment and the use of water and fertiliser. Low-cost Internet of Things (IoT) technologies and advanced analytics are already beginning to help farmers analyse data on weather, temperature, moisture, prices, etc., and provide insights into how to optimise yield, improve planning, make smarter decisions about the level of resources needed, and determine when and where to distribute those resources in order to minimise waste and increase yields [114]. Future telecommunications availability is likely to enhance IoT capacity, with agri-tech test beds already under development.

Figure 1.1.7. *An illustration that conveys the idea of many autonomous sensoristic platforms, widely deployed and wireless connected to each other: analysis on the air, the soil and on the health state of the plants can be carried out and the resulting data can be collected and processed together.*

Robotics in precision agriculture has the potential to improve competitiveness and increase sustainability compared to current crop production methods [115] and has become an increasingly active area of research. The global Agri-Food sector could be transformed by advanced **robotic autonomous systems (RAS) technologies** [116]: their use would also have significant societal and environmental benefits. Some examples are reported in *Figure 1.1.8*. For example, fleets of small lightweight robots are now seen as a replacement for traditional high mass tractors, allowing a gradual reduction of compaction, re-aeration of the soil and benefits to soil function. **Field robots** can be deployed to help farmers measure, map and optimise water and irrigation use. Likewise, robots that use precision technologies to apply fertilisers and pesticides within agricultural systems will reduce environmental impacts [118,119].

The **integration of sensor systems** within autonomous robots offers the significant potential for new measurements that would otherwise be unobtainable. Robotic platforms offer the possibility of forensic testing of soil with the geotagging and immediate results from sampling sensors (such as laser-induced breakdown spectroscopy), or secure collection of samples for later analysis in a systematic and uncontaminated manner. Continuous and long-term data collection further enables the modelling of crops over time. Such ground and aerial robotic platforms offer additional prospects for enabling localised extremely high signal-to-noise, high resolution sensing that may not be achieved by passive remote (satellite) or semi-remote sensing

technologies. At the simplest level, these robotic platforms offer the potential to extract close proximity (within 10s of millimetres) reflectance and transmission. Multispectral Imaging (MSI) data helps compensate for the erroneous measures that occur due to the surface topology and orientation of individual crop tissues.

Figure 1.1.8. *Photographs and illustration of both in-air and on-land robotic autonomous systems* [117].

At a more advanced level, the use of robotic manipulators to locate sensors around crops or livestock could enable responses to be tested and examined, through applying artificial stimuli. For example, through applying a focused beam of light at specific areas of crop tissue, and then modulating the spectrum and intensity, it is possible to drive photochemical reactions within specific parts of plants, e.g. stems, young leaves, senesced older leaves, etc., which can then be sensed via multispectral imaging. In this way significantly greater phenotype information may be recovered from across plants than could be achieved by passive fixed imaging detectors alone. Similarly, the cell structures and arrangements within fruits, vegetable and meats may be non-destructively examined in high resolution, e.g. for mapping subcutaneous bruising in fruits or fat ratios in meats. Nutrient and water stress of crops can be assessed by fusing MSI data with other data sources. Combining these assessments with crop growth

models gives a better prediction of yield and loss, which leads to improved farming management and better food supply chain management.

The current challenge is the development of **a new generation** of smart, flexible, robust, compliant, interconnected robotic systems working seamlessly alongside their human co-workers in farms and food factories. Teams of multi-modal, interoperable robotic systems can self-organise and coordinate their activities alongside and within existing Agri-Food systems. Electric farm and factory robots with interchangeable tools, including low-tillage solutions, **novel soft robotic grasping technologies and sensors**, could support the sustainable intensification of agriculture and drive manufacturing productivity throughout the food chain. Future agri-robotic systems should deploy artificial intelligence and machine learning techniques to increase their own productivity.

To achieve this goal, many issues have to be addresses. Considering that the level of complexity in an unstructured, dynamic, open-ended and weather influenced environment like a crop field or an orchard is extremely high, flexible and adaptable locomotion is strongly needed. At the same time, many practical operations, such as fruit collection, requires soft manipulation capabilities and controllable with an extremely high precision. Some examples of soft manipulators are shown in *Figure 1.1.9*.

Figure 1.1.9. *Examples of soft fruit collectors* [117].

Concerning the sensing capabilities, it is becoming increasingly important a broad research on advanced cognitive perception and behaviour. Despite the usefulness of the employment of field robots able to carry out multispectral imaging, there is still the lack of soft autonomous sensor devices that can work in direct contact with the plants. For example, soft electrochemical sensors could be used to extract many

important information about the health of a crop by analysing the liquid secreted by the stomata (microvescicles situated on the leaves surface), as it is shown in *Figure 1.1.10*. To do this, there is the need to find suitable soft materials to be coupled with compliant conductive electrodes, current collectors, autonomous powering and remote communication elements. These perspectives and considerations are the main reasons because of which soft robotic and electronic technologies can reveal to be crucial for the future development of precision agriculture.

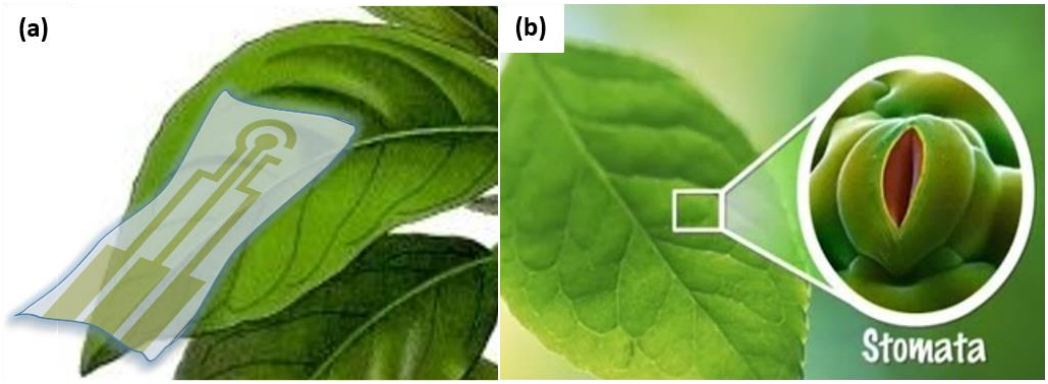

Figure 1.1.10. (a) *Illustration showing a thin conductive three-electrodes chip on a soft deformable substrate: thanks to its mechanical properties, it can adapt to the shape and the morphology of a leaf to carry out electrochemical analysis on the liquid secreted from the stomata.* ***(b)*** *The surface of the leaves is characterized by the presence of millions of stomata, microvescicles used by the plants to exchange gases and substances with the surrounding environment. A rigid electrochemical sensor would never be able to achieve a thigh contact with the huge number of stomata present: only soft technology can aim at this purpose.*

1.2 GREEN MATERIALS FOR SUSTAINABLE SOFT TECHNOLOGIES

Industrial and technological mass production and manufacturing processes consume non-renewable resources and the disposal of a large number of consumer-graded products generates damage for the environment. The importance of environmental sustainability leads to a new challenge: to find natural-derived and biodegradable materials to be used as building blocks for the development of innovative green devices and technological solutions [120]. **Modern society is a massive consumer of resources.** Every plastic bag, every electronic device, every means of transport depletes world resources. Fuels for internal combustion engines, plastics and many organic chemicals are directly derived from non-renewable fossil fuels. Semiconductor components and electronic circuits use significant quantities of rare and exotic materials [121]. The pressure on natural resources is huge, not only regarding "peak oil", but also many other vital materials [122]. For example, lithium polymer batteries are ubiquitous in modern portable electronic devices and they could also play a key role in solar technologies to in-home electrical storage [123]. But the planetary reserve of lithium is finite and these new technologies are putting an exponentially increasing demand on the raw material. The same is true, to greater or lesser extent for more mundane materials like copper and rare earth metals like neodymium, both important elements in conventional robotics and electromagnetics. Then, the need for technologies employing renewable resources is becoming more and more impellent.

Besides, not only the resource origin has become a critical issue to address, but also the **ever-increasing presence of non-degradable trash**. From plastic packaging to smartphones, tons of consumer items are thrown away when they reach their end of life, with heavy damage for the environment. **The natural environment is a well-balanced machine**: it operates as a closed system in which new organisms are born, live and die. The raw materials that make up these dead organisms are reused within the system either directly, through digestion by other organisms higher up the food chain, or by gradual decay into constituent molecules that then enter the food chain near the bottom. **The degradation of man-made material**, on the other hand, does not result in uniformly benign effects. For example, non-biodegradable polyethylene bags take upwards of 500 years to decay and can have immediate impact on living creatures [124]. Plastic fragments are digested by many organisms, depending on their size. Large pieces resemble the natural food of larger animals and when consumed can block their digestion. Microscopic pieces are consumed by plankton and other microorganisms

where they are concentrated and then consumed by organisms higher up the food chain [125] (*Figure 1.2.1*).

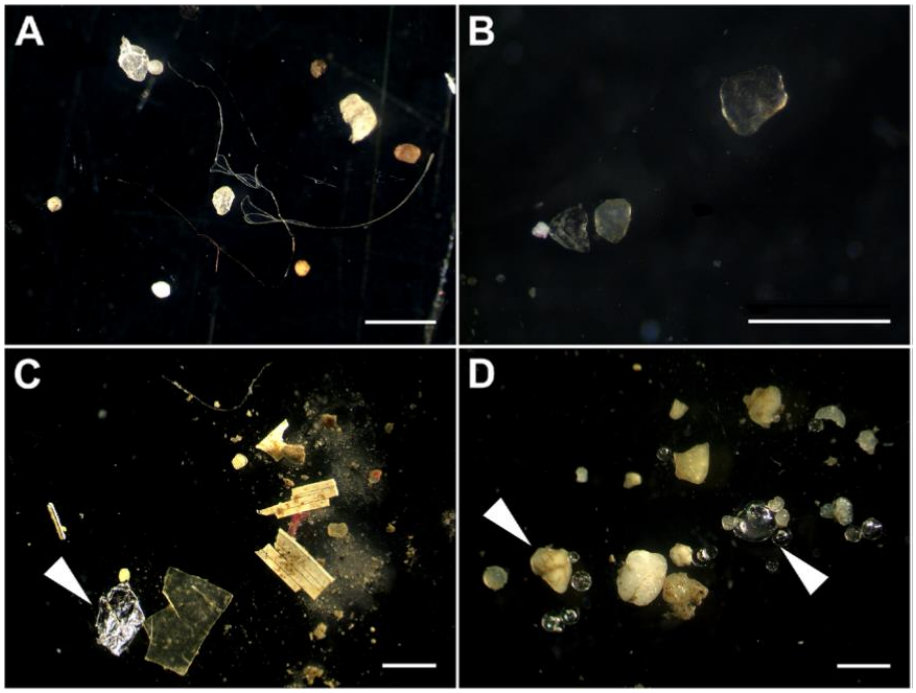

Figure 1.2.1. *Microplastics in sediments from the rivers Elbe* ***(A)****, Mosel* ***(B)****, Neckar* ***(C)****, and Rhine* ***(D)****. Diverse shapes (filaments, fragments, and spheres) are present and not all items are microplastics (e.g., aluminum foil (C) and glass spheres and sand (D), white arrowheads). The white bars represent 1 mm* [125].

Because of these reasons, sustainability, industrial ecology, eco-efficiency, and green chemistry are guiding the development of the next generation of materials, products, and processes. Biodegradable plastics and bio-based polymer products based on annually renewable agricultural and biomass feedstock can form the basis for **a portfolio of sustainable, eco-efficient products** that can compete and capture markets currently dominated by products based exclusively on petroleum feedstock. The development of new materials should then rely on the use of natural-derived and renewable raw products that can form novel composites easily and safely biodegradable in the environment.

Concerning **biodegradability**, many similar but different definitions can be found. A general explanation of the concept can be provided by saying that

biodegradation occurs when microorganisms feed themselves with complex organic matter and release simpler organic compounds. A polymeric material, for example, is considered to be biodegradable if environmental microorganisms can break the chemical bonds of the polymeric chains: complex macromolecules are then usually converted in carbon dioxide, water and small organic molecules. If the biodegradation process occurs in the presence of oxygen it is called aerobic, while in absence of oxygen the process is referred to as anaerobic and methane is also produced in addiction. Through biodegradation, then, the organic matter of a natural or artificial material is reabsorbed by the environment without leaving a trace.

Among natural-derived polymers, **cellulose** is the most abundant renewable organic material produced in the biosphere, with approximately 5×10^{11} metric tons being generated yearly. Unfortunately, a mere 2% is recovered industrially [126]. It is a linear syndiotactic homopolymer composed of D-anhydroglucopyranose units (AGUs), which are linked by β-(1→4)-glycosidic bonds (*Figure 1.2.2(a)*). Cellulose is a colorless, odorless and nontoxic solid polymer; it possesses many interesting properties, such as great mechanical strength, biocompatibility, hydrophilicity, relative thermostabilization, high sorption capacity, and alterable optical appearance [127]. These features enable cellulose to be applied to a vast array of fields. Moreover, cellulose polymeric chains can be easily chemically functionalized in order to obtain a broad class of derivatives with different chemical and physical properties. Other natural-derived **carbohydrates** suitable to be used as biodegradable raw materials are chitosan (*Figure 1.2.2(b)*), chitin, starch, glycogen, pectin [128]. Silk, a **protein fibre** (*Figure 1.2.2(c)*), can be used as well to manufacture natural-derived textiles [129]. Other protein-derived substances are collagen and gelatine. **Bioplastics** are also becoming more and more studied and employed as a replacement for non-degradable plastic derived from petroleum [130,131]. Some plastic materials, such as polycaprolactone (PCL) (*Figure xx1.2.2(d)*), come from petrochemical products but are biodegradable anyway; polylactic acid (PLA) (*Figure 1.2.2(e)*) is a synthetic bioplastic obtained by the processing of bio-derived monomers. Poly(hydroxyalcanoates) (PHA) (*Figure 1.2.2(f)*) instead are directly extracted from bacteria [132]. Researchers and companies all around the world are putting many efforts in the attempt to improve the chemical-physical properties of such biodegradable polymers in order to push and accelerate their efficient use in technological industry. Using such biodegradable materials to **develop renewable replacements for currently non-renewable technologies**, it would be possible to reach a sustainable and stable state where resource peaking can be forestalled indefinitely. One area where this has high potential is in **soft robotics and electronics**. In fact, soft technologies aim at the replacement of traditional rigid materials with new softer ones: then, why not natural-derived and biodegradable too? Soft technology's necessity to find novel solution and change many traditional paradigms constitutes a major opportunity to develop truly sustainable soft robotic and sensing devices.

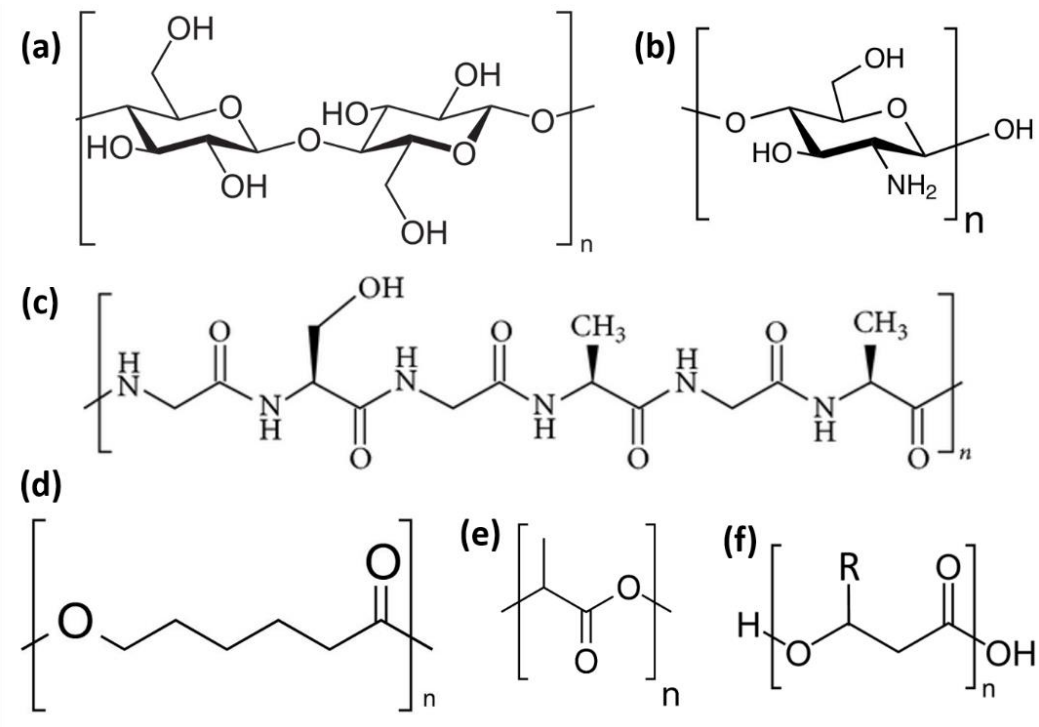

Figure 1.2.2. *Chemical structures of some natural polymers:* ***(a)*** *cellulose,* ***(b)*** *chitosan,* ***(c)*** *silk fibroin,* ***(d)*** *polycaprolactone,* ***(e)*** *polylactic acid,* ***(f)*** *poly(hydroxyalcanoates).*

Novel **functional materials** can be made from benign and readily available building blocks, thus reducing resource pressures, and can even be made to degrade safely within the environment. They can be used to develop smart soft actuators, like electroactive ionic polymers, for **locomotion and manipulation** [133–135]. A large focus of recent research in ionic actuators has been on **ionic liquids** [136], organic salts that are liquid at room temperature. They are highly eco-friendlier with respect to traditional organic solvents and they are also highly stable in air compared to water, enabling the actuator to operate outside aqueous environments. Biodegradable flexible and stretchable composites materials can constitute the main body of the soft robots and devices, where all the functional elements can be integrated and interconnected. The issue of the **power source** of soft devices can be faced as well from an environmental point of view: both the unit supplying the energy and the fuel should be biodegradable and sustainable. Microbial fuel cells (MFCs) employ anaerobic bacteria to transform the chemical energy, contained in organic matter, to electrical energy. A soft robotic device equipped with these cells can use the produced electrical energy to become

energetically autonomous. For decades, MFCs have been constructed using rigid plastics, polymeric membranes and expensive toxic elements. Recently, however, less conventional, biodegradable materials have been successfully applied. Natural rubber has proven to be a viable substitute to conventional membranes over long term operation where the act of biodegradation actually aided performance [137]. Other materials such as paper [138], gelatine, PLA and lanolin have all demonstrated their suitability as viable working components in MFCs [139].

Entirely biodegradable and autonomous soft robots could play a key role in facing many strategic issues of modern society, like for example **bioremediation and environmental monitoring.** In fact, the increasing impact of industrial and agricultural activities on the environment makes necessary the development of sophisticated means of monitoring environmental pollution and of initiating one-site environmental clean-up. Biodegradable robots could be deployed on-site to monitor pollutant levels and to concentrate, treat and remove pollution. They can be manufactured in large numbers and safely released into the environment. In contrast to conventional non-biodegradable machines which must be constantly tracked and collected at the end of their operational life, biodegradable robots do not need to be tracked or recovered because they will degrade benignly in the environment. Instead of deploying and recovering a small number of robots, hundreds, thousands or even millions of biodegradable robotics could be safely deployed in the knowledge that they will do no harm to the environment. Their safe degradation can also be exploited for the realization of **disposable devices** that can find massive applications as a wide range of household consumer objects from active-ergonomic tools to medical devices and treatments such as active wound dressings. Even more everyday items such as food packaging could be made from active soft robotics: for example, they could bend and twist in hands and impart more information about the contents and its properties than conventional packaging. At last, soft biodegradable electronics can be integrated in **wearables and clothing** as smart and active wearable devices. They can be useful, for instance, to monitor physiological condition or to interact with portable electronic devices. All the above mentioned cases are examples of application fields where the employment of natural and biodegradable raw materials can be particularly beneficial.

These are only few examples that underline the strategic importance of the development of natural-derived and biodegradable soft robotics and electronics devices. The formulation, fabrication and characterization of novel composite smart materials and elements in line with this paradigm is the main purpose of the presented project, as it is reported more in detail in *Section 1.3*. The subsequent integration of each functional element on a single platform or body is equally a fundamental task to be addresses, but it is not dealt with in this work.

1.3 AIM OF THE PROJECT: SOFT BIODEGRADABLE FUNCTIONAL MATERIALS

An autonomous soft robotic system can be seen as a living organism composed by many components, as it is graphically schematized in *Figure 1.3.1*. First, a **body** is required to contain the organism and to provide means of locomotion and actuation through the **limbs**. A **stomach** provides a means of converting environmental energy into a form that the organism can use (e.g. electrical), a **reservoir** is needed to store the produced energy and a **circulatory system** can deliver it throughout the body. With the **sense of touch**, the robot can perceive the nature and the shape of the external environment. Finally, the **brain** is the control system for the organism, in charge of homeostatic regulation, sensor and motor control, reasoning and goal-directed behaviour, helped by a **nervous system** that connects every functional element.

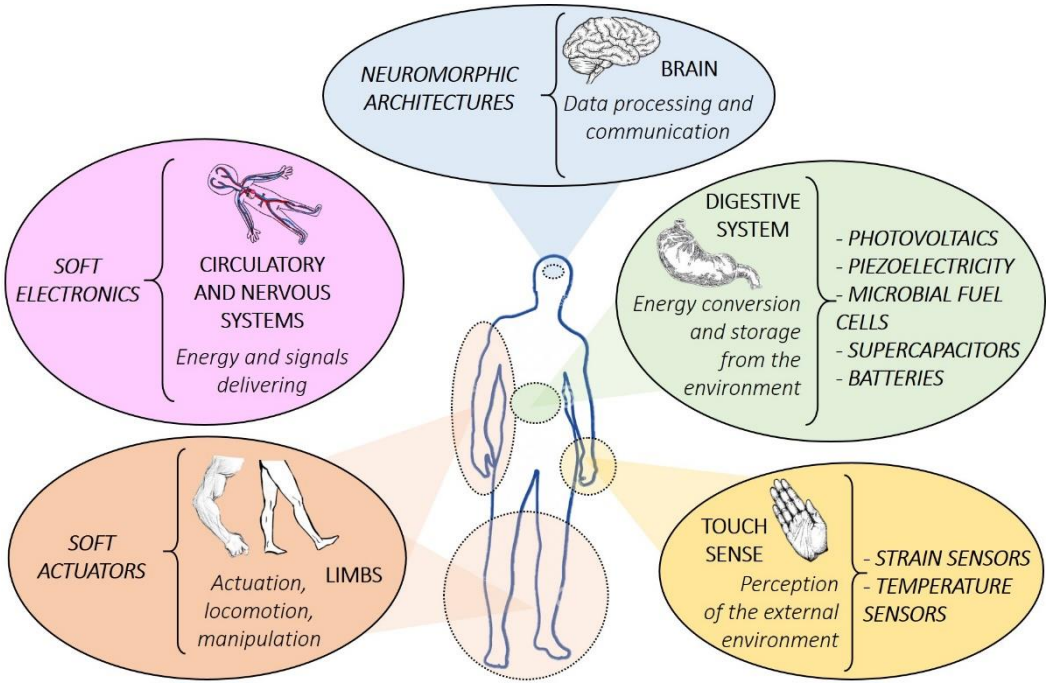

***Figure 1.3.1**. Graphic representation of the parallel between a living organism and a soft robot. Both of them need different smart and functional elements or systems to perform different functions such as mechanical actuation, energy harvesting and storage, sensing and communication.*

Electroactive actuators, supercapacitors, batteries, antennae, piezoelectric elements, strain sensors, electronic circuitry and microbial fuel cells are all examples of functional components that can play the aforementioned roles, but they need to be integrated on soft deformable platforms and interconnected to each other. Moreover, as highlighted in the previous *Section 1.2*, biodegradable soft robots and devices would be of strategic importance in the perspective of environmental sustainability. Then, **natural-derived polymers and substances** should be used as building blocks for the development of such smart components.

The aim of the current Ph.D. project is the use of **natural-derived** and **biodegradable** polymers and substances as building blocks for the development of **smart composite materials** that could operate as functional elements in a soft robotic system or device. The insulant **polymeric matrix** provides soft, flexible and/or stretchable mechanical properties, while the "smart" behaviour is achieved by the integration and the coupling of both **electronic** and **ionic conductors**. In fact, through the combination of different kinds of electrical conduction (electronic and ionic) in a soft solid matrix, it is possible to tightly associate electrical to mechanical energy. *Figure 1.3.2* reports a graphic visualization of the employed building blocks and the obtained smart composite materials.

A hydrophilic polymeric matrix soaked with an aqueous electrolyte forms an **electroactive hydrogel (EAH)**, a soft material able to display a reversible and well-controlled underwater mechanical actuation in response to an applied electric field. This kind of smart material can be used to provide soft locomotion and manipulation in underwater environments. An overview on EAHs and the related results obtained in this project are reported in *Section 2*. Instead, **ionogels** can be obtained by coupling a polymeric matrix with an ionic liquid [140], that is an organic salt, liquid at ambient conditions. Through the fabrication of a couple of compliant conductive electrodes on the opposite sides of the ionogel, electric signals can be used to trigger and control electromechanical soft actuation in plain air, a key feature for soft robots and devices. In this work, traditional office copy paper and a poly(3-hydroxybutyrate) bioplastics are used as biodegradable polymeric building blocks. An overview on such ionogel-metal electroactive composites and the related obtained results are reported in *Section 3*. A similar system can be employed as an **electrolytic double-layer supercapacitor**, able to store electrical energy by means of ionic accumulation. Here, not only the cellulose polymeric matrix, but also the employed ionic liquids are natural-derived and eco-friendly. This theme is dealt with in *Section 4*.

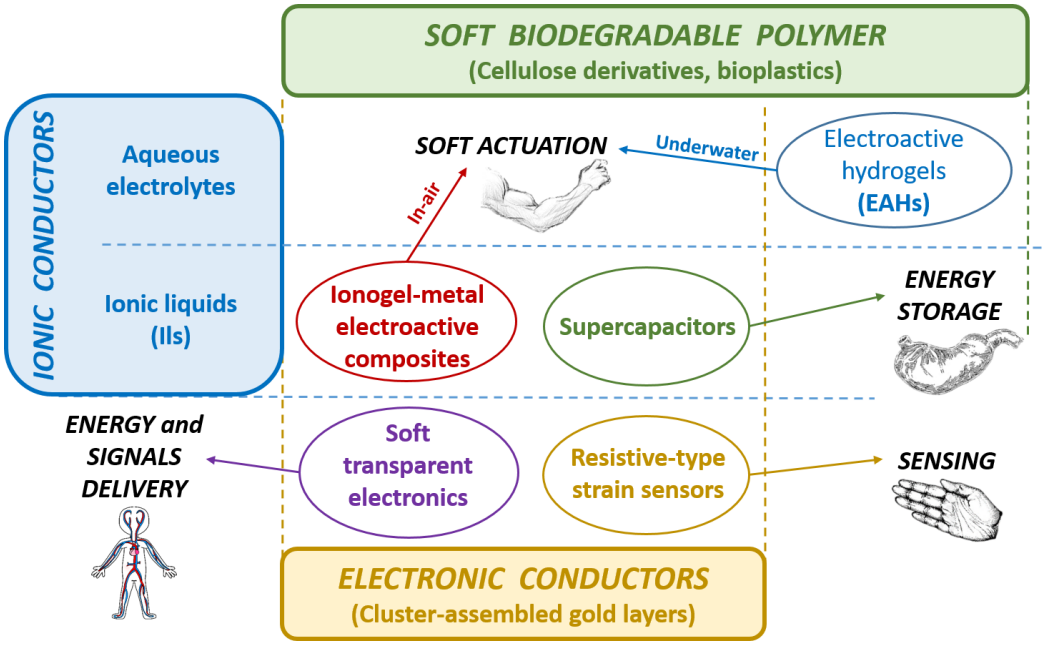

***Figure 1.3.2**. Conceptual map of the smart composite materials developed in the current Ph.D. project. They are obtained by the integration of different biodegradable polymers with ionic and/or electronic conductors and each of them is meant to perform a different function in a soft robotic system or device.*

Finally, **transparent and flexible electronic** circuitry can be achieved through the deposition of thin electronic conductive layers on the surface of soft thin films (in this case, biodegradable and transparent cellulose acetate sheets). Moreover, a variation in the curvature of the sheets is associated with a change in the ohmic resistance of the conductive layer: thanks to this, such composite films can be employed as **strain sensors** for soft robots and devices. *Section 5* reports an overview on the topic and the results obtained in this work. In all these cases, the fabricated electrodes are composed by cluster-assembled gold layers obtained with the use of a **supersonic cluster beam deposition (SCBD) technique**, described in detail in the next *Section 1.4*. The meaning of this work is the development of a set of soft functional composite materials that can be employed to perform different functions and duties in future biodegradable soft robotic systems and devices.

1.4 ENABLING TECHNOLOGY: SUPERSONIC CLUSTER BEAM DEPOSITION (SCBD)

The fabrication of conductive, resilient, well-adherent and durable metal electrodes coupled with soft polymeric materials still constitute a challenging technological task for the realization of electroactive actuators as well as soft electronics. Noble metal conductive electrodes can be deposited on the surface of soft films by means of many techniques: chemical reduction [141,142], hot pressing [143,144], electro-plating [145], sputtering [146], physical vapour deposition [147]. But the mechanical mismatch between the metallic layer and the polymeric films usually leads to low adhesion and delamination under deformation. Carbonaceous species, like active carbon, graphene and nanotubes, as well as conductive polymers, are also employed for the fabrication of thin electrodes by hot pressing [148], layer-by-layer casting or deposition [149], dip, drop or spin coating [150]. However, the manufacturing of such electrodes is usually time-consuming, expensive and it requires high loadings of active material. Like in the case of graphene, several production techniques exist, each of them characterized by advantages and disadvantages [151].

In this work, **supersonic cluster beam deposition (SCBD)** technique is employed for the fabrication of thin and conductive cluster-assembled gold layers on the surface of the different polymeric substrates of choice. A photograph of the experimental apparatus is shown in Figure *1.4.1(a)*, while *Figure 1.4.1(b)* reports a more detailed schematic. Briefly, the Au nanoparticles are produced in a **pulsed micro-plasma cluster source (PMCS)**, where a high-voltage discharge generates an argon plasma that erodes a solid metallic precursor: the ejected Au atoms condense in clusters. The mixture of clusters and inert gas exit the PMCS through a nozzle toward the expansion chamber as a supersonic beam of electrically neutral clusters. Here the nanoparticles are focused and size-selected through an aerodynamic focuser and then they expand as a supersonic beam into the **expansion chamber** kept at the high vacuum pressure of 1×10^{-7} Torr through a turbo-molecular pump with a flow rate of 1900 L/s and backed by a roots pump. Then, the beam intercepts the skimmer, a cone with a 2 mm hole in the summit aimed to maintain a differential vacuum between the expansion chamber and the implantation chamber, to preserve the supersonic characteristic of the beam and to further size select the beam. The skimmer connects the expansion chamber with a **deposition chamber** where the target samples are stored. Here, the clusters are characterized by a size distribution from 3 to 10 nm and a low kinetic energy (0.5 eV per atom) and they hit the substrates.

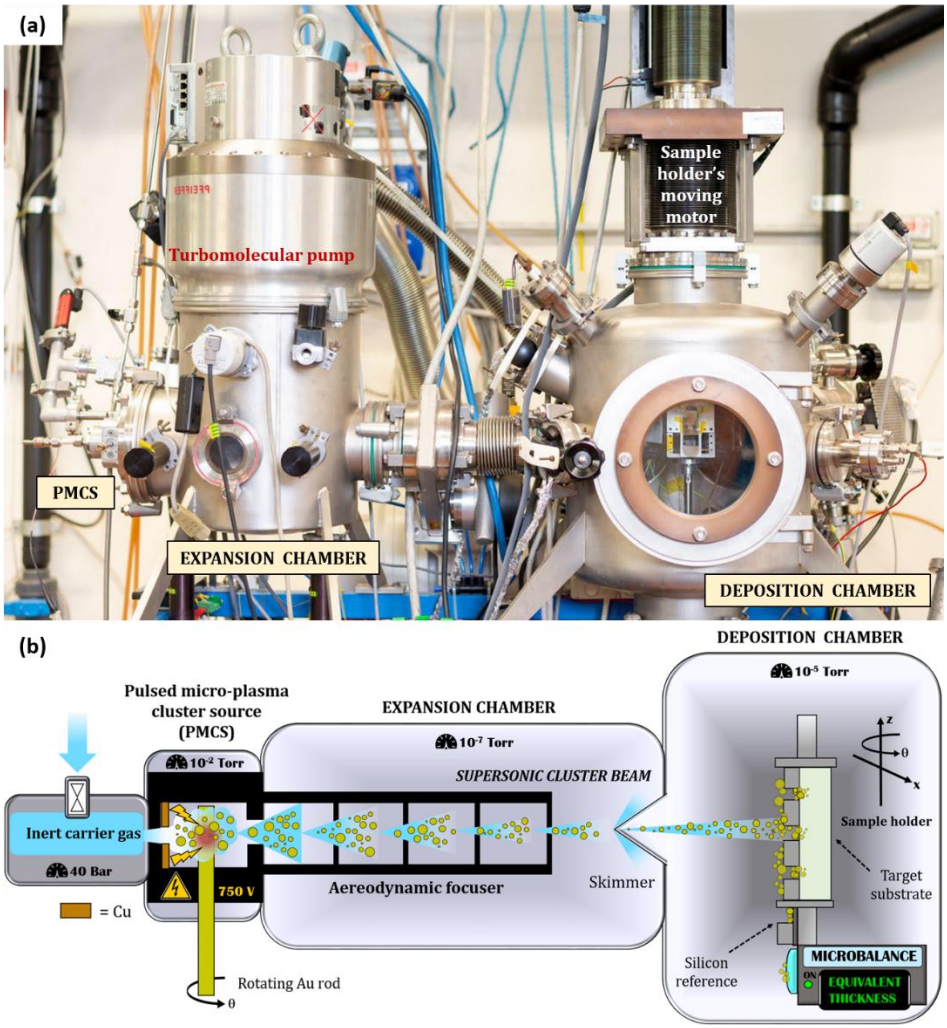

Figure 1.4.1. (a) *Supersonic cluster beam deposition (SCBD) apparatus. The pulsed microplasma cluster source (PMCS) is connected by a nozzle to the expansion chamber, in turn separated from the deposition chamber by a gate (photo by Marco Ferrari, www.marcoferrari.studio).* ***(b)*** *Schematic of the apparatus and working principle of SCBD technique. Initially, with an electric discharge, a plasma of inert gas (argon) is generated in the PMCS chamber: Au atoms are sputtered from a precursor gold rod and condense in neutral clusters. The carrier gas follows a pressure gradient and it carries the clusters though an aerodynamic focuser that selects their size; then, the beam exits from a nozzle and it supersonically expands in the expansion chamber. Finally, the beam passes through a skimmer and it reaches the deposition chamber, where the clusters hit the target substrates (that can be patterned with the use of stencil masks). A quartz microbalance is used to monitor the amount of deposited matter and silicon references can be used to subsequently check the thickness of the deposited layer.*

If the substrate is a soft polymeric material, the clusters enter the polymeric matrix with a **soft implantation**, forming a nanocomposite interface with a gradient of mechanical properties without inducing any chemical or physical alteration [152,153]. The samples are mounted on a moving sample holder that in combination with stencil masks superimposed on the targets, allows large area implantation and patterning. The deposition chamber is kept at a pressure of 1×10^{-5} Torr through a turbo-molecular pump having a flow rate of 520 L/s and backed by the same roots pump used for the expansion chamber. A quartz microbalance is used to measure in real time the total amount of deposited gold and the deposition rate. Here, the operational principles of (*a*) the PMCS and (*b*) the aerodynamic focuser are described more in detail. Then, (*c*) further information about the target samples manipulation and the cluster-assembled Au properties are provided, together with (*d*) a summary of SCBD technique's benefits.

(a) Pulsed micro-plasma cluster source (PMCS)

A PMCS is characterized by high stability in clusters generation and high throughput. Its working principle can be summarized into three stages: the vaporization of the target material, the clusters-gas mixing and the extraction of the clusters from the source. The PMCS source core is composed by a hollow cylindrical ceramic body. Its entrance is matched with a pulsed valve that injects a burst of Argon at high-pressure (40 bar) inside the source. A copper nozzle is placed between the valve and the ceramic body. The ceramic side opposite the valve is connected to a nozzle that provides the gateway to the expansion chamber. The clusters precursor is provided by a metallic rod placed inside the ceramic chamber perpendicularly to its axis. A photograph of is shown in *Figure 1.4.2(a)*. The nanoparticles synthesis process is schematized in *Figure 1.4.2(b)* and it can be summarized as follows: initially, the cavity is kept in vacuum at the same pressure of the connected expansion chamber (~ 10^{-7} Torr). Then the valve is opened for about 250 µs letting the argon (Ar) flows in. Here, the high-pressure gas creates a high-pressure and high-density region (smaller than one millimetre) close to the metal rod, for thermodynamic reasons [154]. After 490 µs since the valve closed, a voltage of 750 V is applied for 80 µs between the metal rod (cathode) and the copper nozzle (anode). The high potential difference triggers a discharge that leads to the gas ionization. The so produced ions accelerate under the high electric field towards the cathode, forming in this way a plasma plume concentrated in the small high density region, inducing the plasma to erode the rod. In order to allow a uniform sputtering process all along the period while the source is used, the rod is kept rotating by a stepper motor. The erosion of the rod leads to the formation of an oversaturated gas of metal atoms, which condense inside the ceramic body forming metal clusters suspended in the inert gas. Finally, the pressure difference between the source and the expansion chamber drives the cluster-gas mixture through the nozzle to the expansion chamber, and accelerates it to a supersonic-speed up to 1000 m/s [154].

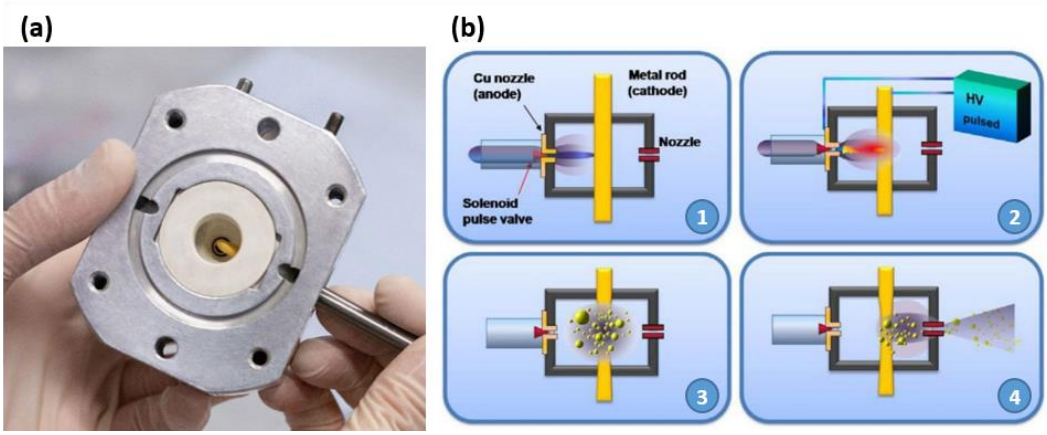

Figure 1.4.2. (a) *Photograph of the pulsed micro-plasma cluster source (PMCS). It can be seen the ceramic body encapsulated inside an aluminium housing, the tip of the gold rod inside the inner chamber and a titanium rod-holder (photo by Marco Ferrari, www.marcoferrari.studio).* ***(b)*** *Schematic working principle of the PMCS: initially, the solenoid valve opens for about 300 microseconds, allowing the entry of Argon gas at 40 bars. A voltage of about 750 V is then applied at the cathode, leading to the ionization of the gas and to the formation of a plasma plume able to sputters the metal atoms of the rod. The ablated metal atoms aggregate to form clusters and then, due to the pressure difference with the expansion chamber, a supersonic expansion of the cluster-gas mixture is established, leading to the evacuation of the mixture from the source* [155].

(b) Aerodynamic focuser

The beam of neutral metallic nanoparticles enters the deposition chamber and it has a divergence less than 50 mrad [156] and a clusters size distribution centred around 4 nm [152]. Such highly focused beam is obtained through the aerodynamic focuser that consists of a series of hollow cylinders having an aerodynamic lens at the end. A schematic is shown in *Figure 1.4.3*. These lenses consist of metal discs with a central hole with a diameter smaller than the internal diameter of the hollow cylinder. The unfocused beam is forced to pass through a series of these hollow cylinders and lenses. The sudden change in diameter occurring at the end of every cylinder results in an abrupt change in the direction of flow lines. This leads to a narrowing of the beam diameter and a size-select effect on the mass of the metal clusters [157]. In this work, 4 lenses stages are used: the firsts 3 lenses have a 2 mm hole while the latter has a 1 mm hole.

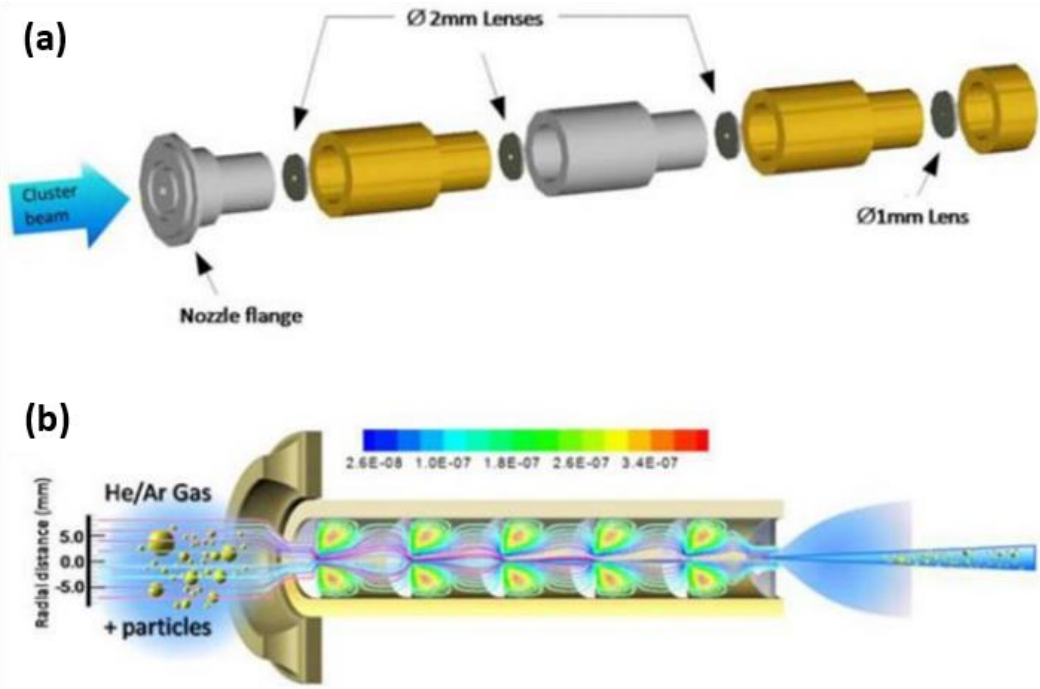

Figure 1.4.3. (a) *Expanded view of the aerodynamic focuser used in the SCBI apparatus: the three aerodynamic lenses having a diameter of 2 mm and the last with a diameter of 1 mm are visible. The cylinders that form the focuser are made of steel and brass and mounted alternately, in order to avoid the seizing of the threads.* ***(b)*** *Schematic representation of the aerodynamic focuser and its working principle* [155].

(c) Targets manipulation and cluster-assembled Au properties

Figure 1.4.4 reports a photograph of the inner cavity of the deposition chamber. It can be seen a hexagonal samples holder provided with three stepper motors: two of them are dedicated to move the samples holder along the plane perpendicular to the direction of the cluster beam and the latter is used to rotate it around its z-axis. With this system, it is possible to move the target substrates in different direction in order to have the cluster beam covering large area samples and also to deposit the metal clusters over multiple samples in the same deposition process. Moreover, every single side of the hexagonal samples holder could be provided with a smaller sample holder equipped with servomotors that can rotate by 180 degrees with a high angular resolution, allowing a double face implantation. All of this constitutes a considerable speed up for the fabrication of nanocomposite materials.

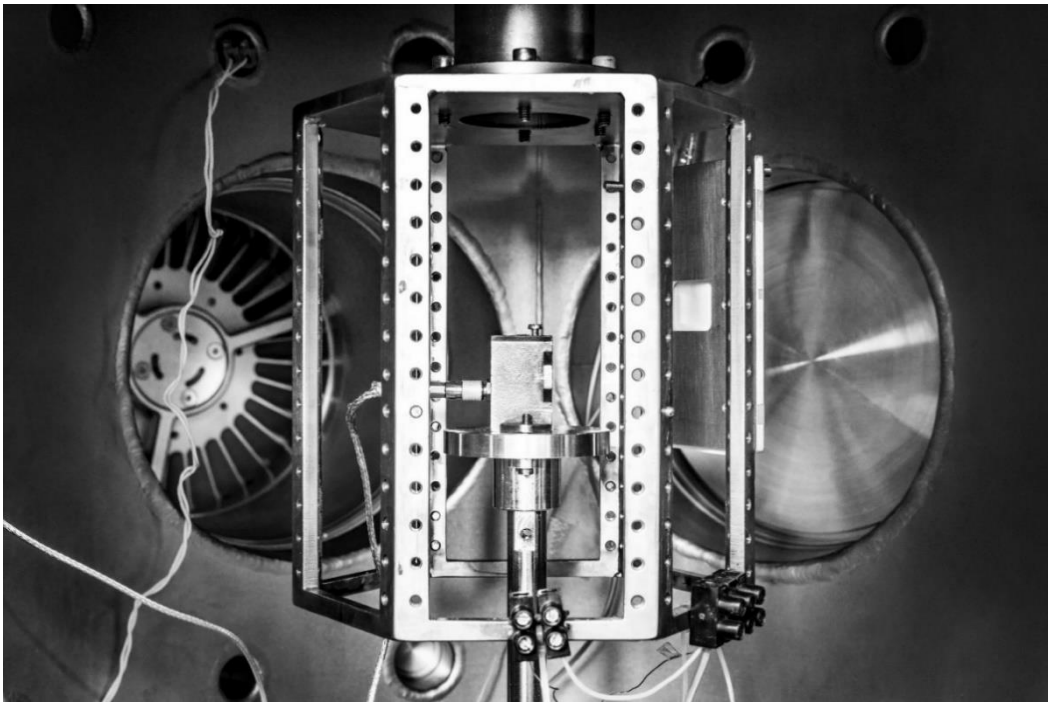

Figure 1.4.4. *Photograph of the position chamber's inner cavity. It can be seen the hexagonal samples holder and the quartz microbalance placed in its centre (photo by Marco Ferrari, www.marcoferrari.studio).*

As can be seen from the picture, a **quartz microbalance** is placed in the centre of the samples holder. By moving the holder on the z- or the x-axis, it is possible to have the cluster beam to alternatively hit both the target substrates and the microbalance: in this way **the exact mass of the deposited Au can be measured in real time**. This is an extremely useful tool that allows to deposit specific target amounts of Au clusters with high precision. Knowing the density of the Au, it should be possible to use the measured mass to calculate the corresponding thickness of the deposited film. However, cluster-assembled Au films have a different porosity and density than traditional crystalline Au (19.30 g/cm^3); moreover, when the clusters hit a soft polymeric matrix, they partially implant into the surface and it is not easy to foresee the exact degree of implantation and the resulting thickness of the metallic layer. Therefore, it is useful to introduce a new quantity named ***equivalent thickness*** **(t_{eq})**, defined as the thickness of the metal thin film produced by the same amount of clusters and deposited on rigid and highly smooth substrates (like glass or silicon) where no implantation phenomena occur.

The implantation chamber is provided also with several electrical contacts exploited to measure the electrical properties of the nanocomposites during the deposition and the growing of the metallic layer. Thanks to this and to presence of the quartz microbalance, it is possible to measure in real time both the electrical conductivity and the equivalent thickness and their values can be univocally correlated. In this way, then, it is possible to target specific ohmic resistance values by depositing the corresponding amount of metallic clusters.

(d) Benefits of SCBD technique

After a detailed explanation of its operational features, here's a summary of the benefits correlated to the use of the SCBD technique, that can be regarded also as a sort of printing technology:

- Formation of **cluster-assembled metallic electrodes** characterized by a **higher surface area** and porosity than closed-packed atomic aggregates of the same elemental specie. The clusters size distribution is centred around 4 nm;
- A highly collimated supersonic beam that allow an **easy patterning** with the use of stencil masks;
- **High control and precision** (nm-range) on the amount of deposited metal;
- **Tuneable ohmic resistance** of the deposited metallic layers;
- A low kinetic energy of the clusters (0.5 eV per atom) that does not lead to any chemical of physical modifications of the target substrates;
- **Partial interpenetration** of the clusters inside a soft polymeric matrix, which grants a **robust adhesion** and a nanostructured interface with high surface area;
- **Solvent-free** and **room-temperature** technique;
- Suited for the metallization of every kind of material that can undergo a vacuum treatment;
- Suitable for the production of clusters of a wide range of metals and metal oxides, as well as carbon, as long as there is a conductive solid precursor.

2. Cellulose-Based Electroactive Hydrogels (EAHs)

2.1 OVERVIEW ON EAHs UNDERWATER ACTUATORS

2.1.1 Hydrogels and electroactivity

Soft stimuli-responsive materials are extremely promising for applications in soft robotics. They combine soft mechanical properties similar to those of biological tissues (elastic modulus usually between 10^3 and 10^8 Pa) with the ability to sense external stimuli and react to them by changing their physical and/or chemical properties. In many cases, this results in a macroscopic deformation. Then, they can be used as smart sensors but also actuators: external stimuli can be used to control their properties and their change of shape in order to carry out soft mechanical motion.

Among many kinds of stimuli-responsive materials [36,158], electro-responsive ones are extremely interesting, since nowadays electric signals can be easily generated and controlled with extreme precision. **Electroactive hydrogels (EAHs)** are hydrophilic soft polymeric materials with the intrinsic ability to controllably change their shape and size in response to electrical stimuli and they can display soft mechanical actuation in underwater environments at micro and meso scale [159–162].

Basically, a hydrogel is obtained when solvated polymeric chains start to link together forming highly branched macromolecules. The obtained mixture of is known as “sol” because the molecules are still dissolved in the solvent. If the branching process continues, then at some point all the macromolecules bind to each other and a unique non-soluble fully interconnected structure is formed: a gel. This fully interconnected structure is called gel [163]. The interconnections between the different chains can result from physical interactions like hydrogen bonds, ionic interactions or entanglements, forming so-called physical gels, or from chemical bonds, forming chemical gels. When the polymeric chains of a gel possess hydrophilic side groups and the inner polymeric structure can be stretched to host other molecules, gels can absorb a large amount of water and they are called hydrogel. The presence of liquid-like behavior (viscosity) on molecular length scales combined with solid-like macroscopic properties (elasticity) makes them very unique systems, with many aspects in common with biological tissues, such as softness, high water content and water permeability [164]. A schematic illustration and a picture of a polymeric hydrogel are presented in *Figure 2.1.1*.

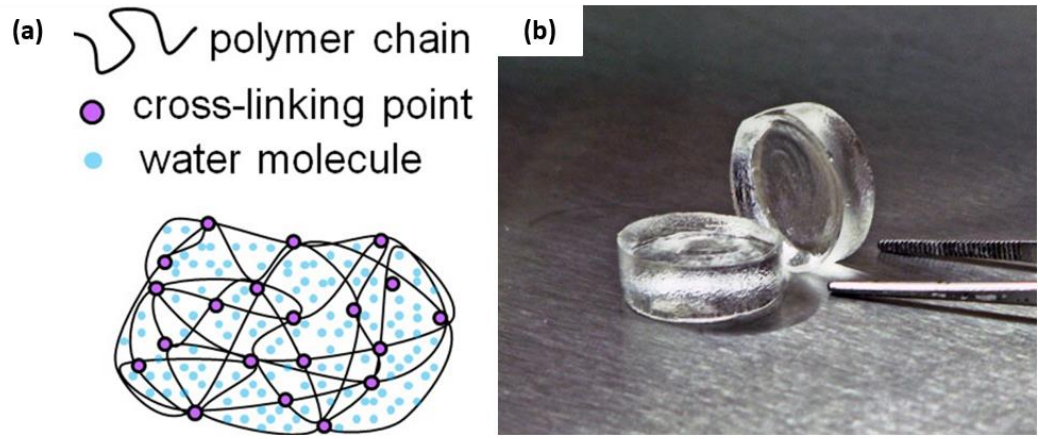

Figure 2.1.1. (a) *A schematic representation and* ***(b)*** *a picture of an average cross-linked polymeric hydrogel that has absorbed water molecules.*

Even though they can be widely engineered and functionalized to address many purposes, standard hydrogels are inert materials, mainly characterized by their mechanical properties and their water absorption. Electroactive properties arise if the polymeric backbone bears covalently bound ionic groups (fixed to the polymeric matrix and unable to move independently) coupled by mobile counterions that are free to move in the solvent inside the gel under the effect of an applied electric field. All electroactive hydrogels are then composed by these elements: a stretchable and flexible polymeric matrix, an absorbed aqueous solution, covalently bound ionic groups and mobile counter-ions (see *Figure 2.1.2(a)*). In an underwater environment, only the mobile counterions can move accordingly under the effect of an applied electric field and the resulting asymmetric ionic migration is the cause of the electro-mechanical deformation of the gel. An example of EAH underwater actuation example is reported in *Figure 2.1.2(b)*.

A typical example is represented by polyacrylic acid gel deprotonated with NaOH, so that Na^+ can act as the mobile counter ion of bound COO^- anionic groups [165]. *Figure 2.1.3* reports the chemical structure of a deprotonated polyacrylic acid hydrogel cross-linked with ethylene glycol diacrylate (EGDA).

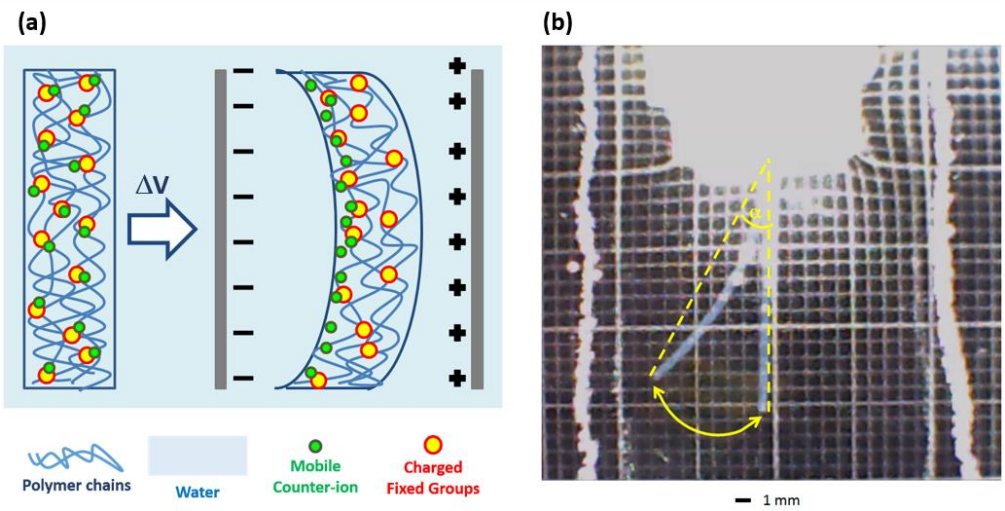

Figure 2.1.2. (a) *Schematic representation of the structure and the main elements of an electroactive hydrogel: a three-dimensional polymeric matrix, covalently bound ionic groups, mobile counter-ions and the water. Under the application of an electric field, only the mobile ions can migrate and the asymmetric redistribution of ions and water leads to a macroscopic deformation;* ***(b)*** *The overlap of two pictures acquired during the underwater electromechanical deformation of a real EAH when an electric field was applied by mean of two platinum electrodes* [162].

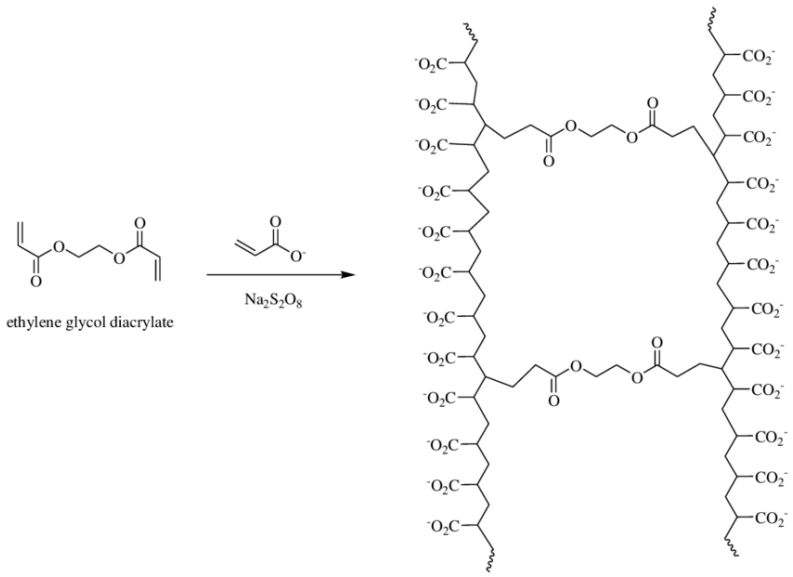

Figure 2.1.3. *Chemical structure of a deprotonated polyacrylic acid (PAA) hydrogel cross-linked with ethylene glycol diacrylate (EGDA).*

EAHs are usually characterized by studying their **swelling/shrinking equilibrium** in different solutions, their **mechanical properties** by tensile tests and their **electroactivity** by monitoring their spatial deformation under the application of an electric field. Due to their capability to readily convert electrical energy into mechanical motion, EAHs have huge potential to be employed as sensors and actuators in a variety of forefront technological applications, such as underwater soft robotics, bio-hybrid systems, cells-based devices and haptic interfaces production [166–169]; EAHs have been widely studied for applications in biotechnologies, soft robotics and smart fluidics [160,170,171], although few of them come from natural polymers [172,173] an increasingly important feature for present and future technology.

2.1.2 Electro-mechanical model

Several distinct mechanisms have been proposed (in some cases including quantitative predictions) [174–178] and, in each case, specific experimental results were interpreted as corroborating a determined mechanism. The variety of interpretations arises from the complexity of the system, the broad range of concepts involved (chemical equilibrium, polymer physics, osmosis, electro-osmosis, electrostatics in electrolytes, electrophoresis, electrochemistry, etc.) and the large number of experimental variables (different gels, synthesis protocols, experimental configurations).

When an electro-active hydrogel is immersed in a saline solution with a lower ionic concentration than the inner one (like in the case studied in this work), the electro-mechanical deformation is due to the **dynamic accumulation and depletion of ions** on the two different sides of the gel at the solution interface in the presence of the applied electric field [177]. More in detail, the mobile Na^+ cations accumulate at the cathodic gel-solution interface, causing a decrease in the osmotic pressure localized therein. As a result, that portion of the hydrogel shrinks. At the same time, the anodic gel-solution interface undergoes a dynamic depletion of Na^+ cations, so that the osmotic pressure increases and that region of the hydrogel swells. As a consequence of this asymmetric swelling/shrinking equilibrium, a cantilever-shaped hydrogel blocked at one side will bend towards the cathode. *Figure 2.1.4* reports a schematic visual explanation of such mechanism. According to this model, the swelling influences the actuation performance in two ways. Firstly, the electro-mechanical actuation is more pronounced in those ambient solutions where the variations of the swelling ratio S_r are larger for small variations of the local Na^+ concentration. Furthermore, the mechanical actuation also depends on the cantilever's thickness and the polymer chain stretchability, which depend, in turn, on the hydrogel swelling entity.

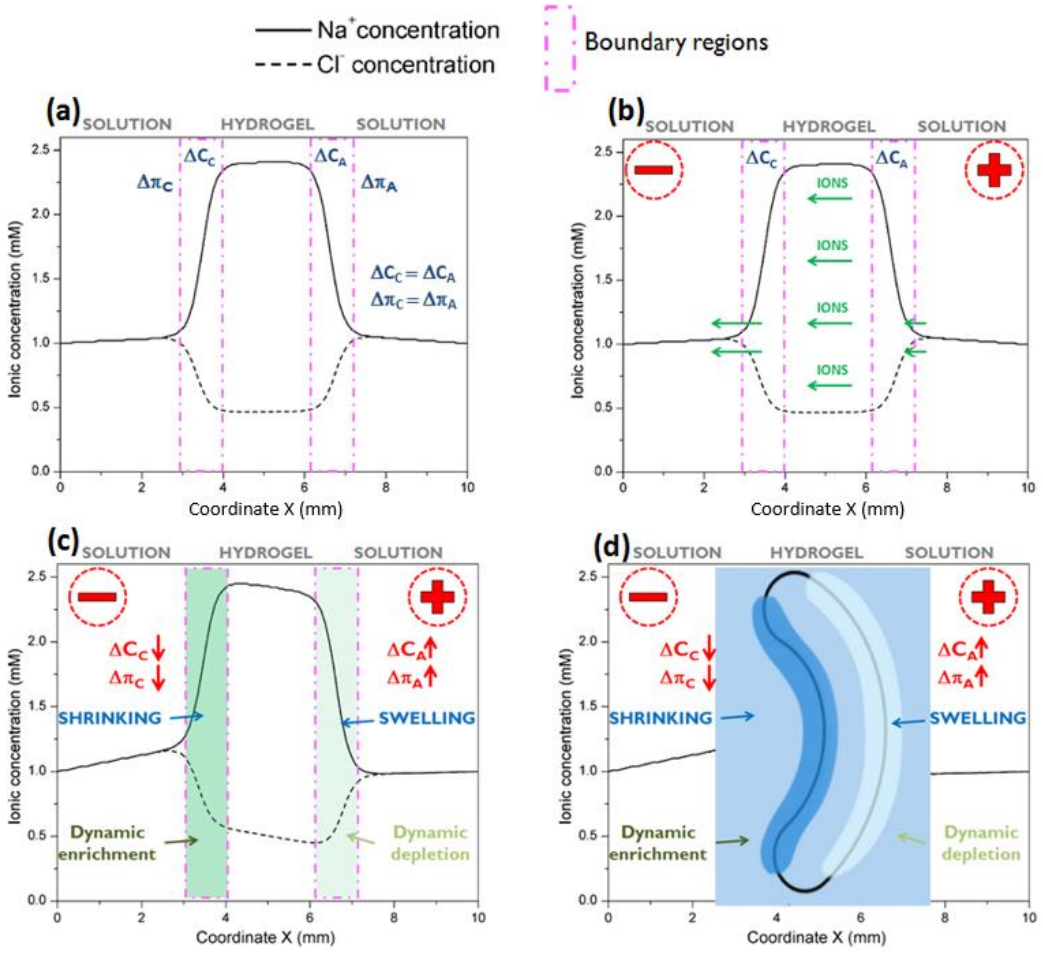

Figure 2.1.4. *Na^+ and Cl^- mobile ions concentration profiles before and during the application of a ΔV; outside the gel Na^+ and Cl^- are in equal amount, while inside the gel there are additional Na^+ associated to anion groups covalently bound at the polymeric chains.* ***(a)*** *The difference in the ionic concentration inside and outside the hydrogel as well as the osmotic pressure is equal at both sides (anodic and cathodic), then the swelling in uniform;* ***(b)*** *At the application of an electric field, ions begin to migrate and the higher flux is towards the cathode (since Na^+ are more than Cl^-);* ***(c)*** *A dynamic enrichment of ions occurs at the anodic boundary region, leading to an overall reduction in the ionic difference and in the osmotic pressure, that results in the shrinking of that area; at the anodic boundary region, an opposite phenomenon occurs and it undergoes a more pronounced swelling;* ***(d)*** *the induced asymmetric swelling/shrinking results in a macroscopic deformation of the EAH* [177].

2.1.3 Challenges of EAHs and aim of the research

Electroresponsiveness at low applied voltages is of particular interest, especially under the standard potential of water electrolysis (1.23 V) [179]. **Sub-volt electromechanical actuation** is particular difficult to obtain with electroactive actuators macroscopic in two dimensions (at least). Furthermore, the materials mechanical properties are of primary importance to ensure high durability of the system and to increase the value of the net forces triggered by the deformation; in this sense, Young's modulus values larger of at least 10^5 Pa are desirable [180]. Also, **robust hydrogel** could be fabricated or modeled into more articulated shapes able to provide a more complex and sophisticated three-dimensional soft actuation.

In order to improve these responsive and structural key features, the formulation and development of EAHs-based nanocomposites constitutes a strategic aspect [181]: this can be achieved by incorporating organic or inorganic nanoparticles or nanostructures into the polymeric matrix during the synthesis step [182,183]. Depending on their nature and on the interactions with the polymer macromolecular structure, the **nanofillers** can either enhance constitutive characteristics of the starting material (e.g. mechanical or thermal properties) or trigger specific physical and chemical properties, so that they can be used to provide new functionalities and to obtain engineered nanocomposites with tailored functional properties [184]. EAHs-based nanocomposites have already been produced with the use of anionic and cationic polymeric networks (e.g. poly acrylic acid, polystyrene sulfonate and chitosan) and different nanofillers, ranging from conductive carbonaceous nanostructures to inorganic nanoclays [185–187]. Significant improvements in the mechanical properties have been observed for relatively low filler loadings (from 1% wt to 10% wt). Moreover, besides being a structural reinforcement for the hydrogels, carbon-based nanostructures also favour the mobile ions migration across the polyelectrolyte, thanks to their charge transfer and ion exchange capabilities [188]. However, this strategy did not lead to a significant improvement of the nanocomposites sensitivity to the electric field and the actuation voltages for macroscopic benders were still larger than the water splitting potential threshold.

One the main objectives of this research is the use of natural and biodegradable polymers to obtain smart materials. Concerning electroactive hydrogels, two cases can be distinguished: green polymers can be used *(a)* as nanofillers inside the hydrogel matrix, or *(b)* they can constitute themselves the main polymeric network of an EAH.

(a) Use of cellulose nanocrystals (CNCs) as nanofillers

Among various nanofillers, cellulose rod-like nanocrystals (CNCs) have recently attracted a great deal of interest due to their appealing properties, such as high surface area, low density, mechanical strength and piezoelectricity [189]. Moreover, they can be chemically modified with simple processes, and are readily available, renewable and biodegradable. Hydrogels/CNCs-based nanocomposites have been already developed using temperature, light, pH and ionic strength responsive host macromolecular networks [190–193]. The nanocrystals contributed to the matrix formation by physically cross-linking the polymer chains through hydrogen bonding and its inclusion resulted in an increase of the material mechanical properties, as well as in a modulation of its swelling ability and responsive behaviour. However, according to bibliographic research, no examples of nanocomposites based on electro-active hydrogels with physically embedded CNCs operating as bending actuators are reported in the literature so far. Nevertheless, the use of CNCs as nanofillers for electro-active hydrogels would be an interesting strategy to produce tough and high-performance electro responsive soft systems, able to display sub-volt electromechanical actuation with low power consumption and minimum perturbation of the surrounding environment.

The objective of the present work is the physical embedding of **cellulose nanocrystals** into a vinylic-based electroactive hydrogel [162], in order to obtain a hybrid EAH/CNCs nanocomposite material with improved electroresponsiveness and mechanical properties. Considering that higher robustness allowed an easier shaping of the samples, the nanocomposite hydrogel is also used to design and manufacture a prototype with many actuators able to bend together and to display a more complex three-dimensional soft actuation, interesting for applications in the fields of microfluidic and underwater soft motion. More specifically, the system design is inspired by underwater valves or pumps able to “open” and “close” regulating the fluid fluxes, or by ciliate organisms composed by thin and soft wedges through which they can provide underwater mobility. The detailed results are presented in *Section 2.2* and they are also reported in a scientific paper published by *Smart Materials and Structures* [194].

(b) Cellulose-based EAH to mimic algae fluctuations

Cellulose is a natural-derived polymer and its use in the context of electroactive hydrogel can allow to obtain green and biodegradable soft actuators free from petroleum-derived or toxic reagents. Many examples of cellulose-based hydrogels obtained through physical or chemical cross-linking can be found in the literature for applications in many fields, such as drug delivery, tissue engineering and biotechnology [195]. In recent years also EAHs have been developed using natural polymers

[133,172,173,196], an increasingly important feature for present and future technology, but according to bibliographic research there are no examples of all-cellulose electroactive hydrogels used as underwater electromechanical actuators nor to mimic to effectively mimic the behaviour of biological species.

A case of particular interest is the **fluctuating motion of natural-occurring algae forests**. In aquatic ecosystems, both marine or fluvial, algae and aquatic plants play many roles: they are primary producers of organic matter and micro-habitats for an enormous fauna of microorganisms; they contribute to the self-purification of water and they cause a local slowdown of the water flow. They are renowned for their antifouling properties, so interesting and efficient that many studies tried to replicate them with artificial solutions [197,198]. Considering also their use as nutritious food in human society, for many years algae have been massively cultured in natural, controlled or artificial environments [199] and many studies have been tried to understand how external factors affect their growth and properties. One of the key factors is the hydrodynamic environment and the water flow that causes the movement and fluctuations of algae [200–206]. Such motion influences their growth and productivity [207], the exchanges of nutrients and carbon dioxide as well the rates of photosynthesis [208]. Although there is a lot of research about natural algae, few examples can be found regarding the use of artificial ones. Materials science can help in finding new materials able to mimic some of the typical properties of algae, that can be used for specific applications like Chapman et al. did [198], but also to create hybrid habitats where artificial algae can cohabit with other living organisms [200]. A novel approach combining smart materials and high-definition free-form manufacture technologies can be explored and electroactive hydrogels (EAHs) may represent the material of choice.

The purpose of the reported project is to combine the formulation of smart and **cellulose-derived polymers** with **3D printing techniques**, in order to demonstrate that green EAHs can be synthesized and used to design and realize artificial algae forests whose motion can be finely controlled thanks to electroactive properties and to the design of the system. In this way very specific motion patterns can be induced not with a water flow but with low power electric impulses and in future works it will be possible to study how these patterns influence the surrounding habitat (natural or artificial, which can include living organisms, microorganisms, sediments, particulate, other aquatic plants). Fused Filament Fabrication (FFF) is the technique of choice to design and manufacture a compact yet versatile system able to integrate many hydrogel's samples and to control their motion, mimicking the fluctuations of a small forest of algae. In *Section 2.3* a preliminary study is reported, where no biological species are involved yet. The obtained results are also reported in a scientific paper published by *Materials Research Society – Communications* [209].

2.2 CELLULOSE NANOCRYSTALS EMBEDDED IN POLY(HEMA-co-AN-co-VBS) EAH

2.2.1 Cellulose nanocrystals (CNCs) and hydrogels synthesis

An aqueous suspension of cellulose nanocrystals (CNCs) was obtained through the acidic hydrolysis of the amorphous regions of cellulose fibres [192] by the group of Prof. Mauro Comes Franchini in the Department of Chemistry of the University of Bologna. A schematic of the nanocrystals process is reported in *Figure 2.2.1(a)*, where an acidic hydrolysis was carried out. The resulting suspension had a concentration of 13 mg/mL and the nanocrystals possessed a rod-like shape with a length of 1–10 µm and a diameter of 30–50 nm, as revealed by SEM images (*Figure 2.2.1(b)*). Their physical properties are almost the same of longer cellulose microfibrils and some of their more interesting features are mechanical strength, renewability and biodegradability. The use of sulphuric acid in the hydrolysis process resulted in the functionalization of some of the cellulose hydroxyl side groups with sulfonates and the zeta potential (ζ) measurements revealed a negative value of −51 mV (signal of good stability). More details about CNCs synthesis and characterization can be found in *Section 6.1.1(a)*. Their mechanical strength and the presence of covalently bound anionic groups are the main features because of which it is worth to use them as nanofillers inside the polymeric matrix of an electroactive hydrogel.

To synthesize thin films of electroactive hydrogel a UV radical photo-polymerization process was carried out on an aqueous solution containing the three different vinylic co-monomers: 2-hydroxyethylmethacrylate (HEMA), acrylonitrile (AN) and sodium 4-vinylbenzensulfonate (Na-4-VBS). HEMA is the main biocompatible and hydrophilic specie, providing features typical of hydrogels. AN was used to improve the mechanical properties, more precisely the tensile strength and the elongation at break [210]. Na-4-VBS provides both the covalently bound anionic groups and the mobile counterions and it is responsible for the electroactive properties of the hydrogel. A monomers molar ratio of 65:30:5 was employed. Ethylene glycol dimethacrylate (EGDMA) was used as the cross-linker, necessary to keep together the growing polymeric chains and to form a three-dimensional material, while 2,2-dimethoxy-2-phenylacetophenone (DMPA) was used as UV photo-initiator.

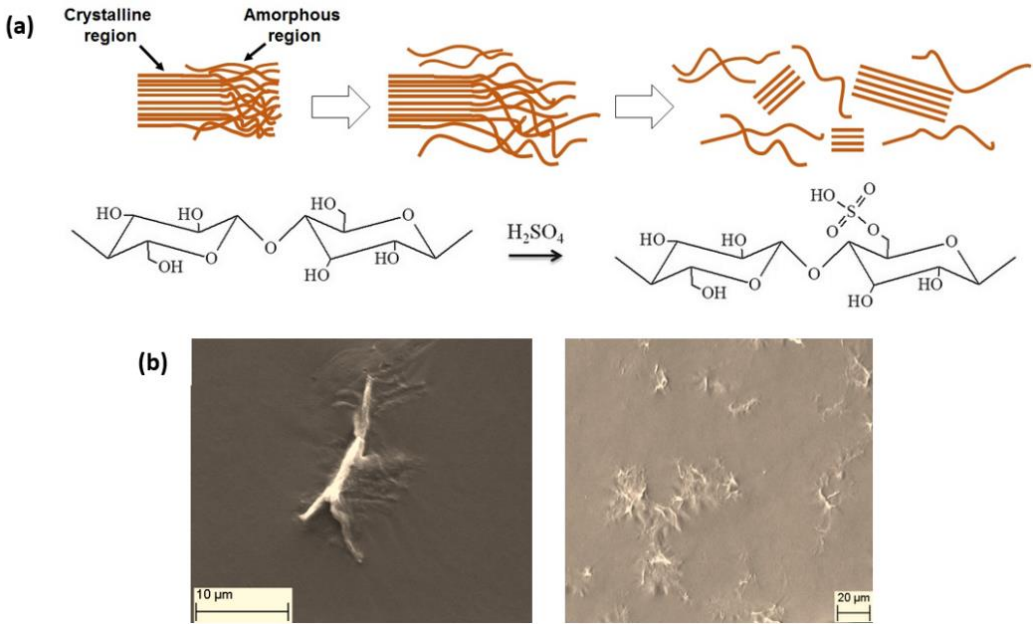

Figure 2.2.1. (a) *Schematic of the acidic hydrolysis of the fibers amorphous regions, leading to sulfonate-bearing cellulose nanocrystals* ***(b)*** *SEM images showing the morphology and the dimensions of the obtained cellulose nanocrystals (CNCs).* [194]

Different amounts of cellulose nanocrystals were added to the polymerizing mixture, in order to act as nanofillers inside the polymeric matrix, varying their w/w ratio with respect to the overall weight of the reactants used: 0.10% (CNC0.1%), 0.42% (CNC0.4%), 0.83% (CNC0.8%) and 1.44% (CNC1.4%). Hydrogels without nanocrystals (CNC0) were also synthesized for comparison. The resulting mixture was injected into a molding apparatus and exposed to UV light to start the polymerization process. According to the thickness of the spacers employed, it was possible to achieve freestanding layers of the composite materials with thicknesses of 100 and 50 µm in their relaxed state straight after synthesis. A schematic of the nanocomposites fabrication protocol and of the cross-linked hydrogel structure is reported in *Figure 2.2.2*. More details about the synthesis procedure can be found in *Section 6.1.1(a)*. Its advantages can be considered to be its easiness, speed and the absence of organic solvents.

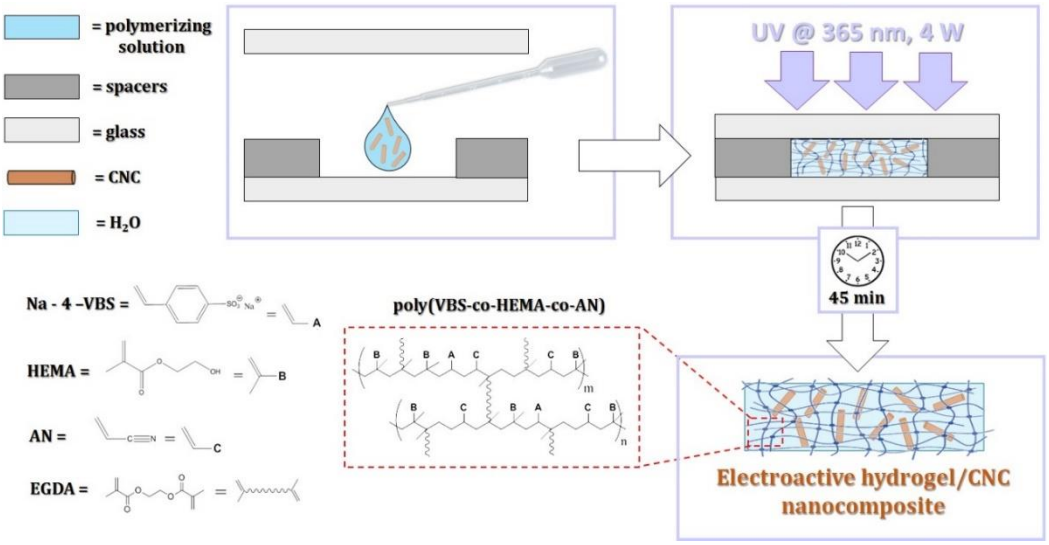

Figure 2.2.2. *Manufacturing protocol for the poly(HEMA-co-AN-co-VBS)-CNCs nanocomposites. The chemical structures of the polymer and its monomers are shown* [194].

2.2.2 Swelling and mechanical properties

Hydrogels water absorption is due to the hydrophilicity of the polymeric structure and to the osmotic pressure arising when the ionic concentration inside the gel (C_g) is higher than the concentration in the surrounding solution (C_s). When a hydrogel is immersed in aqueous solutions with low ionic concentrations, it absorbs water molecules inside its polymeric network and it increases in size (swelling); when the surrounding ionic concentration increases, water molecules are expelled and the hydrogel's size decreases (shrinking). The structural reticulation degree also influences the maximum swelling of a hydrogel: usually, a high cross-linking limits the water absorption, and vice versa. Such swelling/shrinking equilibrium is of great importance for electroactivity in EAHs, in fact electromechanical deformation is a consequence of an anisotropic swelling/shrinking induced by an asymmetric ionic migration under the application of an electric field (according to the dynamic enrichment/depletion model [177]).

Because of this, the swelling of poly(HEMA-co-AN-co-VBS) – CNCs was studied in aqueous solutions with different amounts of NaCl (their preparation is described in *Section 6.1.2(a)*). *Figure 2.2.3* reports the values of the Swelling ratio S_r for all the hydrogel samples. The swelling behaviour of CNC0 showed a logarithmic-like trend, with S_r values being higher in diluted NaCl solutions and in pure water. More details about the swelling/shrinking equilibrium of poly(VBS-co-HEMA-co-AN) without cellulose nanocrystals can be found a previous work [162]. The swelling ratios of samples embedded with CNCs are systematically slightly lower than those of CNC0, especially in the more diluted solutions.

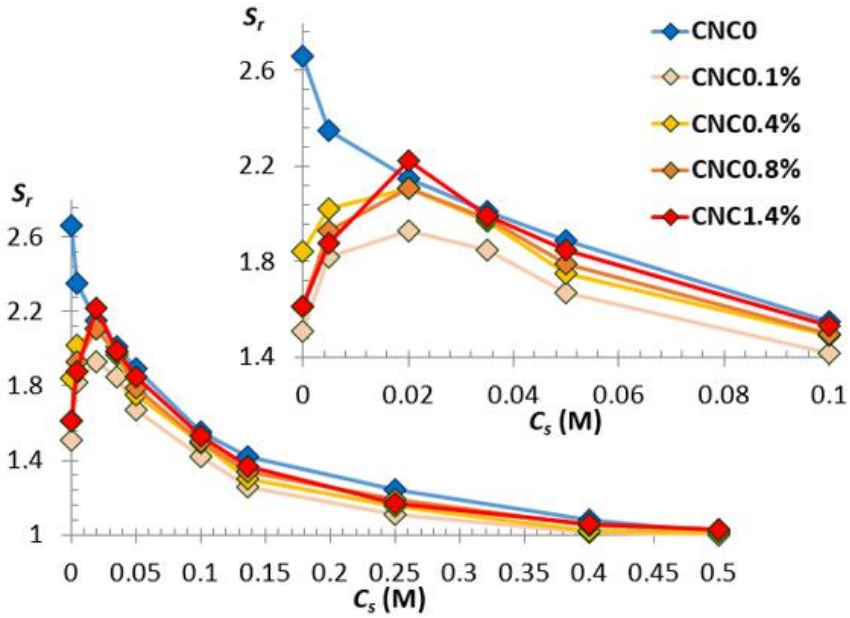

Figure 2.2.3. *Graph reporting the values of the swelling ratio S_r of the hydrogels, plotted against the NaCl concentration of the aqueous solution where they were immersed; S_r showed to be higher in diluted NaCl solutions and systematically slightly lower for the nanocomposite hydrogels with embedded CNCs* [194].

This behaviour can be interpreted by considering two main factors. First, CNCs act as nanofillers inside the gel and they occupy a portion of the polymeric matrix, forming hydrogen bonds with the polymer chains and because of this their presence reduces the amount of water molecules which can be absorbed by the material. In contrast with this effect, the role of the CNCs superficial sulfonate groups must be taken into account. In fact, these sulfonates are deprotonated at neutral pH and they can drag a number of Na^+ cations from the outside solution inside the gel matrix, increasing the inner ionic concentration C_g, the osmotic pressure and the overall swelling. It is therefore

reasonable to speculate that in saline solutions the presence of CNCs affects the hydrogels swelling entity by mean of two opposite effects. The overall S_r values resulted to be lower than the ones of CNC0, especially in the more diluted NaCl solutions, where the number of Na^+ cations to drag in is minimum (or null in the case of pure water).

Mechanical tensile tests were conducted on CNC0 and CNC1.4% samples in order to assess how the presence of CNCs nanofillers affected the mechanical properties of the electroactive hydrogels. Stress–strain curves are reported in *Figure 2.2.4*: as can be seen, both samples showed the same elastic behaviour up to an elongation of about 13% of their original length. After this elongation, the breaking point was immediately reached without any plastic deformation. This behaviour is not influenced by the presence of CNCs. On the other hand, the Young's modulus of the two materials was easily calculated as (120 ± 3) kPa for CNC0 and (200 ± 2) kPa for CNC1.4%. These measurements assessed the potential of CNCs to operate as a reinforcement for the gel even at small filler amounts (1.4% w/w in the present case) by enhancing the Young's modulus of about the 60% of its original value and the tensile strength also increased from a value of 17 kPa to 25.5 kPa, which constitutes a significant improvement of the hydrogel's mechanical properties. More detailed information on the experimental setup and calculations can be found in *Section 6.1.3*.

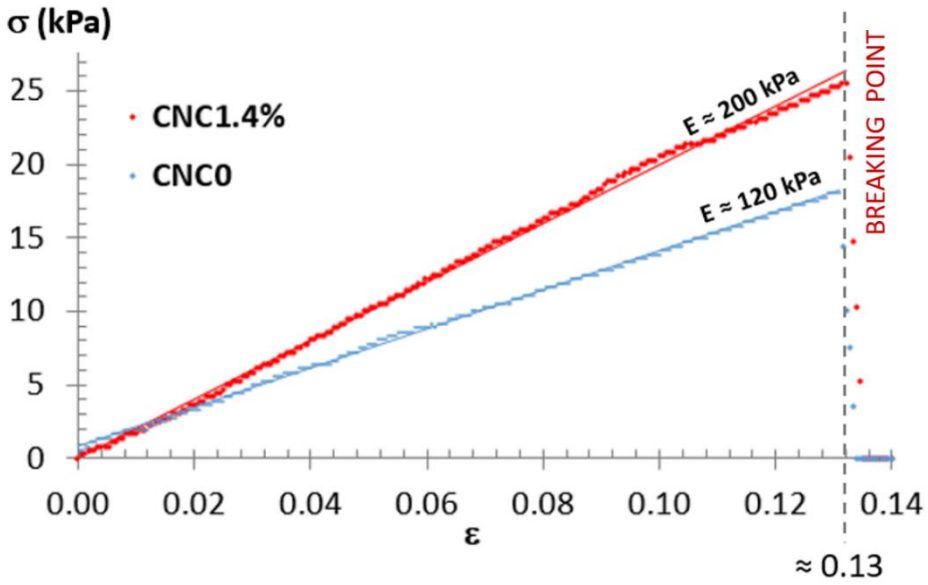

Figure 2.2.4. *Graph reporting the stress-strain curves of CNC0 and CNC1.4% obtained though mechanical tensile tests. Both of them show an elastic behavior and the maximum elongation, but the presence of CNCs increased the Modulus of Young (E) and the tensile strength* [194].

2.2.3 Electromechanical actuation

Electro-mechanical tests were carried out in order to evaluate how the presence of the CNCs affected the electro-responsiveness of poly(VBS-co-HEMA-co-AN) EAH under the application of low applied potential: from 3 V down to 5 mV. When an electro-active hydrogel is immersed in a saline solution with a lower ionic concentration than the inner one, the electro-mechanical deformation is due to the dynamic accumulation and depletion of ions on the two different sides of the gel at the solution interface in the presence of the applied electric field (see *Section 2.1.2*). According to this model, electro-responsiveness is higher in those ambient solutions where the variations of the swelling ratio S_r are larger for small variations of the local ionic concentration. In the present case, the swelling variation is particularly high when the samples are immersed in water solution with low ionic concentration (as reported in the graph previously shown in *Figure 2.2.3*). Because of this solution A (NaCl 0.005 M) was used for the electro-mechanical tests. 140 μm-thick (swollen thickness) films of CNC0, CNC0.4% and CNC1.4% were tested in a cantilever configuration immersed in Solution A, with the use of gold plated electrodes placed at 1 cm from each side of the beams (the thickness here is referred to the swollen state in Solution A). The experimental setup is schematized in *Figure 2.2.5*. More details about the experimental set up are reported in *Section 6.1.4(a)*.

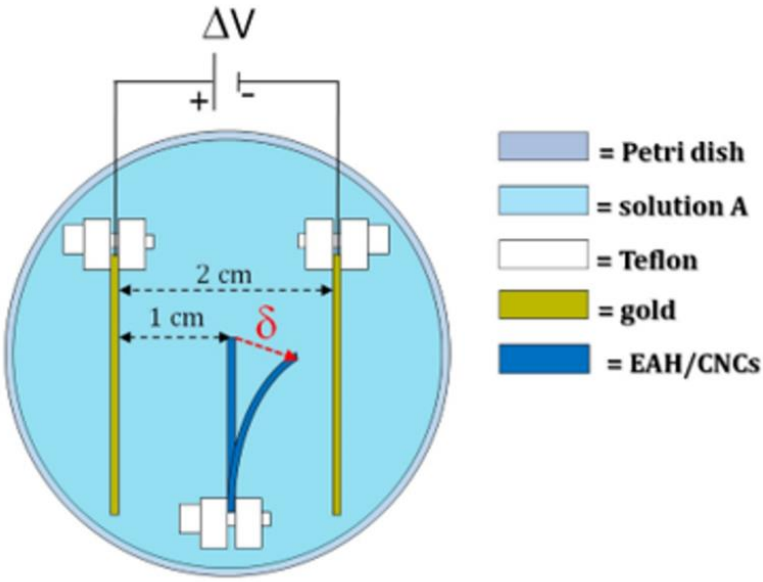

Figure 2.2.5*. Representation of the experimental setup employed for the electromehcanical tests on EAHs films shaped as cantilevers, tested in a 5 mM NaCl aqueous solution. Two rectangular gold plated electrodes were used to apply the electric field* [194].

Under the application of an electric field, all of them showed a reversible bending towards the cathode. *Figure 2.2.6* reports the values of the bending angle α and of the average angular speed ω plotted against ΔV. As can be seen, in a low voltage range going from 0.2 to 3.0 V, both α and ω increased with the applied potential. The observed plateau in the bending angle profile is due the fact that the geometrical configuration of the testing setup enabled a maximum bending angle of about 30-35°. On the other hand, the angular speed showed a parabolic trend. At 1 V (under the potential of water electrolysis) the actuators showed a bending angle above 20° and an angular speed of around 2 °/s, which is a remarkable result in the framework of soft underwater actuators of macroscopic dimensions. At 3 V they displayed an angular speed of about 14 °/s. Apparently, the water electrolysis at the electrodes did not influenced the EAHs actuation. It appeared that the hydrogels embedded with cellulose nanocrystals exhibited slightly higher bending angles, but in these conditions it was difficult to observe any significant difference compared to the bare hydrogel CNC0.

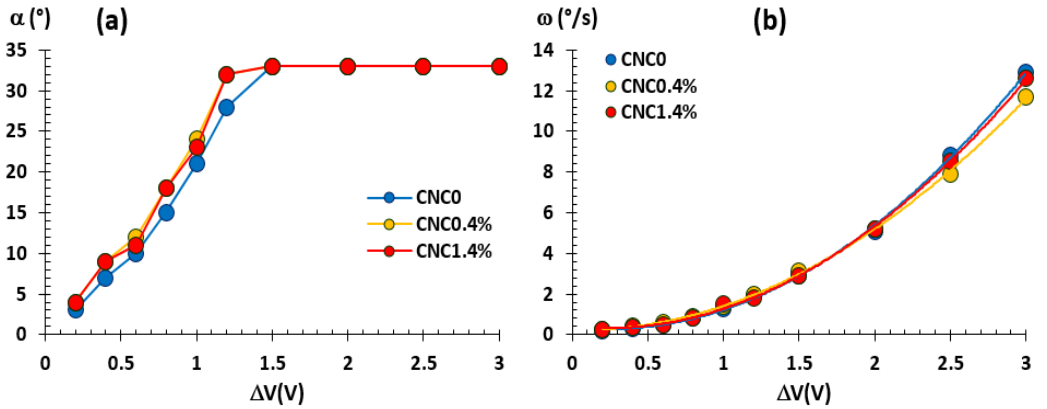

Figure 2.2.6. (a) *Bending angle α and* ***(b)*** *average angular speed ω of 140 μm-thick hydrogels with different amounts of CNCs, tested in Solution A with gold electrodes, plotted against ΔV. CNC1.4% and CNC0.4% are compared to the bare CNC0 hydrogel without the cellulose nanocrystals: it can be seen how their electro-mechanical actuation is almost the same in this range of applied potential* [194].

Then the mV-range actuation ($\Delta V < 100$ mV/cm) was investigated more in depth in order to assess the minimum applied potential able to trigger a mechanical response. According to the dynamic enrichment/depletion model [177], both the tip displacement and bending rate of the actuators are known to increase as the cantilever thickness decreases. Then 65 μm-thick samples for both CNC0 and CNC1.4% where used, in order to enhance their response to sub-volt applied potentials, and an inverted microscope

was used to accurately observe any difference in their electro-mechanical behavior for small tip displacement. Despite the lower thickness, CNC0 did not exhibit any significant motion in this potential range, while CNC1.4% showed an electro-active behavior with measurable tip's displacement and linear speed. In *Figure 2.2.7(a)* optical microscope images of the tip displacement are shown. The actuator was even responsive to applied electric fields down to 5 mV/cm. The graph of *Figure 2.2.7(b)* reports the maximum tip displacement and the values of $v_{1/2}$, calculated as the tip's average linear speed from the rest point to the half of its trajectory (since in the last part of its movement, the gel considerably slow down its speed). As it can be seen, the tip had a maximum displacement of 1 mm and an average speed of 100 μm/s at 100 mV/cm, while at 5 mV/cm it showed a maximum displacement of almost 100 μm and an average speed around 10 μm/s.

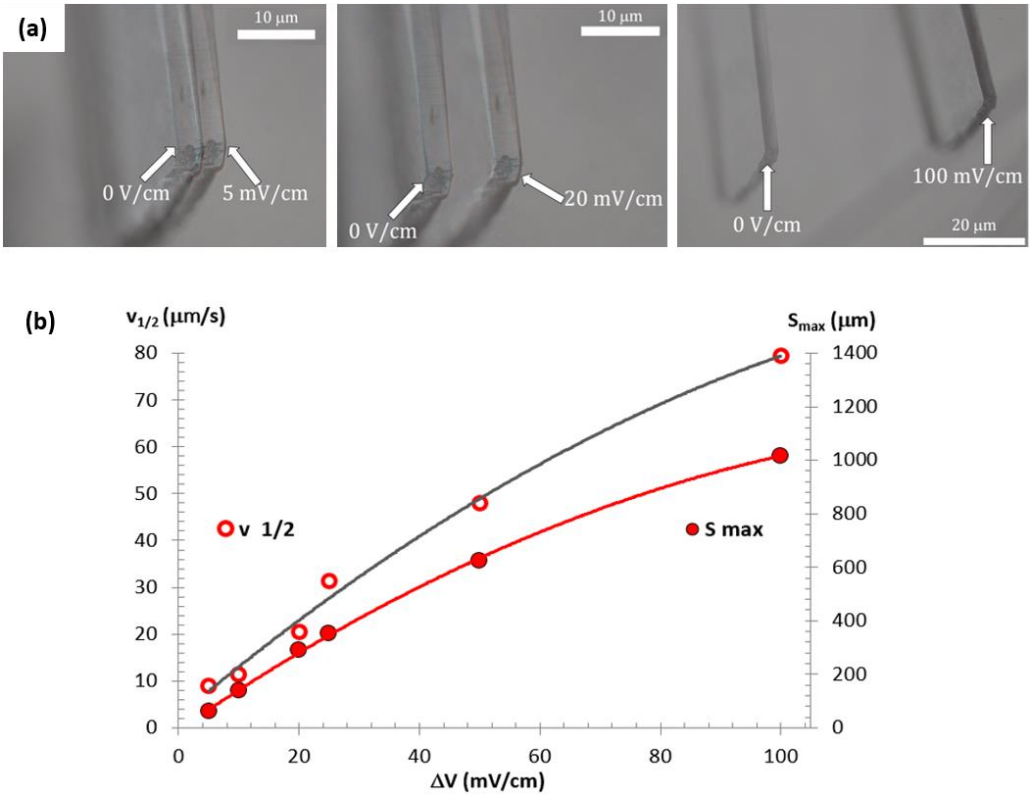

Figure 2.2.7. (a) *Overlay of optical microscope images showing the tip's displacement of a 65 μm-thick CNC1.4% actuators, tested in Solution A (NaCl 0.005 M). It can be seen how they were responsive even for applied potentials down to 5 mV/cm;* ***(b)*** *Graph reporting the values of the tip's maximum displacement and of its average linear speed, calculated considering its movement from the rest point to the half of its trajectory, plotted against ΔV.* [194].

This enhanced high-sensitivity at few mV/cm has never been reported for EAHs actuators macroscopic in two dimensions and it has never been measured with such accuracy even for micro-cantilevers (at least in two dimensions). This improved electro-responsiveness is then caused by the embedding of the functionalized CNCs. In fact, thanks to the deprotonated sulfonate groups they bear on their surface, the negative charge distribution inside the hydrogel is modified. These localized sulfonates offer additional fixed anionic sites that facilitate the mobility of the Na^+ mobile cations across the hydrogel matrix, therefore improving the ions transportation efficiency in the weak-field regime and enhancing the electro-responsiveness of these nanocomposite EAHs. This behaviour is particularly interesting for biotechnological and soft robotic applications that need soft components at the micro- and meso-scale able to respond to extremely weak electric signals.

2.2.4 Electroactive demonstrator prototype

The embedding of CNCs increased the mechanical properties and the electro-responsiveness (at extremely low values of applied potential, from 5 to 100 mV/cm) of poly(HEMA-co-AN-co-VBS) EAH, giving the opportunity to fabricate a demonstrator prototype able to display a geometrically more complex electro-mechanical actuation. The system design was tailored to mimic the motion of a millimeter-size underwater valve or pump able to “open” and “close” in response to electric stimuli, which is of great interest for microfluidic applications, or to mimic the behavior of ciliate organisms composed by thin and soft wedges through which they can provide underwater mobility. The model design is reported in *Figure 2.2.8(a)*. The core component is a 140 μm-thick CNC1.4% circular membrane, swollen in Solution A and shaped into tapered cantilevers, having a common basis consisting of the peripheral region of the membrane, which was fastened onto an appropriate ABS frame. A top view of the structure is shown in *Figure 2.2.8(b)*. More technical information about the used set up can be found in *Section 6.1.4(a)*.

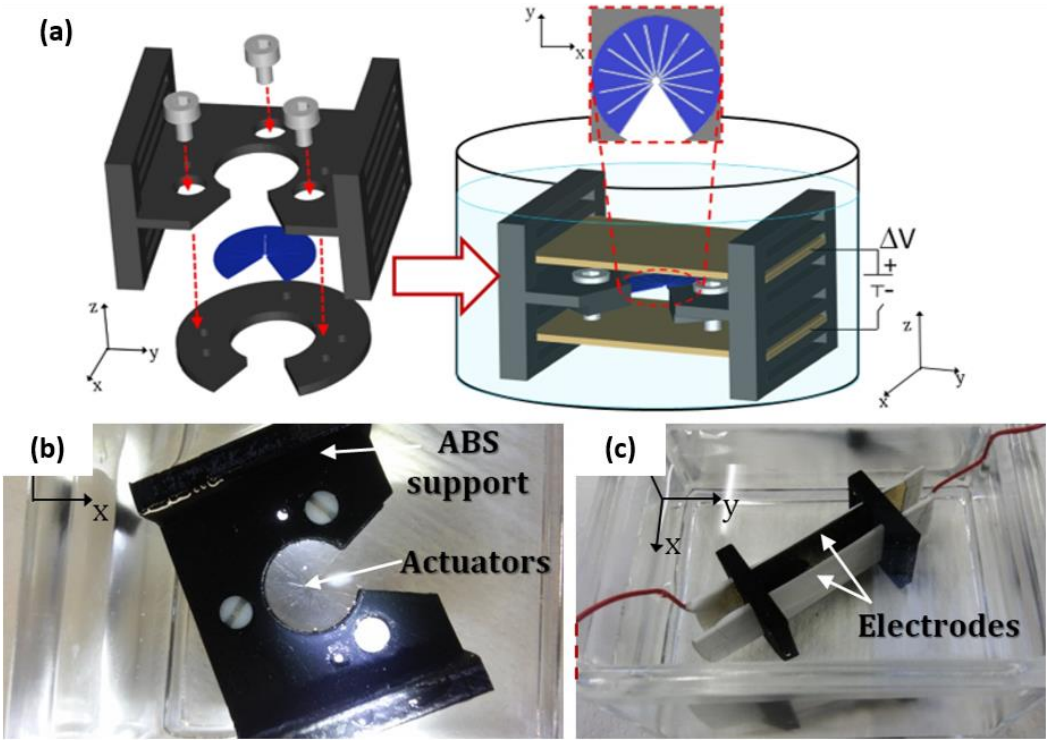

Figure 2.2.8. (a) *Model design and* ***(b-c)*** *photographs of a demonstrator prototype composed of series of 13 triangular 140 μm-thick soft actuators of CNC1.4%, arranged in a circular geometry. An ABS support fixed the actuators between two gold electrodes.* [194].

The valve was tested in Solution A, with gold plated electrodes fixed at 1 cm from each side of the valve, as shown in *Figure 2.2.8(c)*. At an applied potential of 2 V/cm the valve was able to open from +30° to -45° in 4 seconds with an average angular speed of 18.8 °/s, while its maximum bending angle was from +30° to -65° (average ω of 6.8 °/s). At an applied potential of 1 V/cm (*Figure 2.2.9*) it opened from +30° to -28° in 7 seconds with an average angular speed of 8.3 °/s, while its maximum bending angle was from +30° to -40° (average ω of 4.1 °/s).

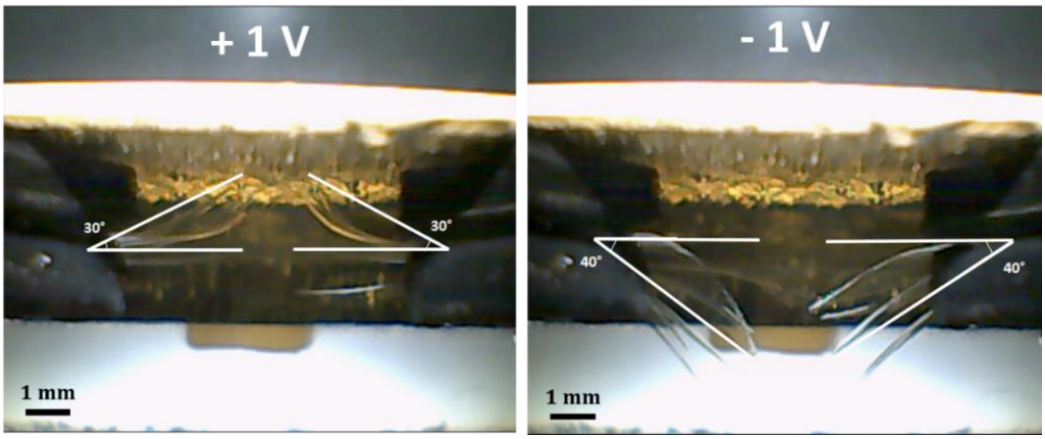

Figure 2.2.9. *Cross-section photographs showing the actuation of the demonstrator prototype. It is possible to see the upper electrode, while the lower does not compare in the photos. Under the application of 1 V all of the tapered cantilevers bended at an angle of about 30°; by inverting the bias, the actuators bended in the opposite direction at about 40°.* [194]

These results demonstrate the successful use of natural-derived cellulose nanocrystals (CNCs) as nanofillers inside the polymeric matrix of the electroactive hydrogel poly(HEMA-co-AN-co-VBS). The obtained nanocomposite hydrogels showed higher electroresponsiveness especially at low applied potentials, down to 5 mV/s. The incorporation of CNCs also improved the EAH's mechanical properties (the elastic modulus increased by the 60% of its original value) and this allowed the fabrication of a demonstrator prototype integrating many different actuators moving together to achieve a more cooperative and complex underwater soft actuation. Then the developed material possesses suitable mechanical and electroactive properties to be used for the fabrication of soft components and hybrid devices able to display sophisticated underwater actuation, in a reversible and remotely controllable fashion in response to weak electric signals.

2.3 CELLULOSE EAHs FOR ALGAE MOTION MIMICKING

2.3.1 Cellulose-based EAHs synthesis

The adopted synthesis process is water-based, focused on the use of natural-derived polymers and lacking harmful reagents. It also does not require high temperatures or advanced instrumentation. To obtain cellulose-based electroactive hydrogels in the shape of thin films with a green polymeric matrix, two cellulose derivatives were used as natural-derived building blocks: Na-carboxymethylcellulose (Na-CMC) and 2-hydroxyethylcellulose (HEC). Another biocompatible polymer, branched polyethylenimine (PEI) was used as chemical cross-linker. Their chemical structures are reported in *Figure 2.3.1*.

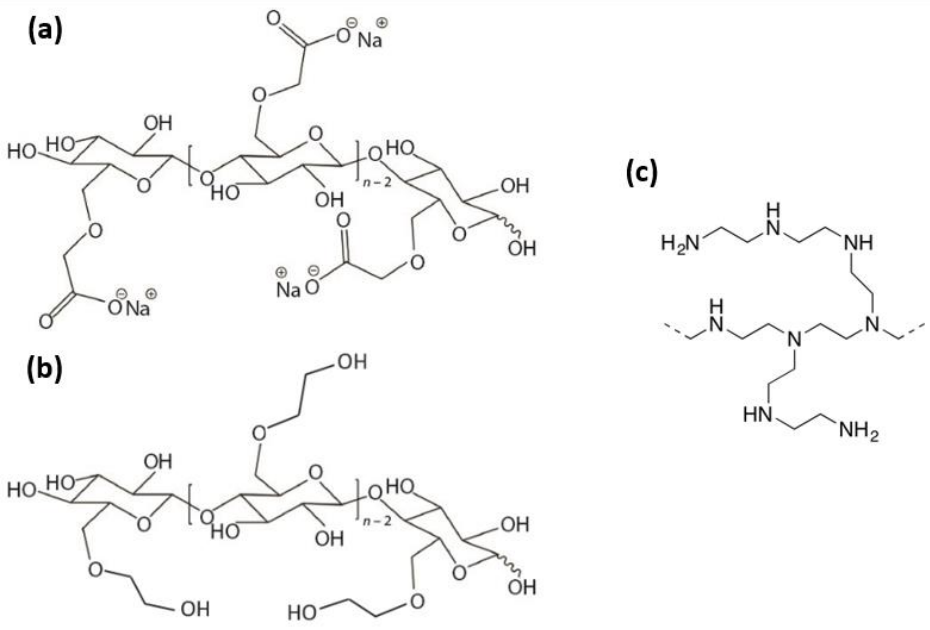

Figure 2.3.1. *Chemical structures of the polymers employed as building blocks for the synthesis of the natural-derived EAH:* ***(a)*** *Na-carboxymethylcellulose,* ***(b)*** *2-hydroxyethylcellulose,* ***(c)*** *polyethylenimine.*

All the reagents were dissolved in pure water and then injected into an open mold with a thickness of about 0.5 mm. Water was then evaporated in mild vacuum conditions and then at 70 °C the polycondensation reaction was activated. In this way thin and transparent films of electroactive hydrogels were obtained, able to swell and absorb water when immersed in aqueous solutions. More detailed information about the hydrogel's synthesis are reported in *Section 6.1.1(b)*.

2.3.2 Swelling/shrinking equilibrium

To obtain a fingerprint of this novel cellulose-based EAH, its swelling/shrinking equilibrium was studied in aqueous solutions with different ionic concentration. The water uptake of these class of electroactive polymers derives from their hydrophilicity, but there's also the influence of the osmotic pressure, that arises from the difference in the ionic concentration inside the hydrogel (C_g) and in the surrounding solution (C_s). *Figure 2.3.2(a)* shows a graph reporting the Swelling ratio S_r of the hydrogel's samples after soaking them in NaCl aqueous solutions at different salt concentration (C_s) [211]. As can be seen, the theoretical behaviour is confirmed, since the water uptake increased in the more diluted solution, reaching a peak value of 27.4 in the NaCl 0.005 M. *Figure 2.3.2(b)* reports the values of S_r plotted against pC_s and it can be seen how they are almost interpolated by a straight line of *Equation 2.1*:

$$S_r = (\sigma \times pC_s) + S_{r,0} \qquad [Eq.\ 2.1]$$

In this case σ is equal to 5.45 and it indicates how much the water uptake is sensitive to variations in the solution's salt concentration. $S_{r,0}$ is equal to 15.00 and it represents the virtual value that S_r would have in a 1 M NaCl solution. The gathered information on the hydrogel's swelling are essential to understand and even to predict its electroactivity. In fact, the S_r trend suggests that the ionic concentration inside the gel (C_g) is higher than in the outside solution (C_s) and therefore the dominant driving electromechanical mechanisms should be the dynamic enrichment/depletion model proposed by Doi et. al [177] (see *Section 2.1.2*). According to it, the mechanical deformation of these class of hydrogels derives from an asymmetric change in the osmotic pressure between the two sides of the hydrogel and the surrounding solution, which is caused by an asymmetric change in the local ionic concentration under the application of an electric field. The obtained swelling curve shows that in diluted salt solutions a small variation of C_s causes the gel to highly change its swelling/shrinking equilibrium. This is an important assessment because it means that water solutions with

low salinity, similar to natural-occurring sweet water, represent a good environment for this EAH to display electro-mechanical actuation.

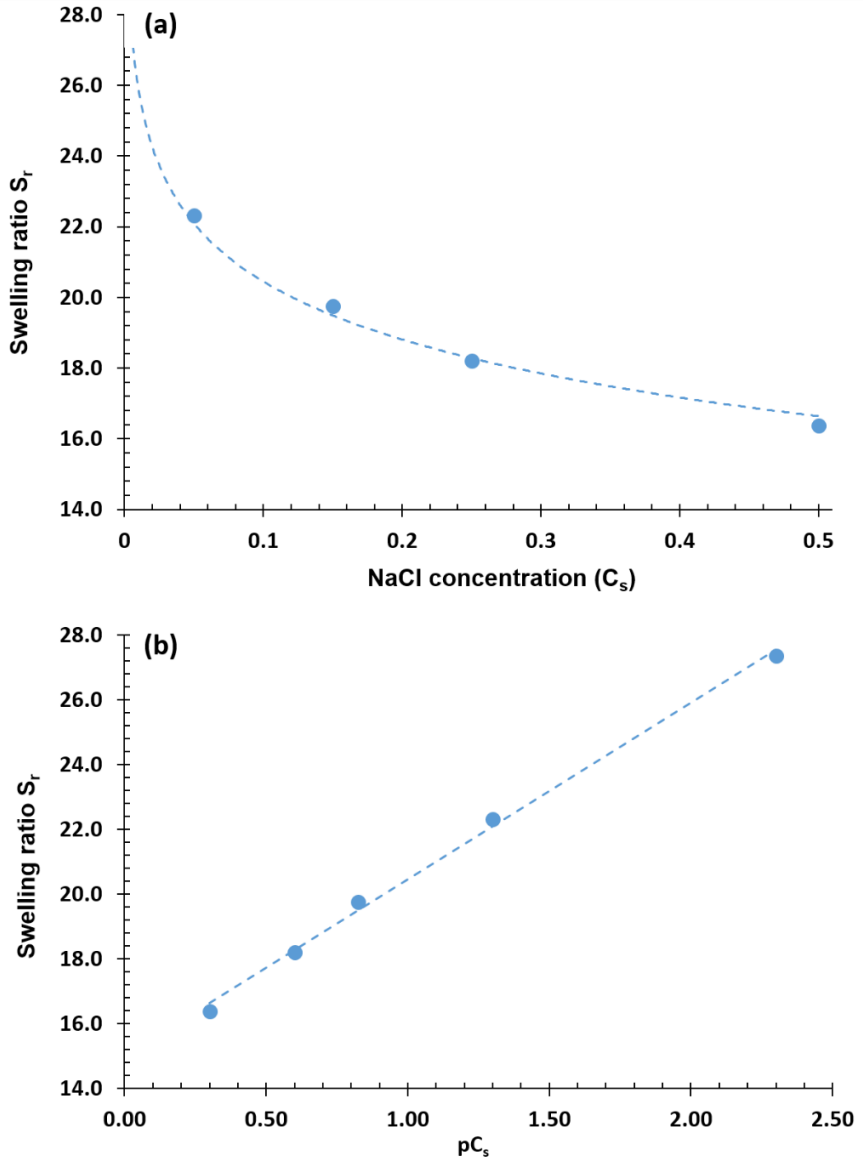

Figure 2.3.2. *Graphs reporting the swelling ratio's values of cellulose-based EAH samples when they are immersed in aqueous solutions with different concentrations of NaCl.* ***(a)*** *S_r is plotted against the NaCl concentration and it can be seen how the swelling is higher in the more diluted solutions;* ***(b)*** *S_r is plotted against pC_s and its almost linear trend confirms a logarithmic dependence on the ionic concentration of the surrounding solution.* [209].

2.3.3 Electroactivity and mimicking of algae motion

Electro-mechanical tests were carried out on films of hydrogel cut in a cantilever shape in a 0.005 M NaCl aqueous solution, whose saline concentration is similar to that of natural occurring sweet water. The samples swollen thickness was about 1 mm. More detailed information about the used set up are reported in *Section 6.1.4(b)*. Under the application of an electric potential ΔV, the samples displayed a reversible bending towards the cathode, as can be seen in *Figure 2.3.3*.

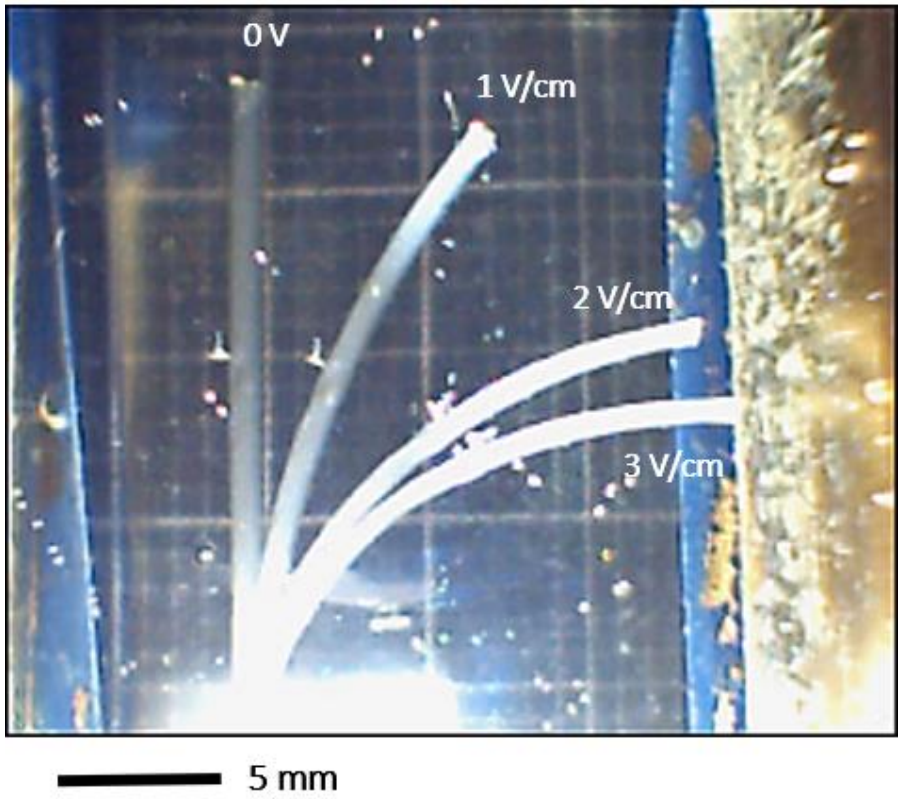

Figure 2.3.3*. Overlaying of pictures taken during the electromechanical characterization of a single cantilever-shaped hydrogel immersed in an aqueous solution of NaCl 0.005 M. It can be seen how it bends towards the cathode according to the applied potential.* [209].

Figure 2.3.4 shows a graph reporting the values of the bending angle α and the average angular speed $\omega_{1/2}$ at different applied potentials. As can be seen, the samples are sensitive even for low applied potentials of 0.25 V/cm, with α = 3.1° and $\omega_{1/2}$ = 0.16 °/s. Both parameters increased at higher applied potential, reaching maximum values of α = 65.1° and $\omega_{1/2}$ = 10.9 °/s at 3 V/cm. Under the application of 1 V/cm, a value under the potential of water electrolysis and then of great interest for real underwater applications, α = 22.3° and $\omega_{1/2}$ = 0.89 °/s at 3 V/cm.

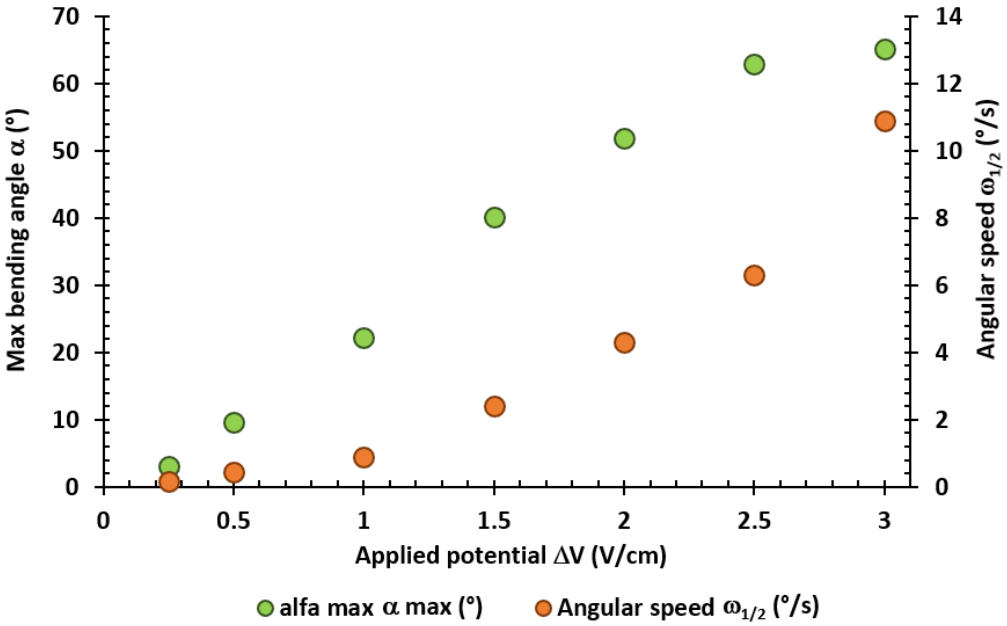

Figure 2.3.4*. Graph reporting the values of the bending angle α (green spots, left axis) and the average angular speed $\omega_{1/2}$ (orange spots, right axis) of the cantilever actuators. As can be seen, both the values increase for higher applied potentials.* [209]

Once the swelling and electroactive properties of this novel cellulose-based EAH have been characterized in low salinity water solutions, a step towards real applications was achieved by developing a system through which combine several actuators of different shapes (multi-arm cantilevers and algae-like) and to control their motion with the application of an alternating potential, in an attempt to mimic the undulatory behaviour of a small forest of algae moved by water flow.

3D fuse filament fabrication (FFF) was selected as a rapid and versatile technique to manufacture a modular testing apparatus and custom-shaped die cutters for the hydrogel samples. The testing apparatus was solely composed of ABS 3D-printed components which could be assembled by either sliding or interlocking connections (*Figure 2.3.5(a)*). By suppressing the need for external joints among the parts (e.g. screws and bolts) it was significantly improved the compactness of the apparatus and avoid the presence of conductive elements which could perturb the electric field configuration in the testing region. Moreover, this design allowed to freely deploy the various elements on the system in different number and positions. As for the hydrogel cutters (*Figure 2.3.5(b)*), we assessed the possibility to design and 3D print a die which replicates the profile of arbitrary shaped multi-arm cantilevers and even realistic algae starting from a vector image or Non-Uniform Rational Basis-Splines (NURBS) curves.

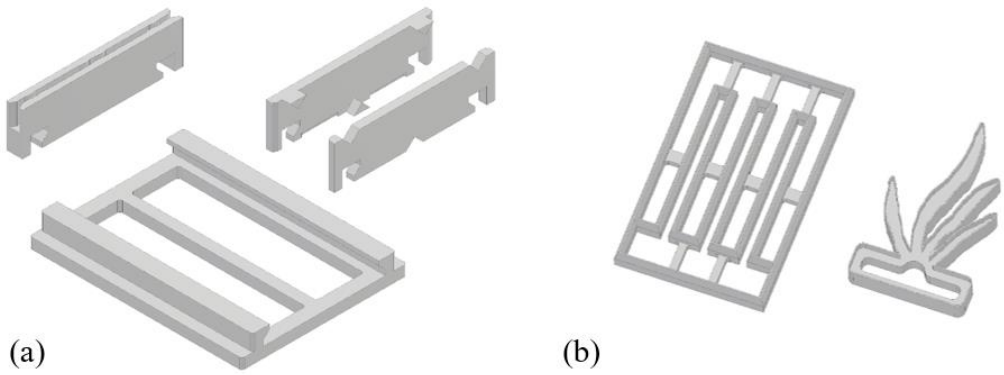

Figure 2.3.5*. Three-dimensional design of the components 3D printed through Fused Filament Fabrication technique.* ***(a)*** *Base frame with two rails that acts as a positioning support for both the electrode clamps and the hydrogels clamps (detachable into two interlocking parts).* ***(b)*** *Custom die cutters used to give specific shapes to hydrogels films.* [209].

The fabricated cutters were effectively used to shape hydrogel films in a single punching operation preventing any longitudinal stress on the samples, which is a considerable advantage with respect to other cutting techniques. The resulting custom-shaped actuators can be seen in *Figure 2.3.6(a)*. With the aid of this experimental system it was possible to successfully deploy and control the motion of multiple arrays of actuators in several configurations: from 2 to 5 arrays of different shape, with the electrodes placed at distances from 3 to 8 cm and with potentials ranging from 0.25 to 1.0 V/cm. It was stated that even for low applied potentials of 0.25 V/cm all the actuators

simultaneously bended towards the cathode and under the effect of an alternating potential they displayed an undulatory motion that resembled the one typical of real algae.

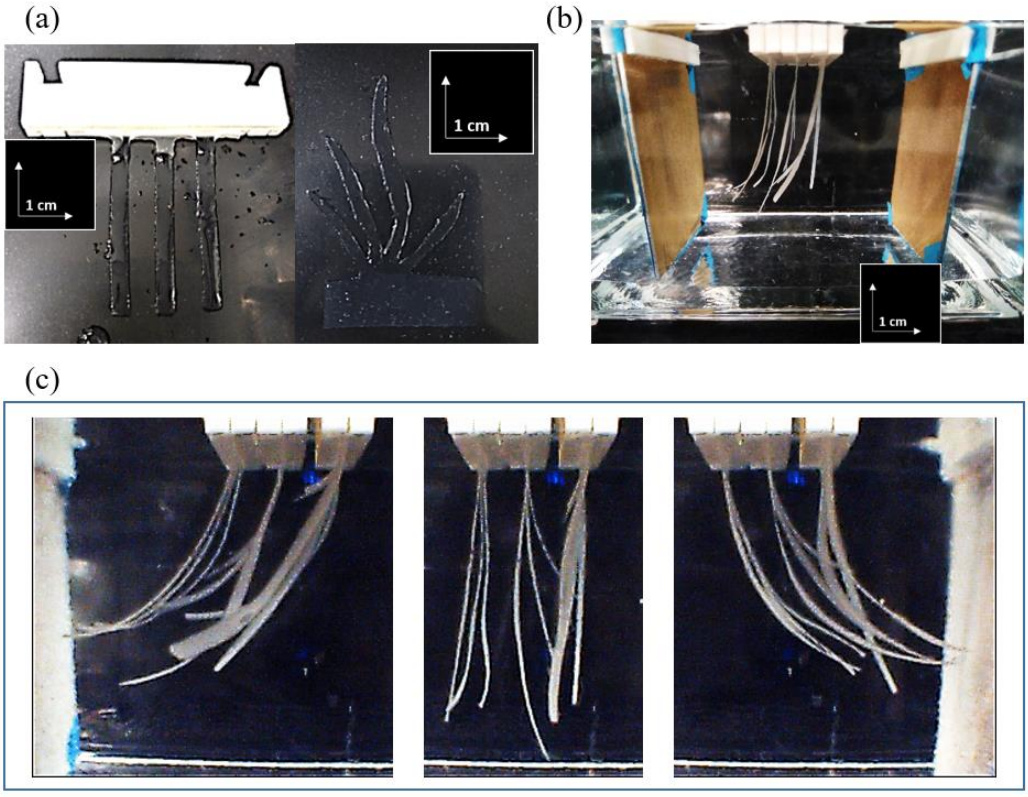

Figure 2.3.6. ***(a)*** *Custom-shaped hydrogel actuators modelled by using the die cutters;* ***(b)*** *Picture showing one of the experimental setups, with three arrays of parallel actuators and the electrodes placed at a distance of 8 cm;* ***(c)*** *Pictures showing the simultaneous bending of the actuators under an applied potential of 1 V/cm (both opposite polarities) compared to the rest position with no applied potential (the picture in the middle). The test was carried out to mimic the fluctuations typical of natural algae forests under the effect of a water flow.* [209].

Figure 2.3.6(b) shows one of the experimental setups, with three arrays of actuators and the electrodes placed at 8 cm. *Figure 2.3.6(c)* includes three pictures showing the simultaneous bending of the actuators under an applied potential of 1 V/cm (both opposite polarities) compared to the rest position with no applied potential (the picture in the middle). *Section 6.1.4(b)* reports more detailed experimental information.

These results were obtained with an electroactive hydrogel derived from cellulose derivatives and a biocompatible cross-linker (polyethylenimine). The swelling properties as well the electroactivity of this novel formulation were tested and studied. Then a specific experimental setup was designed and realized in order to use many actuators all together to mimic the typical fluctuations of natural occurring algae, but in this case the motion was induced by small electric impulses rather than by a water flux. By the combination of natural polymers, smart materials science and 3D printing technique it was then possible to move a first step towards the design and the realization of hybrid habitats where one day artificial and controllable algae could cohabit with real living organisms or microorganisms typical of aquatic natural environments.

3.

In-Air Soft Actuators from Natural Polymers

3.1 Overview on Electroactive In-Air Soft Actuators

3.1.1 Ionic electroactive polymers, ionogels, actuators

As highlighted in *Section 1.1.2*, soft (elastic modulus between 10^3 and 10^8 Pa) stimuli-responsive materials can sense physical or chemical stimuli in the surrounding environment and to change their shape accordingly, generating a net mechanical force. Their soft mechanical properties allow them to safely interact with biological entities and/or fragile objects and they are of extremely interest for applications in soft robotics [3,212]. Among them, **electro-responsive materials** are particularly efficient since electric signals can be easily generated and controlled with extreme precision.

Ionic electroactive polymers (IEAPs) are chemically or physically cross-linked polymeric materials that constitute a promising solution for the development of soft electromechanical actuators, since they can provide large physical bending in response to a low applied potentials (0.2 to 5 V) as a consequence of the migration and spatial redistribution of mobile ions in their inner structure, when it is filled with a suitable liquid medium. In fact, under the application of an electric field, an asymmetric ionic migration occurs across the polymeric matrix, according to the size and charge of the mobile species. This results in a higher concentration of the liquid phase at one of the electrodes, inducing a localized swelling and a macroscopic bending deformation of the system. A simple schematic of the electromechanical actuation is presented in *Figure 3.1.1*. These actuators can readily and reversibly convert low power electric signals into mechanical work. Electroactive hydrogels (EAHs) (*Section 2*) can provide underwater soft actuation when an electric field is applied in a liquid environment by mean of a couple of remote electrodes, but they cannot operate in plain air.

To perform in-air electromechanical actuation, the most used materials are perfluorinated polymers, like **DuPont's *Nafion***, obtained through the incorporation of perfluorovinyl ether groups terminated with sulfonate groups onto a tetrafluoroethylene backbone (*Figure 3.1.2*) [213–216]. But apart from the polymeric component, the use Nafion or other IEAPs as soft actuators able to operate in plain air needs that two main requirements must be satisfied: the stabilization of the liquid phase inside the polymeric matrix and the fabrication of electrodes in direct contact with the IEAPs surface.

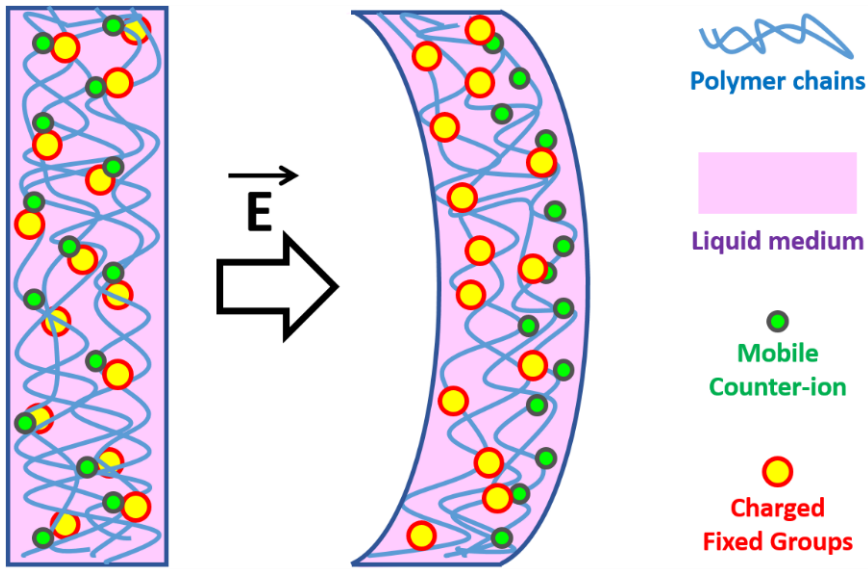

Figure 3.1.1. *Simple schematic of the electromechanical deformation that IEAPs undergo under the application of an electric field. It is possible to see the fixed ionic groups covalently bound to the polymeric chains, and the mobile counterions able to migrate from one side to the other of the polymeric matrix. The anisotropic ionic migration leads the ions and the surrounding liquid medium to accumulate at one side of the material and the resulting asymmetric swelling/shrinking causes a physical deformation in the polymeric composite.*

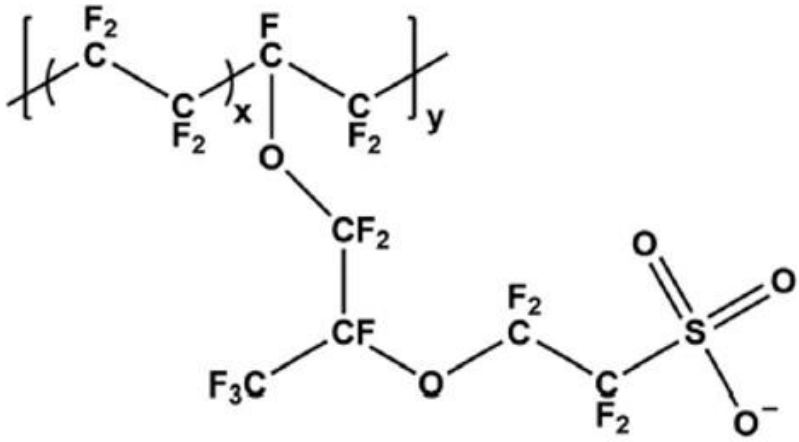

Figure 3.1.2. *Chemical structure of DuPont's Nafion, one of the most known fluoropolymers used for the development of ionic electromechanical actuator.*

Considering IEAPs swollen with **aqueous electrolytes**, the water has the main role to dissolve and solvate the mobile ions: it's their asymmetric migration that trigger the mechanical deformation. But water undergoes electrolysis at only 1.23 V and it also evaporates in air, limiting the operational stability of the actuator. Because of this, an alternative solution was found in the use of **ionic liquids (ILs)** [140,217]. They are organic molecular salts whose melting point is below ambient temperature and then they present as liquids in ambient condition. In fact, even if they are composed by cations and anions, their molecular structure does not favor the formation of a stable crystal lattice as it happens for the more common inorganic salts. Because of this they are liquid compounds with very unique features: low vapor pressure, ionic conductivity, high electrochemical stability (up to 4 V in certain cases), unconventional solvating properties, easiness of chemical modifications and functionalization. They are also greener alternatives to traditional organic solvents. Imidazolium-based ionic liquids are one of the most diffused families (some examples are reported in *Figure 3.1.3*). By blending ILs with suitable IEAPs, homogeneous ionogels (IGs) can be obtained: solid soft materials containing a stable liquid phase composed by ions able to migrate under the effect of an electric field [218].

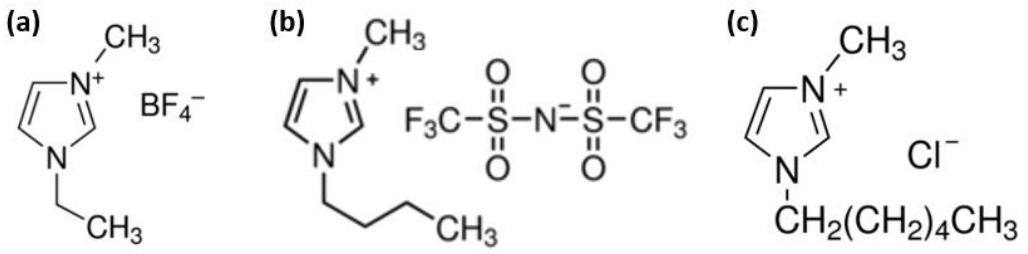

Figure 3.1.3. *Chemical structure of three different imidazolium-based ionic liquids:* ***(a)*** *1-ethyl-3-methylimidazolium tetrafluoroborate (EMIM(BF_4)),* ***(b)*** *1-buthyl-3-methylimidazolium bis(trifluoromethylsulfonyl)imide (BMIM(Tf_2N)) and* ***(c)*** *1-hexyl-3-methylimidazolium chloride (HMIM(Cl)).*

To properly work as in-air soft actuators, ionogels still need the **integration of compliant conductive electrodes** on their surface and they need to be characterized by strong adhesion, low mechanical mismatch with the underlying gel and the ability to bend without damaging. According to the nature of the electrodes, it is possible to distinguish two different classes ionic electromechanical actuators in air: **ionic polymer – metal composites (IPMCs)** and **carbon – polymer composites (CPCs)**. IPMCs are characterized by the use of noble metals to obtain highly conductive thin electrodes. Several techniques have been used for their fabrication: chemical reduction, hot

pressing, electro-plating, sputtering, physical vapour deposition, inkjet printing [141,143,144,146,219–221]. CPCs instead have electrodes based on carbonaceous species, like active carbon, graphene and nanotubes (they can also be functionalized) [222–226]. They were introduced as an alternative to noble metals for the production of chemically modified porous electrodes with higher flexibility. Their great porosity in many cases brought to a higher surface area with the underlying ionogel and then a greater number of ions that can be accumulated. The most diffuse techniques for the assembly of CPCs are hot pressing, layer-by-layer casting or deposition, dip, drop or spin coating. Besides, also conducting polymers, such as poly(3,4-ethylenedioxythiophene):poly(styrene sulfonate) (PEDOT:PSS) and polyaniline, were used as electrodes for ionogels by mean of drop, dip or spin coating [227,228].

Then, when combined with suitable ionic liquids and compliant electrodes, IEAP-based ionogels can be used to convert electric signals into mechanical actuation in plain air. A simple schematic of in-air actuation is reported in *Figure 3.1.4*.

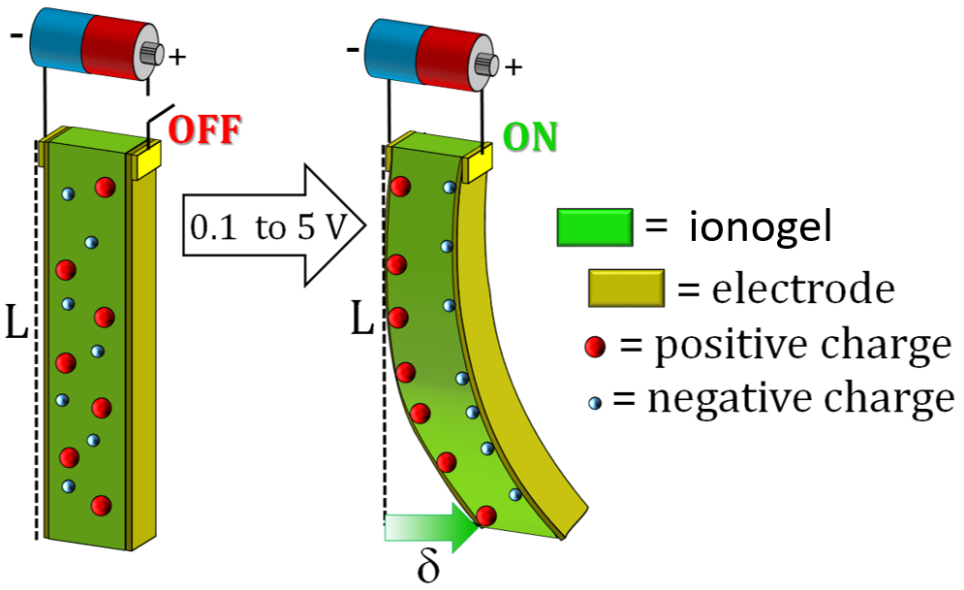

Figure 3.1.4. A *simple schematic of electromechanical actuation in plain air. The ions are provided by the ionic liquid and the compliant electrodes undergo the same bending of the ionogel* [2].

3.1.2 Challenges and aim of the research

Regarding in-air electromechanical actuators based on ionic electroactive polymers and ionogels, many operational features are pursued: electroresponsiveness at low applied potentials, wide mechanical deformation, fast actuation, **durability** over thousands of working cycles and in different working conditions, **resistance to the humidity**, good mechanical properties and the possibility to achieve a mechanical displacement different from the most traditional bending of a cantilever-shaped actuator. Some of these features relay on the polymeric matrix, some on the ionic liquid, other on the electrode's material and structure and other again depends on the interactions between all these components.

Nevertheless, the production of well-adherent, highly conductive and thin electrodes able to undergo stable cyclic deformations along with the polymeric substrate is maybe the most important and a critical task. **Metallic electrodes** used in IPMCs usually present low adhesion with the underlying polymer and they undergo cracking phenomena after few deformation cycles, due to the metal-polymer mechanical mismatch [229,230]. This problem is particularly relevant considering that these electrodes usually have a thickness ranging from 1 to 30 μm, which covers a significant portion of the actuator, typically from 50 to 100 μm thick [231–233]. Furthermore, standard electrode fabrication approaches are rather time consuming, and the use of reactive chemicals, high process temperature and pressure do not allow to extend these methods to a wide number of soft ionic polymers [143,144]. Moreover, some of the used technique, like hot pressing and electro-less plating, are characterized by a difficult process control and reproducibility. More compliant electrodes can be fabricated by using **carbonaceous species** such as graphene, carbon nanotubes, active carbon or conductive polymers [151,234,235], in the carbon -polymer composites (CPCs). However, the manufacturing of carbon-based electrodes is time-consuming, expensive, it requires high loadings of active material and it is difficult to obtain electrodes with good electrical properties typical of single crystallites [151], while organic conductive polymers such PEDOT-PSS are toxic. Moreover, carbon-based and organic electrodes are strongly hygroscopic, meaning that their electromechanical performances vary with the humidity level of the surrounding environment: this is a highly undesirable thing since it makes their actuation more uncontrollable and unreproducible, limiting their potential for real world applications [236,237].

Focusing instead on the polymeric component of electroactive actuators, many IEAPs have been studied and produced in the last decades, but very few of them match the requirements of environmental sustainability coupled with operational stability in different working conditions. Perfluorinated polymers like **Nafion** or **PVDF** represent one of the most performant solutions, but their monomers are toxic and carcinogenic, their production requires high costs, high temperatures and pollutant solvents, and the products are unsafe and not easily degradable [213–216,238,239]. Less toxic polymers have also been used [240–245], such as **polyvinylic species**, but they still come from petroleum derivatives, they are not biodegradable and their mechanical properties are usually weaker. More recently, natural-derived polysaccharides have been used, **cellulose** on top, to fabricate electromechanical resonators at high frequencies, but with low displacement [134,135,246–248]. Nevertheless, all these polymers are water-absorbent or moisture sensitive, hindering the actuators to stably operate in unpredictable environmental conditions [249].

The aim of this work is the use of natural-derived biodegradable polymers as the main component of ionogels and to fabricate the electrodes by mean of **supersonic cluster beam deposition (SCBD)** [153,154,250], in an attempt to overcome some of the critical features of other metallization techniques. SCBD is a manufacturing technique that allows the fabrication of thin cluster-assembled metallic electrodes onto polymeric substrates. It relies on the use of highly collimated supersonic beams seeded with neutral metallic nanoparticles directed onto a target. The resulting electrodes may be partially implanted into soft polymeric matrices and they are characterized by high conductivity, large surface area, robust anchorage to the substrate and mechanical resiliency against deformations, as previously demonstrated [2,251,252]. A detailed description of this technique is reported in *Section 1.4*. In the first presented case (a), **cellulose paper sheets** are used as a hosting matrix for an ionogel and their typical foldability is exploited to shape the actuators as electroactive springs; in the second case (b), the **bacterial bioplastic poly(3-hydroxybutyrrate)** constitutes the only polymeric component of an electromechanical actuator unaffected by environmental humidity and stable over thousands of cycles.

(a) Spring actuators from paper sheets

Cellulose is the most abundant polymeric material produced in the biosphere and it is widely employed for the development of a rapidly increasing number of eco-friendly, safe, recyclable and biodegradable industrial goods [253,254]. **Paper** is the most popular product made of cellulose and it has aroused interest for forefront technological applications, such as deformable electronics, environmental energy harvesting, microfluidics and biosensing [255–257]. The use of paper substrates for the

development of platforms with embedded capability to sense, adapt and interact with the external environment is now considered a promising route for the production of lightweight, flexible and foldable, yet mechanically robust, smart systems that can be structured and eventually integrated into 3D architectures [258–260]. The capability of paper to be folded and cut to assume complex topologies as in the traditional arts of Origami and Kirigami [261], has stimulated efforts towards the realization of paper-based devices able to modulate their shape in response to external physical and chemical stimuli [262]. **Electroactive paper-based actuators** can represent an interesting solution for the development of a new family of low-cost functional devices that can be fabricated by mean of simple manufacturing processes [263,264]. The two main strategies to manufacture paper-based ionic actuators relies on the blending of raw cellulose and ionic liquids, followed by casting or filtration, and, on the other hand side, on the impregnation of cellulose substrates with the electrolyte. Ionic electroactive polymer - paper hybrid nanocomposites have also been fabricated using both approaches by implementing functional nanostructures into cellulose, such as graphene, carbon nanotubes, nanoscale poly(pirrole) and metal oxides nanoparticles. This led to an enhancement of the systems mechanical properties and ion transport ability and an improvement of the actuators frequency response, bending displacement and output force [222,265–268]. Several manufacturing drawbacks affect the fabrication of IEAP-paper composites, such as time-consuming preparations and material post-processing, relatively low ionic liquid uptakes and a non-homogeneous dispersion of the nanofillers inside the cellulose matrix [265,267,269].

The metallization of IEAP-paper composite materials has been carried out with few traditional techniques, but SCBD technique has been never tried before. Also, the achievement of electromechanical actuation motility profiles that could overcome the unidirectional bending typical of cantilevered shaped components has not been reported in the literature for IEAP – paper actuators, while the generation of more complex and motions is desirable to broaden their application range [260,261]. In fact, the possibility to produce freestanding elements able to display linear displacement and twisting motion as single elements that could be directly implemented into bio-inspired lightweight smart devices would favor the design process and simplify the manufacturing and assembly of these systems.

The objective of the present work is the production and characterization of a **paper/ionogel/metal electroactive composite** able to display a spring-like electromechanical actuation. The ionogel of choice is a poly(acrylate) copolymer and it can be coupled with an ionic liquid and plain sheets of paper by a soaking procedure and a subsequent photo-polymerization process. Supersonic cluster beam deposition (SCBD) is the technique of choice for the fabrication of thin compliant electrodes. The structural,

mechanical and electrochemical properties of the composite material are here characterized and then the foldability typical of paper is exploited to obtain and test a **spring-shape actuator** able to provide a linear electromechanical displacement. The detailed results are presented in *Section 3.2* and part of them are also reported in a scientific paper published by *Smart Materials and Structures* [251].

(b) Humidity-resistant actuators based on the bioplastic PHB

A sustainable but still unexplored alternative to perfluorinated IEAPs may be represented by bioplastics, since they are natural-derived and biodegradable, and they present suitable mechanical and hydrophobic properties [130,131,270]. Although they are not ionic polymers (because the polymeric chains do not have any ionic group covalently bound), mobile ions can be supplied by blending with a proper ionic medium. Among bioplastics, **poly(3-hydroxybutyrate) (PHB)** is a plastic polyester produced by bacteria [132,271,272], usually processed by hot extrusion or casting from chloroform. As reported by Emadian et al. [131], PHB possesses an excellent biodegradability both in the soil and in water. In the field of electromechanical actuators, the only use of PHB regards the work of Cai et al. [273], where it was used as a mere reinforcement for a cellulose-based electromechanical resonator. According to bibliographic research, no examples of bioplastic-based ionic electromechanical actuators can be found.

The aim of this work is the use of biodegradable PHB as the only polymeric backbone for the development of a **natural-derived**, **hydrophobic** and **plastic-like** electromechanical actuator. To do this, non-ionic PHB polymeric chains is blended with a suitable ionic liquid to produce bioplastic-based ionogel thin films through a simple solvent casting process from acetic acid. Thin cluster-assembled gold electrodes are fabricated by mean of SCBD technique. The composites mechanical properties, moisture absorption, ionic conductivity, double-layer capacitance and electromechanical actuation are here characterized and tested. The tested actuation shows to be stable over thousands of cycles and unaffected by the humidity level of the surrounding environment. The detailed results are presented in *Section 3.2* and they are also reported in a scientific paper published by *Sensors and Actuators B: Chemical* [274].

3.2 PAPER/IONOGEL/METAL SPRING ACTUATORS

3.2.1 Paper/ionogel hybrids manufacture and characterization

Standard white paper for inkjet printing (Favini A6, 55 g/m^2) was chosen as the main substrate, thanks to its strong mechanical properties, foldability, porosity and biodegradability. Paper sheets were combined with an ionogel consisting of a UV photo-crosslinked poly(acrylic acid-co-acrylonitrile), namely poly(AA-co-AN), blended with the ionic liquid 1-ethyl-3-methylimidazolium tetrafluoroborate EMIM(BF_4), to confer electroactive properties. To obtain a hybrid material composed by an interpenetrated network of cellulose and ionogel, an aqueous polymerizing solution was prepared by dissolving together the monomers acrylic acid (AA) and acrylonitrile (AN) together with the cross-linker ethylenglycoldimethacrylate (EGDMA), the UV photo-initiator 2,2-dimethoxy-2-phenylacetophenone (DMPA), the ionic liquid EMIM(BF_4), tetraethylammonium fluoride (TEAF), halloysite nanoclays (HNCs) and poplyvinylpyrrolidone (PVP). TEAF is an organic salt whose mobile ions of different size can increase the asymmetry of the ionic accumulation at the electrodes and then the overall electromechanical deformation. HNCs are natural clay nanoparticles with a very peculiar aggregation structure [275]. They were added because it was shown that they can polarize the ionic liquid molecules and to promote their dissociation [276]. PVP was added in a small amount because it was shown to increase the toughness of the resulting ionogel.

The paper/ionogel hybrid composite manufacture involved a first step when a paper piece was soaked inside the liquid polymerizing solution, so that the cellulose interconnected pores filled up with the ionogel precursor. Then, after the absorption, the impregnated sheet was exposed to UV light to trigger the photo-polymerization reaction and obtain an interconnected network of cellulose fibers and ionogel. A schematic of the hybrid paper/ionogel platforms preparation is reported in *Figure 3.2.1*. After the photo-polymerization process, the weight of the samples increased of about the 35% of the original weight of the paper sheets and this was a useful information to estimate the amount of ionogel absorbed inside the paper fibres. Poly(AA-co-AN)-based freestanding ionogel films were also synthesized independently from paper/ionogel composites: this was done to study the inner porosity of the pure ionogel and to

compare its value with the other samples. A more detailed description of the experimental procedure is reported in *Section 6.1.1(c)*.

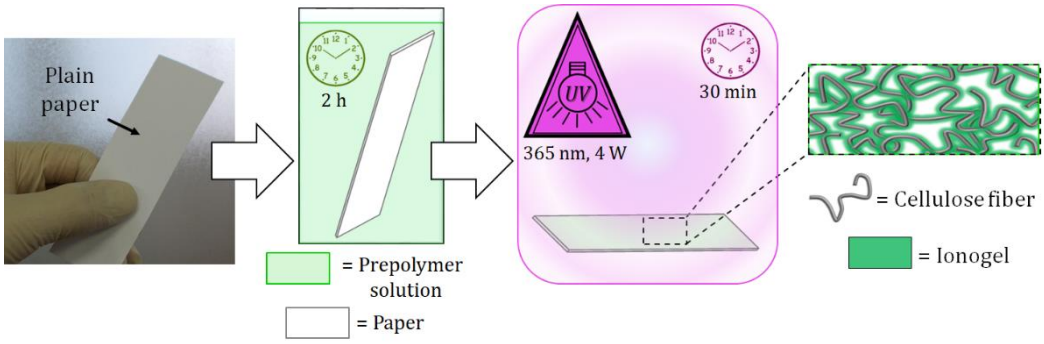

Figure 3.2.1. *Schematic of the preparation of the electroactive paper/ionogel composite films. Soaking of paper sheets inside the polymerizing solution was followed by UV photo-polymerization of the absorbed monomers* [251].

To get insights on the porosity of the modified paper network, BET analysis was used to measure the total surface area of the original plain paper, the pure poly(AA-co-AN)-based ionogel and the paper/ionogel hybrids. The profiles of the isotherms obtained for all the samples are reported in *Figure 3.2.2* and they are compatible with the presence of pores in the materials having different characteristic length scales, from the nano- to the meso-scale. From the t-plot analysis it was possible to calculate the values of the total surface area and specifically the area of the micropores only (with a diameter smaller than 2 nm). Such values were calculated for the three different samples and they are reported in the table in *Figure 3.2.3*. It is possible to notice how the ionogel itself has a much lower BET surface area with respect to plain paper. Nevertheless, the resulting paper/ionogel hybrid composite possessed an even higher BET surface of 1.93 m^2/g. Also the total area of micropores of plain paper (1.00 m^2/g) clearly increased after the addition of the ionogel (1.73 m^2/g). This means that the higher BET total area is prevalently due to the formation of new micropores, whose contribution changes from the 57% for plain paper substrates to 90% for the paper/ionogel composite. Moreover, the emergence of well-defined peaks in the BJH distribution (red line in Figure 3-b) can be correlated to the presence of additional micro pores in the hybrid material due to the organization of the cross-linked ionogel along the fibrous structure.

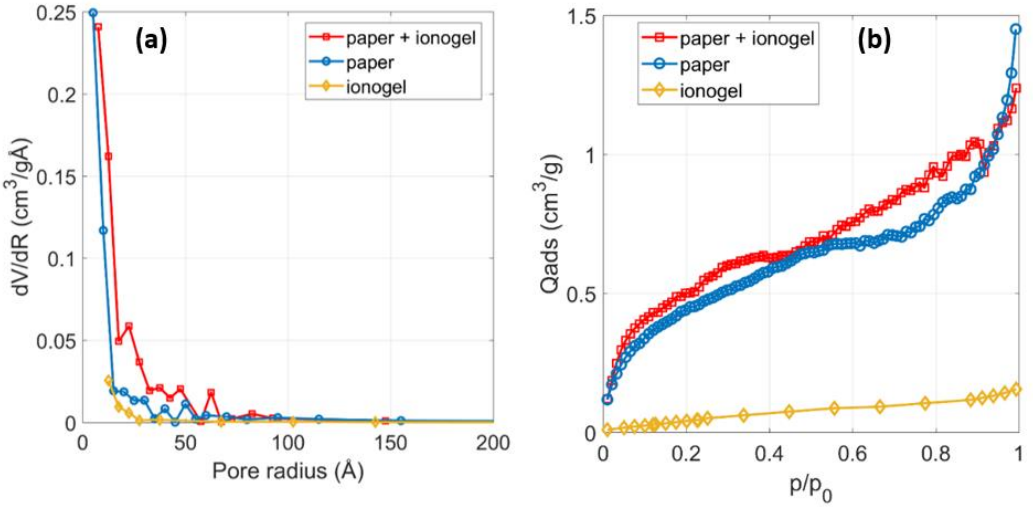

Figure 3.2.2. ***(a)*** *Nitrogen adsorption iosotherms of the prepared samples, showing the precence of pores with different length scale.* ***(b)*** *BJH distributions. The profile of the red line, related to the paper/ionogel network, shows structured peaks connected to the emergence of micropores, characteristic of the hybrid material.* [251].

	BET surface area (m^2/g)	Micropores area (m^2/g)
PAPER	1.74 ± 0.14	1.00 ± 0.01
IONOGEL	0.11 ± 0.01	0.03 ± 0.01
PAPER/IONOGEL	1.93 ± 0.12	1.73 ± 0.01

Figure 3.2.3. *BET total surface area and micropores area for standard paper, poly(AA-co-AN)-based ionogels and for the paper/ionogel hybrids* [251]. *In this case, the terms "micropores" is referred to those cavities with a diameter lower than 2 nm.*

These observations were also confirmed by atomic force microscopy (AFM) imaging. The obtained scans are reported in *Figure 3.2.4* and even from a qualitative point of view it can be noticed a more pronounced surface roughness of the paper/ionogel composite. The root mean square roughness (R_{rms}) was calculated on an area of 0.25 μm^2, resulting in (17 ± 2) nm for paper and (34 ± 5) nm for paper/ionogel. The same measures were carried out on a wider area of 4 μm^2, resulting in (46 ± 4) nm for paper and (136 ± 10) nm for paper/ionogel. These results, combined with those of BET analysis, demonstrate that the photopolymerization of the ionogel solution absorbed by the paper increased the original roughness of the paper fibres and also their superficial area, especially the surface of micropores (diameter < 2 nm). Detailed information on the experimental procedure of BET and AFM analysis are reported in *Section 6.1.5* and *Section 6.3.1* respectively.

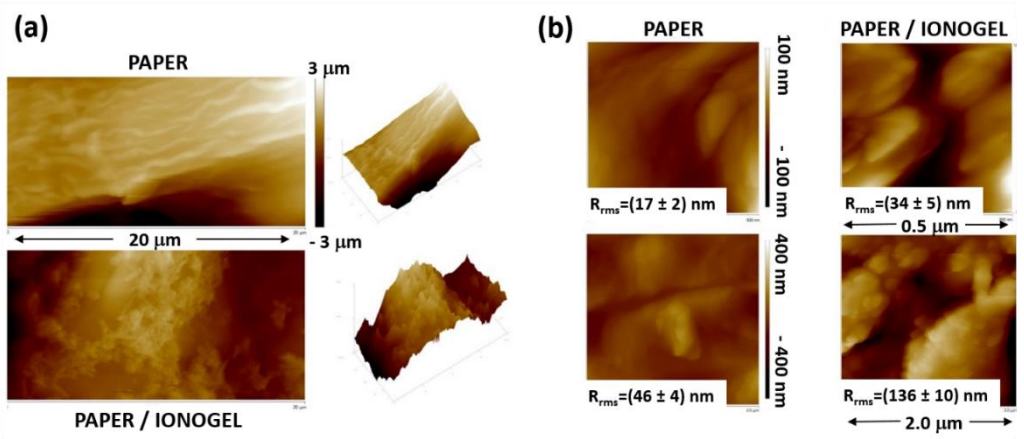

Figure 3.2.4. *AFM scans of paper and paper/ionogel composites.* ***(a)*** *20 x 10 μm scans and three-dimensional profiles;* ***(b)*** *2.0 x 2.0 and 0.5 x 0.5 μm scans, showing that the paper/ionogel samples possess a higher value of the root mean square roughness (R_{rms}).* [251].

3.2.2 Cluster-assembled gold electrodes with SCBD

A couple of gold electrodes was then fabricated on the two opposite sides of the paper/ionogel composite with the use of supersonic cluster beam deposition (SCBD). It is a technique that exploits a pulsed microplasma cluster source to sputter a metal precursor and generate metallic cluster in an inert gas atmosphere. Thanks to a pressure gradient, the clusters are delivered by the gas through an aerodynamic focuser, then the beam undergoes a supersonic expansion and finally hit the sample. Depending on the mechanical properties of the substrate and the deposition conditions, the Au clusters can partially implant underneath the surface of the substrate forming a nanostructured three-dimensional interface. The amount of deposited gold can be finely controlled thanks to the presence of a quartz microbalance. Detailed information about this technique are reported in *Section 1.4*. It was the selected method because it works at ambient temperature (heat can damage polymeric materials) and it can provide thin nanostructured electrodes characterized by good conductivity, electrochemical stability, high interfacial area with the underlying polymer, strong adhesion and stability to bending. A low sheet resistance R_s (or high sheet conductivity) is an important feature for electromechanical actuators. In order to study its correlation with the amount of deposited Au on the surface of paper/ionogel samples, both the R_s and the gold equivalent thickness t_{eq} (see *Section 1.4*) were measured in real time during the deposition process. *Figure 3.2.5(a)* reports in the graph the evolution of R_s over time, which was monotonically decreasing, while *Figure 3.2.5(b)* reports the thickness growth up to a value of 200 nm (equivalent with a mass of 160 $\mu g/cm^2$): it showed to be quite constant and it was approximated with the linear equation t_{eq} (nm) = 0.195 x t (s), obtaining an average growth rate gr = 0.195 nm/s.

Using this approximation, R_s values have been plotted against t_{eq}, as shown in the graph in *Figure 3.2.6*. It can be seen how for the first 5 nm of equivalent thickness, R_s has a value of about 1 x 10^8 Ω: there were not yet any electronic conductive paths between the deposited Au cluster, but an extremely low conductivity was observed, typical of ionic liquids. Then, after about 5 nm, deposited Au clusters began to form electronic conductive paths and the sheet resistance dramatically decreased. At 20 nm, R_s is about 1 x 10^3 Ω and further on it decreased much slower approaching a plateau. Thanks to this knowledge, an equivalent thickness of 150 nm (Au mass = 116 $\mu g/cm^2$), corresponding to a sheet resistance of about 20 Ω, was chosen as a suitable value for the presented paper/ionogel/Au composite. This choice was made by considering that, after 150 nm, higher amounts of Au resulted only in a minimal decrease in the sheet resistance value. More detailed information about the experimental setup and procedures are reported in *Section 6.2.1*.

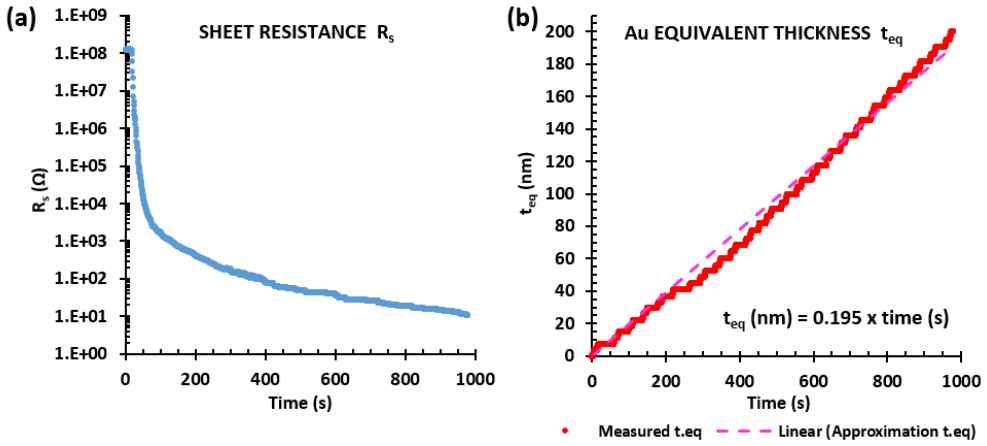

Figure 3.2.5. *Graphs reporting the evolution in time of the in-situ measured* ***(a)*** *sheet resistance R_s and* ***(b)*** *equivalent thickness t_{eq} regarding the cluster-assembled Au layer deposited through SCBD technique on the surface of a paper/ionogel hybrid composite. The thickness growth was approximated with a linear interpolation* [251].

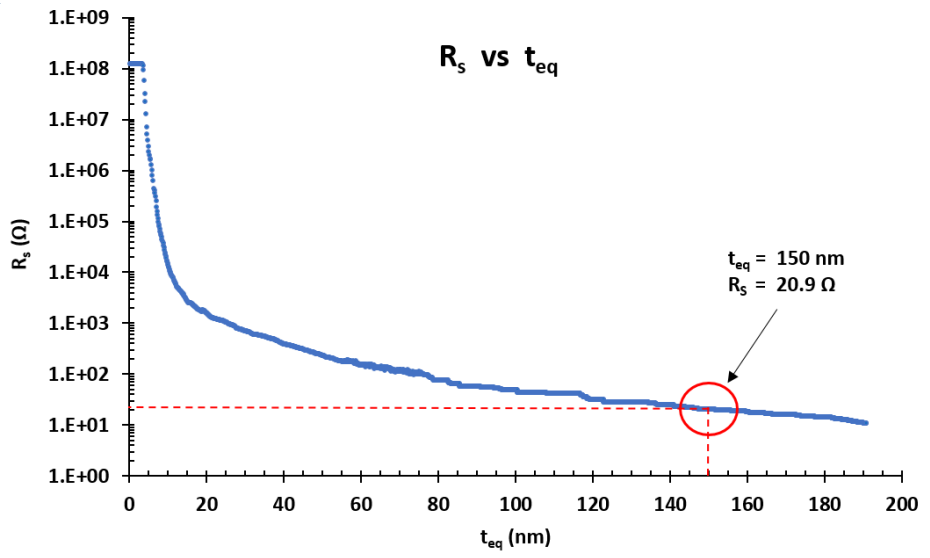

Figure 3.2.6. *The graph reports the values of R_s (in the logarithmic scale) plotted against the corresponding values of t_{eq} (obtained from the linear approximation) regarding the cluster-assembled Au layer SCBD-deposited on a paper/ionogel hybrid composite. The point at 150 nm and corresponding to a sheet resistance of 20.0 Ω was the one chosen for the electrochemical and electro-mechanical characterization* [251].

Figure 3.2.7(a-b) reports two pictures acquired with a reflection optical microscope and they show the separation between the metallized region of the samples and the bare paper/ionogel area. It can be observed a homogeneous gold coating of the fibrous structure with a sharp and well-defined edge, as typically obtained by using SCBD technique [36]. Au nanostructured morphology was also checked with scanning electron microscopy (SEM), as shown in *Figure 3.2.7(c)*. SEM was also used to observe the cross-section of the samples (*Figure 3.2.7(d-f)*), showing the paper fibers surrounded by the cross-linked ionogel.

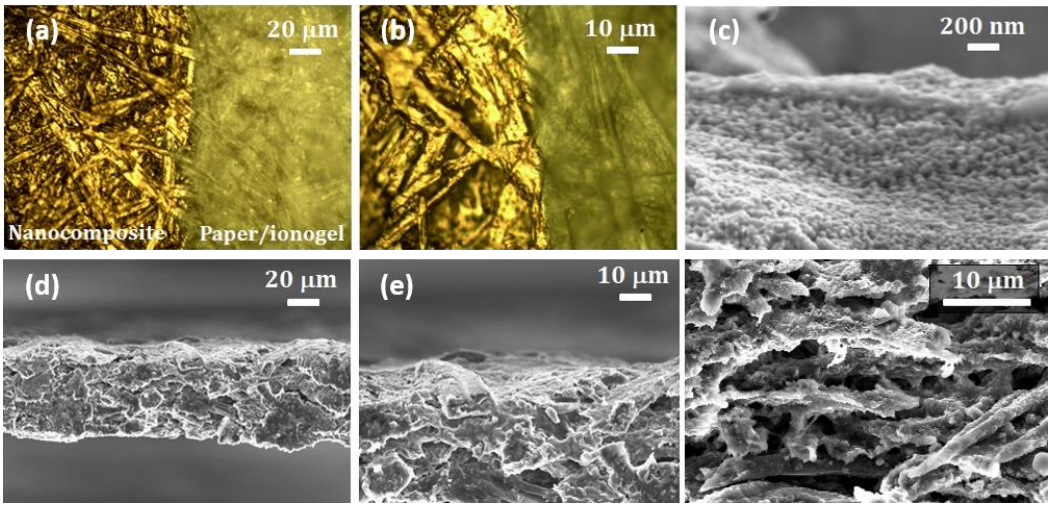

Figure 3.2.7. *Imaging on the the paper/ionogel/Au nanocomposite materuals:* ***(a, b)*** *optical microscope picterus showing the edge of the SCBD-deposited electrode;* ***(c)*** *SEM picture of the cluster-assembled Au electrode, the cross-section view is tilted by 3°;* ***(d-f)*** *SEM pictures of the composite's cross-section.* [251].

Paper/ionogel/Au composites were also obtained by fabricating gold electrodes with a conventional physical vapor deposition (PVD), in order to check how their electrochemical properties are affected by the used technique. The employed apparatus was an Edwards Coating System (model E306A): the process was carried out at a vacuum level of 5×10^{-4} Torr and about 0.5 g of gold were sublimated with a current of 60 A. The result was a couple of electrodes with a thickness of about 200 nm (checked with the help of an in-situ quartz microbalance) and a sheet resistance of 10 Ω.

3.2.3 Electrochemical characterization

The electrochemical characterization was carried out in order to investigate the charge transfer phenomena taking place inside the composite material, as well measuring the charge accumulation at the electrodes once an electrical potential is applied. Both are important features that affect also the electro-mechanical actuation. Furthermore, the analysis was conducted in order to qualitatively and quantitatively compare the behaviour of the samples metallized by mean of SCBD (Paper/Ionogel/SCBD) or using standard PVD (Paper/ionogel/PVD). Detailed information about the preparation of the samples and their contact with the used instrumentation are reported in *Section 6.2.2*.

To do this, the technique of electrochemical impedance spectroscopy (EIS) was chosen, because it can operate at extremely low applied potentials without damaging the samples. Through the application of an alternating potential of 5 mV at different frequencies and in absence of electrochemical redox processes, this technique allows to study ionic migration and accumulation inside the composite material and at the interface with the electrodes. Through the analysis of the current intensity and delay as a function of the frequency of the applied potential it was possible to obtain the Nyquist plot (the imaginary part of the impedance Z_i against the real part of the impedance Z_r) and the Bode plot (the absolute value of the impedance $|Z|$, the electrode's capacitance C and the current delay ϕ against the potential frequency) and they are reported in *Figure 3.2.8*.

By taking into consideration the profiles of the curves, the electric behaviour of both Paper/ionogel/SCBD and Paper/ionogel/PVD can be approximated with an equivalent circuit like the one reported in *Figure 3.2.9*. The most significant information is the equivalent series resistance ESR and the double layer capacitance C_{dl}. ESR is the sum of many resistive elements placed in series: usually the predominant one is the ionic conductivity inside the inner matrix, secondly the electrolyte-metal interface and the electrode resistance as well. ESR value can be obtained from the Nyquist plot by the intersection of the first semicircle with the Z_r axis, but also from the Bode plot in the intermediate frequency region: where the current is almost in phase with the applied potential (ϕ is near to 0°), $|Z|$ is influenced only by the ESR and they have the same value. Considering the geometry of the analysed sample, ESR can be used to estimate the ionic conductivity σ of the material: usually, a lower ESR or a higher value of σ mean a faster electromechanical actuation.

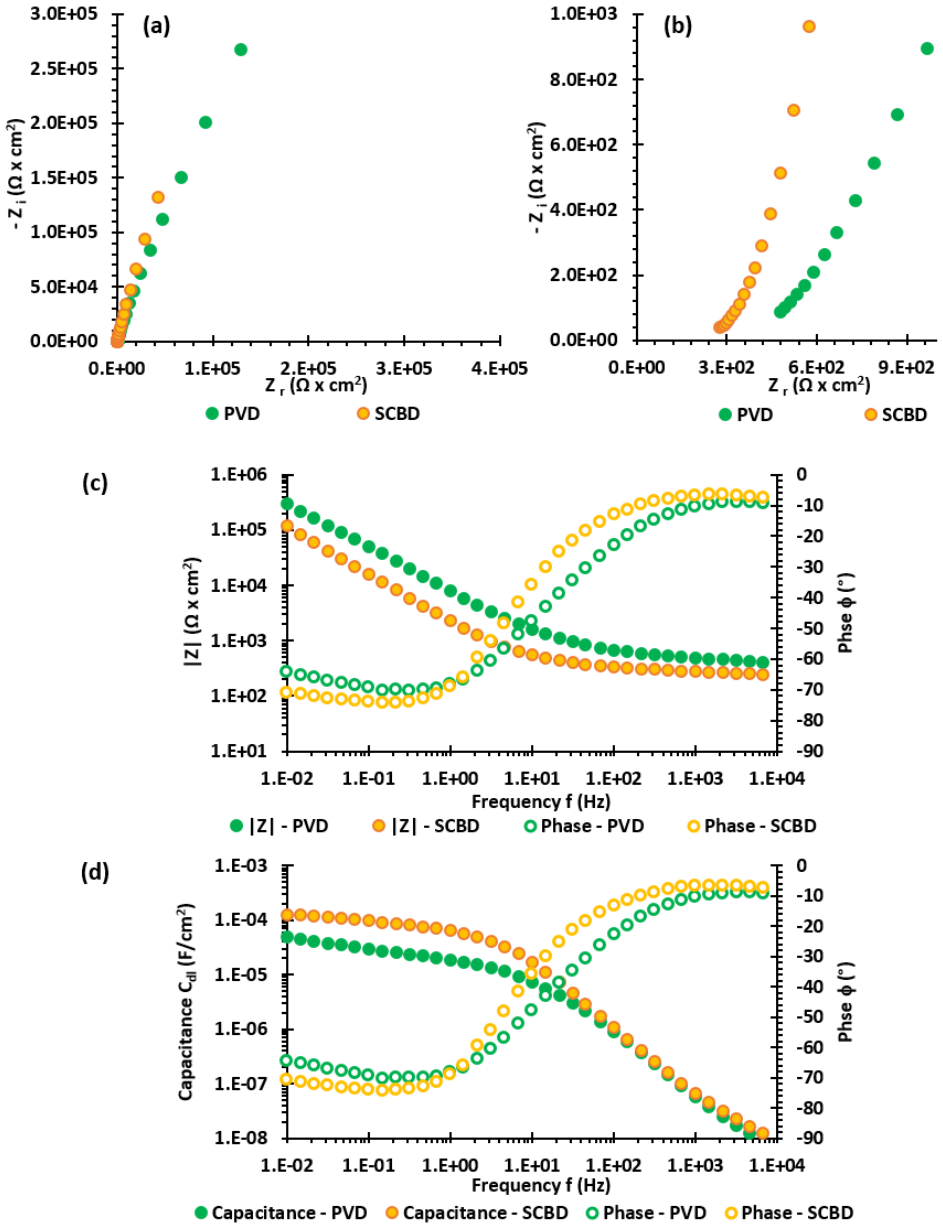

Figure 3.2.8. *Results of the EIS analysis on the paper/ionogel composites with electrodes fabricated by mean of PVD (green dots) or SCBD (yellow dots);* ***(a-b)*** *Nyqvist plot and its magnification reporting the imaginary part of the impedance Z_i against the real part of the impedance Z_r;* ***(c-d)*** *Bode plots reporting the absolute value of the impedance $|Z|$, the electrode's double layer capacitance C_{dl} and the current delay ϕ against the frequency of the applied potential.* [251].

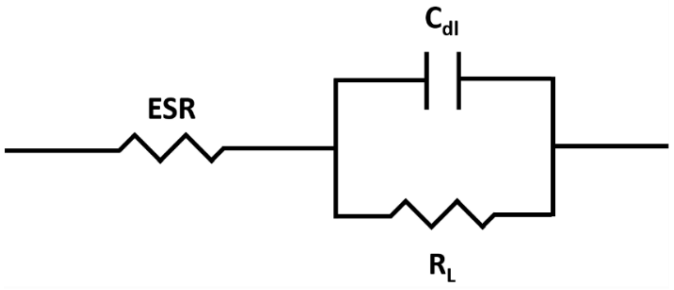

***Figure 3.2.9**. Equivalent circuit that models the electric behaviour of Paper/ionogel/SCBD and Paper/ionogel/PVD composites. The equivalent series resistance ESR is mainly due to the ionic conductivity and the contact resistance between the paper/ionogel composite and the electrodes; C_{dl} is the double-layer capacitance at the electrodes interface; the leakage resistance R_L refers to the electronic conductivity of the paper/ionogel composite.*

The double layer capacitance is a measure of the amount of charge (ions) that is possible to accumulate at the interface between the ionogel and the electrodes at a certain applied potential. While a pure capacitive element should be characterized by a current delay ϕ of -90° with respect to the applied ΔV, in this case the capacitance is not ideal since the ionogel-electrode interface is nanostructured: the ions are not atoms, but they are molecules of complex shape and in the case of SCBD the electrodes morphology is cluster-assembled and it presents many pores of nanometric dimensions. Because of this, the lowest value of ϕ was between -70° and -80° and the maximum capacitance value can be obtained at the lowest frequency of 0.01 Hz. The resistance placed in parallel with C_{dl} is the leakage resistance R_L of the paper/ionogel: even if the electric current inside the composite material is mainly carried out by the ionic migration, an exiguous electron flow exists due to the presence of ionic liquids, whose chemical structure is able to conduct a very small number of electrons. This is the reason why in this case ϕ reaches a minimum value at about 0.5 Hz and then slightly increases when frequency is reduced. Considering the results obtained for Paper/Ionogel/SCBD and Paper/Ionogel/PVD, both of them behave similarly and according to the proposed equivalent circuit. R_L was in the order of 10^6 Ω for both the two kind of analyzed samples: it's a high value that does not prevent the ionic accumulation at the electrodes. Regarding the equivalent series resistance and the double layer capacitance, which are the most relevant parameters, it was obtained that ESR = 439 Ω x cm^2 and C_{dl} = 48.3 μF / cm^2 for Paper/Ionogel/PVD, while ESR = 264 Ω x cm^2 and C_{dl} = 126 μF/cm^2 for Paper/Ionogel/SCBD. Also, by calculating C_{dl} according to the mass of the electrodes couple, the difference in the efficiency between SCBD and PVD appears even higher: C_{dl} = 0.062 F/g for Paper/Ionogel/PVD and C_{dl} = 0.54 F/g for Paper/Ionogel/SCBD. It clearly

appeared that the use of SCBD technique provided a couple of electrodes more efficient with respect to PVD. In fact, the lower ESR is due to a tight contact and partial interpenetration between the Au clusters and paper/ionogel matrix. Moreover, the higher interfacial area also reflected in a higher double layer capacitance that is expected to improve the extent of the electromechanical deformation. Thank to this, SCBD proved to be a more suitable technique to fabricate the electrodes of paper/ionogel/Au electroactive composites, also considering that it works at room temperature without damaging the polymeric substrate and that the fabricated electrodes are lighter. SCBD was then used to metallize the samples for the electromechanical actuation.

3.2.4 Spring electro-mechanical actuation

After the electrode fabrication, spring-like paper/ionogel/Au actuators were easily obtained by cutting the samples into strips (40 x 2.5 mm) and by shaping them into cylindrical helixes, by folding the components along a 2 mm diameter plastic tube. This process was optimized in order to ensure a controlled shape relaxation of the paper after release from the folded configuration, so to obtain helixes with a total length of 12 mm, having two coils with a radius of 15 mm and a pitch equal to 5 mm. Photographs of the paper/ionogel/Au actuators are shown in *Figure 3.2.10(a)*, both in a planar and in a helix-shape geometry. According to the actuation mechanism observed for poly(AA-co-AN)-based ionogel cantilevers, which display a unidirectional bending towards the anode in response to an applied potential, the presented paper/ionogel/Au helicoids were designed to exhibit an actuation pattern that comprises simultaneous twisting and longitudinal displacement along the helix main axis, as schematized in *Figure 3.2.10(b)*. This behavior is induced by the asymmetric ionic migration and accumulation that takes place inside the composite material. When the electrode on the inner side of the actuator behaves like an anode and the outer one acts like a cathode, the ionic liquid swells the outer side of the paper/ionogel while shrinking its inner side. The overall asymmetric contraction and expansion results in a longitudinal elongation and transversal shrinkage of the spring-like actuators. Such helix configuration has already been studied in the electroactive ionic polymers framework to produce spring-like actuators using Nafion [277,278], however this approach has never been explored for cellulose and paper-based electroactive ionic actuators. Electromechanical actuation tests were then conducted on the helix-shaped paper/ionogel/Au samples using a custom-designed setup equipped with a wave generator and a power supply. The helixes were clamped at one of their free end and suspended vertically in order to display motion along the azimuthal direction. More information about the setup and the electric contacts employed are provided in *Section 6.2.3*.

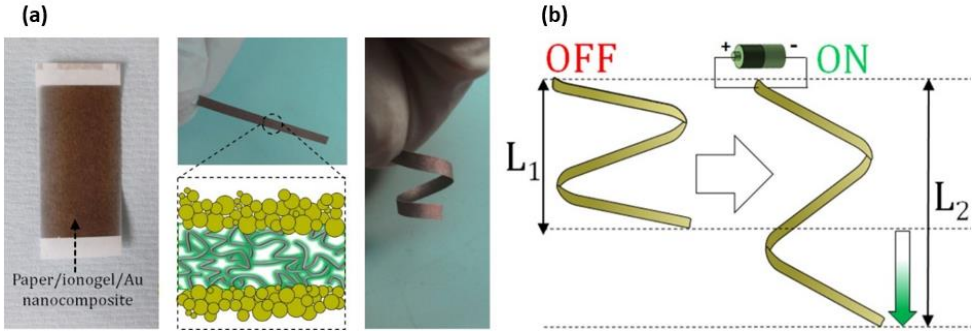

***Figure 3.2.10**. **(a)** Photographs and schematics of the paper/ionogel/Au electroactive composite, that was cut and then folded into a cylindrical helix. **(b)** Schematic illustration of the electroactive displacement of the helix-shaped samples in the longitudinal direction.* [251].

Figure 3.2.11(a-b) reports photographs of a sample's actuation. In the voltage range tested, from 1 to 5 V, the induced mechanical response showed to be reproducible and reversible. *Figure 3.2.11(c)* reports the value of the helix tip's longitudinal displacement ΔL as a function of the applied potential. As expected, ΔL increased with the applied potential, ranging from 0.5 mm at 1.5 V to 1.2 mm at 3 V and up to 2 mm at 5 V. The effective strain of the actuator, calculated as the ratio between the ΔL and its original length L_0, ranged then from 4% to 16%. In all the cases, the actuation linear speed was approximately 0.1 mm/s. This longitudinal elongation was associated with a transversal contraction that was of 1.7 mm at an applied potential of 4 V (see *Figure 3.2.11(b)*). The actuators exhibited stable electromechanical actuation when stimulated by square waves with an amplitude of 3 V with frequencies of 0.5 Hz and 0.1 Hz, displaying a systematic decrease in the linear motion as the frequency was increased, in line with their actuation profile explored applying constant voltages. The electro-mechanical response was also tested at 10 Hz, with a voltage amplitude of 3 V: even if the helical structure exhibited a response that involved wider regions of the whole structure along the z-axis, as a new vibration mode closer to its resonant frequency, no longitudinal displacement could be measured. The electromechanical actuation was then monitored over 5000 actuation cycles by applying a square wave with amplitude of 2.5 V and frequency of 0.25 Hz, in order to assess their durability by measure their displacement over thousands of cycles. The results are reported in *Figure 3.2.11(d)*. The initial value of ΔL was of 0.45 mm and it's possible to see that after 5000 cycles the displacement retention ΔL_{ret} was of 88% of its original entity, meaning that there was no massive deterioration of the samples in these working conditions.

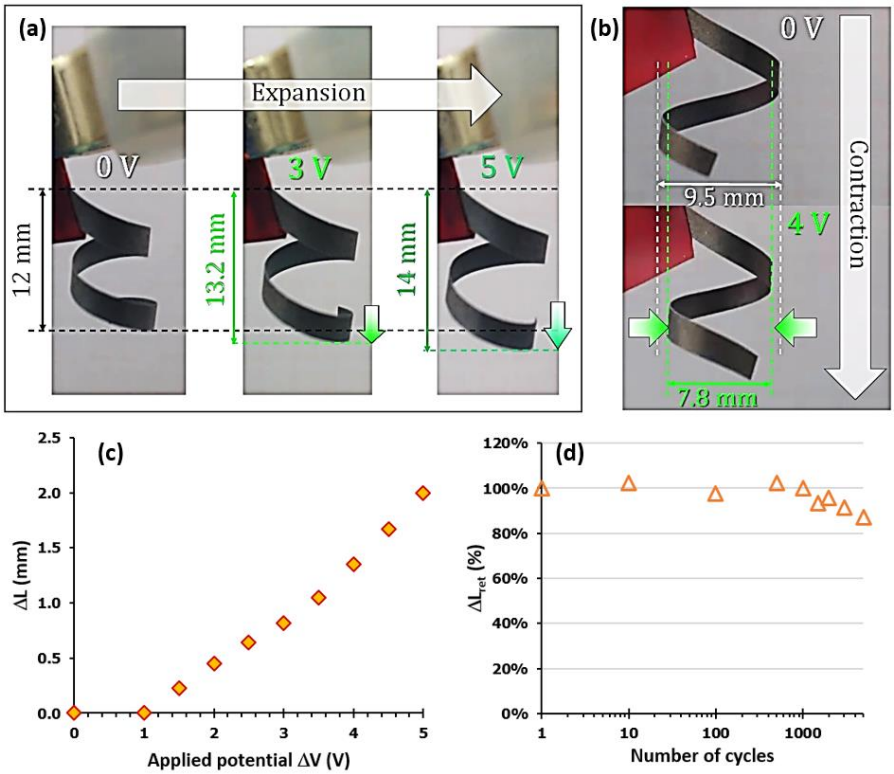

Figure 3.2.11. *Spring-like actuation of the paper/ionogel/Au electroactive composites;* ***(a)*** *Pictures showing the longitudinal displacement ΔL at the application of 3 and 5 V;* ***(b)*** *Pictures showing the transversal contraction at the application of 4 and 5 V;* ***(c)*** *Graph reporting the longitudinal displacement ΔL as a function of the applied potential ΔV;* ***(d)*** *Graph reporting the displacement retention values (ΔL_{ret}) against the number of actuation cycles, with an applied potential of 2.5 V at an alternated frequency of 0.25 Hz.* [251].

Considering all the obtained results, it was assessed that the integration of conventional plain paper with an ionogel led to the formation of an electroactive composite material with the mechanical properties of paper and improved porosity and surface area. The fabrication of cluster-assembled Au electrodes with SCBD allowed an efficient ionic accumulation at the ionogel-metal interface and exploiting the foldability typical of paper a spring-like geometry was achieved, able to provide longitudinal electromechanical actuation with good stability up to 5000 cycles. Not less importantly, the 74% (in weight) of the overall smart composite material is represented by natural-derived and biodegradable paper. The presented results are also reported in a scientific paper published by Smart Materials and Structures [251].

3.3 BIOPLASTIC ACTUATORS BASED ON PHB

3.3.1 PHB-IL ionogel synthesis and characterization

Poly(3-hydroxybutyrrate) (PHB), a bioplastic produced by bacteria, possess many interesting properties such as natural derivation and biodegradability combined with the features typical of conventional plastic materials: bendability, tensile strength, hydrophobicity, lightness (chemical structure shown in *Figure 3.3.1*). Because of this, in this work PHB was used for the first time as the only polymeric matrix for the development of an electroactive actuator. To obtain an electroactive ionogel from PHB, it was then necessary to provide ionic couples with different size and shape and a liquid medium in which these ions can migrate under the effect of an electric field. Ionic liquids (ILs) are organic salts in the molten state at room temperature and they are an optimal solution to serve both as the active ions and the liquid phase. ILs also possess an extremely low vapor pressure that avoids evaporation of the liquid at ambient conditions, which is a key factor for the design and manufacture of electromechanical actuators meant to operate in air. The hydrophobic ionic liquid 1-Butyl-3-methylimidazolium bis(trifluoromethylsulfonyl)imide BMIM(Tf_2N) was chosen to be blended with PHB due to its good miscibility with the polymer, as evaluated on an empirical basis. The organic salt tetrabuthylammonium fluoride (TBAF) was also added since the presence of a quaternary ammonium salt in ionogel-based actuators showed to improve their electromechanical performances: in fact, the presence of other ions in addition to those of the ionic liquid leads to a higher ionic mobility and asymmetry, both of them beneficial to electromechanical actuation [22]. PHB represented the 45% of the total mass, BMIM(Tf_2N) the 51.5% and TBAF the 3.5%. The molecular structures of the employed compounds are reported in *Figure 3.3.1(a)*.

To fabricate thin ionogel layers, a solvent casting process from acetic acid was adopted, similarly to the one proposed by Anbukarasu et al. [279], which is much eco-friendlier than the traditional one with chloroform. It basically consists in the dissolution of the compounds in acetic acid at 110°C, the subsequent injection of the liquid solution inside an aluminium mold (shown in *Figure 3.3.1(b)*) and in the evaporation of the acetic acid in oven. *Figure 3.3.1(c)* shows a picture of one of the obtained PHB-IL thin film. This fast and simple procedure (about 45 minutes from dissolution to casting) allowed to obtain flexible thin films of PHB-IL ionogel with a thickness of 50 μm and 200 μm (according to the volume of poured solution). More detailed experimental information is reported in *Section 6.1.1(d)*.

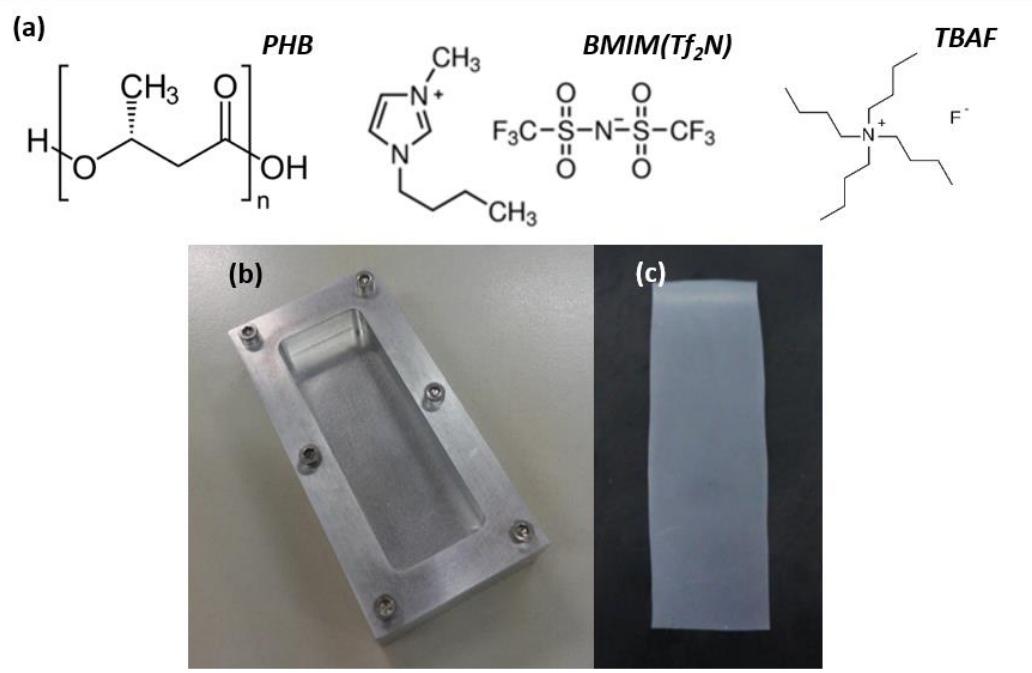

Figure 3.3.1. ***(a)*** *Chemical structures of the employed compounds: poly(3-hydroxybutyrrate), 1-Butyl-3-methylimidazolium bis(trifluoromethylsulfonyl)imide, tetrabuthylammonium fluoride;* ***(b)*** *Photograph of the aluminium mold employed in the solvent casting process;* ***(c)*** *Picture of one of the obtained PHB-IL ionogel thin film.* [274].

Because the electromechanical performance of electroactive ionogels may be affected by the moisture absorbance, this feature was checked in two different high humidity conditions: inside an incubator with humidity level of 95% and open-air in the traditional humid climate of the Po Valley [280]. In both cases no water absorption was observed, a feature typical of traditional plastic materials. This is a unique feature in the field of IEAPs [249]. In fact, ionic polymers are always water-soluble or water absorbent and this represent a huge limit for real-world applications of electromechanical actuators, since different humidity conditions will affect and change their properties. Instead, PHB-IL ionogels showed to be moisture resistant because of the high hydrophobic character of both PHB and BMIM(Tf_2N).

The mechanical properties of the samples were characterized by means of tensile tests and a representative stress-strain curve is reported in *Figure 3.3.2*. An elastic behavior was observed up to an elongation of about 1% of the sample's original length. The calculated elastic modulus was 303 MPa, which is around 5 times lower than the one

reported for pure PHB films casted from chloroform (ca. 1.5 GPa [272]). For higher elongations, the relationship between stress and strain is no longer linear and a plastic behavior is observed. The overall tensile strength and the elongation at break were also calculated and resulted equal to 10.9 MPa and 11.1%, respectively, while pure PHB films casted from chloroform possess a tensile strength of about 30 MPa and elongation at break of about 9% [279]. A more detailed experimental procedure is reported in *Section 6.1.3*. These results highlight how the presence of the ionic liquid is important not only to provide active mobile ions, but also to soften PHB, rendering its elastic modulus similar to that of low density PET, rubber and swollen Nafion. In fact, the IL is likely to act as a plasticizer, breaking the crystallinity and the order of the inner polymeric chains.

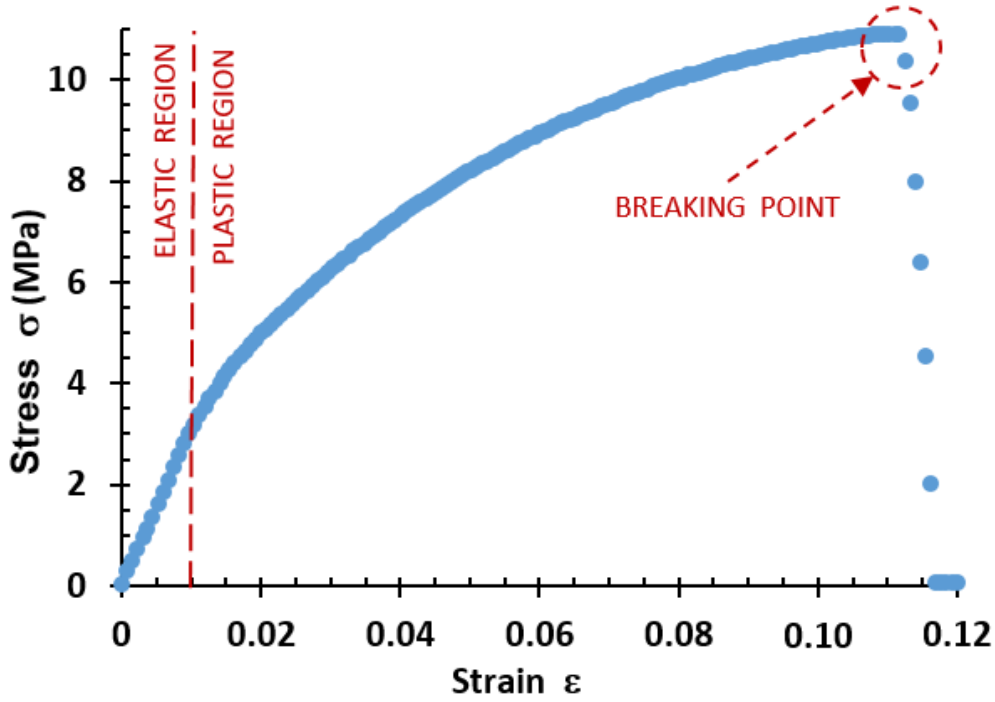

***Figure 3.3.2**. Graph reporting the stress – strain curve of PHB thin films. It was obtained by mean of tensile tests. It's possible to see the elastic region (up to a strain value of 0.01) where the σ and ε are directly proportional, while in the plastic region they are not. The samples broke at an elongation of about the 11% of their original length (ε = 0.11)* [274].

3.3.2 Electrodes fabrication and electrochemical properties

Cluster-assembled gold electrodes were fabricated on both sides of the PHB-IL ionogel films using supersonic cluster beam deposition (SCBD). This metallization technique was chosen because it operates at ambient temperature and it allowed the fabrication of highly conductive, stable, well-anchored and very thin (t_{eq} = 150 nm) conductive layers without damaging the polymeric matrix. The use of gold guaranteed low sheet resistance R_s, which is important to provide the actuators with uniform electric signals across the electrodes. Moreover, since they are deposited onto a soft polymeric matrix, the gold clusters (with a diameter from 3 to 10 nm) partially penetrate underneath the target surface, leading to a strong adhesion and anchorage of the metallic film to the polymer, and to the formation of a nanostructured metal – ionogel interface. A detailed description of the technique is provided in *Section 1.4*. The low equivalent thickness of the electrodes (150 nm) was selected to both minimize the mechanical mismatch between the metallic layer and the polymer without affecting the bending ability of the material and to achieve low sheet resistance of about 10-12 Ohm. Such t_{eq} corresponds to an Au mass equal to 116 μg/cm^2. *Figure 3.3.3(a)* shows a schematic of the PHB-IL-Au composite materials while *Figure 3.3.3(b-c)* reports few pictures of the samples before and after the metallization process. More detailed information about the experimental procedure are reported in *Section 6.2.1*.

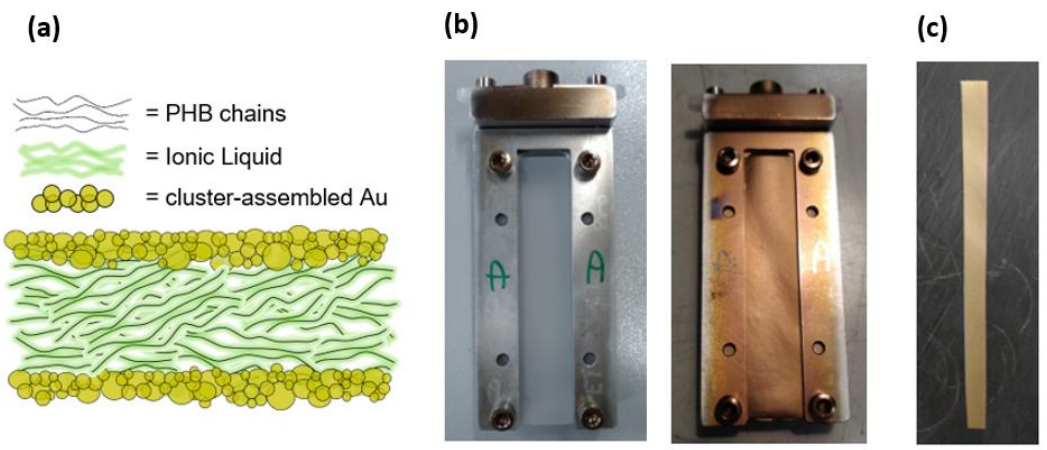

***Figure 3.3.3**. **(a)** Schematic structure of PHB-IL-Au composites; **(b-c)** Picture of a ionogel mounted on a custom sample holder, before and after metallization and cutting.* [274].

Figure 3.3.4(a) reports optical microscope images acquired before and after the metallization and it can be seen how the thin gold layer did not change the ionogel's surface morphology at the microscopic level. SEM images are also presented (*Figure 3.3.4(b-d)*), showing the PHB-IL-Au composite's cross-section and a detailed view of the cluster-assembled electrode, revealing the nanostructured gold morphology.

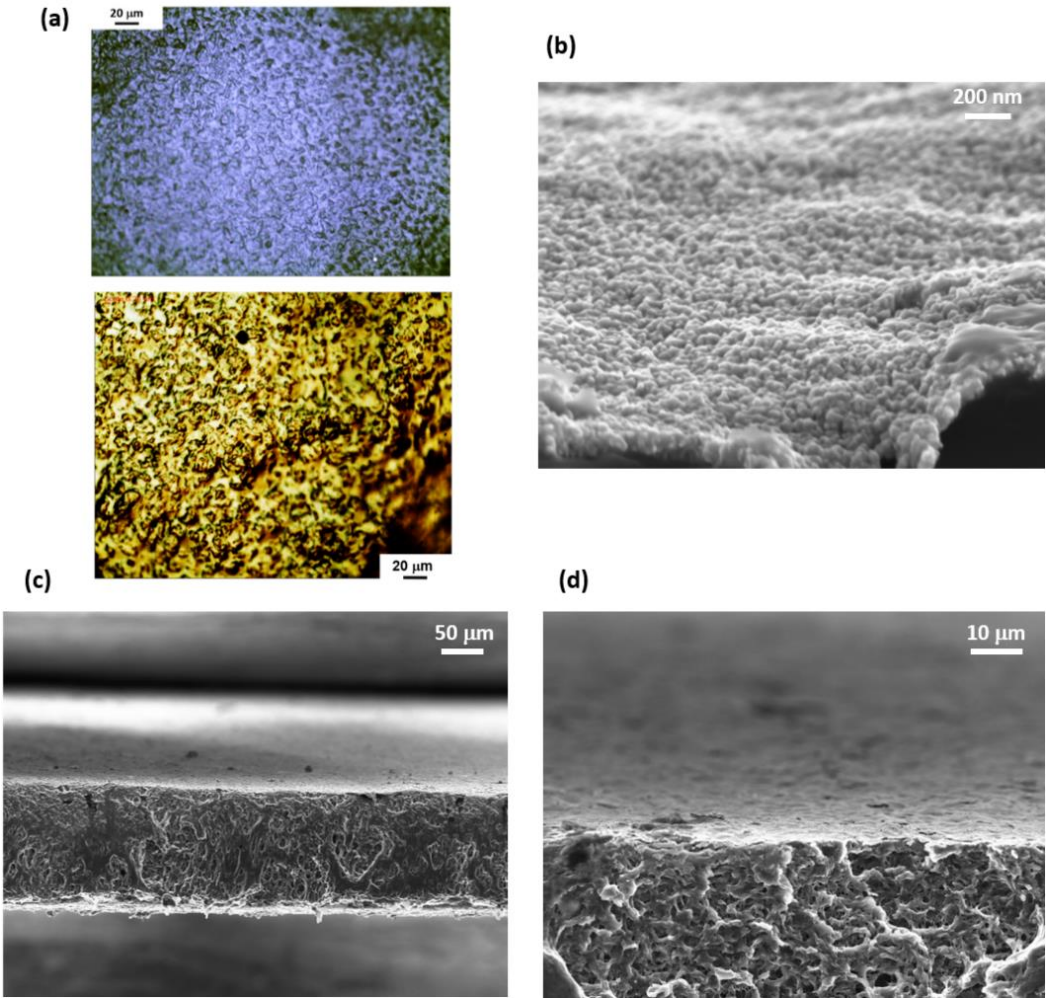

***Figure 3.3.4**. Imaging of the PHB-IL-Au composites. **(a)** Optical microscopy of the ionogels surface, before and after the metallization via SCBD; **(b)** SEM picture (50000 X) showing the nanostructured electrodes morphology; **(c-d)** SEM pictures (200 and 1000 X) showing the cross-section of the composites.* [274].

Since the electromechanical actuation relays on the ionic migration inside the ionogel and the ionic accumulation at the electrodes interface, these phenomena were studied by mean of electrochemical impedance spectroscopy (EIS). The tests were initially carried out at ambient conditions and they were repeated in controlled nitrogen atmosphere. Detailed information about the employed set up and contacts are reported in *Section 6.2.2*. An alternating potential of ± 5 mV was applied at the two opposite electrodes of the samples and the current intensity and delay were measured as a function of the potential's frequency.

Then, Nyquist plot (*Figure 3.3.5(b)*) was obtained by plotting the inverse value of the impedance's imaginary component (Z_i) against its real component (Z_r). In the Bode plots (*Figure 3.3.5(c, d)*) the absolute value (logarithmic scale) of the impedance |Z|, the logarithm of the double – layer capacitance C_{dl} and the current phase ϕ (°) are reported as a function of the logarithm of the frequency f of the applied potential. From the shape of the obtained curves, the electric behaviour of the analysed samples can be approximated with an equivalent circuit like the one reported in *Figure 3.3.5(a)* (the same observed for the paper/ionogel/Au composites reported in *Section 3.2.3*).

ESR is the sum of any resistive element placed in series, but the main contribution is due to the ionic conductivity of the ionogel. As can be seen from the Bode plot, at high frequencies ϕ = 0°, meaning that the system behaves like a pure resistance. Then the corresponding |Z| value can be regarded as the equivalent series resistance ESR = 5.32×10^3 Ω x cm^2. Since the electric charge inside the ionogel is transported by mobile ions, this value can be used to calculate the characteristic ionic conductivity $\sigma = 6.58 \times 10^{-7}$ S/cm. The same values can be obtained from the Nyquist plot, by considering the intersection between the data line and the Z_r axis. The relatively high value of the obtained resistance is probably due to the insulating nature of the PHB and suggests that the ionic motion across the ionogel is slow. Nevertheless, such a low conductivity implies low values of the ionic current, a feature that usually improves operational durability and stability of the actuator. At low frequencies instead a real capacitive element should display ϕ = -90°, but in this case the double layer capacitance C_{dl} was not ideal, since it regards the accumulation of molecular ions of different size and shape at the interface with a nanostructured cluster-assembled electrode. Then, at the lowest frequency, ϕ reached a value of almost -75°. The not ideal capacitive behavior was also confirmed by the almost vertical profile in the Nyquist plot. More specifically, at the lowest frequency (0.01 Hz), C_{dl} = 322 μF/cm^2. Considering the extremely low amount of electrode material (considering both the electrodes, t_{eq} = 150 nm, Au mass = 232 μg/cm^2), the calculated specific capacitance was of this value of 1.39 F/g, proving the formation of a high interfacial active surface between the electrodes and the underlying ionogel.

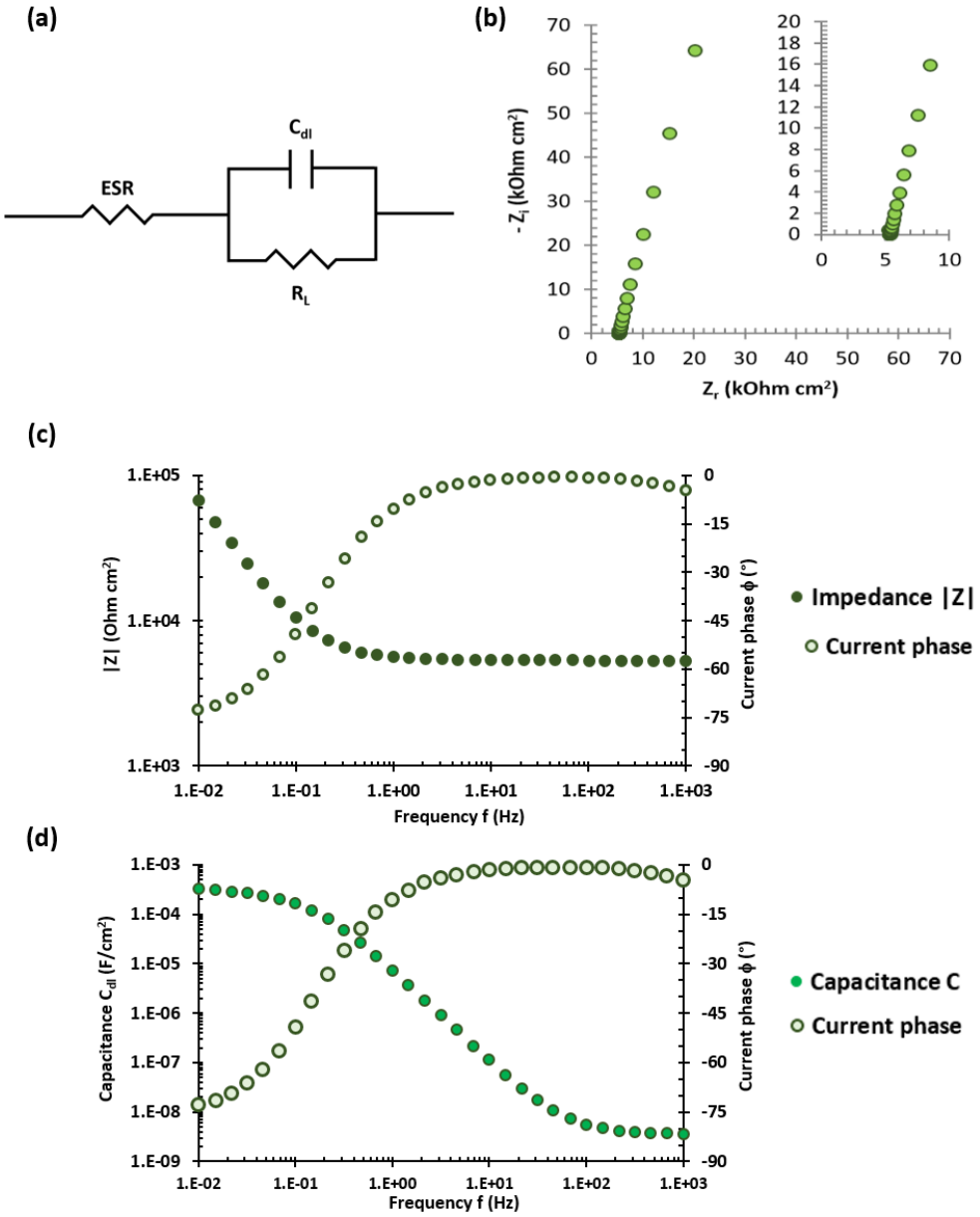

Figure 3.3.5. *Results of the EIS analysis on the PHB-IL-Au composite films.* ***(a)*** *Equivalent circuit that models the electric behaviour of the samples: an equivalent series resistance, a double layer capacitance and an electronic/leakage resistance are present.* ***(b)*** *Nyquist plot and its magnification reporting the imaginary part of the impedance Z_i against the real part of the impedance Z_r;* ***(c-d)*** *Bode plots reporting the absolute value of the impedance |Z|, the electrode's double layer capacitance C_{dl} and the current delay ϕ against the frequency of the applied potential.* [274].

The formation of an efficient double layer is a key feature for electroactivity and thanks to these results it was demonstrated the possibility to fabricate a composite material by blending together an electrically insulating bioplastic and an ionic phase, without losing ionic mobility. At last, the ionic liquid inside the ionogel was also characterized by a slight electronic conductance and the measured R_e was 5.12×10^5 Ohm x cm^2. This high value means that electronic conduction inside the materials can be considered negligible with respect to the ionic conduction, that is the key factor for electroactive properties.

The same results were obtained by repeating the tests in controlled nitrogen atmosphere, proving that ionic migration and accumulation were not influenced by the humidity in the surrounding environment, as it happens for the most of ionic electromechanical actuators.

3.3.3 Electromechanical actuation

Electromechanical actuation tests were carried out on 50 μm-thick samples, cut in a cantilever shape with a free length of 30 mm and clamped at one end, both in ambient conditions and in controlled nitrogen atmosphere. Detailed information on the experimental setup and the performed calculations are reported in *Section 6.2.3*. The PHB-IL-Au samples were stimulated with the application of both DC and AC potential at the electrodes, from 0.1 to 7 V at different frequencies (from 0.1 to 1 Hz). The actuators showed to be responsive even at the lowest applied potential of 0.1 V, bending towards the cathode in a reversible way, as can be seen in *Figure 3.3.6(a)* that presents the overlapping of pictures acquired with a camera during the tests. The tip's displacement x (mm) on the X-axis as a function of the applied potentials and frequencies was measured, as well as the curvature k ($cm^{-}1$), that takes into account the cantilever's length, and the strain ε that considers also the thickness. All the values are presented in the tables in *Figure 3.3.6(b-d)*.

(a)

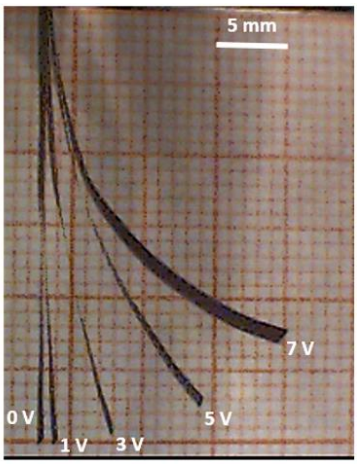

(b)

ΔV (V)	Displacement x on the x-axis (mm)				
	1 Hz	0.5 Hz	0.2 Hz	0.1 Hz	Max. Disp.
0.1	0.1	0.2	0.2	0.2	0.2
0.25	0.2	0.2	0.2	0.3	0.3
0.5	0.2	0.2	0.3	0.4	0.5
1	0.2	0.3	0.4	0.6	1
1.5	0.3	0.3	0.5	0.8	1.6
2	0.3	0.4	0.6	1	2.5
2.5	0.4	0.5	0.7	1.2	3.8
3	0.4	0.5	0.8	1.4	5
4	0.5	0.7	1	2	8
5	0.6	1.0	1.5	3	11
6	0.8	1.3	2.3	4.5	14
7	1	1.8	3.8	7.4	17

(c)

ΔV (V)	Curvature k (um^{-1})				
	1 Hz	0.5 Hz	0.2 Hz	0.1 Hz	Max. Curv.
0.1	0.2	0.4	0.4	0.4	0.4
0.25	0.4	0.4	0.4	0.7	0.7
0.5	0.4	0.4	0.7	0.9	1.1
1	0.4	0.7	0.9	1.3	2.2
1.5	0.7	0.7	1.1	1.8	3.6
2	0.7	0.9	1.3	2.2	5.6
2.5	0.9	1.1	1.6	2.7	8.4
3	0.9	1.1	1.8	3.1	11.1
4	1.1	1.6	2.2	4.4	17.8
5	1.3	2.2	3.3	6.7	24.4
6	1.8	2.9	5.1	10.0	31.1
7	2.2	4.0	8.4	16.4	37.8

(d)

ΔV (V)	Strain ε (x 10^{-6})				
	1 Hz	0.5 Hz	0.2 Hz	0.1 Hz	Max. Strain
0.1	11	22	22	22	22
0.25	22	22	22	33	33
0.5	22	22	33	44	56
1	22	33	44	67	111
1.5	33	33	56	89	177
2	33	44	67	111	276
2.5	44	56	78	133	416
3	44	56	89	155	541
4	56	78	111	221	830
5	67	111	166	330	1077
6	89	144	254	489	1277
7	111	199	416	775	1430

Figure 3.3.6. *Results of the electromechanical characterization of the PHB-IL-Au actuators;* ***(a)*** *Overlapping of pictures acquired during the tests;* ***(b-d)*** *Tables reporting the data on the PHB-IL-Au cantilevers actuation, for different values of applied potential and frequency, according to three different indexes: the tip's displacement projection on the X-axis x (mm), the actuators curvature k (cm^{-1}) and their electromechanical strain ε (pure number).* [274].

The actuator strain values are also plotted against the applied potential in the graph in *Figure 3.3.7*. As can be seen, at 0.1 V the actuators showed a maximum tip displacement of 0.2 mm and a calculated strain of 24.4 × 10^{-6}. For higher applied potentials the entity of the actuation increased as expected. The displacement showed to increase at lower frequencies and vice versa, nevertheless the maximum amplitude

was always achieved by applying a DC voltage. This slow actuation was in line with the value of ionic conductivity found with electrochemical impedance spectroscopy. However, the maximum displacements and associated strains showed to be relatively high: 1 mm (ε = 111 × 10-6) at 1 Volts, 5 mm (ε = 540 × 10-6) at 3 Volts, 11 mm (ε = 1077 × 10-6) at 5 Volts 17 mm (ε = 1430 × 10-6) at 7 Volts.

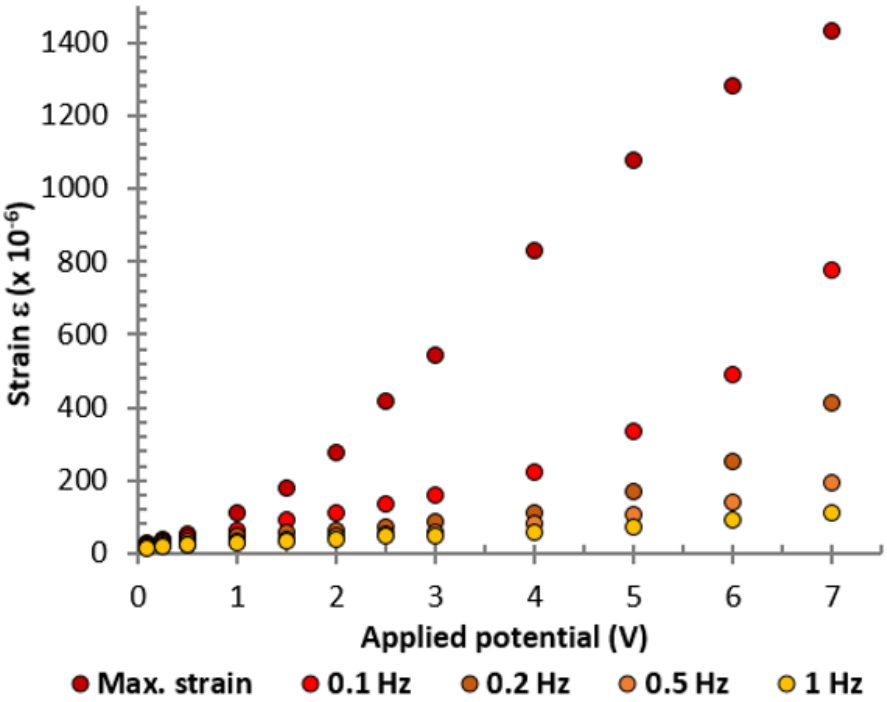

Figure 3.3.7. *A graph showing the strain values of PHB-IL-Au actuators. The samples were stimulated with an AC applied potential of different values and frequency; the maximum strain value was obtained through the application of a DC* [274].

Cyclic tests were also conducted by the application of 2 V at 0.5 Hz and 4 V at 0.75 Hz. The results are shown in *Figure 3.3.8*, where the displacement retention x_{ret} is plotted against the number of cycles. Under the application of 2 V the actuators showed to be stable up to 10^5 cycles and, interestingly, after one thousand cycles the displacement's amplitude increased up to the 125% of the original value, probably because of a mechanical training of the cantilever. This is a significant result, since high stability is an important feature for a durable operation. At higher potentials (4V) the displacement retention (x_{ret}) showed to be lower, reaching values of about 80% at 5 ×

10^4 cycles. This behavior is easily explained by considering that a potential of 4 V is at the limit of the window of electrochemical stability of the used BMIM(Tf2N) [11], meaning that some redox reactions are occurring between the different ionic species inside the ionogel (the ions of the ionic liquid and/or of the TBAF). Like in the case of electrochemical characterization, also the electromechanical actuation showed to be the same in ambient condition and in controlled nitrogen atmosphere, which is a remarkable result in the context of ionic electromechanical actuators.

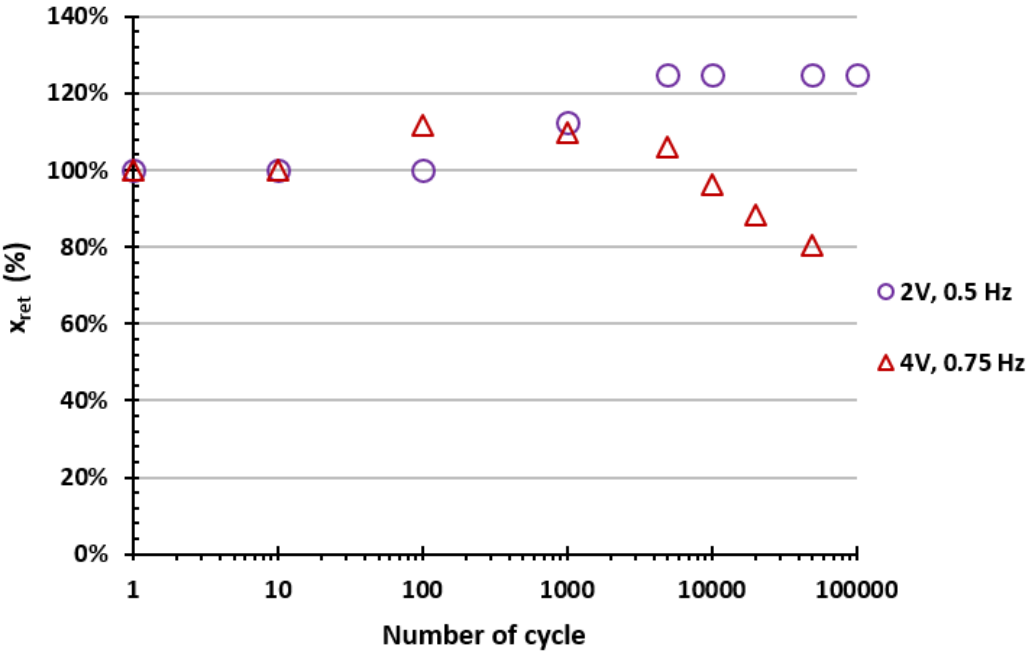

***Figure 3.3.8**. Graph reporting the displacement retention values (x_{ret}) against the number of actuation cycles. The actuators were subjected to an applied potential of 2 V at 0.5 Hz or of 4 V at 0.75 Hz* [274].

These results assessed the successful use of a natural-derived and biodegradable biopolymer like PHB, together with a suitable ionic liquid and cluster-assembled gold electrodes, to develop bioplastic-based electromechanical soft actuators. Their performances are comparable with those of traditional IPMCs, but with the great advantage to be unaffected by the surrounding humidity level and to be derived from a biopolymer. The presented results are also reported in a scientific paper published by Sensors and Actuators B: Chemical [274].

4.

BIODEGRADABLE MICRO-SUPERCAPACITORS

4.1 OVERVIEW ON SUPERCAPACITORS (SCs)

4.1.1 Energy-storage devices (ESDs)

Almost every current technological device and machinery needs a power supply to carry out its functions. Some of them (e.g. domestic appliances) are powered through a direct connection with the electric line, other (e.g. traditional automobile) are equipped with an engine able to autonomously produce the energy they need. Anyway, in both cases, energy storage devices (ESDs) are becoming more and more employed to accumulate the excess electrical energy (charge process) and gradually release it (discharge process) in order to make these devices independent from the power line or the engine (even if for a limited time and/or for a limited number of functions). Besides, the majority of portable devices (e.g. smartphones) are now powered solely by rechargeable batteries, the most common energy storer. Moreover, the necessity to store energy is particularly crucial regarding the so-called "renewable" energy, such as wind and solar: in fact, the energy obtained with these techniques is not immediately ready to be exploited and then it needs to be accumulated until its future employment.

Different kinds of ESDs exist, and they can be differentiated according to their operational principle or to their energetic performance. The **Ragone plots**, reported in *Figure 4.1.1*, are often used to compare and distinguish different devices according to the total amount of energy (E) they can store and the maximum power (P, or P_{max}) they can deliver. These values are usually related to the amount (express in mass or in volume) of the employed active material, i.e. the electrode components of the device.

Batteries and fuel cells are the ones able to store the highest amount of energy in the form of electrochemical energy. Fuel cells exploit the energy coming from a redox reaction: typically, the oxidation of hydrogen and the reduction of oxygen. They need to be continuously provided with the fuel. Instead, in the electrochemical batteries, metallic species are already present inside the device and they can be alternatively oxidized and reduced to gain or release electrochemical energy. Because of this they do not need to be supplied and they are the most diffuse ESD in portable electronics (in particular, Li-ion batteries). Their high energy is due to the huge amount of

electrochemically active entities that can be included inside a medium (liquid or semi-solid) placed between the couple of electrodes and by the fact that the amount of charge-transfer processes is not limited by the electrodes surface. By the way, they can operate at single potential values (the one characteristic of the involved redox process, e.g. up to 3.7 V for Li-ion batteries): it's not possible to charge a battery with an applied potential lower than the redox one and that's the maximum potential it can deliver. Because of this, they cannot deliver the energy at a high power, which is limited also by the resistance of the electronic transfer process and by the diffusion of the active species throughout the medium. Moreover, they usually do not exceed 1000 cycles of charge and discharge [281].

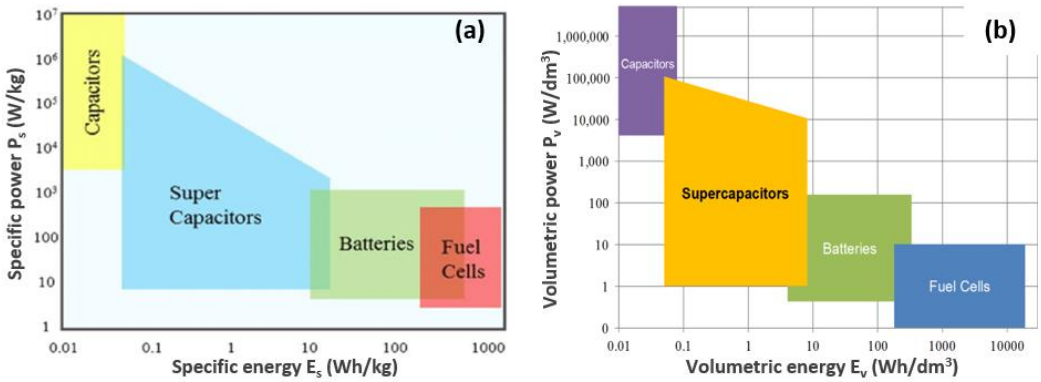

***Figure 4.1.1**. **(a)** Specific and **(b)** volumetric Ragone plots. Every energy storage device (ESD) is characterized by a maximum amount of storable energy (E) and a maximum delivery power (P) and they can be reported in these bi-dimensional plots. Usually, such values are normalized per the mass or the volume of the ESDs electrodes, considered to be the "active" component of the devices. Each type of ESD usually occupy a specific area of the plots, according to its features.*

Capacitors, instead, do not store electrochemical energy. They are usually composed by a dielectric material (e.g. plastic or glass) placed between a couple of parallel electrodes: under the application of a potential difference, a polarization of the dielectric leads to a small charge accumulation at the two interfaces with the electrodes. No electrons are transferred between the dielectric and the electrodes. The amount of the stored charge (Q) is directly proportional to the applied potential (ΔV)

according to the formula Q = C∆V, where C (expressed in Farad = Coulomb/Volt) is the capacitance of the systems. The capacitance itself is provided by the following *equation 4.1*:

$$C = \varepsilon \frac{S}{d} \qquad [Eq.\ 4.1]$$

Where S is the surface of the electrodes, d the distance between them, ε is the dielectric constant of the medium between the electrodes. The amount of energy stored is directly proportional to the capacitance value and to the square of the applied potential (*Equation 4.2*). The maximum power is instead inversely proportional to the equivalent series resistance (ESR) that is the series combination of all the resistive elements of a capacitor (*Equation 4.3*)

$$E = \frac{1}{2} C \Delta {V_{max}}^2 \qquad [Eq.\ 4.2]$$

$$P = \frac{{\Delta V_{max}}^2}{4ESR} \qquad [Eq.\ 4.3]$$

Unlike electrochemical batteries, a capacitor can be charged and discharged in a wide range of potential: they can be gradually charged by low-voltage energy sources up to a final value of several hundreds of Volt than can be delivered with a short impulse at high power. Because of this, and since the resistive contributions in a capacitors are extremely low (the low resistance of the electrodes is usually the only one) they can deliver energy at a dramatic higher power with respect to batteries. Also, because no electrochemical reactions are involved, they can sustain a number of charge-discharge cycles up to the order of 10^6. Nevertheless, the amount of energy coming from dielectric polarization is extremely lower than the one from electrochemical reactions and because of this, capacitors cannot be used to power a device for a long time without a connection with the electric line [282,283].

Supercapacitors [284–286] are more recent devices whose energetic behaviour is halfway between batteries and traditional capacitors, even if, actually, two different charge accumulation mechanisms can be involved. Electrolytic double-layer capacitors

(EDLCs) store electric energy into an electrostatic double layer, while pseudocapacitors are more similar to electrochemical batteries. These two different devices are united by their energetic performance and the usual high surface area of the electrodes.

EDLCs [287] have a similar structure to that of traditional capacitors, but the medium between the electrodes is composed by a liquid or semi-solid electrolyte: under the application of a potential difference, ions migrate towards the electrodes with an opposite charge and they form an electrolytic double-layer at the electrode-electrolyte interface. Carbon-derived porous electrodes are usually employed, characterized by a high surface area able to host a huge number of ions. Such a high active surface and the extremely small interface thickness (in the order of few Angstrom) leads to higher values of capacitance (see *Equation 4.1*) with respect to traditional capacitors and this is the reason because of which EDLCs can store a higher amount of energy. Thanks to the full reversibility of the ionic migration process, they can undergo several charge-discharge cycles. But unlike dielectric capacitors, the maximum work potential is limited by the electrochemical stability of the electrolyte (usually between 1 and 4 Volt) and the ionic migration in the electrolyte and in the electrode's pores leads to a higher equivalent series resistance. Because of this, EDLCs supercapacitors cannot deliver the same power of a traditional capacitor.

Pseudocapacitors [288,289], instead, store electrical energy faradaically by electron charge transfer between electrode and electrolyte. The employed electrodes are usually composed by metallic oxides or conductive polymer and they can exchange electrons with the ions of the electrolyte medium by mean of fast and reversible redox processes, electrosorption or intercalation. Since there is an effective electrons flow between the medium and the electrodes, their charge accumulation mechanism is more similar to that of batteries, but in this case the total number of charge-transfer processes is limited by the available surface of the electrodes. Because of this, pseudocapacitors can store a lower amount of energy with respect to electrochemical batteries.

Hybrid systems [290,291]have also been studied and developed: one electrode mainly store electric energy by mean of an electrolytic double-layer, while the other mainly through pseudocapacitive processes (e.g. lithium ion capacitors).

4.1.2 Electrolytic double-layer supercapacitors: materials and geometries

A lot of interest is recently focused on supercapacitors technology, in the perspective of using these devices as a replacement of electrochemical batteries or a support to them. In fact, the most diffused Li-ion batteries are based on a non-renewable active specie (lithium), they are composed by toxic substances and they have a relatively short lifetime. Moreover, they cannot be charged by low-voltage renewable energy sources like, for example, microbial fuel cells [292]. It would be then of great interest to find novel replacements or to reduce their number by the coupling with different energy storage devices. While traditional dielectric capacitors cannot store enough energy to act as an effective solution, supercapacitors may be designed and engineered to address this issue. In particular, **EDLCs** combine high energy densities with a high number of life cycles and, since they do not involve any electrochemical reaction, their design and fabrication can be easier and cheaper than pseudocapacitors. They can find many applications in the field of consumer electronics, as back-up or emergency power sources, in energy harvesting and in the transport field, as well as in the development of biomedical electronic devices.

Carbon-derived porous materials are the most employed for the fabrication of EDLCs **electrodes**. They combine lightness and high surface area, the most important feature to host a large number of ions and then accumulate a high amount of electrostatic energy. Activated carbon and carbon fibres, graphene, single-walled and multi-walled carbon nanotubes are among the most employed [293,294,303,304,295–302]. However, they are usually characterized by a lower electronic conductance with respect to metals and then they are often combined with thin metallic current collectors. Concerning the **electrolyte medium**, aqueous and organics are the most employed. Inorganic acids, bases and salts dissolved in water form electrolytes characterized by a high ionic conductivity, even if their electrochemical window is limited by the potential of water electrolysis (ca. 1.2 Volt) and they evaporate in ambient conditions [293]. Organic electrolytes are characterized by a higher electrochemical window of stability, but their ionic conductivity is usually lower and they are highly toxic. They usually are volatile substances and they also are not stable in ambient conditions [295]. Besides organic and aqueous, ionic liquids (ILs) can also be employed as electrolytic medium[294,305]. Their low vapour pressure makes them stable in ambient condition, they can be electrochemically stable up to about 4 Volt and their toxicity is much lower compared to organic solvents. Nevertheless, they are also characterized by a lower ionic conductivity.

Initially, supercapacitors were manufactured with a liquid electrolyte and then they needed to be confined by encapsulation. Many commercial supercapacitors are still like this. Unfortunately, this carries the risk of electrolyte's leaking, particularly dangerous in the case of non-aqueous media. Moreover, for applications in micro-, soft and deformable electronics, an **all-solid soft structure** is required. Because of this, in recent years most of EDLCs are developed with the use of various polymeric matrices blended with the liquid electrolytes, resulting in solid thin soft films of gel in which the (solvated) ions are still able to migrate. Such gel electrolytes can be obtained with different techniques using various combinations of polymers and electrolytes; for example, water containing gels are called hydrogels, while ionogels are obtained with ionic liquids. The three-dimensional polymeric matrix can be achieved with chemical bonds between different polymeric chains (chemical gels) but also by exploiting low-strength inter-chains interactions (physical gels) such as dipole-dipole or Van del Waals interactions. Sometimes the combination with a polymer can decrease the ionic conductivity of the electrolyte, but it's a drawback that's worth to pay in order to obtain a system that can be integrated in a soft deformable device. The same can be said regarding microelectronics applications, where the occupied volume has to be reduced to the minimum. To increase the affinity between the gel electrolyte and the porous conductive electrodes, they can be as well blended in the same polymeric matrix: in this way, the electrolyte gel can be combined with another version of itself filled with carbonaceous nanoparticles that forms an interconnected conductive composite electrode. Also in this case, the blending with a polymer usually decrease the electronic conductivity of the electrode materials, make even more necessary to integrate also external high-conductive thin metallic collectors.

For the fabrication of solid-state EDLCs supercapacitors, **two different geometries** are the most employed: the three-dimensional sandwich structure and the bi-dimensional coplanar one. Their schematic structures are reported in *Figure 4.1.2*. In the first structure, a thin film of gel electrolyte is **sandwiched** between a couple of parallel electrodes. This geometry allows to obtain three-dimensional freestanding thin supercapacitors and to exploit all of the exposed surface of the electrodes. The distance between them is related to the thickness of the electrolyte gel, that should also avoid the shortcut between the two faces. The overall geometry is quite easy to achieve even if the direct coupling between the electrolyte and the electrodes can reveal to be challenging [295,306,307].

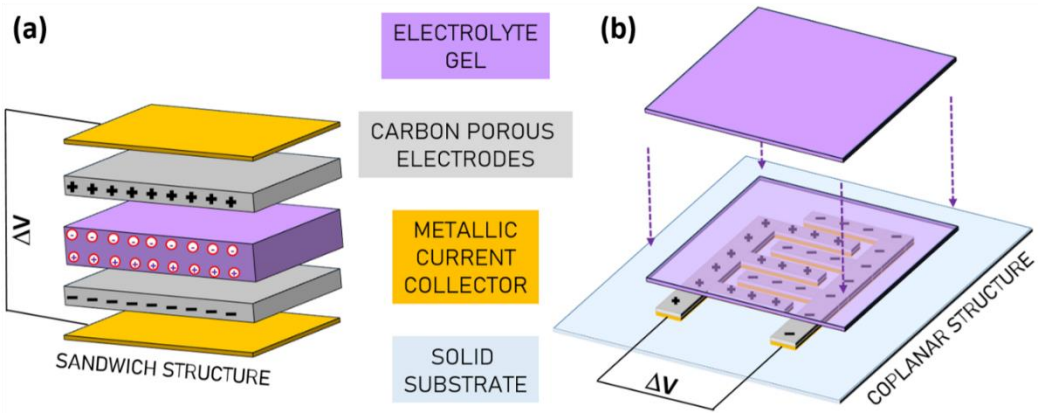

***Figure 4.1.2**. Illustration of the two most employed structures/geometries for the fabrication of gel-based solid supercapacitors. Both of them are characterized by two electrodes (usually based on porous carbon-derivatives) in contact with a gel electrolyte. Metallic current collectors are needed when the carbon-based electrodes possess a low electronic conductivity. **(a)** Sandwich structure, with the electrolyte gel sandwiched or clamped between a couple of parallel electrodes; usually employed for the fabrication of three-dimensional self-standing supercapacitors. **(b)** Coplanar structure, with the electrodes fabricated on the surface of a common substrate and separated by a small gap: different bi-dimensional geometries can be realized (e.g. interdigitated); the electrolyte is subsequently deposited on top of the electrodes as an ionic conductive bridge between them.*

In the **coplanar** geometry the supercapacitor is fabricated on the surface of a target substrate, not as a freestanding device. This can represent a limit, but also an advantage in the perspective of an integration of different electronic components on a same platform. Both the electrodes are then manufactured next to each other on the target substrate, separated by a small gap, and the electrolyte gel is subsequently deposited as a connecting bridge. In this case, the electrodes geometry can have a huge impact on the energetic performance, since the amount of hosted ions is not usually due to the overall surface of the electrodes, but it directly depends only on that surface portion in front of and close to the opposite electrode. Then, for supercapacitors in a coplanar geometry, the electrodes need to be patterned so as to maximize their portion close to each other. Interdigitating is usually the most employed choice, as it is shown in *Figure 4.1.2(b)*. Even if it can easier the electrode fabrication on a support substrate rather than on the gel electrolyte, the manufacturing technique of choice should be compatible with a high precision patterning (on a micrometric scale) [300,301,303].

4.1.3 Biodegradable soft micro-supercapacitors: state of the art and challenges

As mentioned throughout *Section 1*, the development of soft autonomous robotic systems and electronics obtained with natural-derived substances is fundamental for the rise of a next-gen smart biodegradable devices for biomedical, agricultural and environmental monitoring applications. They are meant to be produced in high number thanks to their ability do benignly degrade in the environment. Such devices should also be extremely light and able to interact with very small portion of living organisms, thus the miniaturization of the electronics and functional elements is an important requirement; considering also the need for integration of many components on a same small platform, the occupied volume becomes more important than the weight. The use of biodegradable and non-toxic materials can allow them to safely interact with living organisms and to benignly degrade in the environment at the end of their life time.

In this complex and multifunction systems, energy storage is one of the most crucial functionalities they need to be provided with. Soft gel-based **micro-supercapacitors** can constitute an optimal solution to address this issue, since they can be designed and manufactured onto deformable electronic boards. Considering the need for integration of many elements on a same small platform, the occupied volume becomes more important than the weight. Then, with a suitable choice of the fabrication techniques, micro-supercapacitors can be manufactured and patterned on platforms of different materials. An EDLC supercapacitor ideal for this purpose is not expected to be characterized only by good energetic features, but is also should possess all of the following features:

- **All-solid soft structure**, in order to prevents liquid leakage and the use of bulky encapsulations.
- **Miniaturization**, in order to occupy the lowest possible volume. In a micro-supercapacitor, both the electrodes and the electrolyte gel should be extremely thin (micrometric range).
- Suitability for the manufacturing and the **integration onto a deformable platform** in common with other electronic elements. **Flexibility** and/or **stretchability** are mandatory features for the integration in an all soft body or device.

- **Suitability for stacking**. In fact, the connection in series of many thin supercapacitors can allow to operate at higher potential and to increase both the actual power and stored energy. The EDLC geometry and the manufacturing process should be chosen in order to allow the stacking of many capacitive elements.

- **Stability in ambient conditions**. Considering that such devices may be meant to operate in direct contact with the environment, but also picturing a possible rupture of an eventual encapsulation, these supercapacitors should be able to operate both in controlled conditions as well as in open air. That means, for instance, that the liquid inside the gel should not evaporate in plain air.

- Obtained with the use of **renewable and natural-derived raw materials**. This would allow their production in high amounts without being affected by resource pressure.

- **Biodegradability and safeness of the employed substances**. The micro-supercapacitors should be suitable for a massive deployment without the issue of collecting them since they can degrade safely in the environment.

- An **organic solvent - free manufacturing process** (considering each fabrication step). This requirement constitutes a high advantage in terms of cost (no need for complex and expensive disposal) and environmental sustainability.

Up to date, many researchers realized and characterized prototypes of micro supercapacitors. By the way, none of them was actually able to satisfy all of these requirements. Hu et al. [308] as well as Kyerematen et al. [309] wrote good and wide reviews about the fabrication and the evaluation of micro-supercapacitors. Liu et al. [310] reported a graphene-based planar micro-supercapacitor direct printed and spray-coated on a polyethylene terephthalate (PET) substrate, but they also employed a PEDOT:PSS organic polymer, the organic solvent iso-propanol and the not natural-derived poly(vinyl alcohol) (PVA) aqueous gel electrolyte not stable in ambient condition; moreover, PET is a non-biodegradable plastic substrate, not suited for soft biodegradable electronics. A similar graphene-based coplanar device (total thickness of 25 μm) fabricated on polyimide (PI) was reported by Peng et al. [311], while Pu et al. [303] obtained coplanar graphene oxide (GO)-based supercapacitors on textiles. In both cases, the electrolyte gel is still not natural-derived and not stable in air. Huang et al. [312] obtained 10-20 μm-thick carbide-derived electrodes in a coplanar geometry, but they employed as liquid electrolyte an imidazolium-based ionic liquid dissolved in highly toxic and volatile acetonitrile. Moreover, such works presented bi-dimensional micro-supercapacitors in a coplanar geometry and this structure is not convenient for the

connection in series of many capacitors, since it would require the use of a high surface. Instead, even if three-dimensional sandwich supercapacitors can be characterized by a more challenging miniaturization, they are more suited for multiple connection in series, since many of them can be stacked one over the other without changing the occupied area. In this sense, Wang et al. [297] assembled a very nice EDLC supercapacitor in a sandwich geometry (total thickness of about 9 μm), using carbon nanotubes (CNTs) and polyaniline (PANI) composite electrodes obtained by spray-printing and spin coating; but the electrolyte gel is based on water and then not stable in ambient conditions, while no integration of a flexible substrate is shown; non-green solvents, such as N-methylpyrrolidone, are also employed in the process steps, and the use of organic conductive polymers should be avoided.

There are other works that focused on the use of natural-derived and biodegradable polymers as a thin substrate but even for the realization of the electrodes or the gel electrolytes. Carbohydrates are the most employed for this purpose, cellulose on top: a good review is given by Zhang et al. [313]. Li et. al [314] realized carbon thin electrodes derived from lignin, while Mantravadi et al. [315] studied the use of methylcellulose as the polymeric matrix of ionogel electrolytes; by the way, in none of these two works a full supercapacitor was assembled. Instead, Chen et al. [316] and Nyu et al. [317] reported the development of sandwich supercapacitors using wood and cellulose as raw materials to obtain the carbon for the electrodes, but in the first case the device thickness is 1 mm (not considerable as a micro-supercapacitor), while in the second work cellulose nanofibers (CNFs) are not the only component of the electrodes, but they are combined with the conductive polymer poly(pyrrole) (PPy) and many reagents are used in the process. Moreover, both the realized supercapacitors possess a not natural-derived aqueous PVA electrolyte, not stable in ambient conditions and containing LiCl, a salt containing a strongly non-renewable and in exhaustion resource. Instead, Moon et al. [318] realized a biodegradable gel using agarose as the polymeric matrix; but the aqueous electrolyte is highly evaporable and the resulting supercapacitor is not a micro-device (thickness of 1 mm). Similar results were obtained by Oraon et al. [319] with the use of silicates. Lee et al. [320], instead, were able to develop a fully biodegradable micro-supercapacitor: in a sandwich geometry, the authors fabricated 500 nm-thick transition metal electrodes (Fe, W, Mo and Cr) separated by an agarose-based natural-derived hydrogel. The device was realized onto a poly(lactic-co-glycolic acid) (PLGA) biodegradable substrate as well and the total thickness of about 160 μm makes it a truly biodegradable micro-supercapacitor, with nice energetic performance. I consider their results very impressive. By the way, considering the abovementioned list of important requirements, there are still some points not perfectly addressed. In particular, since the developed device is not an EDLC but a pseudocapacitor, many complex steps are required in the fabrication process. The electrolyte is biodegradable, but still based on

an aqueous solution, strongly limiting stability in ambient condition and its electrochemical window of stability. In fact, the device is then packaged with polyethylene film to prevent water evaporation, strongly affecting the overall biodegradability of the device. Finally, no studies were conducted on a tight integration onto deformable soft platforms.

In conclusion, many interesting materials and devices are being studied and designed for a novel class of advanced EDLCs supercapacitors, but up to now, none of them is able to simultaneously address all of the requirements regarding miniaturization, integration on flexible platforms, environmental sustainability and stability in ambient conditions.

4.1.4 Aim of the research

The aim of the current project is the design and the development of the **first soft ultrathin** (eventually, the thinnest), completely solid and **biodegradable EDLCs micro-supercapacitors** able to **stably operate both in ambient and controlled environments**, **suitable for stacking** in series, **fabricated onto a flexible biodegradable platform** and obtained with a **few-steps organic solvent-free process** by the use of **natural-derived and renewable raw materials**.

Here's the strategy adopted to reach the prefixed goal:

- A **layer-by-layer spray process** is developed for the fabrication of the micro-supercapacitor: water is the only solvent used for the spray-casting of the electrolyte gel, while the electrode fabrication is completely solvent-free.

- **Flexible thin sheets of biodegradable cellulose acetate** are employed as the substrate.

- An innovative **fully biodegradable ionogel** electrolyte is obtained by blending together **cellulose-derivatives** and natural-derived **biodegradable ionic liquids**: **choline aspirin (CholAsp)** (also known as choline acetylsalicylate) and **choline lactate (CholLact)**. They were synthesized by Kaija Pohako-Esko from University of Tartu following a water-based eco-friendly process [321]. Their biodegradability was assessed without a doubt [321,322]. Up to know, this class of ionic liquids was mainly employed as extraction solvents [323] and for few poly(ionic liquid) gels meant as biocompatible coating (but not biodegradable) [324]. While the most employed PVA hydrogels cannot stably operate in air because of water evaporation, the eco-friendly ionogels here presented have the great advantage that **the ionic liquids do not evaporate in ambient conditions and then they won't lose their efficiency**.

- **Thin cluster-assembled gold electrodes** are obtained by mean of solvent-free supersonic cluster beam deposition (**SCBD**) technique (see *Section 1.4*). They can combine high interfacial area with high electronic conductivity.

- A **sandwich geometry** is adopted. The targeted thickness of the final device should be **lower than 5 μm**. Despite the traditional three-dimensionality of the sandwich geometries, such ultrathin structures can be considered almost bi-dimensional. The fabrication technique is **suitable for the stacking in series** of many sandwiches with a resulting thickness not higher than tens of micrometres.

Actually, the current project is at a preliminary stage. The abovementioned objective is supposed to be a medium-term goal. Up two now, two different tasks have been simultaneously carried out and described in the next *Section 4.2*. First, self-standing supercapacitors have been manufactured with different ionogel formulations, varying the type of ionic liquids and cellulose-derivatives (*Section 4.2.1*). Electrochemical tests have been conducted on them to study their double-layer capacitance and ionic conductivity as well as the amount of energy stored and the maximum delivered power (*Section 4.2.2*, *Section 4.2.3* and *Section 4.2.4*). Then, a spray casting apparatus and procedure have been designed and set up for the realization of ultrathin micro-supercapacitors casted on cellulose acetate films (*Section 4.2.5*).

4.2 BIODEGRADABLE MICRO-SCS WITH NATURAL IONIC LIQUIDS

4.2.1 Manufacturing of soft biodegradable self-standing supercapacitors

Initially, self-standing thin supercapacitors were manufactured in a sandwich geometry to study their electrochemical properties and behaviour. The electrolyte ionogels were obtained by blending together cellulose derivatives and natural-derived biodegradable ionic liquids: different formulations were studied in order to evaluate which one was the most promising. In *Figure 4.2.1* the chemical structures of the employed substances are reported: 2-hydroxyethylcellulose (HEC), Na-carboxymethylcellulose (Na-CMC), cellulose nanocrystals (CNCs) and the ionic liquids choline aspirin (CholAsp) (also known as choline acetylsalicylate) and choline lactate (CholLact).

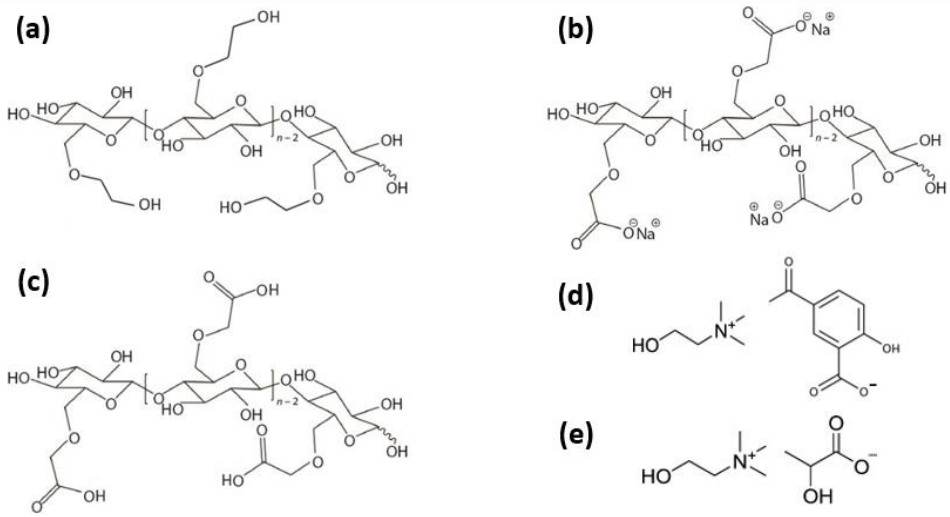

***Figure 4.2.1**. Chemical structures of the employed natural polymers and ionic liquids: **(a)** 2-hydroxyethylcellulose (HEC), **(b)** Na-carboxymethylcellulose (Na-CMC), **(c)** cellulose nanocrystals (CNCs), **(d)** choline aspirin (CholAsp) and **(e)** choline lactate (CholLact).*

The adopted synthetic process was a simple solvent casting technique carried out in water (the only solvent employed in this work on supercapacitors). The ionic liquids themselves were obtained by mean of a water-based reaction [321] by Kaija Pohako-Esko from the University of Tartu. The cellulose derivatives and the ionic liquids of choice were both dissolved in water and the resulting solutions were poured inside a silicon frame on a glass slide. HEC was blended with both CholAsp and CholLact (with mass ratio of 4:6) to compare the effect of the different ionic liquids: after drying the poured solution in oven at 80°, it was possible to obtain free-standing soft thin films of ionogel (60 μm-thick) (*Figure 4.2.2(a)*), where the polymeric chains are kept together by physical interactions. Solution containing Na-CMC and CNCs were also prepared with choline aspirin (the more abundant in the available stocks) with a mass ratio of (5:5), poured inside the frame and let dry at room temperature, obtaining 60 μm-thick ionogels. CNCs were also employed to prepare solutions with ILs with different mass ratios of (3:7 and 2:8), in order to evaluate how a higher amount of ionic liquid would affect the ionogels and the final devices features; these ionogels had a thickness of about 200 μm (*Figure 4.2.2(b)*). A more practical description of the fabrication process is reported in *Section 6.1.1(e)*.

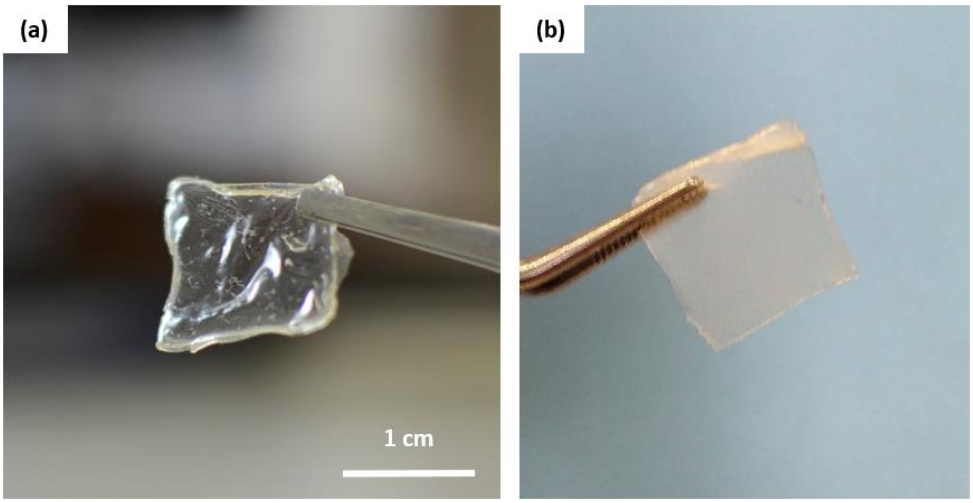

***Figure 4.2.2**. **(a)** HEC-Lact (4:6) and **(b)** CNC-Asp (3:7) self-standing natural ionogels.*

After the synthesis, all the samples were kept in vacuum and then their humidity absorption was checked in ambient conditions (the experimental detail are reported in *Section 6.1.2(b)*). All of them showed to significantly absorb humidity, with a mass increase from the 21% to the 49% of their original dry mass. The detailed samples formulation and humidity absorption data are reported in the table in *Figure 4.2.5*. A

specific explanation should be provided regarding the moisture absorbance of the samples obtained by blending CNCs with CholAsp in a 2:8 mass ratio: the table abovementioned table reports a mass increase equal to + 40%, but this was an underestimation. In fact, a leakage of the ionic liquid was observed in ambient conditions, simultaneously with the humidity absorption: because of this, it was not possible precisely quantifying the entity of these two phenomena.

A couple of cluster-assembled gold electrodes was then fabricated on the two opposite faces of every sample. Supersonic cluster beam deposition (SCBD) technique was employed since Au clusters are generated by an Argon plasma from a solid precursor and then the inert gas itself delivers the clusters to the surface of a target sample. Thank to this, the technique works at room temperature and it does not involve the use of any kind of solvent. Moreover, the Au clusters can partially implant into the surface of soft materials, originating, in this case, a metal-ionogel interface characterized by a high-surface area, which is mandatory for the realization of a high capacitance EDLC supercapacitor. A simple schematization of the ionogel-Au clusters composite material is reported in *Figure 4.2.3*. With this technique it is also possible to achieve a high control on the amount of deposited metal, both in terms of mass and equivalent thickness. All the natural-derived free-standing ionogels were provided with a couple of 8 x 8 mm^2 electrodes with an equivalent thickness (t_{eq}) ranging from 150 to 180 nm (in mass, from 120 to 144 $\mu g/cm^2$). More detailed information regarding SCBD operational principles and experimental procedure can be found, respectively, in *Section 1.4* and in *Section 6.2.1*. *Figure 4.2.4* shows some pictures of the metallized samples taken with a reflection optical microscope.

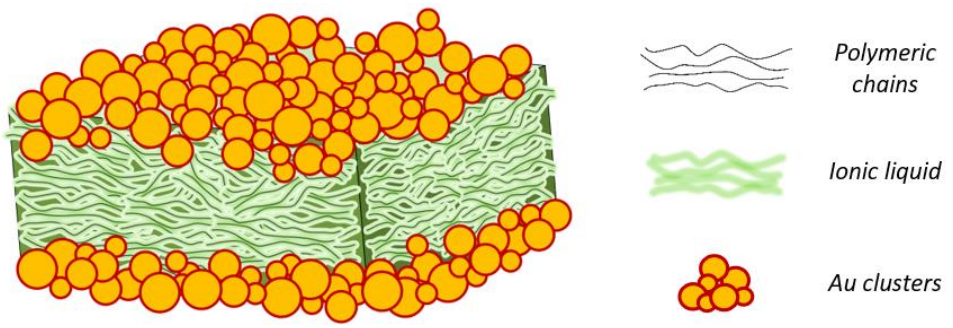

***Figure 4.2.3**. Illustration showing the structure of nanostructured composite material obtained by using SCBD technique to fabricate cluster-assembled Au electrodes on both sides of a soft ionogel. The partial interpenetration into the ionogel's surface gives origin to nanostructured gel-metal interfaces.*

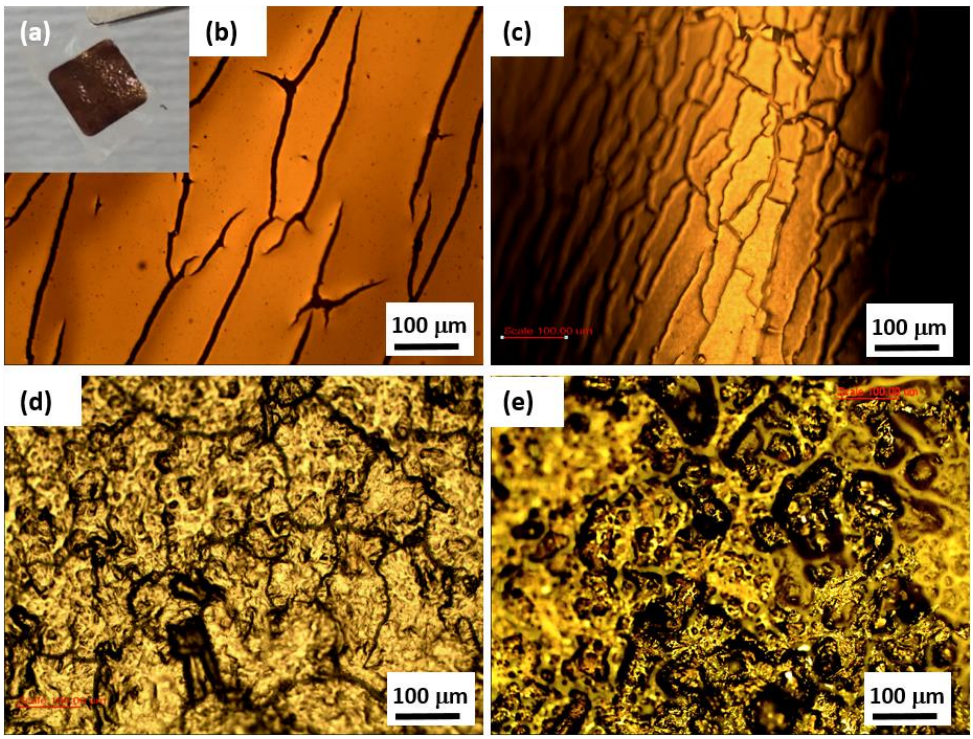

***Figure 4.2.4**. **(a)** Photograph of A HEC-Lact ionogel provided with a 0.63 cm^2 cluster-assembled Au electrode. **(b-e)** Pictures taken with an optical reflectance microscope, showing the surface of the SCBD-deposited electrodes on the ionogels HEC-Lact (4:6), Na-CMC-Asp (5:5) CNCs-Asp (5:5) and CNCs-Asp (3:7) respectively.*

As can be seen from *Figure 4.2.4(a-c)*, the samples obtained with HEC and Na-CMC were characterized by cracks on the electrodes surface, probably due to the high elasticity of these ionogels that caused a significant mechanical mismatch with the electrodes (even if they are cluster-assembled). Considering this, even the smallest mechanical stress due to manipulation of the samples or their moisture absorbance in ambient condition can have caused the electrodes cracking. The consequence of the cracks presence was a high superficial sheet resistance (R_s) up to values of 10^5 Ω. Instead, the samples obtained with the CNCs were more rough, highly flexible but less elastic and no cracks were observed their electrodes surface, with low sheet resistance values in the order of 10^2 Ω. Such a good electrodes quality is a great advantage of the CNC-based ionogels with respect to those obtained with HEC and Na-CMC.. The table reported in *Figure 4.2.5* summarizes the detailed information regarding the synthesis and the metallization of all samples, prior the electrochemical characterization that is reported in the next section.

	Polymer	IL	Mass ratio	$\Delta m_{HA}/m$ (%)	IL's leakage	Au t_{eq} (nm)	R_s (Ω)	Electrodes cracks
HEC-Asp(4:6)	HEC	CholAsp	4:6	+ 42%	No	180	10^5	Yes
HEC-Lact (4:6)	HEC	CholLact	4:6	+ 42%	No	180	10^5	Yes
CMC-Asp (5:5)	Na-CMC	CholAsp	5:5	+ 21%	No	180	10^5	Yes
CNCs-Asp (5:5)	CNCs	CholAsp	5:5	+ 21%	No	180	130	No
CNCs-Asp (3:7)	CNCs	CholAsp	3:7	+ 49%	No	150	250	No
CNCs-Asp (2:8)	CNCs	CholAsp	2:8	+ 40%	Yes	150	415	No

***Figure 4.2.5**. Table reporting the details about the ionogels formulation, thickness, humidity absorption and ILs leakage, as well as the cluster-assembled Au electrodes equivalent thickness (t_{eq}), sheet resistance (R_s) and presence of superficial cracks.*

4.2.2 Electrochemistry: EIS

Three different techniques were used to study the electrochemical and energetic behaviour of the presented biodegradable EDLC supercapacitors: electrochemical impedance spectroscopy (EIS), cyclic voltammetry (CV) and galvanostatic charge-discharge (GCD). The experimental procedures and detailed calculation are reported in *Section 6.2.2*.

EIS was carried out to mainly study the double-layer capacitance (C_{dl}) of the devices and their equivalent series resistance (ESR), that is the combination of all the resistive contributions: the contacts, the electrolyte-metal interface and the resistance associated to the ionic migration inside the ionogel. Also, by looking at how the samples responded at different frequencies (from 10^{-2} to 10^4 Hz) of the applied potential (± 5 mV) it was possible to understand whether these novel natural ionogel-Au clusters composite materials were effectively able to behave like EDLC supercapacitors or not. Th results are reported in the current section. CV technique (*Section 4.2.3*) was employed for a dual purpose: to measure C_{dl} with another technique besides EIS and to detect the

electrochemical windows of stability of these natural-derived ionogels, which is directly related to the maximum potential difference that can be applied without trigger an electrochemical degradation. The samples also underwent galvanostatic cyclic charge and discharge processes at constant current (GCD technique, *Section 4.2.4*) in order to study their C_{dl} and ESR in a real operating conditions, as well as their coulombic efficiency CE (that is the ratio between the delivered energy and the amount necessary to charge it). Also, 10^4 charge-discharge cycles were applied to some samples to study their stability in time. The values obtained with GCD technique were then employed to calculate the total energy stored (E) and the maximum delivery power (P) of the devices, with respect to the mass (specific energy E_S and power P_S) and the volume (volumetric energy E_V and power P_V) of the electrodes material, as it is usually done to evaluate energetic devices.

One of the purposes of this work is to study the electrochemical behaviour of the developed devices both in ambient conditions, when water molecules are present inside the ionogels due to environmental humidity, and in controlled conditions with no presence of humidity. In this preliminary stage of the research, electrochemical tests were carried out inside a glove box in inert N_2 atmosphere, where the ionogel-Au composites should not contain any water molecules. Very soon, a similar electrochemical characterization will be carried out also in ambient conditions.

Initially, all the obtained samples where characterized by EIS technique. *Figure 4.2.6* reports the obtained results for the two samples with 2-hydroxyethylcellulose: HEC-Asp (4:6) and HEC-Lact (4:6). *Figure 4.2.6(a)* shows the Nyquist plot, where the opposite of the imaginary component of the impedance (Z_i) is plotted against the corresponding real component (Z_r) at different frequencies. The almost vertical shape of the curves is a signal of a typical capacitive behaviour for both the samples. By looking at the magnification reported in *Figure 4.2.6(b)*, the intercept with the Z_r axis can be detected and its value corresponds to the ESR of the samples, corresponding to 4.67 kΩ x cm^2 for HEC-Asp (4:6) and 3.12 kΩ x cm^2 for HEC-Lact (4:6). *Figure 4.2.6(c-d)* shows the Bode plots, where the absolute value of the impedance |Z|, the capacitance C and the phase delay ϕ are reported as a function of the frequency of the applied potential. It can be seen how at high frequencies, ϕ is almost equal to 0°, meaning that the current impedance is mainly due to a resistive elements and then equal to the ESR of the samples: their values are the same to those extracted from the Nyquist plot. At lower applied frequencies, instead, ϕ approaches a value of -80°, a clear sign of a real double-layer capacitance C_{dl}, equal to 74.5 μF/cm^2 for HEC-Asp (4:6) and 130 μF/cm^2 for HEC-Lact (4:6).

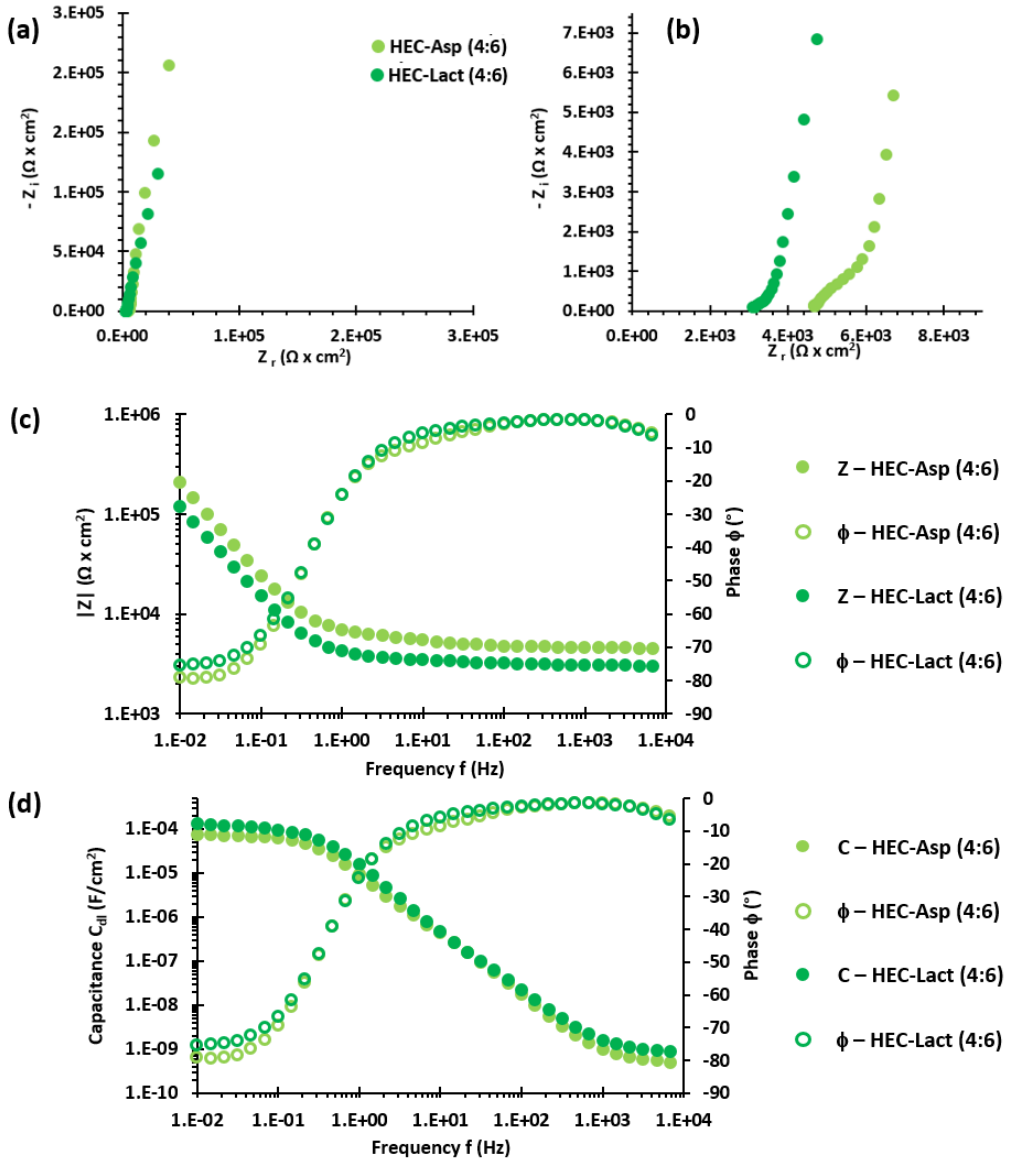

Figure 4.2.6*. Results of the EIS analysis on the samples HEC-Asp (4:6) and HEC-Lact (4:6).* ***(a)*** *The Nyquist plot,* ***(b)*** *its high-frequency magnification and* ***(c-d)*** *the Bode plots are shown.*

With this technique it was then possible to obtain a first important statement: the novel biodegradable composite materials based on cellulose and choline carboxylates, couple with cluster-assembled Au electrodes, can effectively act as supercapacitors, thanks to an ionic migration inside the polymeric matrix and the formation of an electrolytic double-layer at the metal-ionogel interface. Even if the ionic conductivity is not exceptionally high and the values of C_{dl} are lower than the typical ones obtained with carbon-derived porous electrodes, the possibility to manufacture EDLC supercapacitors with the only use of natural-derived and biodegradable raw materials is of considerable novelty.

The EIS analysis also showed that the samples with the choline lactate possess both a higher ionic conductivity and double-layer capacitance, highlighting its higher suitability with respect to choline aspirin. Nevertheless, as mentioned previously, most of the other samples (up to now) were obtained by using choline aspirin since it was the more abundant in the available stocks.

The same EIS characterization was carried out on the samples with a different polymeric matrix: Na-CMC-Asp (5:5) and CNCs-Asp (5:5). The results are shown in *Figure 4.2.7*. As can be seen, both of them possess a higher ESR with respect to the HEC-based ionogels. Na-CMC-Asp (5:5) showed a particularly high ESR = 8.87 MΩ x cm^2 (this value can be extracted from the Bode plot in *Figure 4.2.7(c)*). Its ionic migration is particularly slow and at low frequencies ϕ is close to -80°, meaning that she small passing current is due to the dielectric polarization of the material; then, at the lower frequencies, ϕ approaches a value of 0°. To appreciate and correctly calculate its double-layer capacitance, even lower frequencies need to be applied. Anyway, such a high ESR makes this formulation definitely not suited to work as a supercapacitor. CNCs-Asp (5:5), instead, appeared more promising: even if it has a higher ESR = 32.6 kΩ x cm^2 and a lower C_{dl} = 5.3 μF/cm^2 with respect to the HEC-based ionogels, it definitely behaved like an electrolytic double-layer capacitor.

Considering that the electrodes fabricated on the surface of the CNC-based ionogels are characterized by the best quality, novel ionogels were synthesized with a higher amount of choline aspirin ionic liquid (mass ratios of 3:7 and 2:8): this was expected to improve the electrochemical performance. EIS characterization was then carried out on the samples CNC-Asp (3:7) and CNC-Asp (2:8): the results are shown in *Figure 4.2.8*, together with CNCs-Asp (5:5) for comparison. As can be seen, the new samples with a higher amount of ionic liquid displayed a good EDLC behaviour, with values of ESR and Cdl similar to those obtained with the 2-hydroxyethylcellulose (HEC)-

based ionogels. More precisely, ESR = 6.68 kΩ x cm^2 and C_{dl} = 66.8 μF/cm^2 for CNC-Asp (3:7) and ESR = 2.27 kΩ x cm^2 and C_{dl} = 75.2 μF/cm^2 for CNC-Asp (2:8).

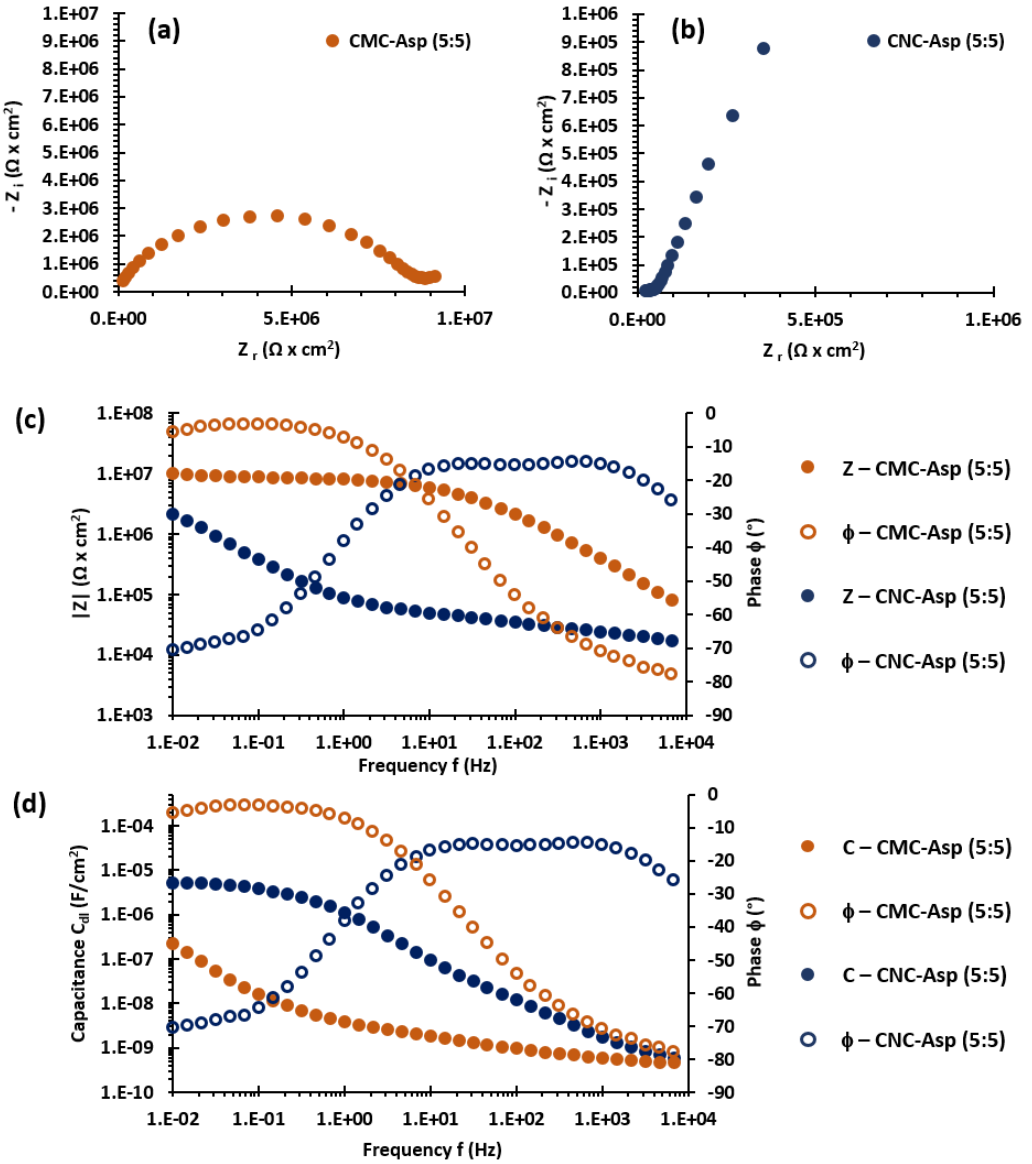

Figure 4.2.7. *Results of the EIS analysis on the samples Na-CMC-Asp (5:5) and CNC-Asp (5:5).* ***(a-b)*** *Nyquist plots;* ***(c-d)*** *Bode plots.*

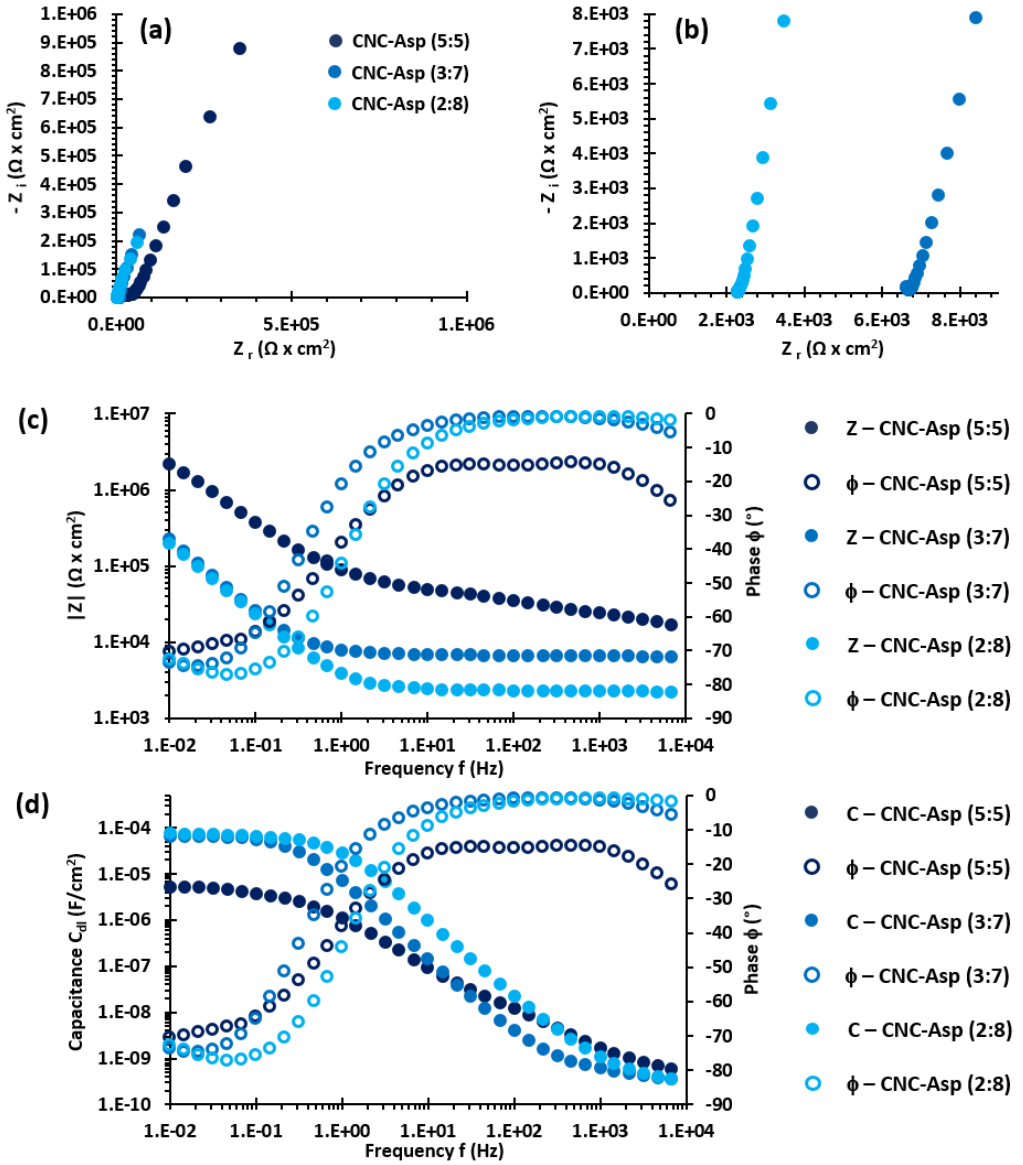

Figure 4.2.8. *Results of the EIS analysis on the samples CNC-Asp (5:5), CNC-Asp (3:7) and CNC-Asp (2:8).* ***(a-b)*** *Nyquist plots;* ***(c-d)*** *Bode plots.*

An overview of the results obtained by EIS analysis is provided in the graph reported in *Figure 4.2.9*, where every different sample was associated to a point in a bi-dimensional space whose orthogonal axis are the ESR and the double-layer capacitance C_{dl} (in the logarithmic scale). The same values are also reported in the table in *Figure 4.2.10*

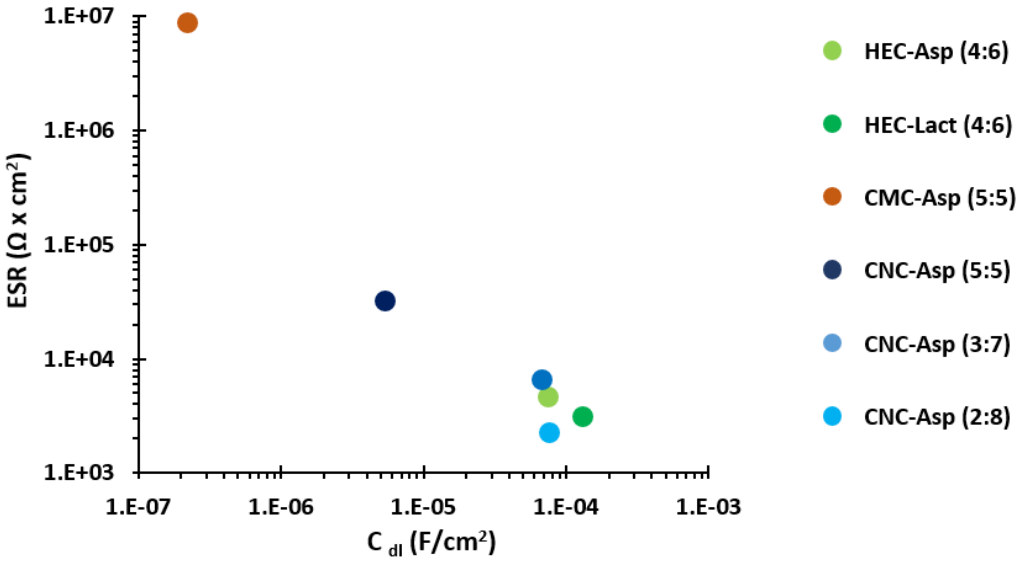

***Figure 4.2.9**. The ESR value of every tested sample is plotted against the corresponding value of double-layer capacitance C_{dl}. Both the axes are in the logarithmic scale.*

	ESR (Ω x cm²)	C_{dl} (F/cm²)		ESR (Ω x cm²)	C_{dl} (F/cm²)
HEC-Asp (4:6)	4.67 x 10^{3}	7.45 x 10^{-5}	CNC-Asp (5:5)	3.26 x 10^{4}	5.30 x 10^{-6}
HEC-Lact (4:6)	3.12 x 10^{3}	1.30 x 10^{-4}	CNC-Asp (3:7)	6.68 x 10^{3}	6.68 x 10^{-5}
CMC-Asp (5:5)	8.88 x 10^{6}	3.43 x 10^{-8}	CNC-Asp (2:8)	2.27 x 10^{3}	7.52 x 10^{-5}

***Figure 4.2.10**. Table reporting the ESR and Cdl values for every sample characterized by EIS technique.*

The overall results can be summarized as follows:

- The combination of cellulose derivatives, biodegradable ionic liquids and cluster-assembled Au electrodes demonstrated the possibility to manufactured EDLC self-standing solid supercapacitors in a sandwich geometry, solely employing natural-derived substances and water as the only solvent.

- Na-carboxymethylcellulose (Na-CMC) employed as polymeric matrix did not provide good results: the ionic conductivity of the embedded ionic liquid is too low to efficiently work as an EDLC supercapacitor.

- 2-hydroxymethylcellulose (HEC) and cellulose nanocrystals (CNCs) have proved to be good polymeric matrices to be blended with the choline-based ionic liquids and to properly act as EDLC supercapacitors.

- Choline lactate provided a lower equivalent series resistance ESR and a higher double-layer capacitance C_{dl} with respect to choline aspirin.

- Higher amounts of ionic liquids inside the polymeric matrix led to lower ESR and higher C_{dl} values.

- The cluster-assembled Au electrodes SCBD-deposited on the CNC-based ionogel were characterized by a good quality, no cracks and low sheet resistance. These features make the cellulose nanocrystals a preferential polymeric matrix for the continuation of the project.

The following electrochemical characterizations were carried out on the best obtained samples (according to EIS results): HEC-Asp (4:6), HEC-Lact (4:6), CNC-Asp (3:7) and CNC-Asp (2:8).

4.2.3 Electrochemistry: CV

Cyclic voltammetry (CV) was carried out on the samples HEC-Asp (4:6), HEC-Lact (4:6), CNC-Asp (3:7) and CNC-Asp (2:8). Initially, they were tested in a capacitive potential range between – 50 mV and + 50 mV, in order to measure the double-layer capacitance with another technique besides EIS. Different scans were performed by varying the scan rate from 2 to 32 mV/s. *Figure 4.2.11* and *Figure 4.2.12* report the obtained graphs, where it can be seen the typical box-like shape of real capacitors for all the samples.

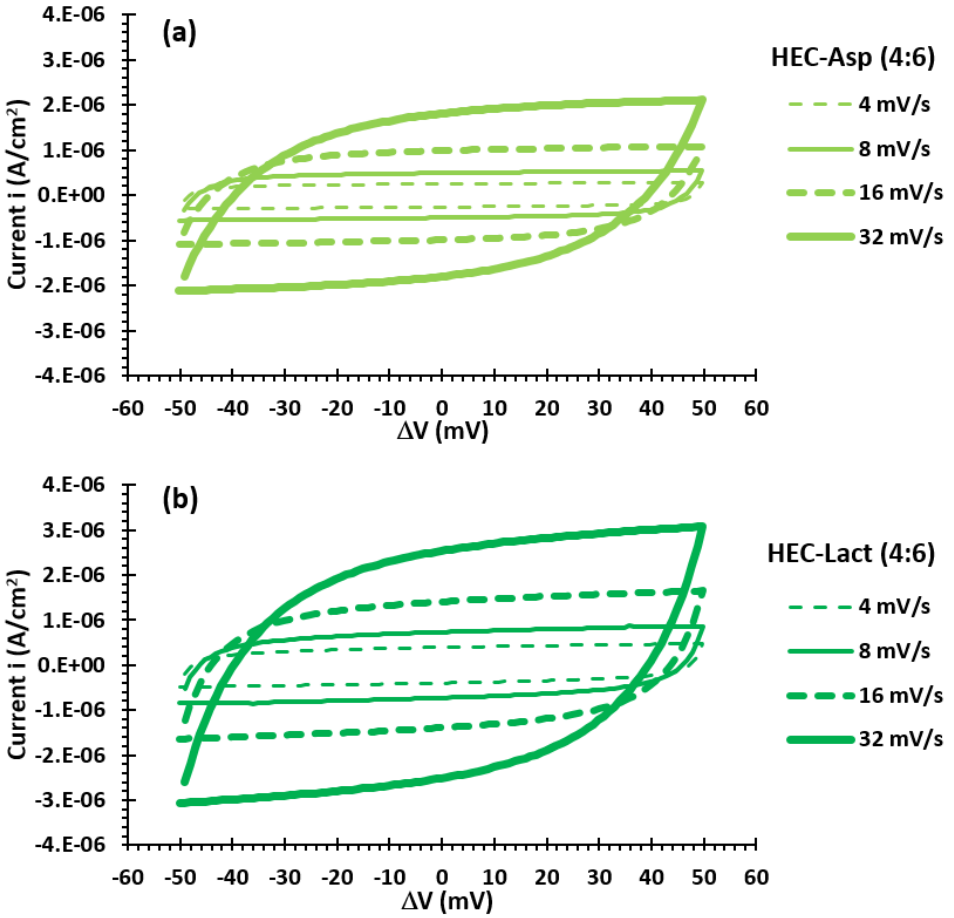

***Figure 4.2.11**. Voltammograms obtained from **(a)** HEC-Asp (4:6) and **(b)** HEC-Lact (4:6). ΔV was varied between -50 mV and + 50 mV with scan rates from 4 to 32 mV/s.*

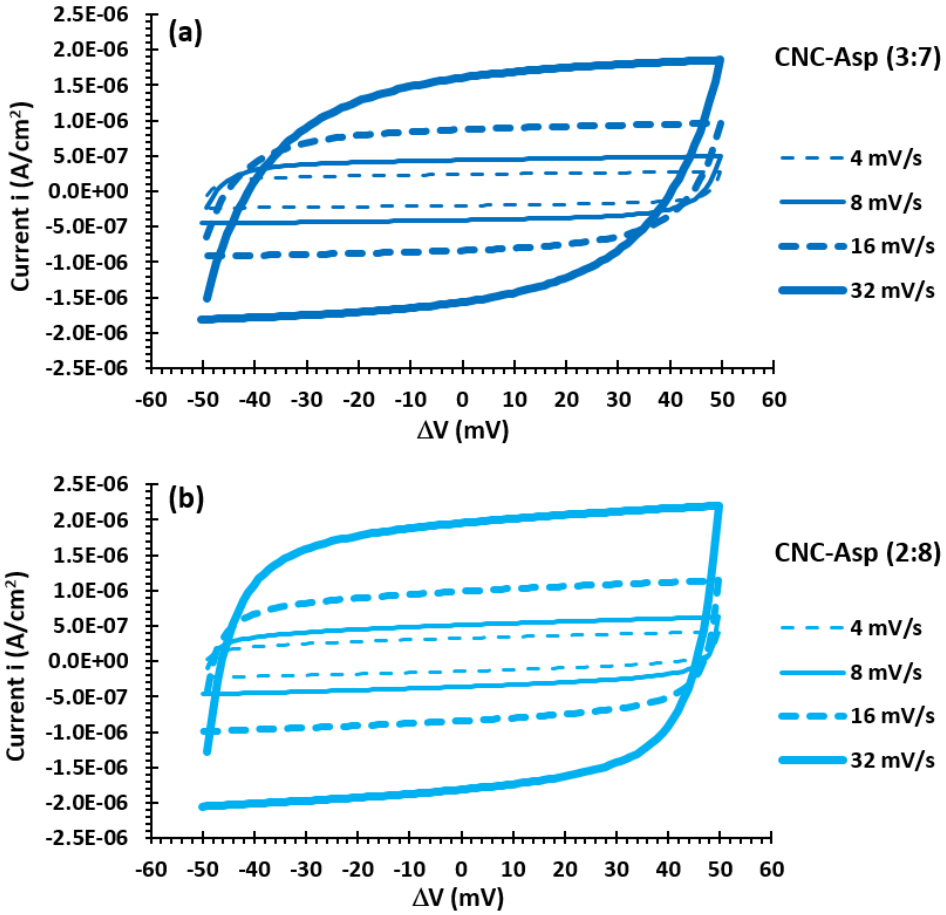

***Figure 4.2.12**. Voltammograms obtained from **(a)** CNC-Asp (3:7) and **(b)** CNC-Asp (2:8). ΔV was varied between -50 mV and + 50 mV with scan rates from 4 to 32 mV/s.*

As typical in capacitive regimes, the measured current should be proportional to the scan rate. To check this feature, an average current value was calculated between ± 5 mV for both positive and negative curves and they were plotted against the scan rate in the graphs shown in *Figure 4.2.13*. As can be seen, the plotted points can be well interpolated by a linear fit, showing a good correlation between the applied scan rate and the capacitive current.

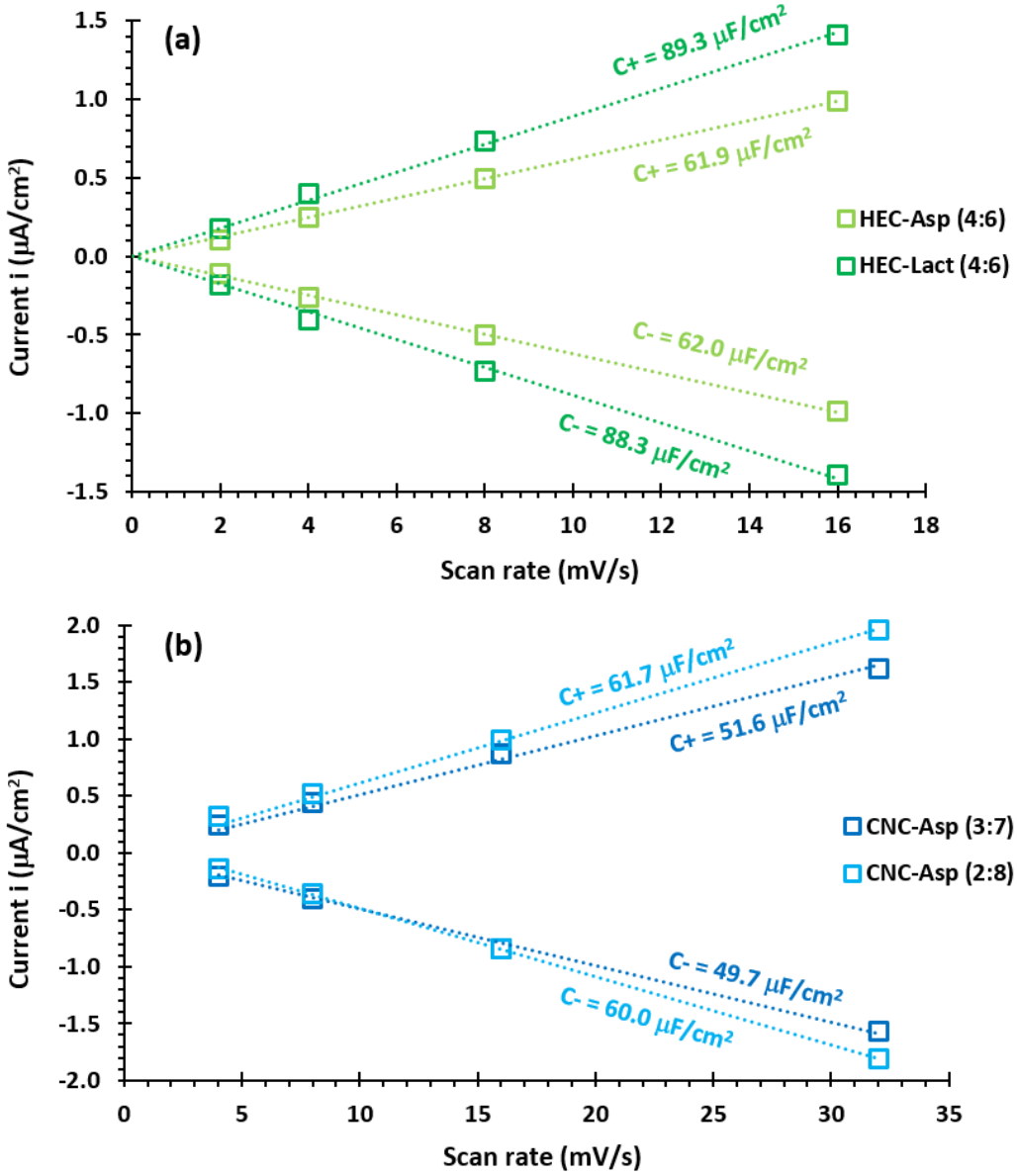

***Figure 4.2.13**. Considering the voltammograms between -50 mV and + 50 mV, an average current value was calculated between ± 5 mV for both positive and negative curves and they were plotted against the scan rate, for both **(a)** the HEC based and **(b)** the CNC-based samples. The angular coefficients of the linear interpolations are reported and their value is a measure of the corresponding double layer capacitance.*

The angular coefficient of the linear interpolations corresponds to the values of the double-layer capacitance C_{dl}, which showed to be very similar regardless the polarization direction, meaning a high symmetry of the two electrodes. More specifically, the calculated values of C_{dl} were 62.0 $\mu F/cm^2$ for HEC-Asp (4:6), 88.8 $\mu F/cm^2$ for HEC-Lact (4:6), 50.7 $\mu F/cm^2$ for CNC-Asp (3:7) and 60.9 $\mu F/cm^2$ for CNC-Asp (2:8), a result that confirms the higher suitability of the choline lactate ionic liquid with respect to the choline aspirin. The calculated values are lower than those obtained through EIS tests, but this is not unusual. In fact, EDLC supercapacitors with nanostructured electrodes are far away to be considered as ideal RC circuits. Both the ions and the pores on the electrodes surface, as well as the channels inside the polymeric matrix, are characterized by different sizes and shapes and the behaviour of the ionic migration and accumulation is not expected to be linear such as in ideal RC circuits where the electric charge is delivered by "zero-mass" and "no-shape" electrons. Then, the system can behave differently when it underwent different stimuli, as in the case of two distinct electrochemical techniques. This is the reason why it is important to characterize such devices with different techniques.

Cyclic voltammetry was also employed to check the electrochemical window of stability of the cellulose-ionic liquids ionogels. *Figure 4.2.14* shows the graph obtained by the application of a potential ranging from -2.5 V to 2.5 V to the HEC-based samples, with a scan rate of 10 mV/s. It can be seen that up to 1.0 V, the measured current remained constant in a stable capacitive regime. After that, under slightly higher applied potentials, a small hump is detected in the current profiles: it's not big enough to be associated with an electrochemical degradation of the ionic liquid, so it can be supposed that it originated by the electrolysis of some undesired water residues inside the ionogel, or to the presence of some impurities. Approaching an applied potential of 2.0 V, the current profile begins to considerably increase its slope and this was assumed to be a sign of the ionogel degradation. It can be then stated that the maximum potential that can be applied to these supercapacitors (in a controlled atmosphere without the presence of humidity) falls in range between 1.0 and 2.0 V. Further characterizations will be needed to detect this limit with higher precision and accuracy.

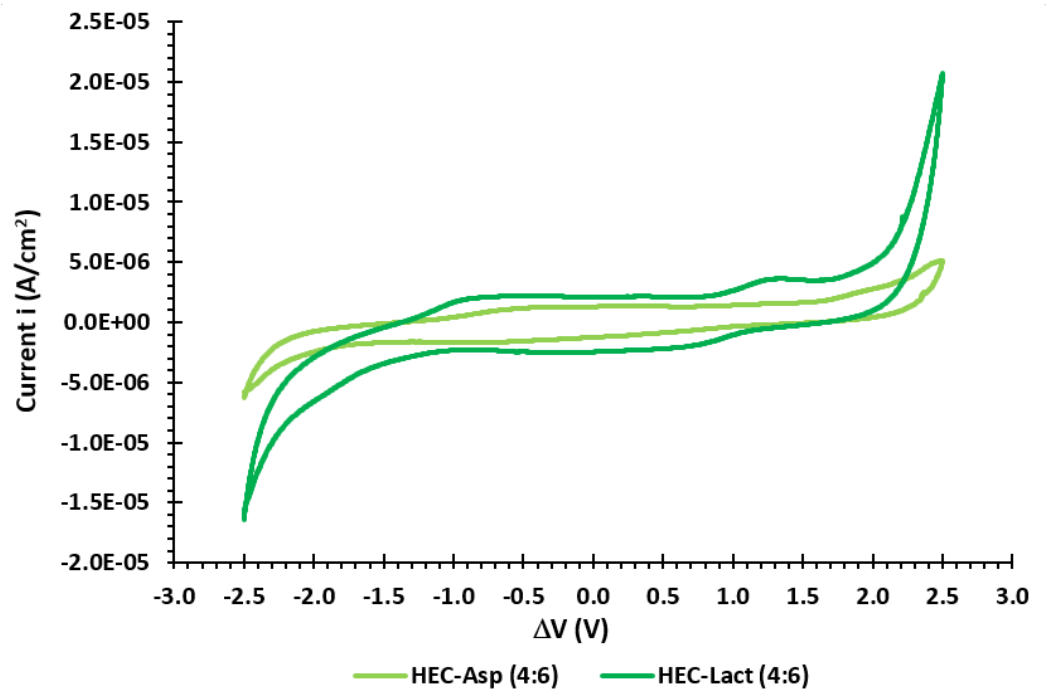

Figure 4.2.14. *Voltammograms obtained from HEC-Asp (4:6) and HEC-Lact (4:6). ⊿V was varied between -2.5 V and + 2.5 V with a scan rates of 10 mV/s. It can be distinguished an approximately capacitive behaviour in the central region of the graph and a faradaic reaction when the absolute value of ⊿V approaches 2 V.*

Thanks to the CV tests it was then possible to measure the double-layer capacitance of the samples with another technique beside EIS: the obtained results well agree with the previous ones. Next, HEC-Asp (4:6), HEC-Lact (4:6) and CNC-Asp (2:8) were characterized by mean of galvanostatic charge-discharge (GCD) technique, in order to test their energetic features and behaviour in a real working condition.

4.2.4 Electrochemistry: GCD and energetic features

The last employed technique was the galvanostatic charge-discharge (GCD) and it was carried out to test the samples HEC-Asp (4:6), HEC-Lact (4:6) and CNC-Asp (2:8) in a context similar to real operating conditions. Different values of a constant current were used to charge the supercapacitors up to a maximum potential (ΔV_{max}) and then they were discharged with an equal but opposite current. In these test, ΔV_{max} was set to 1.0 V to have the certainty to operate without degradation of the ionic liquid, but this value is likely to be increased in future tests. The graphs reported in *Figure 4.2.15* and in *Figure 4.2.16* show the ΔV values in function of the time, under the effect of a constant current of 10, 15, 20 and 25 $\mu A/cm^2$.

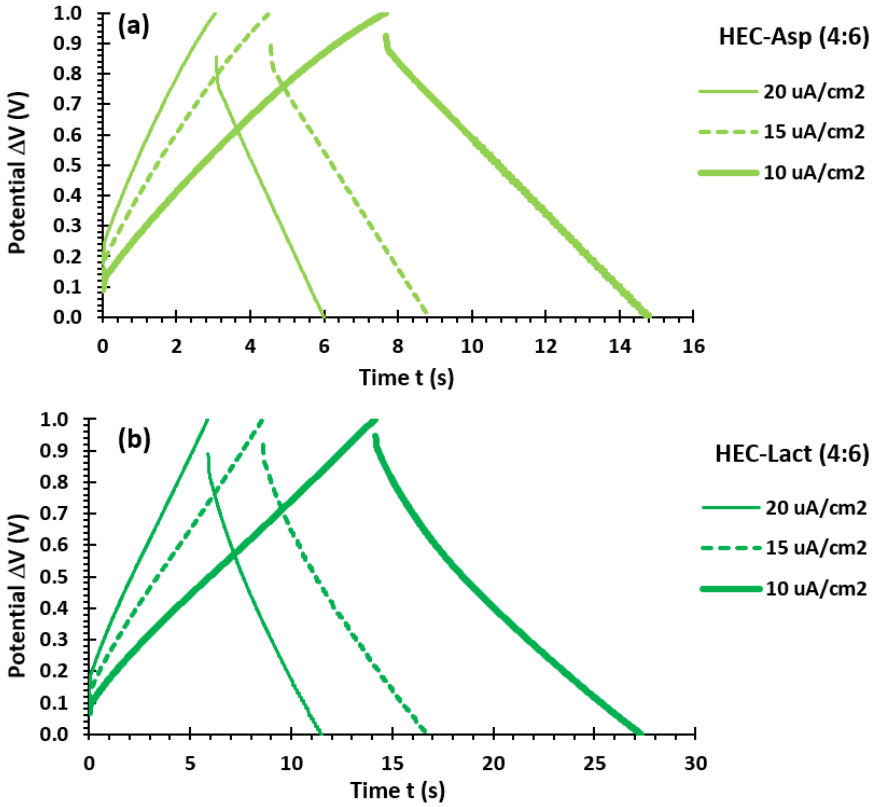

***Figure 4.2.15**. The potential difference between the two opposite electrodes of the HEC-based ionogels as a function of the time during the charge (up to a ΔV_{max} = 1.0 V) and discharge of the supercapacitors under constant values of current (from 10 to 20 $\mu A/cm^2$).*

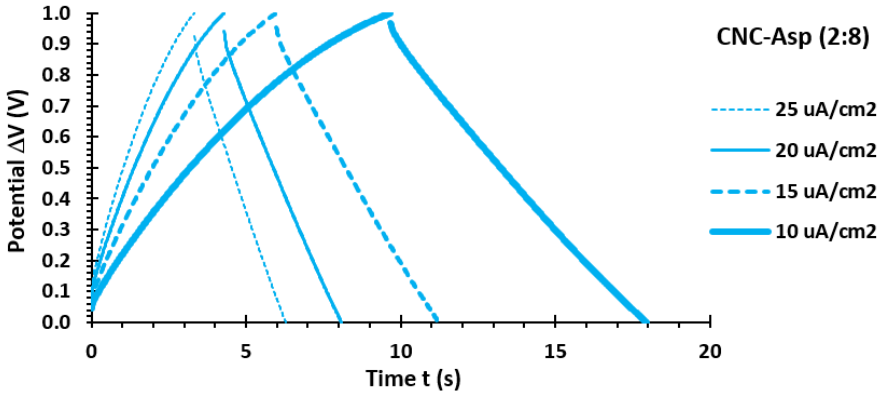

***Figure 4.2.16**. The potential difference between the two opposite electrodes of the CNC-Asp (2:8) ionogel as a function of the time during the charge (up to a ΔV_{max} = 1.0 V) and discharge of the supercapacitors under constant values of current (from 10 to 25 $\mu A/cm^2$).*

The charge and corresponding discharge ramps can be appreciated: the higher the passing current, the faster the device accumulates and delivers the electric charge. Higher values of capacitance are reflected by a higher time of charge (T_c) and discharge (T_d). With these tests, it was possible to calculate again the double-layer capacitance, the ESR and also the coulombic efficiency CE (the detailed calculations can be found in *Section 6.2.2*). Also in this case, the not ideal character of these systems led to small variations according the different current's entity. All the calculated values are reported in the Table in *Figure 4.2.17*.

	HEC – Asp (4:6)			HEC – Lact (4:6)			CNC– Asp (2:8)		
	ESR ($k\Omega xcm^2$)	C_{dl} ($\mu F/cm^2$)	CE (%)	ESR ($k\Omega xcm^2$)	C_{dl} ($\mu F/cm^2$)	CE (%)	ESR ($k\Omega xcm^2$)	C_{dl} ($\mu F/cm^2$)	CE (%)
10 $\mu A/cm^2$	6.02	71.3	93.0%	4.53	132	92.8%	2.40	82.9	85.7%
15 $\mu A/cm^2$	5.67	64.7	94.9%	4.33	122	94.2%	2.23	78.9	88.0%
20 $\mu A/cm^2$	5.54	58.8	96.1%	4.01	112	95.6%	2.20	76.0	88.6%
25 $\mu A/cm^2$							2.18	74.0	88.9%

***Figure 4.2.17**. Table reporting the values of ESR, C_{dl} and CE obtained varying the constant charge and discharge current for the different samples characterized through GCD technique.*

The overall results are in good agreement with those previously obtained through different electrochemical techniques and a summarizing table is reported in *Figure 4.2.18*. It is again confirmed that CholLact is more performant then CholAsp and that the increase of the ionic liquid content improves the electrochemical performances by both lowering the ESR and increasing the C_{dl}.

	HEC – Asp (4:6)		HEC – Lact (4:6)	
	ESR (kΩxcm²)	C_{dl} (μF/cm²)	ESR (kΩxcm²)	C_{dl} (μF/cm²)
EIS	4.67	74.5	3.12	130
CV	-	62.0	-	88.8
GCD	5.54 - 6.02	58.8 - 71.3	4.01 - 4.53	112 - 132
	CNC – Asp (3:7)		CNC – Asp (2:8)	
	ESR (kΩxcm²)	C_{dl} (μF/cm²)	ESR (kΩxcm²)	C_{dl} (μF/cm²)
EIS	6.68	66.8	2.27	75.2
CV	-	50.7	-	60.9
GCD	-	-	2.18 - 2.40	74.0 - 82.9

***Figure 4.2.18**. Summarizing table reporting the values of ESR and C_{dl} obtained for the HEC-based and CNC-based samples characterized through ESI, CV and GCD techniques.*

The stability of HEC-Asp (4:6), HEC-Lact (4:6) and CNC-Asp (2:8) was then tested under the application of 10^4 cycles of charge and discharge at 20 μA/cm² or 25 μA/cm², during which the capacitance retention C_{ret} as well as the coulombic efficiency were continuously monitored. The results are reported in the graph in *Figure 4.2.19* and they revealed appreciable. After 10^4 cycles, the supercapacitors with the 71%, the 85% and the 74% respectively of their original capacitance values. Moreover, the coulombic efficiency increased cycle by cycle, reaching a final value of about the 98% in every case. A similar behaviour was obtained when measuring the electroactive displacement of the PHB bioplastic-based electromechanical actuators (*Section 3.3.3*), whose behaviour

slightly improved over cycles. Despite they are smart materials designed to carry out different functions, both of them relied on the ionic accumulation in a similar nanostructured ionogel-Au interface: this is probably the common feature that can explain this singular behaviour.

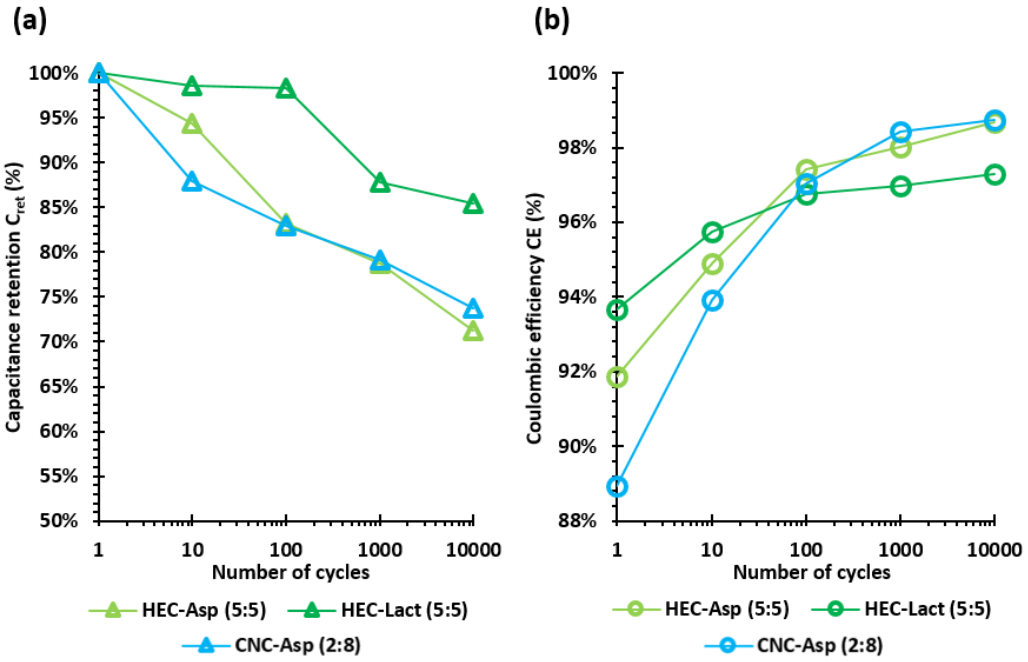

***Figure 4.2.19**. **(a)** The capacitance retention C_{ret} and **(b)** the coulombic efficiency CE are reported against the number of GCD cycles for the samples HEC-Asp (4:6) and HEC-Lact (4:6) (at 20 $\mu A/cm^2$) and for the sample CNC-Asp (2:8) (at 25 $\mu A/cm^2$).*

At last, the results obtained from the GCD measurements (C_{dl}, ESR and ΔV_{max}) were used to calculate the total amount of energy stored (E) and the maximum delivery power (P) normalized for both the mass (specific E_S and P_S) and the volume (volumetric E_V and P_V) of the electrodes material. The calculations were conducted according to the equations presented in *Section 4.1.1* and also reported more in detail in *Section 6.2.2*. The graphs in *Figure 4.2.20(a-b)* reports the values of the power plotted against the values of the energy, as in a typical Ragone plot. Figure *4.2.20(c-d)*, instead, reports the obtained values superimposed to the Ragone plots already presented in *Figure 4.1.1*. It can be seen how in both, the energetic performances of the hereby presented natural-

derived and biodegradable EDLCs falls right in the area typically occupied by supercapacitors. Considering that cluster-assembled Au electrodes are substantially heavier but thinner than the carbon-based electrodes usually employed, it's easy to understand why the specific E_S and P_S appear to be less outstanding then their volumetric analogous. Even if the results here obtained are not comparable to the top-class prototype supercapacitors in the world, they have the great advantage of being completely natural-derived, biodegradable and obtained without the use of toxic substances and/or organic solvents. Moreover, in few years, more and more, these won't be considered anymore advantages, but mandatory requirements.

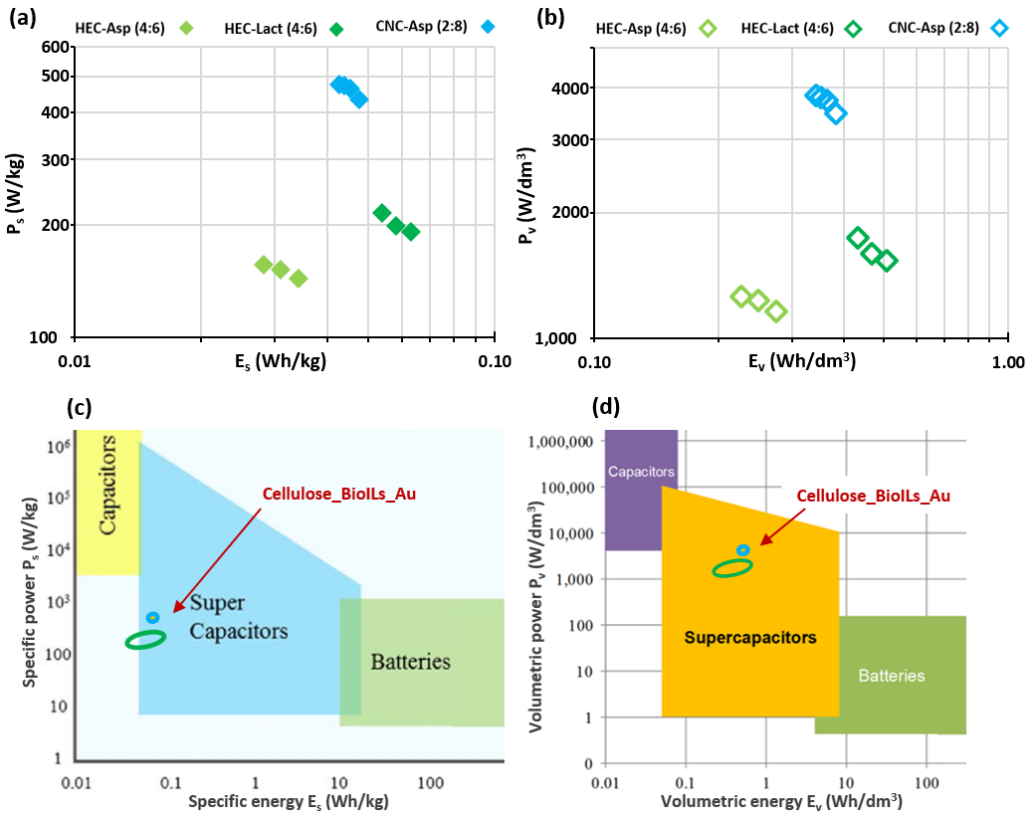

Figure 4.2.20*. The graphs reported the values of energy stored and delivery power obtained by the GCD characterization of the samples HEC-Asp (4:6), HEC-Lact (4:6) and CNC-Asp (2:8). It is shown the relationship between energy E and power P normalized per both the* ***(a)*** *electrodes mass and* ***(b)*** *the electrodes volume. Figures* ***(c-d)*** *show the area covered by these values superimposed to the Ragone plots previously presented in Section 4.1.1.*

So, in this work, completely natural-derived and biodegradable self-standing ionogels were designed and developed with the use of cellulose derivatives and two choline carboxylates ionic liquids, with a casting process that involved water as the unique solvent. Cluster-assembled Au electrodes were fabricated by mean of solvent-free SCDB technique on the opposite sides of the electrolyte gels (in a sandwich geometry) and the study of their electrochemical properties assessed their correct functioning as supercapacitors.

Even if all the reported tests have been conducted in a controlled atmosphere, these novel devices are expected to address one of the main issues of current supercapacitors, that is the simultaneous employment of eco-friendly electrolytes and the possibility to stably operate in plain air. Up to now, this problem has not been solved yet with an efficient solution. I am confident that the hereby presented EDLC supercapacitors can be able to operate in ambient conditions since the employed biodegradable ionic liquids do not evaporate and they should remain inside the ionogel, assuring a correct functioning.

The reported results represent a preliminary study in order to assess a proof of concept about the energetic performance of these innovative composite materials and also to find and to study different ionogel formulations. Different aspects have still to be optimized, such as the best mass ratio between polymer and ionic liquid, the more suited type of cellulose derivative, the surface quality and the thickness of the electrodes. For example, looking at the presented results, it is logical to suppose that the combination of CNCs with choline lactate (not yet tested) would improve the obtained energetic performances. Moreover, cluster-assembled carbon layers can also be produced by mean of solvent-free SCBD technique and they can be integrated as intermediate layers between the ionogel surface and the gold electrodes, eventually leading to a higher interfacial area and an increased double-layer capacitance. I am confident that through more study it will be possible to further improve the energetic features of these supercapacitors.

Lastly, while the self-standing samples were characterized, a process was studied and developed to allow the efficient and reproducible fabrication of ultrathin supercapacitors onto biodegradable and flexible cellulose acetate sheets. The obtained preliminary results are reported in the next *Section 4.2.5*.

4.2.5 Automated layer-by-layer spray process for ultrathin micro-supercapacitors

As already mentioned in *Section 4.1.4*, the ultimate goal of this project on supercapacitor is the development of **soft ultrathin** completely solid and **biodegradable EDLCs micro-supercapacitors** able to **stably operate both in ambient and controlled environments**, **suitable for stacking** in series, **fabricated onto a flexible biodegradable platform** and obtained with a **few-steps organic solvent-free process** by the use of **natural-derived and renewable raw materials**. The work reported in the previous sections was focused on the search for a suitable formulation and synthesis of self-standing, soft and solid ionogels, using only biodegradable substances and a water-based solvent casting process. It was also assessed the suitability of the SCBD technique for the fabrication of cluster-assembled Au electrodes and a nice electrochemical characterization was carried out.

At the same time, a study was conducted in the search for a process that could allow the fabrication of ultrathin supercapacitors onto a flexible biodegradable substrate, in a reproducible, automatable and scalable way. Moreover, the manufacturing process should also be suitable for an easy stacking in series of many EDLC elements. To achieve this goal, the following shrewdness were adopted:

- **Flexible thin sheets of biodegradable cellulose acetate** were employed as the substrate.

- **An automated spray-casting process** to deposit extremely thin ionogel layers on the substrate

- A **layer-by-layer spray process** for the fabrication of an entire micro-supercapacitors. In fact, both the ionogel's and the electrodes precursors can be dispersed in a gas phase, by mean of spray casting and supersonic cluster beam deposition, respectively. *Figure 4.2.21* show a schematic illustration of the process.

- A "bi-dimensional" sandwich geometry. By targeting extremely thin total thicknesses (lower than 5 μm), the resulting device can almost be considered to be bi-dimensional, a great advantage for microelectronics application. Moreover, this technique can also reveal to be suitable for a layer-by-layer stacking in series of many ultrathin supercapacitors by keeping constant the occupied area of the substrate.

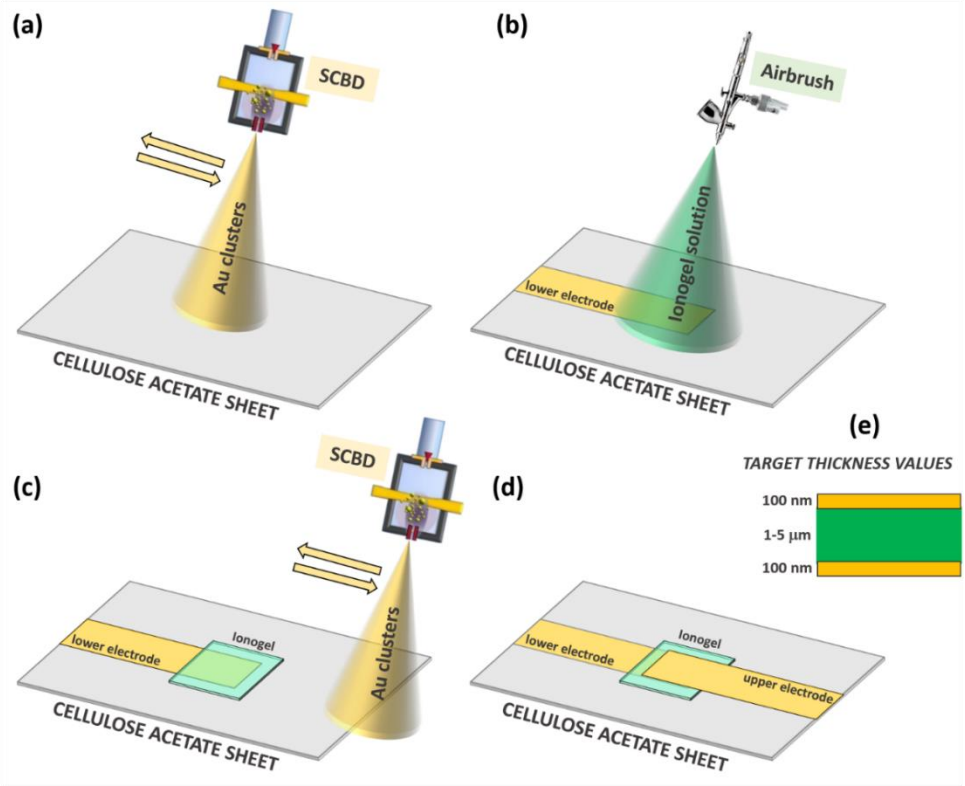

***Figure 4.2.21**. Schematic illustration of the layer-by-layer spray process for the deposition of an entire micro-supercapacitor on a biodegradable cellulose acetate sheet.* ***(a)** Deposition of the lower cluster-assembled Au electrode by mean of SCBD;* ***(b)** spray-casting of the biodegradable ionogel* ***(c);** SCBD-deposition of the upper electrode.* ***(d)** Resulting bi-dimensional sandwich supercapacitor.* ***(e)** Target thickness values (not in scale).*

Initially, a water solution of Na-carboxymethylcellulose (Na-CMC) and choline aspirin (mass ratio 5:5) was prepared (the same employed for the fabrication of the self-standing ionogels presented in *Section 4.2.1*). The solution was then poured inside the cup of a standard airbrush connected to a nitrogen line at a pressure of 2 bar. With this, it was possible to spray the solution over a cellulose acetate (CA) sheet by manually controlling the nozzle opening time. A step-by-step spray process was carried out with every step consisting in 20 seconds of spray and 40 seconds of waiting to allow the solidification (by water evaporation) of the deposited solution. Different samples were spray-casted by varying the number of the repeated steps, from 10 to 80. The superficial morphology of the deposited thin films was monitored and some pictures are reported in *Figure 4.2.22*.

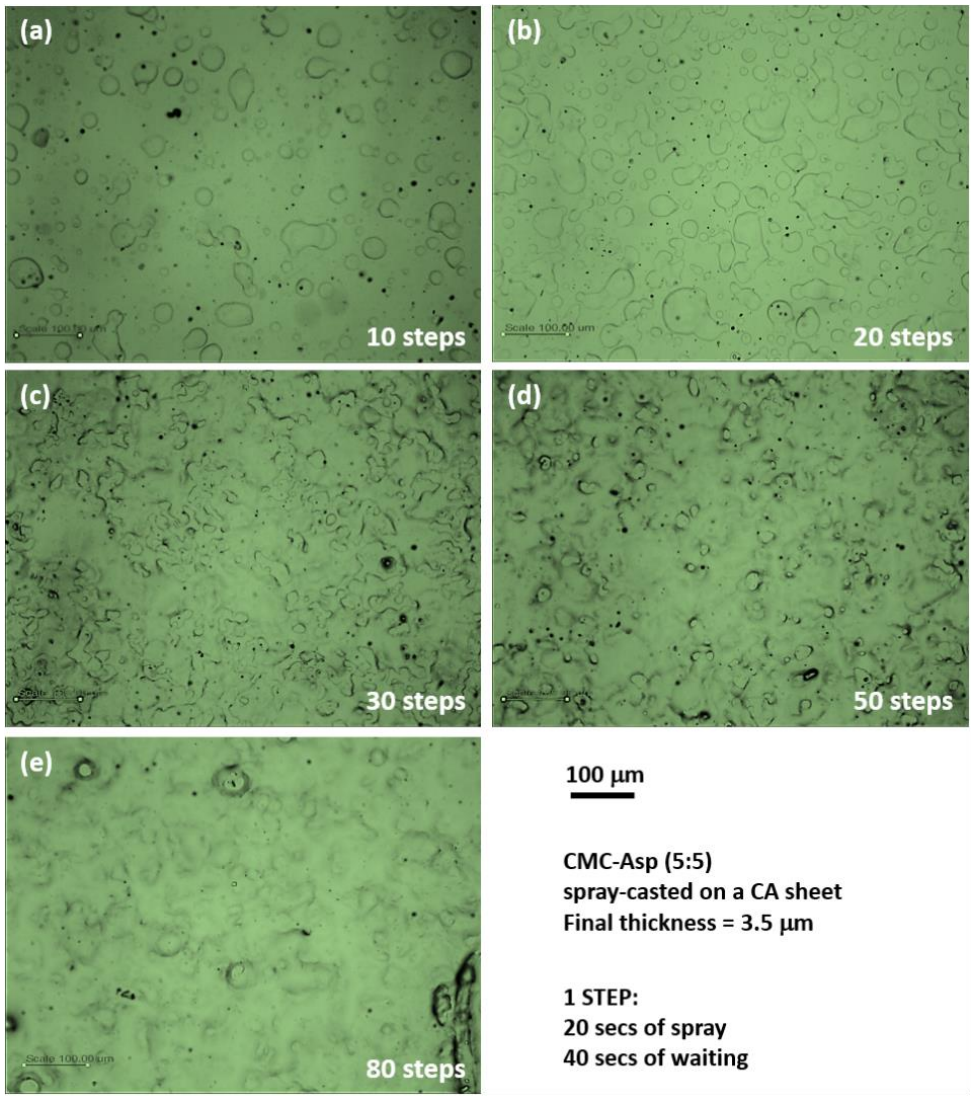

***Figure 4.2.22**. Pictures showing the variation in the superficial morphology of the CMC-Asp (5:5) ionogel spray-casted on a CA sheet, according to the number of repeated steps.*

As can be seen, it appeared that up to 20 steps were not enough to achieve a full coating of the underlying CA sheet. After 30 steps, a rough continuous surface began to form and after 80 steps smoother homogenous surface was observed. The final measured thickness was of ca. 3.5 µm. It was then assessed the possibility to produce extremely thin cellulose-based ionogels by mean of spray-casting.

Then, an automated spray-casting process was designed and realized by coupling the airbrush and a 3D printing apparatus. More in detail, a PowerWASP EVO 3D printer was employed and the traditional extruder was substituted with the airbrush. A photograph of the apparatus is reported in *Figure 4.2.23(a)*. With this, it was possible to use a dedicated software to accurately control the relative position and the motion between the airbrush's nozzle and the substrate, leading to a process characterized by high precision and accuracy, repeatability and operator independence. More details about the spray-casting deposition of the ionogels are reported in *Section 6.1.1(e)*.

A full supercapacitor was then deposited on a CA sheet using a solution of cellulose nanocrystals (CNCs) and choline aspirin (mass ratio 2:8) as the ionogel precursor, since it was suggested to be the more promising formulation accordingly to the experiments carried out on the self-standing ionogels (reported in the previous sections). Following the procedure shown in the illustration of *Figure 4.2.21*, a 100 nm-thick cluster-assembled Au electrode was firstly deposited on a CA substrate, showing a very low sheet resistance of about (4 Ω). Then, a CNC-Asp (2:8) thin ionogel was spray-casted above one of the electrode's terminal regions (*Figure 4.2.23(b)*) and finally the second 100 nm-thick electrode was SCBD-deposited on top (*Figure 4.2.23(c)*). More experimental details about the electrodes deposition process are reported in *Section 6.3.1*.

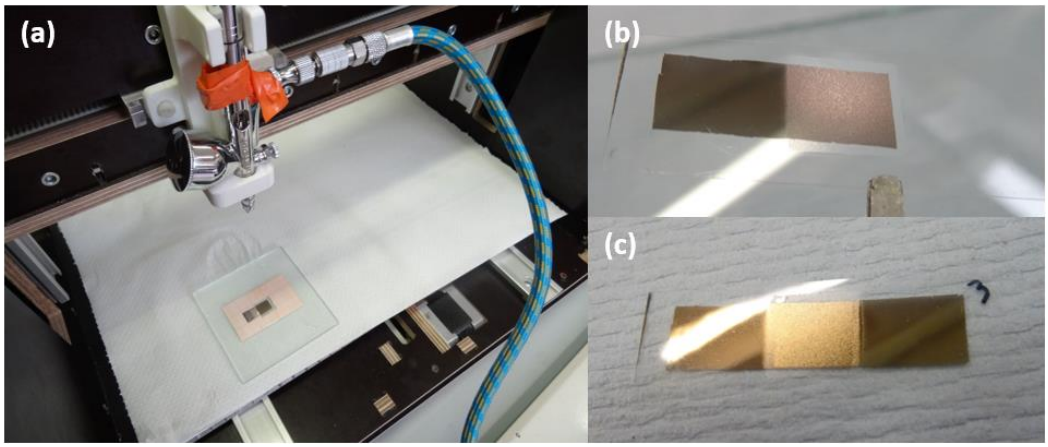

***Figure 4.2.23**. **(a)** Photograph of the developed automated spray-casting apparatus. The airbrush, connected to a gas-line, was coupled to a PowerWASP EVO 3D printer in place of its extruder. **(b)** Photograph showing the CNC-Asp (2:8) ionogel spray-casted onto a 100 nm-thick cluster-assembled Au electrode on a cellulose acetate film. **(c)** Photograph showing the full "bi-dimensional" supercapacitor, with the second electrodes was SCBD-deposited on top of the ionogel.*

Figure 4.2.24 reports a couple of pictures showing the surface morphology of the full supercapacitor.

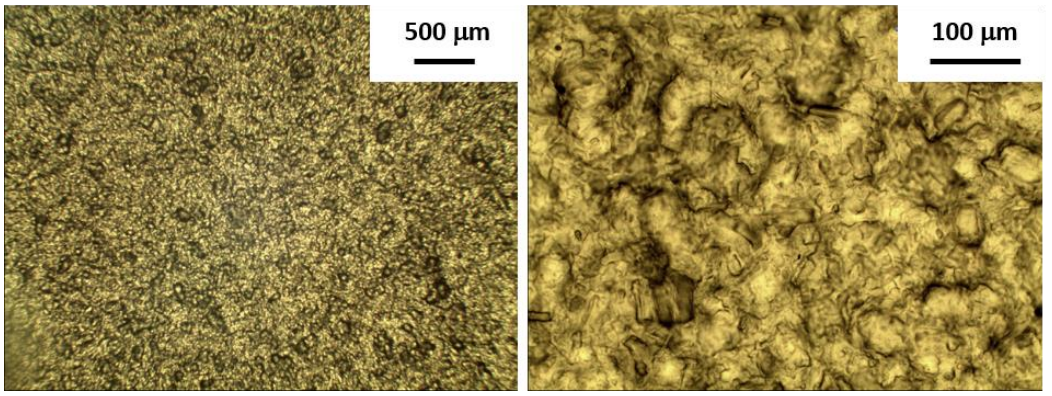

***Figure 4.2.24**. Pictures taken with a reflectance optical microscope, showing the superficial morphology of a bi-dimensional full supercapacitor layer-by-layer deposited on a cellulose acetate sheet. A spray-casted CNC-Asp (2:8) thin ionogel is sandwiched between a couple of 100 nm-thick cluster-assembled Au electrodes deposited via SCBD.*

In the end, atomic force microscopy (AFM) was employed to study the morphological and mechanical properties of the obtained device. An average roughness of 1.5-2 μm was detected. Indentation measurements were also carried out. The obtained results highlighted a singular structure where softer bulges are delimitated by a harder interconnected three-dimensional reticulum (*Figure 4.2.25(a, b)*). This observed heterogeneity can be due to the fact that during the water evaporation, the CNCs aggregate in a sort of reticular structure and the ionic liquid tends to occupy the empty space. *Figure 4.2.26(c)* shows the distribution of the measured elastic moduli and the average value was calculated to be of 3.39 ± 0.103 MPa. The experimental details about these measures are reported in *Section 6.3.1*. This was the last obtained result concerning the project line on biodegradable supercapacitors. The layer-by-layer deposited full device will soon be electrochemically characterized to test its energetic performances.

In this work all-natural derived EDLC supercapacitors were designed and obtained by using solely biodegradable and benign raw materials, completely avoiding the use of toxic reagents, non-degradable substances and organic solvents. Natural-derived ionic liquids were employed for the first time in this field as the electrolyte medium. Solvent casting from water and solvent-free supersonic cluster beam deposition (SCBD) were the two employed techniques for the fabrication of self-standing

solid and soft supercapacitors: different formulations have been electrochemically tested and evaluated. An automated spray-casting process was then designed and applied for the fabrication of ultrathin "bi-dimensional" supercapacitors on biodegradable flexible cellulose acetate films. The obtained results only constitute a preliminary stage: different several ionogel formulations will be tested and evaluated, and both the metallization and the spray-casting processes will be optimized. AFM will become a routine technique for the study and the comparison of the several produces samples. In the end, layer-by-layer stacking in series on many supercapacitors will be addressed and the energetic performances will be tested also under mechanical stress and deformation.

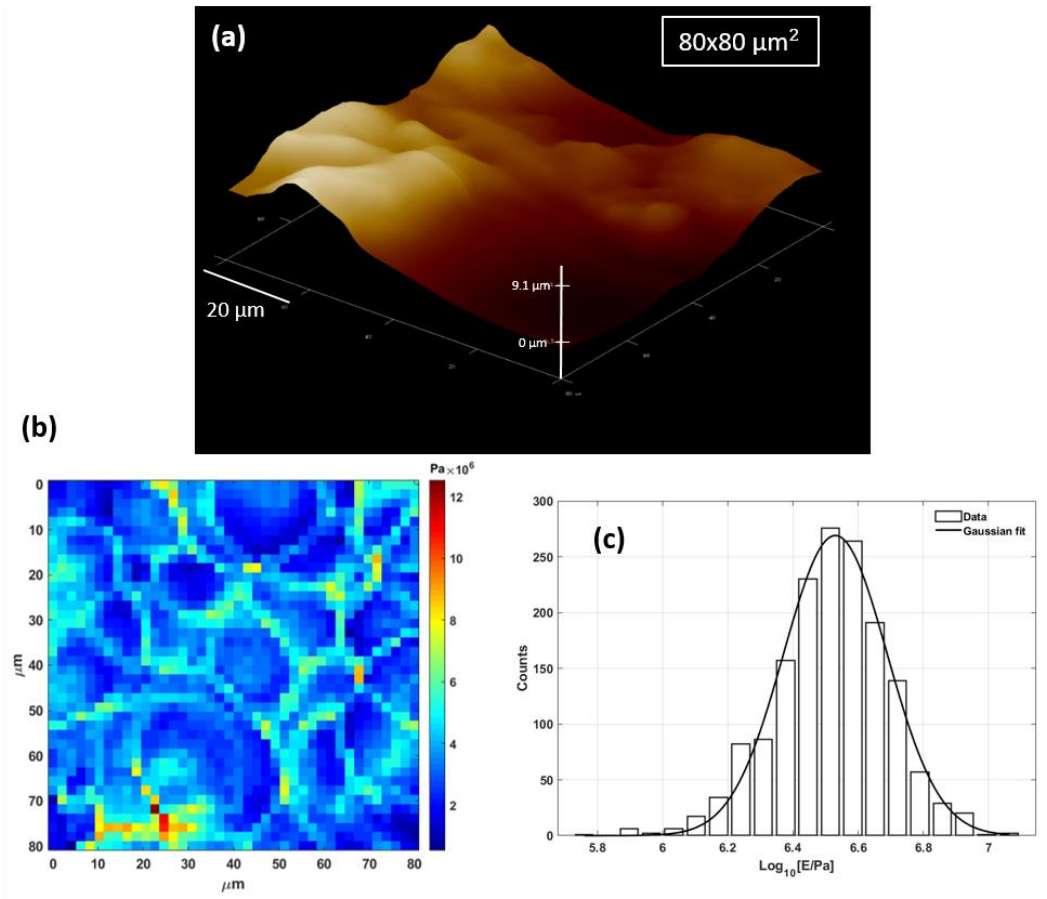

Figure 4.2.25. *Results of the AFM measures carried out on the full supercapacitor layer-by-layer deposited on a CA sheet.* ***(a)*** *One of the performed morphological scans;* ***(b)*** *map showing the elastic modulus obtained in different points of a square matrix through indentation measurements;* ***(c)*** *distribution of the measured elastic moduli*

5.

Biodegradable Transparent Electronics and Strain Sensors

5.1 Overiview on Printable Transparent Electronics and Strain Sensors

5.1.1 Printable transparent conductive films (TCFs)

Flexible and transparent electronics is of fundamental importance in the development of efficient, stretchable, and wearable optoelectronic devices such as organic photovoltaics (OPVs), organic light-emitting diodes (OLEDs), e-readers, touch screens and electronic papers [313,325–329]. Also, soft robots, sensors and devices need to be controlled by similarly soft and deformable electronic circuits in order to effectively exploit all of their potential. To do this, there is the need for **transparent conductive films (TCFs)** that should exhibit high optical transmittance and high electronic conduction even under severe deformation. The most commonly employed transparent conductor is Indium tin oxide (ITO) characterized by high transmittance (>90%) and low sheet resistance (R_s < 30 Ω). However, ITO is brittle and prone to cracking and moreover its supplying is becoming critical.

Novel emerging materials such as **conductive polymers**, **metal grids**, **carbon nanotubes (CNTs)**, **graphene**, and random networks of **metal nanowires** (Ag/Cu NWs) have been explored as alternatives to ITO [330–333]. Preparation processes like spin-coating, drop-casting, spraying, dip-coating, and metering-rod [334–336] can allow to obtain TFCs with comparable properties than ITO, but these solution-phase methods are hard to be scaled up. The combination of printing techniques with solution-processable TCF materials provides a promising solution to the scale-up problem, using flexible and transparent polymeric substrates such as **polyethylene terephthalate (PET)**, **polyimide (PI)** and **polydimethylsiloxane (PDMS)**. Many different techniques can be employed, such as inkjet printing, gravure printing, screen printing, and offset printing [337–339]. Some examples of self-standing TCFs are reported in *Figure 5.1.1*.

The formulation of **printable conductive inks** is one of the main crucial task to be taken into account: the composition and the physical properties such as viscosity and surface tension are pivotal for achieving high printing accuracy and resolution. An ideal ink should be inexpensive, easy to prepare, stable against aggregation and precipitation and able to provide a final high conductivity [342,343].

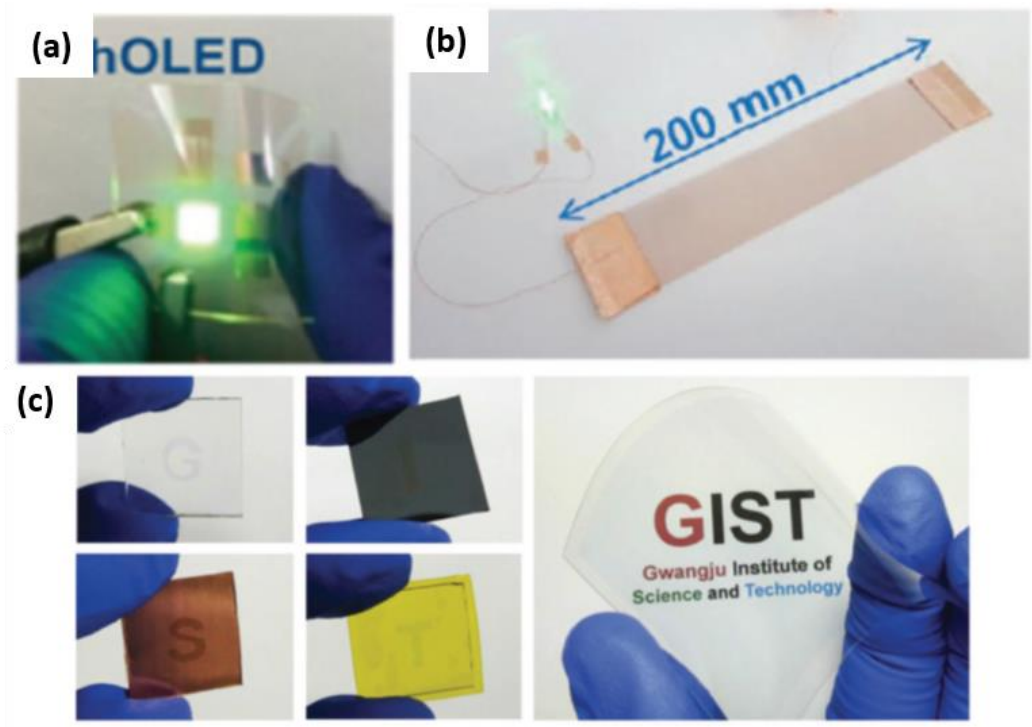

***Figure 5.1.1**. Examples of manufactured self-standing TCFs. **(a)** Flexible green phosphorescent OLED device* [329]. ***(b)** A LED circuit with 200 mm long flexible transparent conductive electrodes* [340]. ***(c)** H_2SO_4-treated PEDOT:PSS films transferred onto various substrates, including a glass slide, a silicon wafer, Cu foil, Kapton tape, and large-area PET foil* [341].

Graphene has attracted increasing attention in recent years, due to its high carrier mobility at room temperature, excellent Young's modulus, high conductivity and light transmission [61,344]. Through the chemical reduction of graphene oxide (GO) it can be obtained graphene with high electrical conductivity but it cannot be well dispersed in common solvents. N,N-dimethylformamide (DMF) and dichloroethane can be used for the direct dispersion of graphene [345,346], however, the low concentration and high boiling point of these solvents are two main obstacles for high-performance TCF fabrication. Differently, GO has oxygen containing groups on its surface and it can be well dispersed in polar solvents such as water, ethanol, acetone, and ethylene glycol (EG) [347,348], although its electrical conductivity is relatively poor. Similar dispersion problems are encountered with CNTs; furthermore, the high aspect ratio and strong van der Waals attraction make CNTs prone to stick together and form large bundles [349,350].

Metal NWs, especially Ag NWs, can be considered one of the most promising solutions thanks to their low cost, high transparency and conductivity, intrinsic flexibility, and solution-processable properties [351]. Several structure parameters of metal NWs including aspect ratio, smoothness, size uniformity, and purity could affect the final performance of TCFs. A typical method for the synthesis of Ag NWs is the reduction of silver nitrate in the presence of poly(vinylpyrrolidone) (PVP) in ethylene glycole [352] and the so-obtained NWs can be dispersed in water as well as other polar solvents such as ethanol and isopropyl alcohol to form a stable ink [353]. Cu NWs possess almost the same conductivity with a lower production cost, but they are sensitive to oxygen and moisture, leading to poor conductivity with the formation of copper oxide [354]. Metal NPs such as silver and copper NPs (Ag/Cu NPs) are among the most conductive materials due to their high free electron density. Many methods have been reported for their synthesis such as chemical reduction routes and polyol process [219,355,356]. The fabricated metal NPs can then be dispersed in various solvents such as glycerol, ethanol, acetone, and toluene to form stable ink [357,358]. The greatest drawbacks of Ag NPs are their high cost, low solid content, and electromigration behavior, while lower-cost Cu NPs are susceptible to oxidation, resulting in a remarkable reduction in conductivity.

Different from the above-mentioned TCF materials, **conductive polymers** such as polythiophenes, polyanilines and PEDOT:PSS usually have a lower electrical conductivity. However, their solution-processable property, tailorable solubility, and electron affinity by attaching side chains to the polymer backbone endow them with printable, easy-controlled, and flexible properties [359]. In addition to all of these conductive solutes and solvents, specific binders and additives such as polymers, porphyrin, DNA, and cellulose derivatives are also necessary for enhancing the dispersion stability, wetting, and loading density of various conductive inks [360,361]. Some examples of conductive inks are reported in *Figure 5.1.2*.

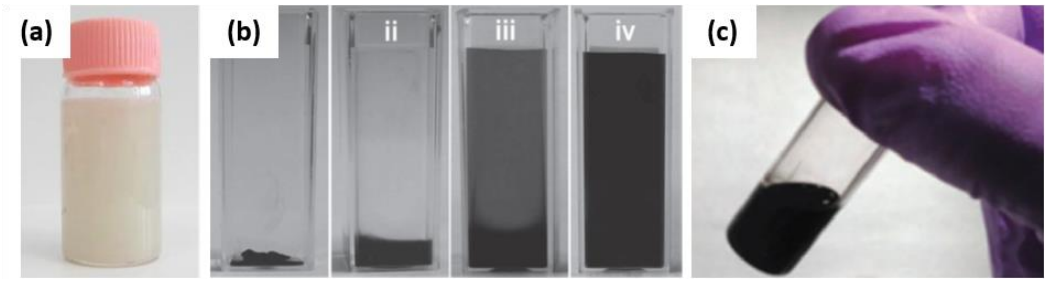

***Figure 5.1.2**. Photographs of prepared printable conductive inks. **(a)** Methylcellulose solution with silver nanowires* [362]. ***(b)** Dissolution of soluble SWCNTs in water, for 0 min, 10 min, 1 h and 2 days* [349]. ***(c)** Graphene conductive ink obtained by dispersing graphene powder in a 85:15 mixture of cyclohexanone/terpineol* [363].

After the formulation of suitable printable inks, the printing process could be carried out to obtain desired TCFs on various flexible substrates, such as the above-mentioned PET, PI and PDMS. However, the **printing resolution** and **substrate adhesion** are usually dissatisfied. In fact, on a smooth homogeneous surface, the geometry and pattern resolution of printing techniques are mainly determined by the wettability of the depositing ink liquid with respect to the substrate. This means that the reasonable control of the wettability of a substrate surface and the bonding force between the patterns and substrates are crucial elements to be taken into account for high-resolution printing [364–369]. Good adhesion between the patterns and substrates depends on the interface features and it is essential for achieving flexible optoelectronic devices. In this direction, the addition of **adhesion promotion layers** such as silane coupling agents can improve the adhesion by altering the chemical nature of the substrate surface [340,370,371]. Besides, **additional post-processing** is required for solving issues such as high surface roughness, low conductivity and weak substrate adherence. For example, the presence of polymer stabilizers can considerably reduce the electronic conduction and therefore, an additional film sintering step is required for their removal [372]. Traditional thermal annealing technique has been proved effective in the decomposition of polymer stabilizers as well as lowering the contact resistance [373], but high annealing temperatures (usually above 200 °C) are incompatible with the rapid processing requirement and commonly used thermally sensitive substrates. Some alternative annealing techniques such as plasmonic welding, microwave, laser, and intense pulse light have therefore been developed to substitute the traditional thermal annealing method [363,374–376].

5.1.2 Resistive-type strain sensors

Strain sensors are composite materials able to transduce mechanical deformations and strains into electrical signals, that can be easily read and correlated to the forces acting on the sensors. Recently, following the development of smart deformable devices, the demand for high-performance smart flexible strain sensors is growing. Thanks to their facile interaction with biological matter and long-term monitoring capabilities, they can be employed to monitor physical, chemical, biological, and environmental status of both human body and agricultural plantations with high efficiency and minimum discomfort [377–380] (*Figure 5.1.3(a)*). Soft sensors can be attached onto the clothing and even directly mounted on the human skin or plants leaves for the real-time monitoring of physiological activities [381]. They can display all of their potential in many applications fields, such as body health monitoring [382], human movement detection [383–386] (*Figure 5.1.3(b)*), soft robotics [387], artificial muscles,

structure health monitoring [388] and human–machine interfaces [389]. Ideally, their use in no limited to the interaction with humans: the monitoring of plants and animals as well as the interaction with them is equally fundamental in the field of precision agriculture and breeding. Besides their high efficiency, strain sensors must fulfill several minimum requirements including high stretchability and/or flexibility, durability, **low power consumption**, **biocompatibility**, and **lightweight**. Recently, several types of strain sensors have been proposed by using nanomaterials coupled with flexible and stretchable polymers. Indeed, nanomaterials represent the functional sensing elements owing to their outstanding electrical, mechanical, optical, and/or chemical properties while polymers constitute the flexible support materials thanks to their flexibility, stretchability, human friendliness and durability. *Figure 5.1.3* shows some examples of strain sensors employed for different purposes.

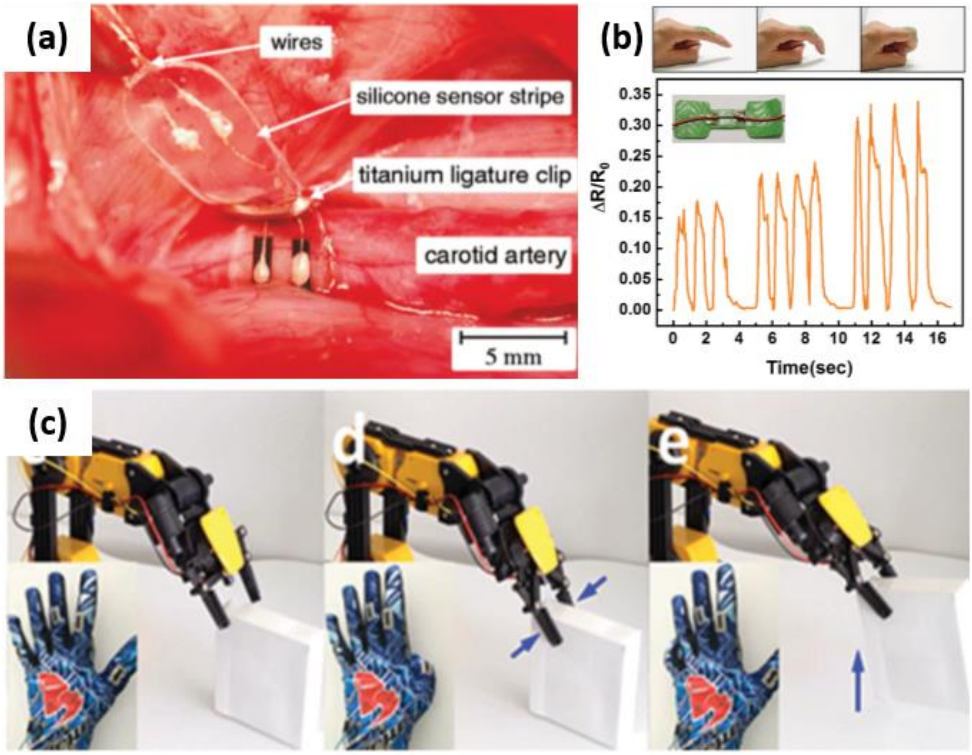

Figure 5.1.3. *Examples of strain sensors employed for different purposes.* ***(a)*** *Capacitive-type strain sensor wrapped around the carotid artery of a pig* [380]. ***(b)*** *Wrinkled CNT-Ecoflex strain sensor used to monitor human movement. The graph reports the relative change in resistance while bending the strain sensor at joint area of finger* [386]. ***(c)*** *Remote control of a gripper robot by the use of a smart glove system based on strain sensors* [390].

One of the most diffuse kind of strain sensors are of the **resistive-type**, typically composed of thin electrically conductive films coupled with flexible substrates (a schematic illustration is reported in *Figure 5.1.4(a)*). When the composite structures are stretched or bent, microstructural changes in the conductive films lead to a change in their ohmic resistance as a function of the applied strain. After the release of the strain, the conductive film reestablishes its original state and electric resistance. One of the mechanisms that correlate the strain and the ohmic resistance is the disconnection mechanisms: in fact, in conductive thin films made of nanomaterial conductive network, electrons can pass through overlapped nanomaterials within the percolation network. Stretching of thin films causes some connected nanomaterials to lose their overlapped area and electrical connection, consequently, increasing the electrical resistance. In microstructural point of view, disconnection of overlapped nanomaterials under stretching is caused by the slippage of nanomaterials due to the weak interfacial binding and large stiffness mismatch between nanomaterials and stretchable polymers [381,391]. Beside the disconnection mechanism, another effect can be due to the tunneling current, that is the Crossing of electrons through a nonconductive barrier. In fact, in a nanostructured conductive layer in a percolation regime, electrons can tunnel through closely spaced adjacent nanoparticles [381,392,393]. Within a certain cut-off distance between neighboring nanomaterials, electrons can path through polymer thin layers and form quantum tunneling junctions. Such tunneling current is strongly dependent on the distance between the conductive particles [394]: then, the application of a strain increases the inter-particle distance, resulting in a lower current of tunneling and in a consequent increase in the film electric resistance.

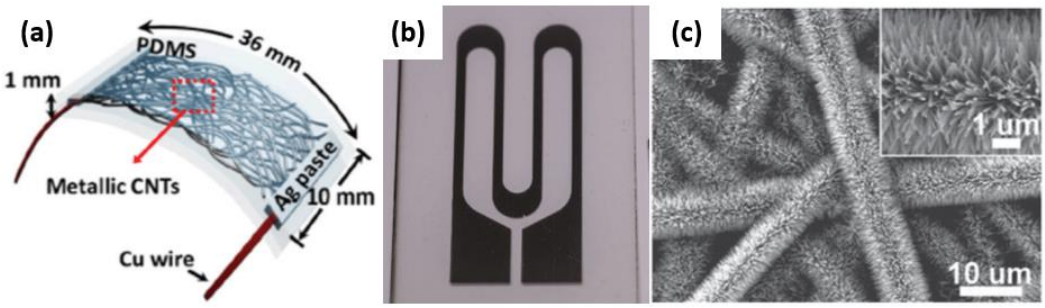

Figure 5.1.4. ***(a)*** *Schematic illustration of a transparent CNT–PDMS composite strain sensor in the form of a sandwich structure* [395]. ***(b)*** *As deposited wrinkled Pt strain sensors, pang* [382]. ***(c)*** *ZnO nanowires hybrid nanobrush structures for high strain sensing* [396].

To date, stretchable strain sensors have been fabricated by using **low-dimensional carbons** (like carbon blacks (CBs), carbon nanotubes (CNTs), and graphene) [397–400], **nanowires (NWs)** [396,401,402] (*Figure 5.1.4(c)*), **nanoparticles (NPs)** [403,404] and their hybrid micro/nanostructures [390,405]. **Silicone-based elastomers** [399,406–409] and **rubbers** (e.g., natural rubber and thermoplastic elastomers (TPEs)) [390,410–413] are the most commonly used polymers as flexible support materials of soft strain sensors. Stretchable strain sensors were fabricated through different processes including filtration method [414,415], printing technology [392,402], transferring and micro-molding methods [416,417], coating techniques [397,418], liquid phase mixing [419,420] and chemical synthesis methods [409,421]. As an example, Hempel et al. [411] realized flexible and sensitive strain sensors by spray coating of graphene flakes on polyethylene terephthalate (PET): the properties such as transparency and electrical conductivity were controlled by the amount of the sprayed solution. Stretchable and soft strain sensors were reported by Muth et al. [398] using embedded 3D printing technique with a viscous nanomaterial ink directly embedded in elastomer films through a deposition nozzle. In other cases, patterned AgNWs percolation networks were transferred to PDMS by filtration method: the AgNWs–PDMS nanocomposites formed highly stretchable and stable electrodes [402,418]. Highly transparent and stretchable strain sensors were also developed by Cai et al. [407] using transparent CNT percolation thin films synthesized by the floating catalyst chemical vapor deposition method; the conductance and optical transparency of the films were controlled by the growth parameters.

The sensibility of this kind of strain sensors is reflected by the **gauge factor GF**, that is the slope of the relative change of the electrical resistance vs the applied strain ε: $GFs = (\Delta R/R_0)/\varepsilon$. Conventional metal-foil based strain gauges possess GFs in the range of 2–5 and semiconductor based strain sensors might bear GFs of 100 or larger [381,411,422]. The CNTs–Ecoflex nanocomposite based resistive-type sensors showed GFs of 1–2.5 by the change of the tunneling resistance upon stretching [423]. AgNWs-PDMS nanocomposite based resistive-type sensors exhibited tunable GFs in the range of 2–14: GFs were controlled by number density of the AgNWs percolation network [381]. Highly sensitive (GFs ≈ 116) resistive-strain sensors have been reported by using ZnONWs-polymer composites [396] (*Figure x.xx(c)*). There are other important features for a resistive-type strain sensor: good linearity of the response, low hysteresis during dynamic load, fast response and recovery time, dynamic durability.

5.1.3 Challenges and aim of the research

Modern electronics research currently aims to overcome several important challenges such as **miniaturization**, **durability**, **cost-effectiveness**, **high performance**. However, most research is focused at developing state-of-the-art devices without a considered **life-cycle assessment**. As the consumer electronics market grows, and the average device lifecycle shrinks, such considerations will become more important to reduce environmental contamination and waste [424]. Then there is the need to avoid the use of synthetic, toxic or not degradable substrates, chemicals and solvents, or to replace them with safe, biocompatible, natural-derived and biodegradable alternatives. Regarding both transparent conductive films and strain sensors, a first sustainable choice can be done in the selection of a suitable flexible substrate. While many of the above-cited examples employed synthetic films such as PET, PEI or PDMS, there are few works that used materials derived from natural polymers as a greener solution. Morfa et al. [425] used cellulose diacetate foils to realize both strain sensors (with Ag interdigitated electrodes) and conductive composites (by blending with carbon black). TCFs were obtained by Jung et al. [426] by physical absorption of MWCNTs in a silk fibroin-cellulose transparent paper, while Xiong et al. [427] blended together cellulose nanocrystals (CNCs), PEI and graphene oxide. A similar transparent conductive composite was realized by Xu et al. [362] through the combination of methylcellulose and AGNWs. In 2018, Nature Electronics published a paper about an implantable biodegradable strain sensor [428]. Considering the manufacturing of the conductive layer on the substrate's surface, printing techniques possess many advantages (as previously mentioned), but probably their main drawback concerns the use of conductive inks. In fact, their formulation is difficult due to the low and selective solubility of CNTs, graphene, NWs and conductive polymers. Moreover, as highlighted in *Section 5.1.1*, the overall process requires many time and reagents consuming steps, from the handling of the conductive nanomaterial's precursors to the post-treatment of the final TCFs. Not less importantly, the use of harmful organic solvents is highly unwelcomed in the perspective of environmental sustainability. Therefore, it would be an appealing strategy to avoid the use of toxic solvents without lose the advantages of printing techniques.

In the present project, TFCs and strain sensors are developed with two sustainable expedients. First, the substrates of choice are made by **cellulose acetate (CA) sheets**, a biopolymer derived from wood pulp and it can be processed to form flexible and transparent fully biodegradable thin films. Its chemical structure can be seen in *Figure 5.1.5*. Secondly, Au nanoparticles are deposited on top of CA films using the **supersonic cluster beam deposition (SCBD) technique** [153,154,250], which can be considered a printing technique that **does not need the use of any solvents**. In fact, gold clusters can be generated in situ from a bulk metallic precursor and then they are

delivered by a carrier gas to the substrate and they deposit on its surface with a strong adhesion. The gas beam seeded with metallic clusters is highly collimated and this makes it possible to pattern the substrate with the use of custom stencil masks. A detailed description of this technique is reported in *Section 1.4*. Its use in the context of TCFs and resistive-type strain sensors leads to many advantages: complete absence of solvents, possibility of patterning with high resolution, high control in conductive layer's thickness, one-step process. So, CA-Au thin composite films are manufactured in the attempt to develop two different smart devices, described right below. The detailed results are reported in the next *Section 5.2*.

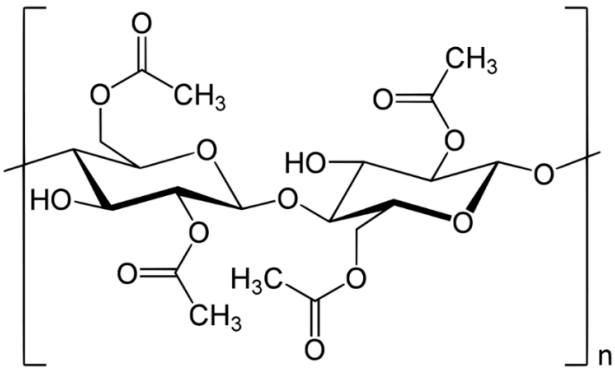

***Figure 5.1.5**. Chemical structure of cellulose acetate (CA) biopolymer.*

(a) SCBD-printed transparent conductive films on cellulose acetate

SCBD technique is used to print cluster-assembled Au layers of different thickness (from 11 to 120 nm) on flexible transparent sheets of biodegradable cellulose acetate. The electric conductivity of the formed Au layer is monitored in situ during the printing process and after the deposition. Different thicknesses are correlated to different values of electrical resistance and transmittance in the UV-Vis spectrum. Their behavior as stable ohmic conductors is tested in a low power electric regime.

(b) Bidirectional resistive-type strain sensor

Au-CA TCFs in a percolation regime are tested as bidirectional strain sensor, by monitoring the variation in their ohmic resistance upon dynamic bending. The relative variation $\Delta R/R_0$ is correlated to both positive and negative bending curvature θ and applied strain ε and the gauge factors were calculated. Their hysteresis, linearity, reversibility and dynamic stability are here studied.

5.2 TRANSPARENT CONDUCTIVE FILMS AND STRAIN SENSORS ON FLEXIBLE CELLULOSE ACETATE

5.2.1 SCBD-printed Au layers on cellulose acetate

Biodegradable, flexible and transparent cellulose acetate (CA) sheets purchased from *Grafix Plastics* were used as the substrates for the printing of thin cluster-assembled gold layers. CA films are characterized by a thickness of 75 μm, a density of 1.32 g/cm^3, an elastic modulus of 2-2.5 GPa and an optical transparency of 90.4%. Moreover, unlike most of CA sheets, the employed plasticizers and additives are derived from natural fats and then they are readily biodegradable. A picture of CA sheets is reported in *Figure 5.2.1*.

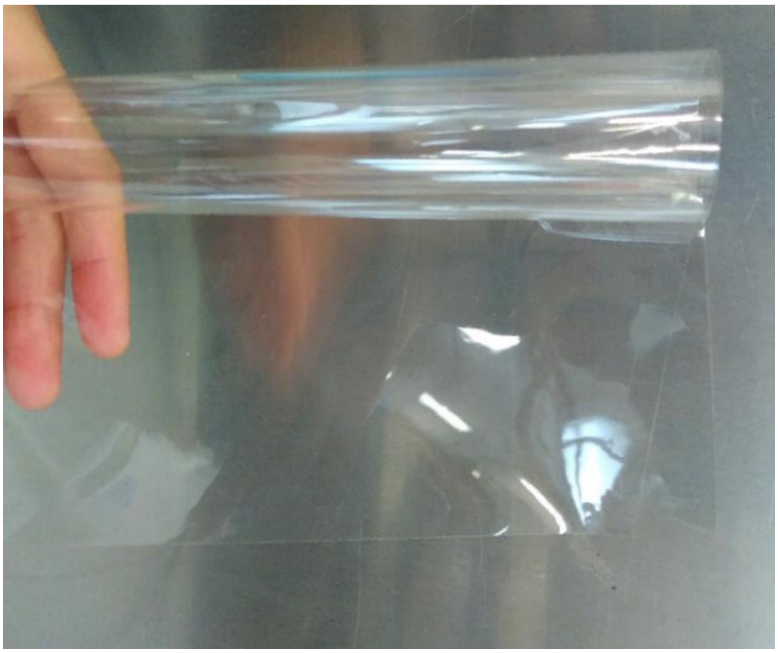

Figure 5.2.1. *Acquired picture of an entire biodegradable, flexible and transparent cellulose acetate sheet.*

Supersonic cluster beam deposition (SCBD) technique was used to deposit Au clusters on the surface of CA films. More specifically, the clusters are generated by a pulsed microplasma source that sputters a metal precursor in an inert gas atmosphere. The gas molecules then follow a pressure gradient and they carry the Au clusters through an aerodynamic focuser and finally to the substrate of choice. With the use of stencil masks to obtain specific patterns, this SCBD can be seen as a printing technique, whose ink is composed by Au clusters dispersed in an inert gas. More detailed information about the operational principles of SCBD are reported in *Section 1.4.* This technique is particularly useful because it allows to control with high precision the amount of deposited material and to obtain metallic layers with a strong adhesion to polymeric substrates, without the use of any solvent. Also, thin cluster-assembled or nanoparticle-based electrodes usually behave differently from bulk metallic electrodes from an electrical point of view and this is the reason for their potential as strain sensors.

Initially, the relationship between the Au equivalent thickness t_{eq} (see *Section 1.4*) deposited on CA samples and the resulting sheet resistance $R_{s,0}$ was investigated. A deposition process was carried out by in-situ measuring the resistance of the growing gold electrode (more experimental details are reported in *Section 6.2.1*) as well as its equivalent thickness.

Figure 5.2.2 shows a graph reporting the evolution of $R_{s,0}$ over time, which was monotonically decreasing, while the graph in *Figure 5.2.3* reports the thickness growth up to a value of 120 nm (equivalent with a mass of 96.5 $\mu g/cm^2$). Its growth rate was quite constant and it was approximated with the linear equation t_{eq} (nm) = 0.173 x t (s), obtaining an average growth rate gr = 0.173 nm/s. Using this approximation, $R_{s,0}$ values have been plotted against t_{eq}, as shown in the graph in *Figure 5.2.4*. The step-like trend shown in the graphs is due to the fact that the cluster beam alternatively hit the quartz microbalance and the target samples. Thanks to this direct correlation, it is possible to tune the resistance of the gold layer on CA sheets according to the amount of deposited Au. It can be seen how for the first 20 nm $R_{s,0}$ changes rapidly and then even a small variation of a couple of nanometers can lead to resistance values very different; instead, when the Au layer becomes thicker, the resistance varies more slowly and then even a difference of 20 or 30 nanometers can affect only slightly the electronic conduction. Such results are in good agreement with the percolation theory that is widely used to explain this kind of phenomena [429].

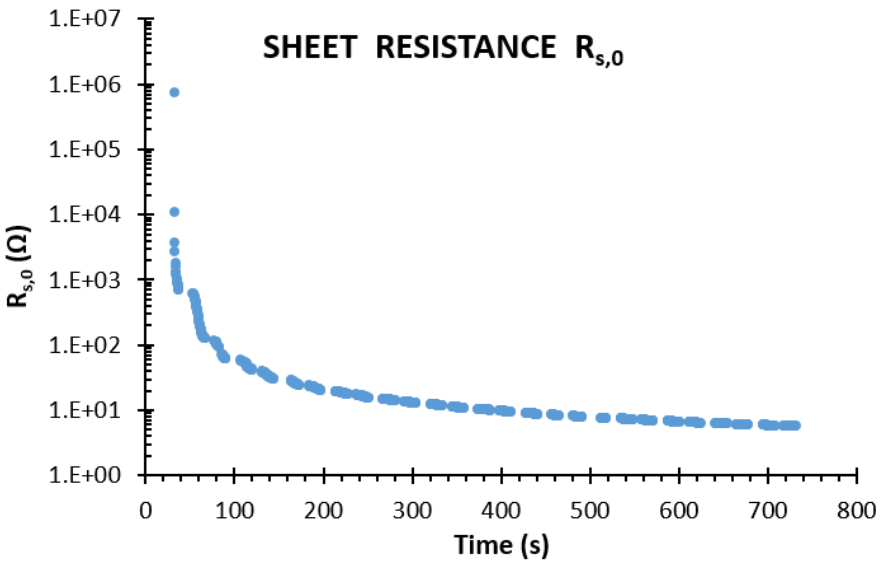

Figure 5.2.2. *Graph reporting the evolution of the original sheet resistance $R_{s,0}$ (logarithmic scale) of the cluster-assembled Au layer deposited on a CA film.*

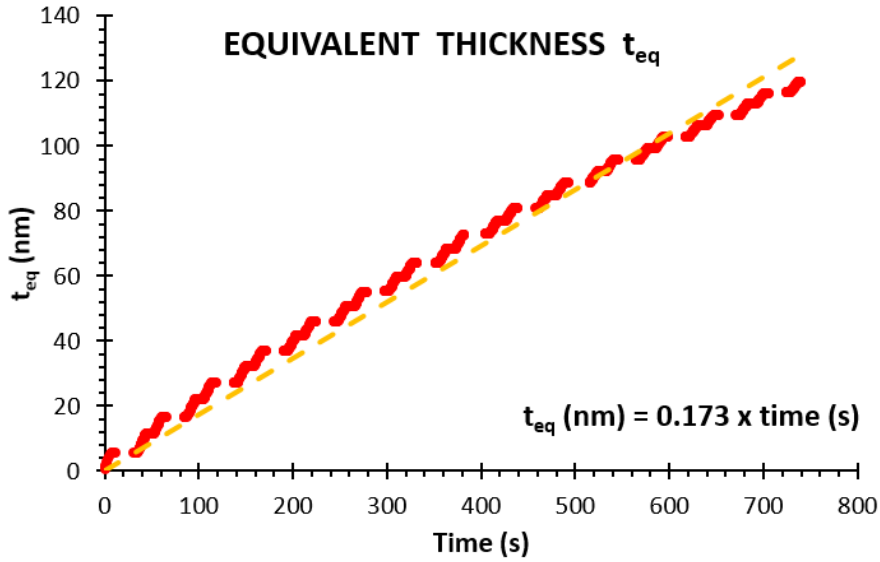

Figure 5.2.3. *Graph reporting the growth over time of the cluster-assembled Au layer (red points) deposited on a CA film. As can be seen, the equivalent thickness t_{eq} increases almost linearly and the linear interpolation is also reported (orange dotted line).*

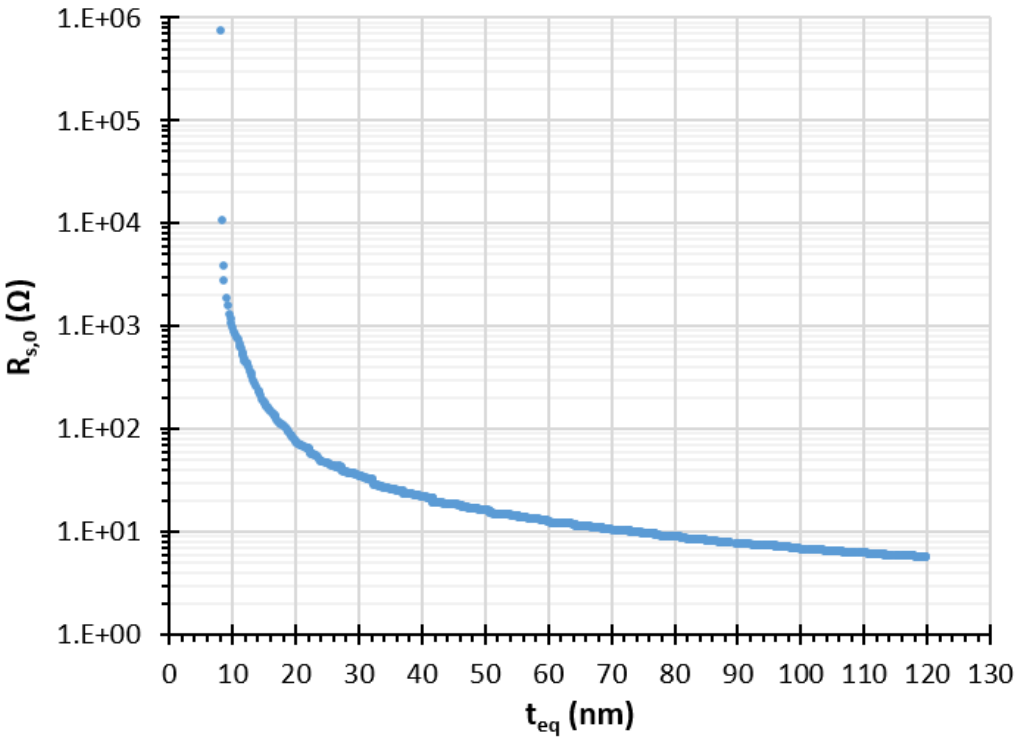

***Figure 5.2.4**. Graph reporting the evolution of the original sheet resistance $R_{s,0}$ (logarithmic scale) against the growing of the cluster-assembled Au layer deposited on a CA film. At the maximum explored thickness of 120 nm, $R_{s,0}$ = 5.7 Ω.*

Then, SCBD was used to print electrodes with different values of thickness and resistance on distinct CA samples: CA11 (Au t_{eq} = 11 nm, $R_{s,0}$ = 678 Ω), CA13 (Au t_{eq} = 13 nm, $R_{s,0}$ = 350 Ω), CA20 (Au t_{eq} = 20 nm, $R_{s,0}$ = 73 Ω), CA35 (Au t_{eq} = 35 nm, $R_{s,0}$ = 26 Ω), CA55 (Au t_{eq} = 55 nm, $R_{s,0}$ = 14.5 Ω), CA85 (Au t_{eq} = 85 nm, $R_{s,0}$ = 8.2 Ω) and CA120 (Au t_{eq} = 120 nm, $R_{s,0}$ = 5.7 Ω). Before the deposition, a couple of conductive pads obtained with the use of silver paste were applied on every CA sample at a distance of 8 mm from each other. The cluster-assembled Au electrodes were then printed as a bridge (8 x 4 mm) between the conductive pads, so that it was possible to check the electronic resistance of the Au layer without directly get in touch with it. A picture of the obtained samples is shown in *Figure 5.2.5*, where it can be partially appreciated the differences in optical transparency.

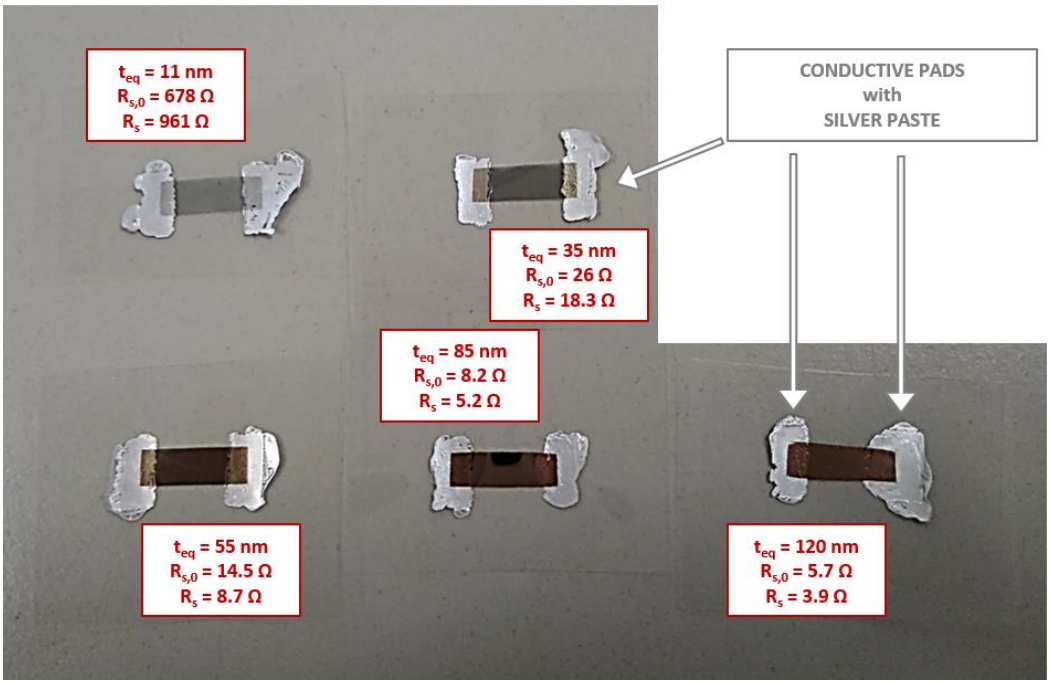

***Figure 5.2.5**. Ca-Au samples. The cellulose acetate sheets were provided with silver paste conductive pads and the SCBD-printed Au layers (of different thickness) as a bridge between the pads.*

By monitoring their resistance after the deposition process, it was observed that $R_{s,0}$ evolved day per day and it took a week to stabilize at a new constant value R_s (in ambient conditions). *Figure 5.2.6* reports the previous $R_{s,0}$ vs t_{eq} graph with the superimposition of the evolved values of R_s. Two different behavior can be noticed, according to the original Au equivalent thickness. All of the samples with $t_{eq} \geq 20$ nm underwent a decrease of $R_{s,0}$ between the 30% and the 40% of its original value; instead, the samples with $t_{eq} \leq 15$ nm underwent an increase of $R_{s,0}$ between the 40% and the 55% of its original value. This behavior can be understood by considering that cluster-assembled Au layers printed with SCBD (in a vacuum atmosphere, with a pressure value of about 1×10^{-5} Torr) are characterized by a high porosity with respect to bulk gold. After the deposition process, when the samples are taken back to ambient conditions at atmospheric pressure, the porous structure tends to slowly become more compact to a certain extent (depending also on the type of substrate on which the layer is in contact with). It appeared that in relatively thick layers ($t_{eq} \geq 20$ nm) the Au clusters slowly get closer and the resulting tighter contact improves the electronic conductivity.

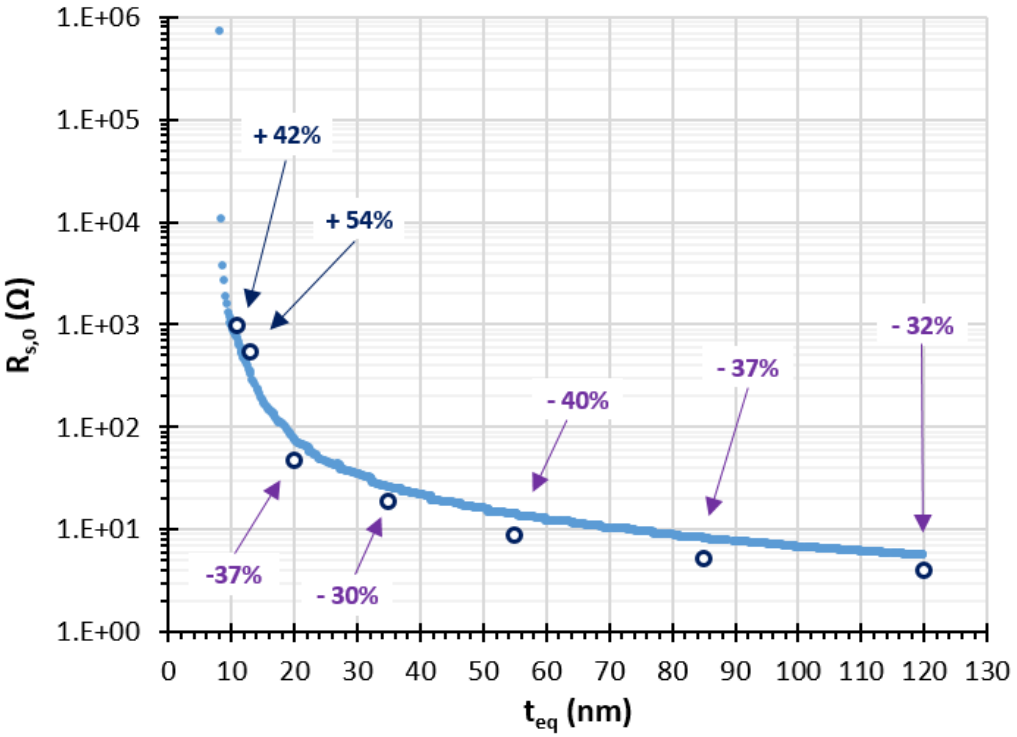

Figure 5.2.6. *$R_{s,0}$ vs T_{eq} curve already shown in Figure 5.2.4, with the superimposition of the evolved sheet resistance values R_s of Ca-Au samples, after a week of monitoring. 20 nm-thick and thicker samples underwent a decrease in the sheet resistance of about the 30-40% of its original value, while samples thinner than 20 nm underwent an R_s increase of the 42% and 54% of the initial value.*

Instead, on the samples with $t_{eq} \leq 15$ nm the coverage degree is considerably lower, as it is proved by the high variation in the $R_{s,0}$ values. Because of this, when at ambient conditions every metallic cluster tends to aggregate with its neighbors, the process leads to the formation of more aggregate islands but to an overall decrease of the electronic paths throughout the Au layer (because the distance between different aggregates becomes higher than the original distance between the single clusters). This is the reason that explains the observed evolution of the sheet resistance of Au layers deposited on CA films with SCBD.

5.2.2 Low-power electrical characterization and optical transparency

One of the objective of this project is the combination of biodegradable CA sheets and printed cluster-assembled Au electrodes to develop self-standing electronic conductors able to stably operate in a low-power regime. To assess the suitability of the obtained CA-Au films to work in this conditions, three of them underwent an electrical characterization at low applied potentials (from 0.5 to 2.0 V). The tested samples are CA13 (Au t_{eq} = 13 nm, R_s = 538 Ω), CA35 (Au t_{eq} = 35 nm, R_s = 18.3 Ω), and CA 55 (Au t_{eq} = 55 nm, R_s = 8.7 Ω). By contacting the couple of silver paste conductive pads to a power supply, the Au layer printed on the CA films acted like a resistive element inside an electric circuit. Each sample was then subjected to cyclic ramps from 0.5 V to 2.0 V and both the electric current i_m and resistance R_m were recorded. More experimental details can be found in *Section 6.2.4*. Of course, since the Au layer geometry is a 4 x 8 mm rectangle, the measured resistance was twice the value of the already checked sheet resistance R_s.

The results of the analysis are reported in the graphs shown in *Figure 5.2.7* (CA13), *Figure 5.2.8* (CA35) and *Figure 5.2.9* (CA55). Looking at the CA13 sample, an average resistance of 1076 Ω was measured and the i vs ΔV curve was linear (*Figure 5.2.7(b)*), as it happens for traditional ohmic conductors. The measured resistance displayed only slight variations according to the applied potential, apparently with no regular trend. Such variations are reported in *Figure 5.2.7(c)*, as ΔR/R (%): their extent is never higher than the 0.15% of the original value and then they can be considered negligible, since they do not affect significantly the current that passes. *Figure 5.2.8* and *Figure 5.2.9* reports the results of the electrical tests carried out on samples CA35 and CA55. The i vs ΔV curves are linear also in this case and the measured average resistances are 36.6 Ω and 17.4 Ω respectively. The ΔR/R variation is always lower than 0.40% but this time it showed to have a more regular trend characterized by an interesting hysteresis. Initially, R_m slightly increases together with the applied potential that passes from 0.5 to 2.0 V. Then, when the applied potential is taken back to 0.5 V, R_m decreases as well but remaining at higher values. This particular behavior should need further investigation to be fully understood. The presence of a small capacitive contribution, due to the cluster-assembled structure of the gold layer or to the Au-Ag contact, can be a possible explanation. In any case, small variations lower than 0.40% do not prevent the ohmic conduction of the tested samples.

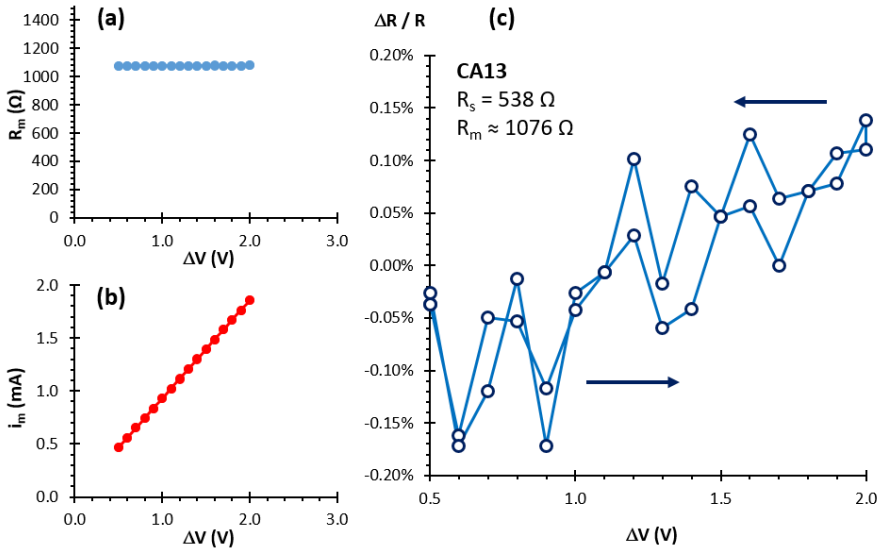

Figure 5.2.7. *Electrical characterization of CA13 (t_{eq} = 13 nm), from 0.5 to 2.0 V.* ***(a)*** *Measured resistance,* ***(b)*** *measured current and* ***(c)*** *ΔR/R (%) against the applied potential.*

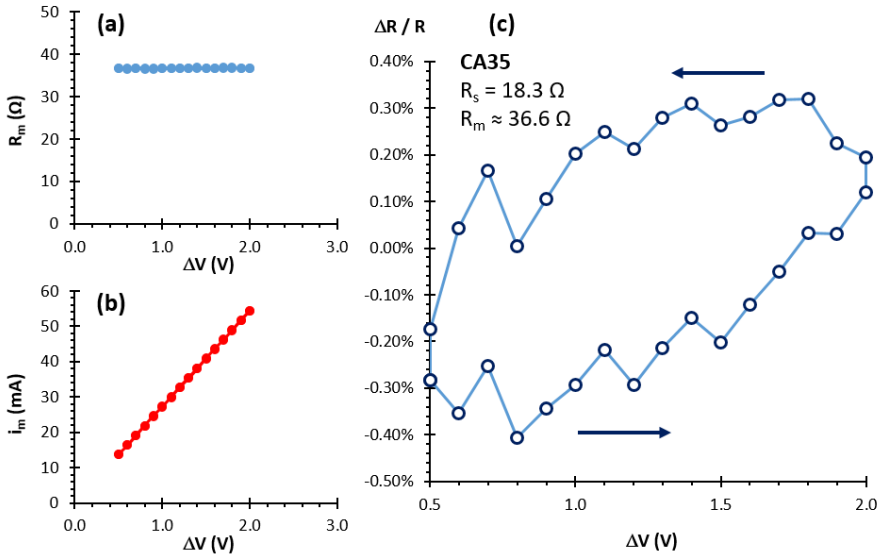

Figure 5.2.8. *Electrical characterization of CA35 (t_{eq} = 35 nm), from 0.5 to 2.0 V.* ***(a)*** *Measured resistance,* ***(b)*** *measured current and* ***(c)*** *ΔR/R (%) against the applied potential.*

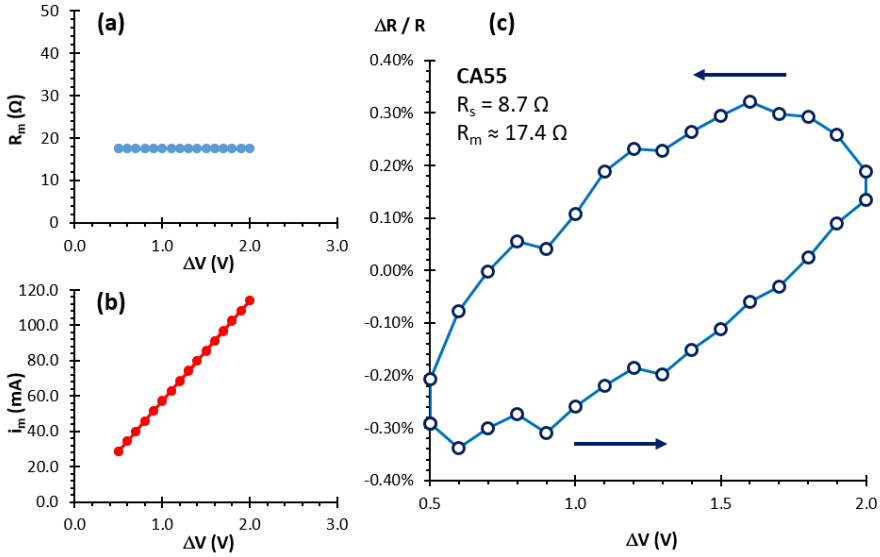

***Figure 5.2.9**. Electrical characterization of CA55 (t_{eq} = 55 nm), from 0.5 to 2.0 V. **(a)** Measured resistance, **(b)** measured current and **(c)** ⊿R/R (%) against the applied potential.*

These results assess the suitability of cluster-assembled Au layers printed with SCBD on cellulose acetate films to stably operate as ohmic conductors in a low power regime, independently from their original thickness or sheet resistance, which is one of the objective of this work. Another aim is to have the Au layer not preventing the optical transparency of cellulose acetate sheets (90.4% according to *Grafix Plastics* data sheets). In fact, transparency in the visible spectrum is a strategic feature for electronics in many applications fields (see *Section 5.1.1*).

Then, the transmittance of the obtained samples with different Au thickness was studied from 350 to 900 nm with the use of a UV-Vis spectrophotometer. T_{av} (%) was calculated as the average transmittance value in the visible spectrum (400-700 nm). The results are reported in the graph in *Figure 5.2.10*. The experimental details are reported in *Section 6.2.5*.

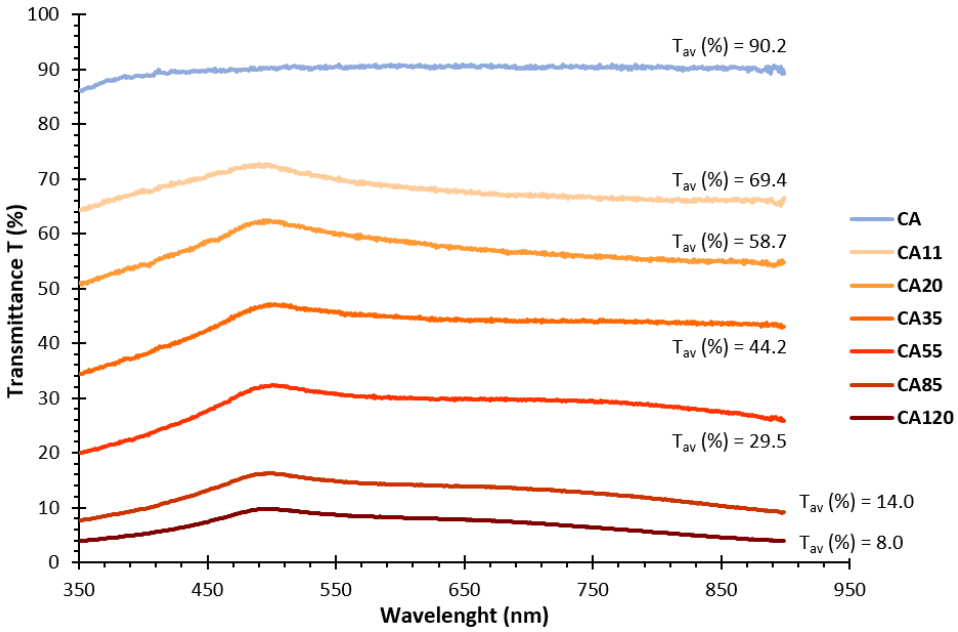

***Figure 5.2.10**. Graph reporting the transmittance (%) in the UV and Vis field of the CA-Au samples with different thickness of the SCBD-printed Au layers. Bare CA sheets have a T_{av} = 90.2% and this value decreases the higher the thickness of the Au layer.*

As it can be seen, bare CA samples has a value of T_{av} equal to 90.2% in good agreement with the value reported in *Grafix Plastics* data sheets. Then the transmittance decreases monotonically with the thickness of the Au layer. The samples with the thicker Au layers (85 and 120 nm) showed to have a poor transmittance in the visible range (T_{av} equal to 14.0% and 8.0%). Instead, CA films with the thinner Au layers (11 and 20 nm) showed a consistent optical transparency: T_{av} is almost the 70% and to 60%, suitable values to be employed in the field of transparent electronics. *Figure 5.2.11(a)* reports the values of T_{av} against the equivalent thickness of the Au layer. It can be seen an exponential trend and because of this Log(T_{av}) as well as the Log(R_s) were plotted against t_{eq} in *Figure 5.2.11(b)*. The values of Log(T_{av}) can be well interpolated by a straight line, confirming that the optical transmittance of the metallic layers has a logarithmic dependence on the Au equivalent thickness. With these tests, it was found a clear correlation between 1) the equivalent thickness of the Au layer printed with SCBD on cellulose acetate sheets, 2) its electrical resistance and 3) the optical transparency of the CA-Au composite films. A summary table is reported in *Figure 5.2.12*. Also, it was checked their low-power operational stability by testing their electronic conduction and ohmic behavior at low applied potentials (≤ 2V). Thanks to this knowledge, it is now possible to couple natural-derived and biodegradable cellulose acetate films with

printed cluster-assembled Au electrodes for the development of self-standing, flexible and stable electronic conductors whose ohmic resistance and optical transparency can be finely and easily tuned. The manufacturing relies on a one-step process that does not involve the use of any solvent.

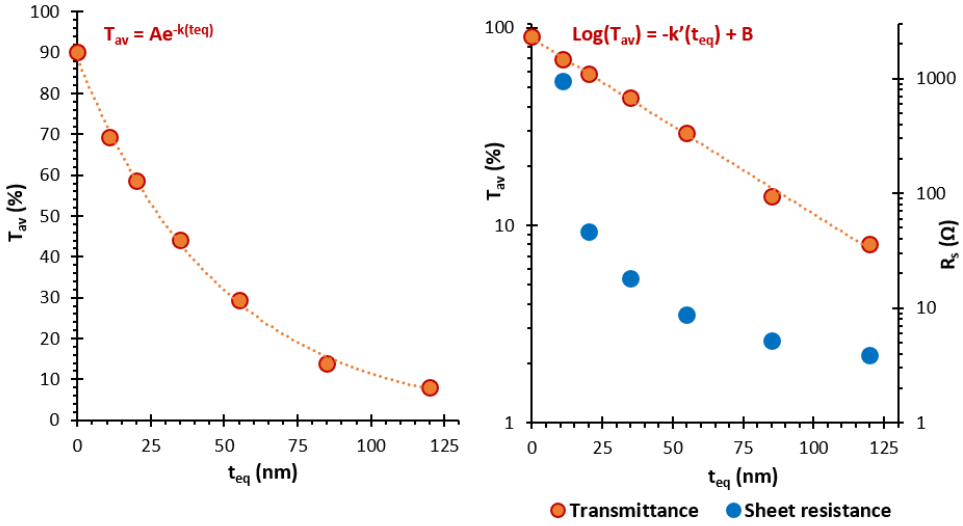

***Figure 5.2.11**. **(a)** T_{av} in the visible spectrum of the CA-Au samples against the Au equivalent thickness. It can be seen an exponential trend. **(b)** T_{av} in the visible spectrum and Rs of the CA-Au samples (both in the logarithmic scale) against the Au equivalent thickness.*

	Au t_{eq} (nm)	Au m (μg/cm²)	Au m (%)	$R_{s,0}$ (Ω)	R_s (Ω)	T_{av} (%)
CA11	11	8.8	0.09	678	961	69.4
CA13	13	10.5	0.11	350	538	68.9
CA20	20	16.1	0.16	73	46	58.7
CA35	35	28.1	0.28	26	18.3	44.2
CA55	55	44.2	0.44	14.5	8.7	29.5
CA85	85	68.4	0.69	8.2	5.2	14.0
CA120	120	96.5	0.97	5.7	3.9	8.0

***Figure 5.2.12**. Summary table for Ca-Au samples. The reported data are the Au equivalent thickness t_{eq}, the Au mass per square centimeter, the Au mass percentage m% compared to the mass to the overall Ca-Au composites, the original sheet resistance $R_{s,0}$ measured during the SCBD printing process, the evolved sheet resistance R_s measured after a week and the average transmittance in the Vis spectrum T_{av}.*

5.2.3 Bidirectional resistive-type low-strain sensors

When the surface of a flexible/stretchable material is only partially covered by metallic nanoparticles (percolation regime), only a finite number of electronic paths exists between them and the electronic resistance is quite high (10^3-10^8 Ω). If the material's surface is subjected to a mechanical strain, the average inter-particle distance increases and the electronic paths reduces, leading to an overall decrease in the sheet conductivity. This correlation between mechanical strain and electronic conductance can be exploited for the development of resistive-type strain sensors, extremely useful tools in soft robotics, wearable electronics and smart integrated systems (see *Section 5.1.2*).

Cellulose acetate sheets are flexible films that can be bent and undergo a surface strain. Among the stably conductive and transparent Au-CA composite films obtained, CA11 (Au t_{eq} = 11 nm, R_s = 961 Ω) is the most promising to be tested as a strain sensor. In fact, by looking at the curve previously reported in *Figure 5.2.6*, it can be seen how with this amount of Au, the conductive layer is still in a percolation regime. Because of this, CA11 samples were used to study how its electronic resistance varies according to an imposed curvature/strain.

Figure 5.2.13 reports a schematic illustration of the tested relationship between bending, strain and measured ohmic resistance. Experimentally, the Au-CA film (conductive area equal to 4 mm x 8 mm) was fixed in the central region of a larger cellulose acetate sheets with a total length L of 40 mm. While one end of the sheet was fixed, the other end was moved towards by a distance ΔL with the help of a linear translator, inducing a certain curvature to the platform. Since the Au layer was placed on the convex side, it underwent a positive curvature (characterized by a curvature angle θ) as well as a positive strain ε and the inter-particle distance increased. According to the known values of ΔL, the corresponding values of θ and ε were calculated with a geometrical approximation. CA11 samples underwent three bending cycles up to three different positive values of θ: + 20°, + 36° and + 57°, by moving the linear translator with a speed of 0.1 mm/s.

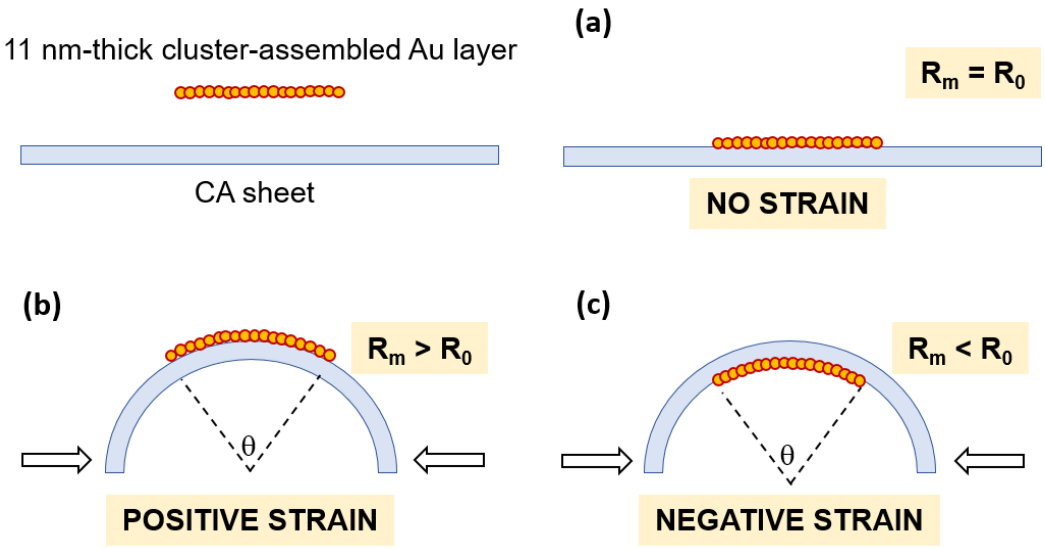

Figure 5.2.13. *Schematic illustration of relationship between bending, strain and ohmic resistance, regarding the CA11 sample.* ***(a)*** *CA sheet is flat, no strain affected it and the measured ohmic resistance has a constant value* R_0. ***(b)*** *With the linear translator, a bending is induced to CA11: the Au layer on the convex side undergoes a positive strain and the measured resistance is expected to increase.* ***(c)*** *When the Au layer in situated on the concave side of the bent CA sheet, it undergoes a "negative" strain and the measured resistance is expected to decrease.*

More detailed information can be found in *Section 6.2.4*. Then, the experimental procedure was repeated with the Au-layer placed on the concave side of the platform, meaning that in this condition the film bending should induce a negative curvature and decrease the inter-particle distance. The ohmic resistance was measured in the same way. The graph reported in *Figure 5.2.14* shows the values of R_m (Ω) as a function of time over the bending cycles (R_m values obtained at negative curvature angles are reported against negative values of time).

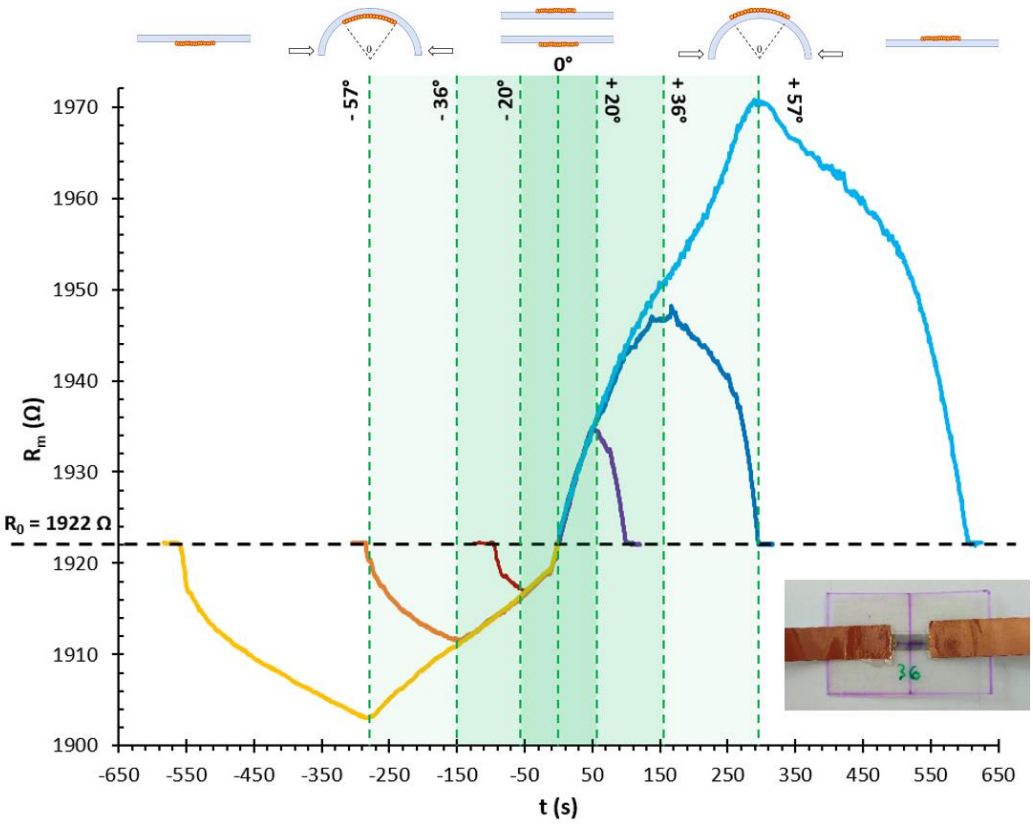

***Figure 5.2.14**. Graph reporting the ohmic resistance over time of CA11 samples while they underwent bending cycles of different entities, up to curvature angles θ of 20°, 36° and 57°. Under a positive curvature (Au layer on the convex side of the bending CA sheet) the measured initial resistance R_0 = 1922 Ω increased up to a value of 1970 Ω; under a negative curvature (Au layer on the concave side) the measured resistance decreased down to 1903 Ω (these R values are plotted against negatives values of time). In the lower right corner of the figure, a photograph of a tested sample is reported.*

Here's a list of the main observations that can be done by looking at the obtained results:

- R_m at the rest state with no applied strain ($\theta = 0°$) has a value $R_0 = 1922\ \Omega$, perfectly in line with the sheet resistance R_s and the Au layer geometry of CA11.
- R_m increases monotonically under the application of positive θ, while it monotonically decreases for negative θ.
- R_m variation are only approximately linear.
- When the absolute value of θ is reduced and the strain decreases, R_m returns to its original value in all cases, even if the return curve is not perfectly symmetrical with the outward one.
- The variation of R_m at positive values of θ is more pronounced than R_m variations at negative values of θ.
- The maximum value of R_m is 1970 Ω at $\theta = + 57°$, while the minimum value of R_m is 1903 Ω at $\theta = - 57°$. The overall maximum variation is of 67 Ω, the 3.5% of the original resistance.

In order to better evaluate the relative variation of the resistance as well as the difference between the outward and the return curves, $(R_m-R)/R = \Delta R/R$ values were plotted against the values of the curvature angle θ as well as the values of the relative linear displacement $\Delta L/L$. The results are reported in *Figure 5.2.15*; also in this case, the data obtained with the application of negative curvature angles are plotted against negative values of the abscissa. The maximum resistance variations were the +2.53% and -0.99% of the original resistance value. It is also more evident that the returning curves are not superimposed on the outward ones and slight hysteresis is noticed. This can be done to an intrinsic property of the CA-Au composites, but also to the fact that by moving back and forth the linear translator, the induced curvature of the film does not follow exactly the same variation in time. From *Figure 5.2.15(b)* it can be seen that $\Delta R/R$ has an almost linear dependence on the curvature angle θ, a really important features for application as a bidirectional strain sensor: with a simple linear correlation it is possible to associate a variation in the ohmic resistance to a precise curvature of the CA-Au film, both negative or positive.

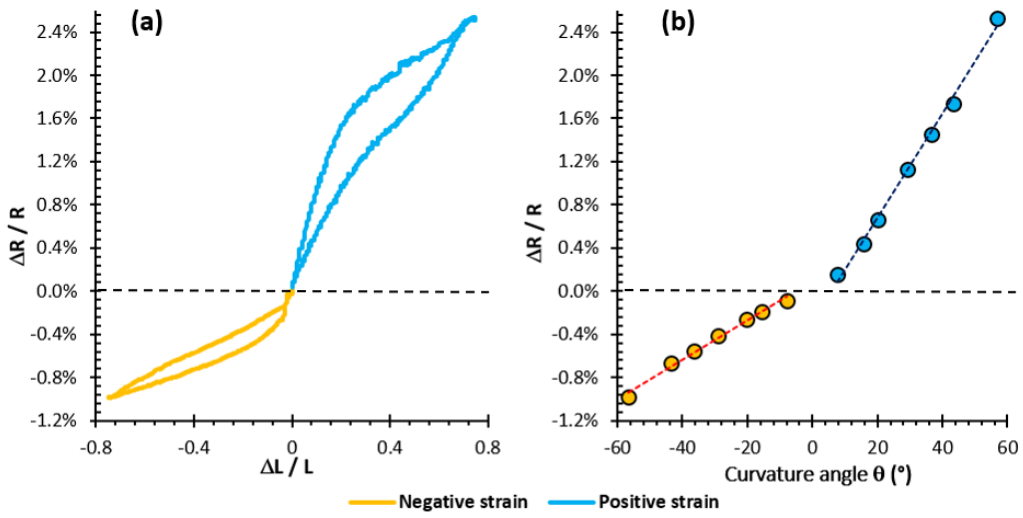

***Figure 5.2.15**. Graphs reporting the percentage variation of the measured resistance ΔR/R (%) values against **(a)** the relative displacement of the linear translator ΔL/L and **(b)** the curvature angle θ. ΔR/R values obtained positive at curvatures are plotted against positive values of the abscissa, while the values obtained at negative curvatures are plotted against negative values of the abscissa.*

A similar linearity can be seen in *Figure 5.2.16*, where ΔR/R is plotted against the values of the mechanical strain ε. In this case, the angular coefficient of the linear interpolation represents the dimensionless gauge factor GF, the most used indicator to express the sensitivity of strain sensors based on variation in the ohmic resistance. In this case, it was found a gauge factor $GF_+ = 5.91$ for positive strains and a factor $GF_- = 2.21$ for negative strains. In a recent work of Xie et al. [430], the authors realized strain sensors by depositing different amounts of Palladium nanoparticles on a flexible polyethylene terephthalate (PET) sheets: the original resistance of the samples are 58 kΩ, 535 kΩ and 9.6 MΩ and at low strains they were characterized by gauge factors GF_+ of 1.42, 36.9 and 51.0, respectively. From these results it clearly appeared how it's possible to achieve high gauge factors by increasing the initial ohmic resistance. In the current work, by printing cluster-assembled Au layers with an original $R_s = 0.96$ kΩ with cellulose acetate sheets, it was possible to obtain a bidirectional strain sensor a $GF_+ = 5.91$ and a $GF_- = 2.21$. Considering that its initial resistance is much lower compared to the samples realized by Xie et al., the adopted strategy turns out to be very promising for the development of strain sensors with an even lower amount of deposited Au clusters, leasing to higher values of initial resistance and likely to better values of the gauge factors.

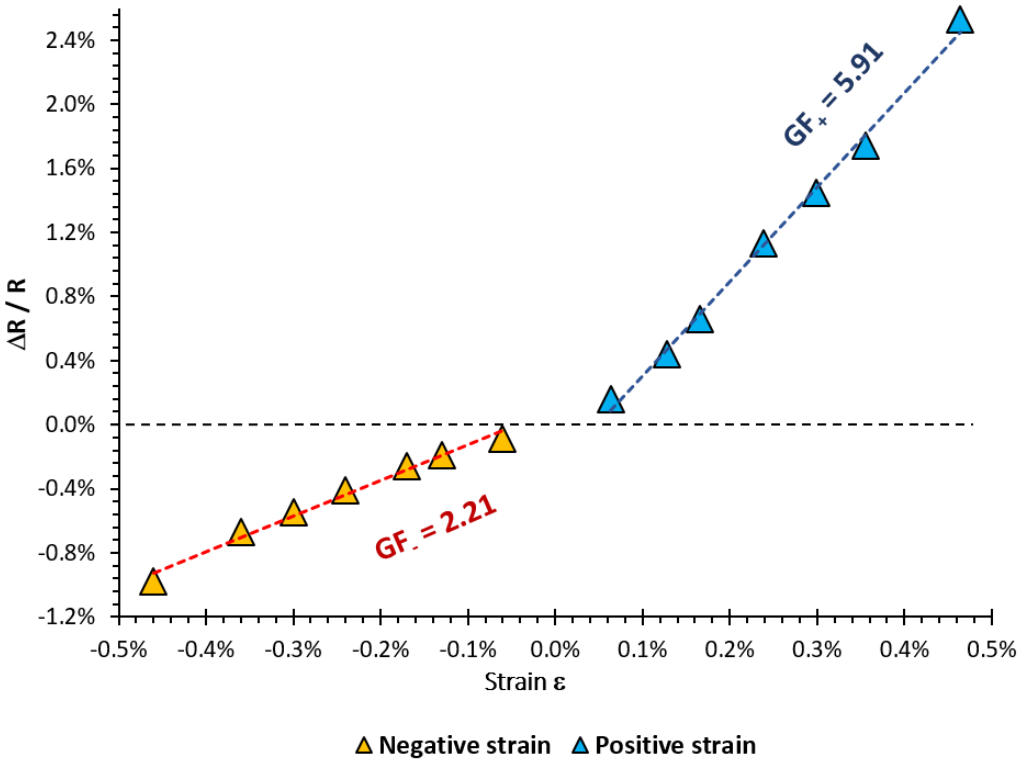

Figure 5.2.16. *Graph reporting the percentage variation of the measured resistance ΔR/R (%) values against the calculated strain ε (%) for both positive and negative curvatures. The obtained data are well interpolated by straight lines and their angular coefficient are the corresponding gauge factors GF.*

Lastly, the samples underwent cyclic bending (both positive and negative) up to 100 cycles to study their stability in time. The results are reported in the graph in *Figure 5.2.17*, more in particular the values of ΔR/R are reported for the 1st, 25th, 50th and 100th cycle when the strain is both zero and maximum (± 0.46%). It can be seen that the amplitude ΔR/R variation remains substantially constant, while instead there is an overall Increase in the resistance of about the 0.5% for negative strains and 1.5% for positive strains. This increase can be due to one or more of three different causes: a) an intrinsic properties of Au clusters deposited on CA sheets; b) the contact between the silver paste conductive pads and the Au layer gradually damages over bending cycles; c) a similar gradual damaging of the contact between the silver pads and the wires connected to the instrumentation. Among these hypothesis, I think that the last two are the most probable and because of this new tests will be carried out trying to improve the quality of the electric contacts.

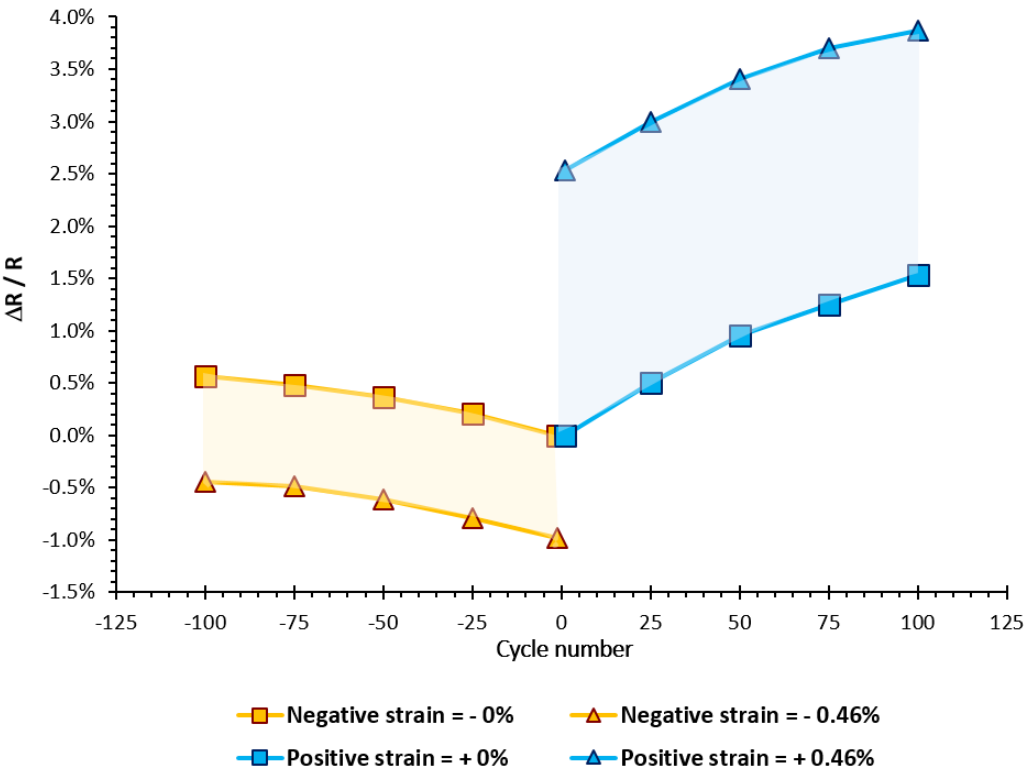

Figure 5.2.17. *Graph reporting the percentage variation of the measured resistance ΔR/R (%) values against the number of bending cycles (up to 100) for both positive strains (positive values of the abscissa) and negative ones (negative values of the abscissa). The square marks represent those points when the strain was 0.00%, while the triangular marks represent the points when the strain was equal to ± 0.46%.*

With these tests it was then assessed that the one-step solvent-free SCBD-printing of cluster-assembled thin Au layer on the surface of cellulose acetate sheets is a suitable strategy for the development of bidirectional resistive-type low-strain sensors characterized by lightness (9.9 mg/cm^2), electrical stability up to an applied potential of 2V, optical transparency (almost 70%), gauge factor like GF_+ = 5.91 and GF_- = 2.21 for strains up to ± 0.46% and composed by natural-derived and biodegradable matter for the 99.91% of their mass. By further increasing the initial ohmic resistance and by improving the quality of the interconnections and the experimental setup, this method will be used to realize strain sensors even more sensitive.

6.
Experimental Procedures and Methods

6.1 HYDROGELS AND IONOGELS

6.1.1 Synthesis and thickness measurement

(a) Poly(HEMA-co-AN-co-VBS) – CNCs electroactive hydrogels

The following experimental description refers to the synthesis of the electroactive hydrogels presented in *Section 2.2* of the current work. Na-4-vinylbenezesulfonate (Na-4-VBS), 2-hydroxymethylmethacrylate (HEMA), acrylonitrile (AN), ethylene glycol dimethacrylate (EGDMA), tetramethylethylenediamine (TEMED), 2,2-dimethoxy-2-phenylacetophenone (DMPA) and dimethyl sulfoxide (DMSO) were all purchased from Sigma-Aldrich.

Cellulose nanocrystals (CNCs) mother solutions was provided by the group of Prof. Mauro Comes Franchini from the Department of Industrial Chemistry, University of Bologna. CNCs were prepared according to a reported procedure, with slight modifications [192]. Briefly, 1.5 g of filter paper Whatmann n°2 was finely cut, then 15 mL of a solution of H_2SO_4 (50% v/v) in water precooled at 5-10 °C with an ice bath was added drop-wise. The mixture was magnetically stirred to ensure wetting of all the paper stripes while maintaining the ice bath, then the temperature was increased at 45 °C. The mixture was left to react under stirring for 2 hours. Hydrolysis reaction was then stopped by diluting the reaction mixture with 60 mL of cold water. The resulting solution was centrifuged (6000 rpm, 15 min) to collect CNCs that were then washed two times with water. Finally, CNCs were re-suspended in 30 mL of water and dialyzed till neutral pH (1-2 days). CNCs were characterized by Dynamic light scattering (DLS). Measurements were performed on a Malvern Zetasizernano-S working with a 532 nm laser beam. ζ potential measurements were conducted in DTS1060C-Clear disposable zeta cells at 25°C. For morphological characterization SEM images were acquired with a SEM Zeiss mod. EVO 50' EP. The concentration of the final solution was determined to be of 13 mg/mL, by drying for two days at 110 °C a fixed amount of solution and weighting the residual organic material.

The poly(HEMA-AN-VBS)-CNC composite hydrogels were fabricated as follows. Na-4-VBS (103.1 mg) powder was weighed, dissolved in pure water (MilliQ type) inside a test tube and a certain amount of the CNCs mother solution was subsequently added (the exact amount is reported in the table in *Figure 6.1.1*). Then, HEMA (788.4 μL), AN (196.5 μL), the cross-linker EGDMA (19.2 μL), the reaction catalyst TEMED (22.4 μL) and the initiation solution (15% w/w DMPA dissolved in DMSO, 30 μL) were sequentially added and the resulting mixture was injected into a molding apparatus composed by two glass slides sandwiching a silicone hollow spacer. After exposing the molding system to UV light for 45 minutes at a fixed distance of 10 cm (the UV apparatus was a UVLS-24 EL series lamp from UVP, provided with a 4 W light bulb, λ = 365 nm), the hydrogels were formed and subsequently peeled off the supporting glass after demolding. According to the thickness of the spacers employed, it was possible to achieve freestanding layers of the composite materials with thicknesses of 100 μm and 50 μm in their relaxed state straight after synthesis. Prior characterization, the samples were soaked in pure water for 24 hours in order to wash any residual unreacted compound. The thickness of the as-prepared hydrogels was equal to the spacer's one. Their thickness in the swollen state was checked with a transmittance microscope, by looking at the cross-section of the samples immersed in the aqueous solution of interest.

	CNCs relative mass (%)	CNCs concentration in the final solution (mg/mL)	Employed volume of the CNCs mother solution (μL)	Employed volume of pure water (mL)
CNC0	0	0	0.0	1302.0
CNC0.1%	0.10	0.5	90.8	1211.2
CNC0.4%	0.42	2.0	363.0	939.0
CNC0.8%	0.83	4.0	726.0	576.0
CNC1.4%	1.44	7.0	1270.4	31.8

***Figure 6.1.1**. Table reporting the employed amounts of the pure water and the CNCs mother solution, according to the final desired nanocrystals concentration.*

(b) Cellulose-based electroactive hydrogels

The following experimental description refers to the synthesis of the electroactive hydrogels presented in *Section 2.3* of the current work. Na-carboxymethylcellulose (Na-CMC, average MW ~ 250000, degree of substitution 1.2), 2-hydroxyethylcellulose (HEC, average MW ~ 250000), polyethylenimine (PEI, branched, average MW ~ 25000, average Mn ~ 10000) and N-(3-dimethylaminopropyl)-N'-ethylcarbodiimide hydrochloride (EDC.HCl) were all purchased from Sigma-Aldrich.

Thin films of cellulose-based EAHs were prepared with the following procedure. 200 mg of Na-CMC were dissolved in 11 mL of pure water, at room temperature, under stirring and by small additions. After 1 hour 150 mg of HEC were added in the same conditions and the solution was left under stirring overnight. Then 1 mL of a solution of PEI 40 mg/mL was added, as well as 1 mL of a solution of EDC.HCl 80 mg/mL. After 1 hour the mixture was injected inside an open mold composed by a thick glass slide and a silicon frame (4x5 cm^2, thickness of about 0.5 mm). Water was then removed by keeping the mold under moderate vacuum for 48 hours and then it was put in oven at 70 degrees for 6 hours (to trigger the polycondensation reaction). The obtained cross-linked thin films were then physically removed from the glass, weighed and washed in pure water in order to remove any unreacted species.

The thickness of the as-prepared hydrogels was equal to the spacer's one. Their thickness in the swollen state was checked with a transmittance microscope, by looking at the cross-section of the samples immersed in the aqueous solution of interest.

(c) Paper/ionogel hybrid composites

The following experimental description refers to the synthesis of the electroactive composite materials presented in *Section 3.2* of the current work. Standard white paper for inkjet printing (Favini A6, 55 g/m^2) was employed as a foldable backbone substrate. Acrylic acid (AA), acrylonitrile (AN), ethylene glycol dimethacrylate (EGDMA), tetramethylethylenediamine (TEMED), 2,2-dimethoxy-2-phenylacetophenone (DMPA) and dimethyl sulfoxide (DMSO), tetraethylammonium fluoride (TEAF), halloysite nanoclays (HNC, kaolin clay, MW = 294.19 g/mol) and poly(vinylpyrrolidone) (PVP) were all purchased from Sigma-Aldrich. 1-ethyl-3-methylimidazolium tetrafluoroborate ($EMIM(BF_4)$) was purchased from Iolitec.

Paper/ionogel hybrid composites were obtained by using standard white paper as a foldable backbone for the photopolymerization of an acrylic-based ionogel. The polymerizing mixture was prepared as follows. A 2 mL solution of deionized water and EMIM(BF_4) (7:3 v/v) was prepared in a 5 ml glass tube and then, after stirring for one hour, 80 mg of TEAF were added. The mixture was subsequently stirred for 3 hours. A solution of 2.2 mL containing AA and AN (4.2:1 v/v) was prepared in a separate glass tube and stirred for 30 minutes. Then, 1.98 mL of this mixture was added to the EMIM(BF_4)/H_2O solution, and 58.4 μL of EGDMA were then injected. After stirring for one hour, PVP was added and dissolved in the solution using a magnetic stirrer for 30 minutes. HNC (92.2 mg) were subsequently dispersed into the mixture that was then kept under stirring overnight. In the end, 90 μl of the initiator solution (15% w/w DMPA in DMSO) were also added.

Paper sheets were cut into 40 x 15 mm^2 pieces by using a scissor and soaked into the polymerizing mixture (3.5 mL) for two hours using a sealed glass container. In this phase, a mild stirring of the solution was kept (150 rpm) to facilitate the absorption of the liquid by the paper. After this operation, the sheets were taken out of the mixture and carefully dried by non-abrasive optical paper (Ross Optical Lens Tissue). UV photo-crosslinking of the imbibed ionogel was obtained by exposing the impregnated sheets to 365 nm wavelength radiation for 30 minutes (the equipment used was a UVLS-24 EL series lamp from UVP, provided with a 4 W light bulb). Samples were then stored and dried overnight under vacuum in order to ensure water traces removal. The pre-polymerizing solution was also employed to synthesize thin films of ionogel without the coupling with the paper backbone, by injection into a silicon spacer on a glass slide and UV irradiation.

(d) PHB-IL ionogels

The following experimental description refers to the synthesis of the electroactive ionogels presented in *Section 3.3* of the current work. Poly(3-hydroxybutyrrate) powder was provided by the Italian company Bio-on. 1-buthyl-3-methylimidazolium bis(trifluoromethylsulfonyl)imide (BMIM(Tf_2N)) was purchased from Iolitec. Tetrabuthylammonium fluoride (TBAF) was purchased from Sigma-Aldrich. Glacial acetic acid was purchased from Riedel-de Haen.

To synthesize ionogels based on PHB, an ionic mixture was prepared by dissolving TBAF (6.9% w/w, equal to a concentration of 0.375 M) in BMIM(Tf2N) and keeping it under magnetic stirring for 24 hours. PHB powder was dissolved in acetic acid (50 mg/mL) preheated at 110°C with the help an oil bath and a heating plate. After 8 minutes of magnetic stirring, the ionic mixture was added (40 μL/mL of acetic acid) and the stirring was kept for other 7 minutes. Then, the solution was poured into a preheated aluminum mold over a surface area of 70 x 25 mm^2 and casted in an oven at 105°C. After 30 minutes, a solid film formed, with thickness varying from ca. 50 to 200 μm, depending on the amount of solution poured (from 1 to 5 mL). The obtained samples were kept in vacuum for at least 16 hours to remove any residual of acetic acid. The ionogels thickness was checked by looking at their cross-section with a reflection microscope.

(e) Cellulose-based ionogels with biodegradable ionic liquids

The following experimental description refers to the synthesis of the natural-derived ionogels presented in *Section 4.2* of the current work. 2-hydroxyethylcellulose (HEC, MW_{av} = 3.8 x 10^5 g/mol) and Na-carboxymethylcellulose (Na-CMC, MW_{av} = 2.5 x 10^5 g/mol, degree of substitution = 1.2) were purchased from Sigma-Aldrich. Cellulose nanocrystals (CNCs, diameter from 4-10 nm, length from 100 to 500 nm) were purchased from Guilin Qihong Technology. The ionic liquids choline aspirin (CholAsp) and choline lactate (CholLact) were kindly provided by Kaija Pohako-Esko, Ph.D. from the Institute of Technology, University of Tartu. The employed 75 μm-thick biodegradable cellulose acetate (CA) sheets were purchased from Grafix Plastics.

To fabricate thin self-standing ionogels, water-based solutions were obtained by dissolving a cellulose derivative and an ionic liquid in distilled water. In all the cases, the concentration of the cellulose derivative was kept constant at a value of 25 mg/mL. The amounts of the ionic liquid were selected accordingly the corresponding mass ratio reported in the table in *Figure 4.2.5* of *Section 4.2.1*. Practically, the correct amount of ionic liquid was weighed inside a round bottom flask. The corresponding volume of water was added and the solution was stirred for about 10 minutes. Then, the correct amount of the cellulose derivative was weighed and gradually added to the solution under magnetic stirring. After at least 1 hour of stirring, about 0.75 mL of solution were injected inside a 1.5 x 1.5 cm^2 silicon frame on a glass slide. The samples with HEC were then dried in oven at 80°, while the others were let dry in ambient conditions. Thin self-standing ionogel (from 60 μm to 200 μm) were then obtained and peeled of the glass. The ionogels thickness was checked by looking at their cross-section with a reflection microscope.

Cellulose-based ionogels were also deposited with a spray-casting technique on the surface of CA sheets (*Section 4.2.5*). The liquid solutions were poured inside the cup of a standard airbrush (shown in *Figure 6.1.2*) connected to a nitrogen line at a pressure of 2 bar. Initially the opening time of the nozzle was manually controlled, as well as the distance between the nozzle and the substrate (15 cm). A step-by-step process was carried out with every step consisting in 20 seconds of spray and 40 seconds of waiting, by keeping a constant distance. Stencil masks were employed to confer specific shapes and dimensions to the deposited ionogels. Then, an automated process was designed and employed by mounting the airbrush in place of the extruder of a WASP PowerWASP EVO (FFF - multifunction) 3D printer (category: FFF Cartesian, Single Bowden Extruder, Non-heated bed, Open chamber). The overall apparatus was already shown in *Figure 4.2.23(a)*. A dedicated software allowed to accurately control the relative position and motion of the nozzle with respect to the substrate.

Figure 6.1.2. *The standard airbrush employed for the spray-casting process employed to deposit ultrathin cellulose-based ionogels on cellulose acetate sheets (as it is reported in Section 4.2).*

6.1.2 Swelling and humidity absorption

(a) Swelling of hydrogels

The hydrogels swelling equilibrium was evaluated in pure water and in aqueous solutions with different NaCl concentrations: Solution A (NaCl 0.005 M), Solution B (NaCl 0.020 M), Solution C (NaCl 0.035 M), Solution D (NaCl 0.050 M), Solution E (NaCl 0.100 M), Solution F (NaCl 0.25 M), Solution G (NaCl 0.4 M) and Solution H (NaCl 0.5 M). They were easily prepared by dissolving in pure water the correct amount of NaCl powder. 100 μm-thick poly(HEMA-co-AN-co-VBS)-CNCs hydrogels (*Section 2.2*), as well as the cellulose-based hydrogels (*Section 2.3*), were weighed two times: right after synthesis (m_0) and after being immersed for 24 hours in one of the NaCl aqueous solutions or in pure water (m_f). The swelling ratio S_r was calculated as the ratio between m_f and m_0 for each value of NaCl concentration. The tests were repeated after 48 hours of immersion and the results did not change. All the obtained values were calculated as an average on at least four different samples of the same kind.

(b) Ionogels humidity absorption

The humidity absorption of the ionogels obtained with PHB (*Section 3.2*) and with cellulose derivatives (*Section 3.3*) was checked in ambient conditions, by weighing the samples right after a vacuum treatment and after 6, 24 and 48 hours passed in ambient conditions. The humidity absorption was estimate by calculating the ratio between the weight variation Δm_{HA} (due to the humidity absorption itself) and the original mass. Since the ionogels obtained with PHB showed to absorb no humidity in ambient conditions, the same experiment was repeated inside an incubator (Galaxy S, RSBiotech) at 37°C with a humidity level of the 95% and they also spent a full foggy night in open air (temperature of about 0°, relative humidity higher than 80%). All the obtained values were calculated as an average on at least four different samples of the same kind.

6.1.3 Mechanical tests

Mechanical tensile tests were carried out on 140 μm-thick poly(HEMA-co-AN-co-VBS)-CNCs hydrogels (just swollen in Solution A: NaCl 0.005 M in pure water) (*Section 2.2*) as well as 200 μm-thick PHB-IL ionogels (*Section 3.3*). In both cases, the samples were cut in a traditional dog-bone shape, having a central region with length L = 35 mm and width w = 4 mm. The cross-section area A was equal to 0.56 mm^2 for the hydrogels and to 0.80 mm^2 for the ionogels. A 10 N load cell (Sauter FH- 10) was used for the force measure. This was mounted on an automated vertical test stand (Sauter TVNM) and both components were provided with metallic clamps. The hardness of such clamps was reduced by fixing soft silicon films on their inner side: in this way, the soft hydrogels and ionogels were not damaged by the clamping. The normal force (FN) on the samples was registered as a function of time using a dedicated software (Sauter AFH—Fast F/D) under a constant traction rate (0.2 mm/s). The stress σ was calculated as FN/A and the strain ε was calculated as the ratio between the samples elongation (ΔL) and their initial length L. By plotting the stress-strain curves, the elastic region was identified as the linear portion of the curve and its angular coefficient represents the elastic modulus of the material. The tests were carried out on three replicates per each sample, showing a relative variation lower than the 6% in every case.

6.1.4 Hydrogels electromechanical tests

(a) Poly(HEMA-co-AN-co-VBS) – CNCs electroactivity

All the electro-mechanical tests reported in *Section 2.2* were conducted in Solution A (NaCl 0.005 M in distilled water). The setup was constituted by a Petri dish containing Solution A, in which two parallel gold-coated aluminium plates produced by physical vapour deposition (Edwards Coating System, model E306A) were positioned at a relative distance of 2 cm using a custom-made support. 100 μm-thick hydrogel films were first swollen in Solution A, where their thickness increased up to 140 μm, and then they were shaped into cantilevers (free length of 25 mm and a width of 2.5 mm) using a cutter and fixed in a Teflon clamp, located 1 cm apart from each electrode. The system

configuration enabled a maximum bending angle of about 30-35°. The voltage (from 0.2 to 3.0 V) was imposed using a power supply (EA-PS 2342-10 B) connected to the gold plates. Video sequences were acquired using a camera connected to a PC and a software was used to calculate the bending angle α (°) and the angular bending speed ω (°/s) of the actuators. The tests were carried out on three replicates per each sample, showing a relative variation lower than the 7% in every case.

The same procedure and setup were employed to investigate in details the bending behaviour of a swollen 65 μm-thick CNC1.4% in the voltage range between 5mV/cm and 100 mV/cm using an inverted microscope (Axiovert 40 CFL, Zeiss) and a CCD camera (True Chrome HD II, Tiesselab) to detect the tip's displacement. To apply voltages in the mV range, a potentiometer was employed. The tests were carried out on three different samples, showing a relative variation lower than the 4% in every case. A membrane of circular shape (100 μm thick) was also fabricated, swollen in Solution A and then cut from its centre using a lancet to shape it into thirteen triangular wedges, having a common basis consisting of the peripheral region of the membrane itself. The membrane was then mounted and clamped between two plastic components by mechanically fastening the basis of the wedges. In this configuration, each triangle constituted a tapered cantilever (basis width of 3 mm and free length of 8 mm). These structures could be simultaneously stimulated by the application of an electric field generated between two gold electrodes. Under the effect of the applied voltage, the soft wedges cooperatively bended in the same direction, mimicking the behaviour of an on/off electro-valve. The device was operated in Solution A and the actuation performance of the benders was monitored during operation using the abovementioned protocol. The supporting device was fabricated by mean of 3D printing, using the fused deposition modelling technique [431]. The material employed for the plastic frames production was acrylonitrile-butadiene-styrene (ABS, Orbi-tech). The ABS support was designed in order to host both the actuating layer and the driving electrodes (the gold plate previously employed), enabling different relative positions between them. The overall set up is reported in *Figure xx*.

(b) Cellulose-based hydrogels electroactivity

The electromechanical tests presented in *Section 2.3.3* were carried out in the solution of NaCl 0.005 M. 1 mm-thick swollen samples were cut in a cantilever shape (18 x 3 mm^2) with a square basis (6 x 6 mm^2) to be fastened by a Teflon support, and they were immersed in the solution. 35 x 10 x 0.3 mm^3 brass-based foils were coated with gold using physical vapour deposition, they were put in the solution 1 cm apart from

each side of the hydrogel and they were used as electrodes to apply an electric potential going from 0.25 to 3 V/cm. A schematic representation is reported in *Figure 6.1.3*. The equipment used for the metal deposition was an Edwards Coating System (model E306A). By using a camera connected to a personal computer, videos were captured for each test and then analysed to calculate the maximum bending angle α (°) of the cantilevers, using an image processing software (ImageJ) and with the help of a millimetric grid. Since the speed of the actuation gradually decreased during the deformation, the average angular speed $\omega_{1/2}$ (°/s) was calculated only considering the first half of the displacement. All the experiments were conducted at room temperature. The tests were carried out on three different samples, showing a relative variation lower than the 5% in every case.

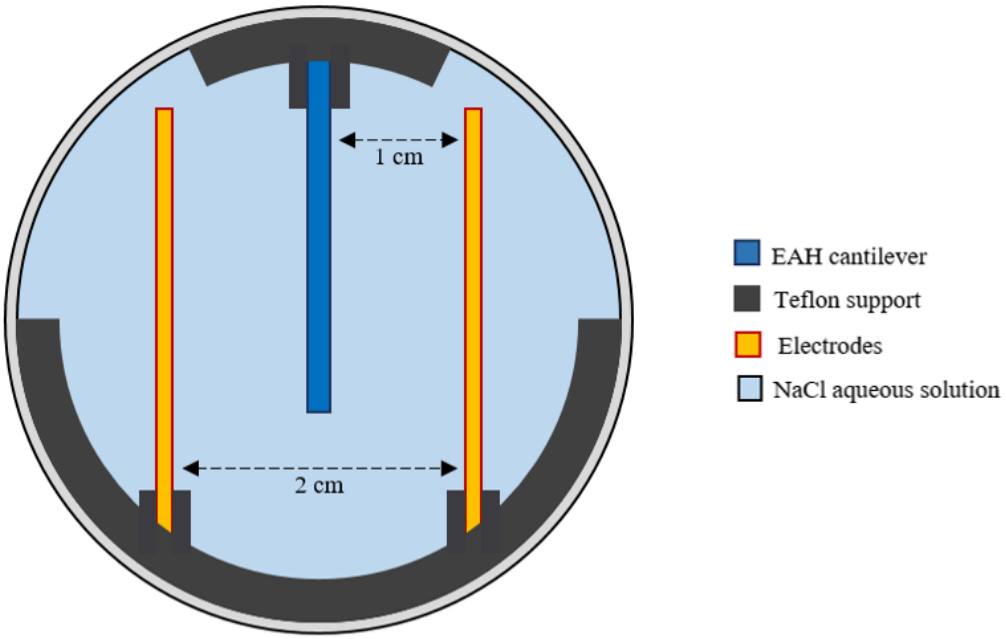

***Figure 6.1.3**. Schematic representation of the employed experimental set up for the electromehcanical actuation tests on EAHs* [209].

Then, a testing system was custom designed and 3D modelled (using Autodesk Inventor software) to properly fit few arrays of hydrogel samples and two metallic electrodes in a modular system composed of multiple parts. A base frame with two rails (80 x 62 x 10 mm^3) acts as a positioning support for both the electrode clamps (6 x 60 x

16 mm^3) and the hydrogels clamps (6 x 60 x 16 mm^3, detachable into two interlocking parts). The clamps were designed with equal hollows fitting the rails profile, so that they can be freely positioned along the base frame to lay out different configurations of the testing elements. The setup parts were manufactured by 3D printing through Fused Filament Fabrication technique (FFF) in Acrylonitrile Butadiene Styrene (ABS) polymer material (using a 3Dline Zeus 3DL printer). Two aluminium plates (60 x 60 x 1 mm^3) were coated with gold using physical vapour deposition and they were used as electrodes. To give to the hydrogel samples a specific precise shape, custom die cutters were modelled and 3D printed by using the same aforementioned solutions. Samples of various thickness (from about 0.3 to 1.0 mm), already swollen in Solution A, were cut in three (4 x 40 mm^2) or four (6 x 40 mm^2) arms cantilevers or in an algae-like shape using the cutters. Multiple arrays of samples (from two to five) were clamped between the electrodes placed at a variable distance (from 3 to 8 cm). With the same instrumentation described before, potentials from 0.25 to 1 V/cm were applied in continuous and also within a frequency range from 0.1 to 0.5 Hz.

6.1.5 BET analysis

Regarding the paper/ionogel hybrid composites presented in *Section 3.2*, the nitrogen adsorption method (Brunauer– Emmett–Teller (BET), t-plot and Barrett-Joyner-Halenda (BJH) analysis [432]) was employed to obtain investigate the porosity and the surface area of the paper before and after the ionogel absorption. This technique was then carried out on both the pristine plain paper and the hybrid paper/ionogel composite, as well as on bare poly(AA-co-AN)-based ionogels. The measurements were performed with a Gemini surface area analyzer (Micromeritics, model 2365).

Before each measurement, samples were first weighted and degassed under a constant nitrogen flux at 80°C for 3 hours using a dedicated unit, in order to remove any contaminants, which may have been adsorbed to the surface of the samples. During the gas adsorption measurements, the values of the relative pressure (p/p_0) ranged from 0.02 to 0.99 for the acquisition of the isotherm plot, while the free space in the test tube was determined by employing helium gas injection prior measurements.

6.2 METAL-POLYMER COMPOSITE MATERIALS

6.2.1 Metallization with SCBD technique

Supersonic cluster beam deposition (SCBD) technique was employed to manufacture cluster-assembled Au electrodes on the surface of the different ionogels and polymeric substrates presented in this project. Since the clusters partially penetrate into the surface of soft materials, the resulting metal-polymer composite materials are characterized by a nanostructured metal-polymer interface. *Section 1.4* reports a detailed explanation on the operational principles of this technique and on the structure of the experimental apparatus.

For all the deposition processes carried out in this work, turbomolecular pumps were initially used to bring the expansion chamber at a pressure of 7.0×10^{-7} Torr and the deposition chamber at a pressure of 1.0×10^{-5} Torr. Gold rods (diameter of 3 mm, length of 16 mm, purity of 99.9%) were purchased from 8853 s.p.a. and they were used as the solid precursor for the production of the Au clusters. The plasma was generated in the source through the injection of Argon at 40 Bar and the application of a $\Delta V = 750$ V between the gold rod (cathode) and a copper counter electrode (anode). A power supply and the valve controller are both contained by a rack connected to the SCBD apparatus. A typical metallization process was carried out with the following parameters: $T_{gas} = 250$ μs, Delay = 490 μs, $T_{Pulse} = 80$ μs and f = 5 Hz, where T_{gas} represents the time interval in which the valve is open, the delay is a waiting time before the application of the 750 V potential for a time equal to T_{Pulse}, and f is the frequency per second of the process. The target samples were mounted on a sample holder inside the deposition chamber that also contained a quartz microbalance: it is employed to have an in-situ measurements of the Au deposited mass and the corresponding equivalent thickness t_{eq} (see *Section 1.4*). Since the position of the cluster beam is fixed, during the deposition process the sample holder was moved up and down in a continuous and regular way, so that the beam can alternatively hit both the target samples and the microbalance. In every deposition process, the abovementioned parameters allowed to have a deposition rate of about 0.5 ± 0.08 μg $\times s^{-1} \times cm^{-2}$, corresponding to a value of 6 ± 1 Å $\times s^{-1} \times cm^{-2}$. The in-situ measured t_{eq} values were also checked ex-situ by measuring with a profilometer (KLA Tencor) the thickness of the cluster-assembled film grown on a silicon substrate mounted aside the target substrates during every deposition process. The deposition chamber also contains some electrical connections that can be used to measure the electrical resistance of the growing cluster-assembled layers (an Agilent 34410A multimeter was employed for this purpose). The measured resistance R_m can be

then used to calculate the sheet resistance $R_s = R_m \times w/L$ (where w is the width and L is the length of the deposited layer).

(a) Electromechanical actuators based on paper and PHB

In order to study the correlation between the amount of Au deposited through SCBD on the surface of paper/ionogel samples (presented in *Section 3.2*) and the ohmic resistance of the resulting Au thin layer, 0.5 × 0.5 cm^2 samples were employed and mounted in the deposition chamber. Both t_{eq} and R_s were measured in-situ and in real time by the quartz microbalance and the multimeter respectively. To carry out the resistance measurements, copper cables were employed to connect a multimeter to the different sides of the samples, previously covered with conductive silver paste: Au layer was then deposited as conductive bridge between the two silver contacts and then its resistance can be measured in real time. The correlation between thickness and resistance was studied up to a value of t_{eq} = 200 nm. Paper/ionogel samples were also provided with Au cluster-assembled electrodes to undergo electrochemical and electromechanical characterizations. For this purpose, the target substrates (40 mm long, 15 mm wide) were fixed on a custom-designed holder that can be mounted inside the deposition chamber. A picture of the employed sample holders is reported in *Figure 6.2.1*. The holder can also be rotated up to 180° along the vertical axis thanks to the use of a servomotor: this allowed the fabrication of cluster-assembled Au electrodes on both sides of the samples in a single deposition process. The final t_{eq} was set to a value of 150 nm (m = 120 μg/cm^2), corresponding to a value of R_s of about 20 Ω. The obtained paper/ionogel/Au hybrid composite materials were then removed from the deposition chamber and cut accordingly to the desired shape. PHB-based ionogels (presented in *Section 3.3*) were provided with cluster-assembled Au electrodes following the same experimental procedure. Also in this case, t_{eq} was set to a value of 150 nm (m = 120 μg/cm^2), corresponding to a R_s value of about 10-12 Ω.

(b) Cellulose-natural ILs supercapacitors

1.5 × 1.5 cm^2 ionogel samples, presented in *Section 4.2* and composed by cellulose derivatives and choline carboxylates ionic liquids (with different formulations), were provided on both sides with cluster-assembled Au electrodes by mean of SCBD technique. The self-standing samples were mounted on a sample holder, able to rotate of 180° along the vertical axis, and they were provided by aluminium stencil masks in order to fabricate Au layers of 8 × 8 mm^2 square shape (a picture is reported in *Figure 6.2.2*). The set values of t_{eq} were of 150 nm (m = 120 μg/cm^2) or 180 nm (m = 145 μg/cm^2). Electrodes with t_{eq} = 100 nm (m = 80 μg/cm^2) were also deposited on a single side of the spray-casted ionogels reported in *Section 4.2.5*.

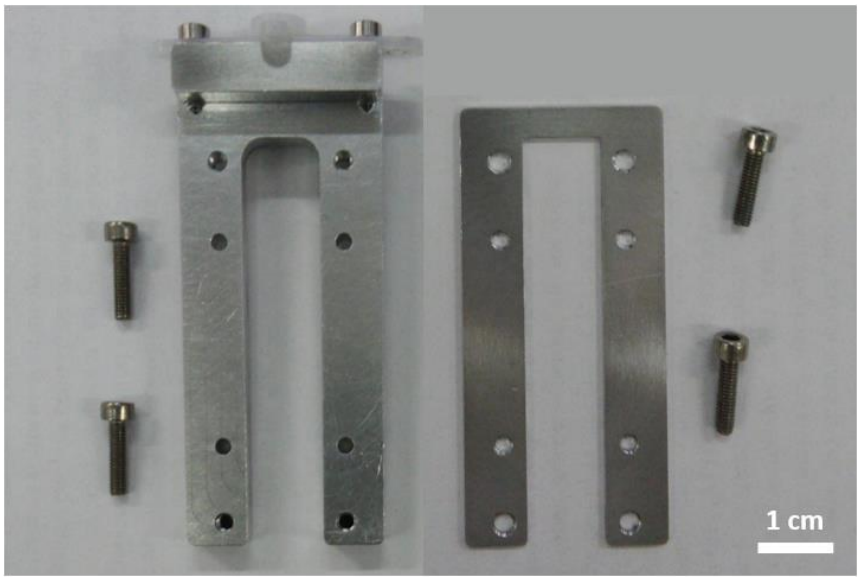

Figure 6.2.1. *Picture showing the disassembled sample holder employed for the fabrication of cluster-assembled Au electrodes on both sides of electroactive ionogels based on paper and PHB.*

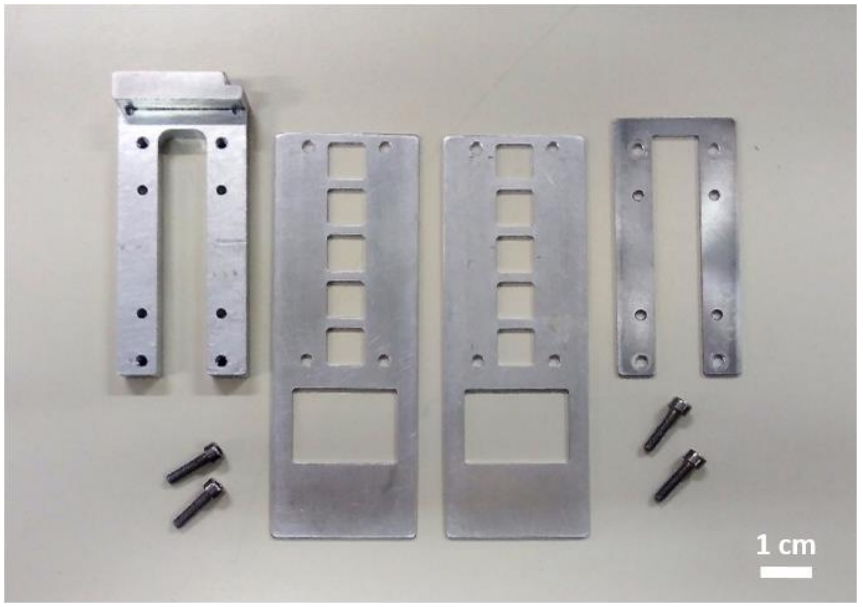

Figure 6.2.2. *Picture showing the disassembled sample holder employed for the fabrication of cluster-assembled Au electrodes on both sides of natural-derived ionogels.*

(c) Au-clusters deposition on cellulose acetate sheets

Section 5.2 reports a study conducted on bidirectional strain sensors obtained by depositing cluster-assembled Au conductive layers by mean of SCBD on the surface of 75 μm-thick biodegradable cellulose acetate (CA) sheets, purchased from Grafix Plastics. The relationship between the equivalent thickness and the sheet resistance of the Au layers was studied by in-situ monitoring their values inside the deposition chamber. T_{eq} was monitored thanks to the use of the quartz microbalance. To monitor R_s, copper cables were employed to connect a multimeter to the different sides of the samples, previously covered with conductive silver paste: the Au layer was then deposited as a conductive bridge between the two silver contacts and then its resistance can be measured in real time. The correlation between thickness and resistance was studied up to a value of t_{eq} = 150 nm. Different CA-Au composites were then obtained by depositing different amounts of Au clusters for each sample, from about 11 nm to 120 nm, using easily obtained paper stencil masks. *Figure 6.2.3* shows six different samples mounted on a sample holder, before and after the deposition process. It's possible to see the silver paste at the opposite sides of each sample: its presence is useful for the subsequent electrical characterization.

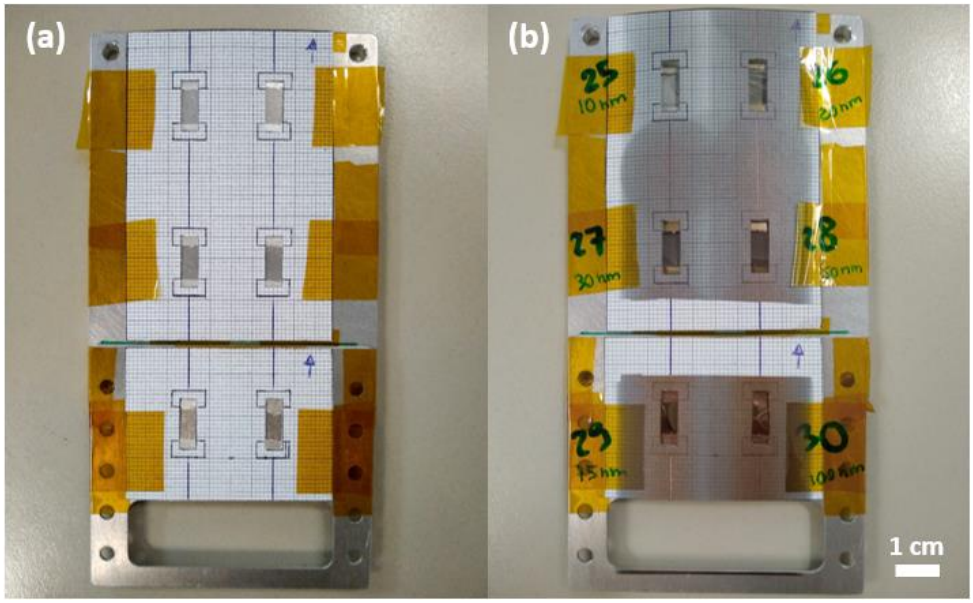

***Figure 6.2.3**. Picture showing six cellulose acetate samples **(a)** before and **(b)** after the deposition of cluster-assembled Au layers by mean of SCBD.*

6.2.2 Electrochemical characterizations

The electrochemical analysis on the presented ionogel-Au composites were carried out using a Gamry potentiostat (model Reference 600) and a Gamry software. The tested samples are, in detail, the 100 μm-thick paper/ionogel hybrid composites (*Section 3.2*) and the 50 μm-thick PHB-based electroactive composite materials (*Section 3.3*), characterized in ambient conditions. The 60 μm-thick ionogels composed by cellulose and natural-derived ionic liquids (*Section 4.2*) were also studied, inside a glove box in inert N_2 atmosphere (oxygen concentration equal to 0.03 ppm). All of these ionogel films have been previously provided with a couple of 8 × 8 mm^2 cluster-assembled Au electrodes (by mean of SCBD technique), on both the opposite sides, in a classical sandwich geometry.

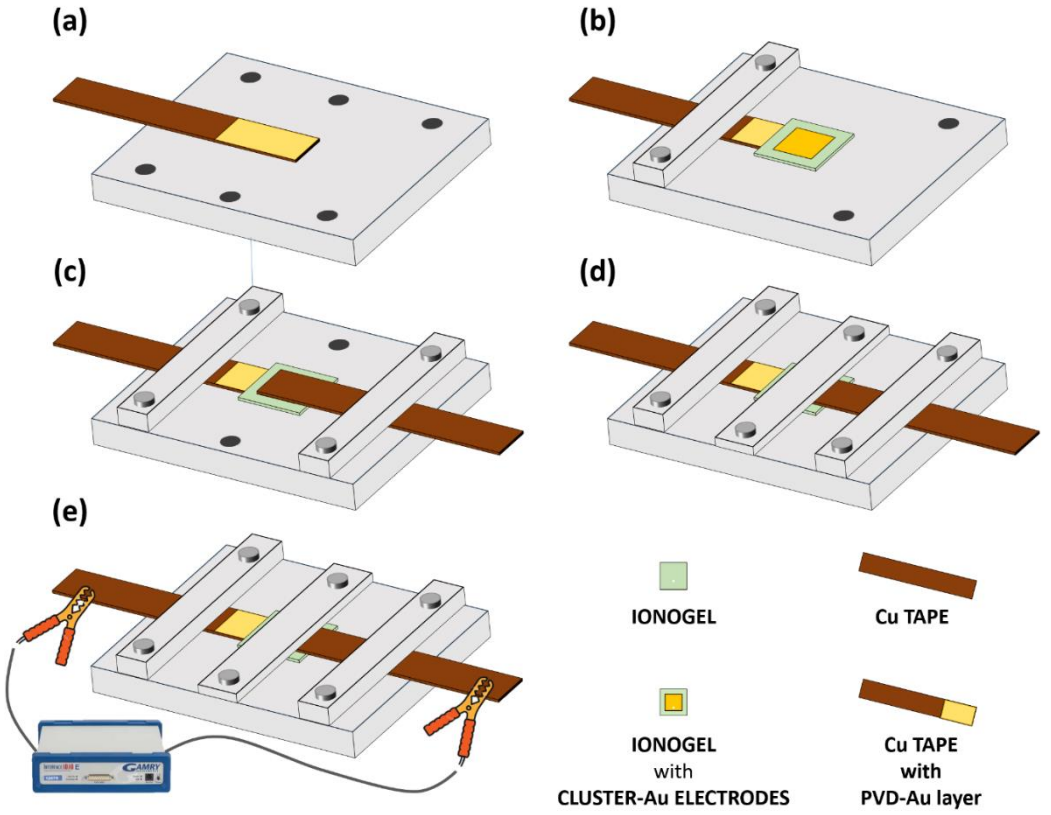

***Figure 6.2.4**. Schematics showing the assembling procedure (from **(a)** to **(e)**) of the setup for the electrochemical analysis. This allowed to have a tight electrical contact between the potentiostat and the samples without causing any damage to the soft ionogels.*

The potentiostat was not directly connected with the samples, because the pressure of the metallic crocodiles would have damaged the soft ionogels. Instead, soft contacts were employed: physical vapour deposition was used to deposit a thin layer of gold on the non-sticky surface of a copper tape. A couple of the so-obtained conductive layers was put in contact with the cluster-assembled Au electrodes of the ionogels using a custom designed 3D-printed insulant basement. The opposite side of the Cu-Au soft layers was connected to the potentiostat and in this way it was possible to carry out the electrochemical measurements without damaging the samples. A schematic representation is shown in *Figure 6.2.4*. The sticky part of the Cu tape was not employed or even detached from its soft substrate: the tape was simply employed as a soft but still robust conductive layer and a proper contact with the samples was ensured by the use of the 3D-printed basement and a tightening achieved with screws and bolts.

Three different electrochemical techniques were used in this work: electrochemical impedance spectroscopy (EIS), cyclic voltammetry (CV) and galvanostatic Charge-discharge (GCD). In all the cases, a two-electrodes set up was employed, with a working electrode and a counter electrode that worked also as the reference one. For all the samples, the obtained values of current, resistance, impedance and capacitance were normalized per the bi-dimensional area A covered by the cluster-assembled Au electrodes, that was equal to 0.64 cm^2. The tests were carried out on at least three replicates per each kind of sample, showing a relative variation lower than the 10% in every case.

(a) Electrochemical impedance spectroscopy (EIS)

This technique was employed to characterize the paper/ionogel hybrid composites (*Section 3.2.3*), the PHB-based electroactive composite materials (*Section 3.3.2*) and the ionogels composed by cellulose and natural-derived ionic liquids (*Section 4.2.2*). It consists in the application of a small amplitude sinusoidal AC at different frequencies superimposed to a set DC. The resulting electrical impedance $|Z|$, as well as its real (Z_r) and imaginary (Z_i) components and the phase delay (ϕ) between the current and the applied potential, are measured and recorded for each value of the AC frequency. In the conducted experiments, an AC = 5 mV was superimposed at a DC = 0 V and the scanned frequency range was between 1×10^{-2} Hz and 1×10^{4} Hz. The Nyquist plot was obtained by plotting the opposite of Z_i against Z_r and the equivalent series resistance (ESR) of the analysed samples can be extracted by the curve's intercept with the X-axis. Bode plots, instead, were obtained by plotting the absolute value of the impedance $|Z|$, the system's capacitance C and the current phase delay ϕ against the AC

frequency. In the case of the tested samples, the capacitance is effectively an electrolytic double-layer capacitance C_{dl} and it was calculated accordingly to *Equation 6.1*:

$$C_{dl}(f) = \frac{-Z_i(f)}{2\pi f|Z(f)|^2} \qquad [Eq.\ 6.1]$$

where A is the bi-dimensional samples area covered by the cluster-assembled Au electrodes. The capacitance C_{dl} of each analysed sample was calculated at those frequencies (usually the lower) where ϕ was between -70° and -80°. When ϕ approaches a value of 0°, instead, |Z| can be considered equal to ESR. In the case of PHB-based ionogels (*Section 3.3.2*), the ESR value was used to calculate the ionic conductivity σ_i according to *Equation 6.2*:

$$\sigma_i\left(\frac{S}{cm}\right) = \frac{th\ (cm)}{A\ (cm^2) \times ESR\ (\Omega)} \qquad [Eq.\ 6.2]$$

(b) Cyclic voltammetry (CV)

This technique was employed to characterize the ionogels composed by cellulose and natural-derived ionic liquids (*Section 4.2.3*). It consists in the application of a cyclic triangular potential AC and the resulting current is then measured and recorder. Initially, different CVs were carried out in a potential range between ± 50 mV by varying the scan rate between 2 and 32 mV/s. In this potential range, no faradic reactions occurred and a capacitive behaviour was observed. 3 cycles were carried out for every test and only the third was taken into account (since the first and eventually the second may not be reliable). The different voltammograms were recorded and for each of them an average current value was calculated considering the current values between -5 mV to +5 mV for both the scanning directions. Then, these average current values can be plotted against the corresponding scan rate values and the angular coefficients of the resulting lines represent the capacitance C_{dl} of the electrolytic double-layers.

Then, CV was also carried out in a potential range between ± 2.5 V, in order to detect the presence of faradic reactions. In fact, a capacitive behaviour is characterized by a constant-slope current profile, while electrochemical redox are identified by the presence of peaks or steps in the current profiles.

(c) Galvanostatic charge-discharge (GCD)

This technique was employed to characterize the ionogels composed by cellulose and natural-derived ionic liquids (*Section 4.2.4*). It consists in the application of a constant current i and in the measurement of the resulting potential difference ΔV between the working and the counter electrodes. In a purely ohmic circuit, the ΔV would remain equal to 0 V, no matter the current flowing. But in a circuit with a capacitance in series, under the application a flow of a constant i, ΔV gradually increases with the time of charge t_c. When ΔV reaches a set maximum value ΔV_{max}, the current flow is reversed and the potential difference gradually decrease down to 0 V in a certain discharge time t_d. In this work, different GCDs were carried out by setting ΔV_{max} = 1 V and by varying the current i from 10 to 20 $\mu A/cm^2$. A typical GCD graph can be obtained by plotting ΔV against the time. 3 cycles were carried out for every test and only the third was taken into account (since the first and eventually the second may not be reliable). Then, the electrolytic double-layer capacitance C_{dl} was calculated according to *Equation 6.3*:

$$C_{dl}(F)\left(\frac{F}{cm^2}\right) = \frac{i\ (\mathrm{A})}{A\ (cm^2) \times t_d\ (s)} \qquad [Eq.\ 6.3]$$

The coulombic efficiency CE, instead, was calculated as the ratio between the time of discharge t_d and the time of charge t_c. If a GCD analysis was carried out on a pure capacitive element, the discharge phase would begin with a ΔV value exactly equal to ΔV_{max}. But if an ESR is found in series of the capacitive element, as it always happens in real EDLCs, the discharge process is characterized by a potential drop ΔU that is proportional to the ESR value and to the flowing current i. Actually, there is no universal consensus regarding the best way to experimentally calculate such potential drop and ESR from GCD. In this work, ΔU was identified accordingly to *Equation 6.4*:

$$\Delta U = \Delta V_{max} - \Delta V_d \qquad [Eq.\ 6.4]$$

where ΔV_d was obtained following the procedure shown in *Figure 6.2.5*. Practically, it was identified the portion of the discharge curve that was the most linear and the closest to the point where the current is inverted. Such portion was linearly extended until the very beginning of the discharge and the corresponding ΔV value was considered to be precisely ΔV_d.

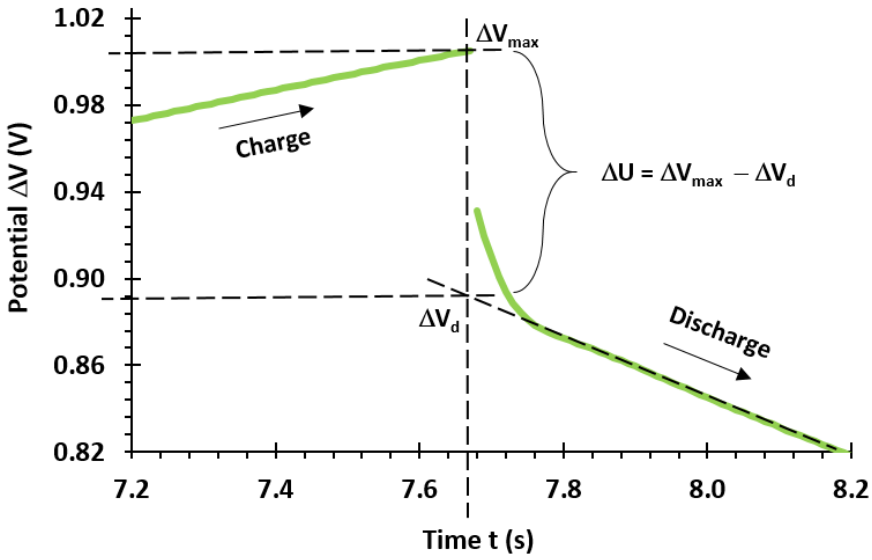

***Figure 6.2.5**. Graphical representation of the procedure employed to calculate the potential drop ΔU during the discharge process when a capacitive element is in series with an ESR.*

Then, ESR was calculated according to *Equation 6.5* [433]:

$$\mathrm{ESR}\ (\Omega \times cm^2) = \frac{\Delta U\ (V) \times A\ (cm^2)}{2i\ (A)} \qquad [Eq.\ 6.5]$$

C_{dl}, CE and ESR where calculated for each analysed sample for different values current flow i. Cyclic tests were also carried out, up to a cycle number of 10^4. CE variation was monitored as well as the capacitance retention C_{ret} (%), calculated as the ratio between C_n and C_0, where C_0 is the capacitance during the third cycle and C_n is the capacitance value obtained at a generic n^{th} cycle. Finally, the obtained data were used to calculate the specific energy stored E_S and delivery power P_S, as well as their volumetric equivalents E_V and P_V, accordingly to *Equation 6.6*, *6.7*, *6.8* and *6.9* respectively.

$$\mathrm{E}_S\ (\mathrm{Wh}/kg) = \frac{1}{2}\frac{\mathrm{C}\ (F) \times \Delta V_{max}(V)^2}{3600 \times m_E\ (kg)} \qquad [Eq.\ 6.6]$$

$$\mathrm{P}_S\ (\mathrm{W}/kg) = \frac{1}{4}\frac{\Delta V_{max}(V)^2}{ESR\ (\Omega) \times m_E\ (kg)} \qquad [Eq.\ 6.7]$$

$$\mathrm{E}_V\ (\mathrm{Wh}/dm^3) = \frac{1}{2}\frac{\mathrm{C}\ (F) \times \Delta V_{max}(V)^2}{3600 \times V_E\ (dm^3)} \qquad [Eq.\ 6.8]$$

$$\mathrm{P}_V\ (\mathrm{W}/dm^3) = \frac{1}{4}\frac{\Delta V_{max}(V)^2}{ESR\ (\Omega) \times V_E\ (dm^3)} \qquad [Eq.\ 6.9]$$

Where m_E and V_E are the total mass and the volume of the cluster-assembled Au electrodes. In fact, as usual for supercapacitors, the power and the stored energy are normalized and compared to each other according to the mass and/or the volume of the electrodes.

6.2.3 Electromechanical in-air actuation

Electromechanical actuation tests in air where carried out on the paper/ionogel/Au hybrid actuators presented in *Section 3.2* and on the electroactive PHB-based ionogel-metal composites reported in *Section 3.3*. In both cases, a power supply (EA-PS 2342-10B) was used to apply a ΔV between the two electrodes and a square wave function generator (Thandar TG503) connected to a control circuit was used switch the signal bias. The tests were carried out on three replicates per each sample, showing a relative variation lower than the 11% in every case.

(a) Paper/ionogel/Au hybrid actuators

Different paper/ionogel/Au samples were firstly cut into strips (40 x 2.5 mm) and shaped into cylindrical helixes, by folding the components along a 2 mm diameter plastic tube. A final helix's length of 12 mm was achieved, having two coils with a radius of 15 mm and a pitch equal to 5 mm. The helixes were clamped at one of their free end and suspended vertically in order to display motion along the azimuthal direction. Soft contacts (like the one employed for the electrochemical tests, described in *Section 6.2.2*)

were employed to put in contact the power supply with the couple of cluster-assembled Au electrodes situated on the opposite sides of the tested strips. Initially a constant ΔV value was applied in a potential range going from 1 V to 5 V. The resulting helix's tip longitudinal displacement ΔL and the actuation linear speed were measured by analysing video sequences acquired with a camera.

The effective strain of the actuator was also calculated as the ratio between the ΔL and its original length L_0. A longitudinal elongation was also observed, associated with a transversal contraction of the helix. Then a square wave AC going from 0 V to 3 V was applied by varying the frequency (0.1 Hz, 0.5 Hz and 10 Hz) to assess the dynamic response of the actuators. In the end, durability tests were performed through the application of a ΔV = 2.5 V at 0.25 Hz for 5000 cycles: the displacement retention ΔL_{ret} (%) was calculated as the ratio between the ΔL value at a generic "n^{th}" cycle and its value at the first one.

(b) PHB-based electroactive actuators

The PHB-based ionogels, provided with a couple of cluster-assembled Au electrodes, were cut in a cantilever shape with a free length L = 30 mm, a width w = 3 mm and a thickness th = 50 μm and they were clamped at one side. A potential difference ΔV (from 0.1 to 7 V) was applied between the two electrodes and a frequency range between 0.1 to 1 Hz was studied. The displacement x (mm) on the X-axis of the actuator's free tip was monitored using a camera and a paper grid. The cantilever curvature k (mm^{-1}) and the strain was ε were calculated according to *Equation 6.10* and *Equation 6.11*[28, PHB] respectively. Cyclic tests were also conducted through the application of an AC of 2 V and 4 V at a frequency of 0.5 and 0.75 Hz respectively, up to 10^5 cycles. The displacement retention x_{ret} (%) was calculated as the ratio between the x value at a generic "n^{th}" cycle and its value at the first one.

$$\mathrm{k}\,(mm^{-1}) = \frac{2x\,(mm)}{L\,(mm)^2} \qquad [Eq.\ 6.10]$$

$$\varepsilon = \frac{2\,th\,(mm) \times x\,(mm)}{L\,(mm)^2 + x\,(mm)^2} \qquad [Eq.\ 6.11]$$

6.2.4 Electrical characterizations

Electrical tests were carried out to study di electrical behaviour of the cluster-assembled Au layers (4 × 8 mm^2) deposited via SCBD on the biodegradable cellulose acetate (CA) sheets (*Section 5.2*). A power supply (EA-PS 2342-10B) was used to apply a ΔV between the opposite sides of the Au layers and an Agilent 34410A multimeter was employed to measure the flowing current. The instrumentation was put in electrical contact with the conductive pads previously provided to the CA sheets with a conductive silver paste (the Au layer was deposited as a conductive bridge between the two separated Ag pads, see *Section 6.2.1(c)*). The ohmic measured resistance R_m (Ω) was calculated as the ratio between the applied potential ΔV and the measured current i_m (A). The tests were carried out on at least three replicates per each kind of sample, showing a relative variation lower than the 8% in every case.

(a) Static regime

Initially, static electrical tests were conducted on three samples with a different Au equivalent thickness (precisely, 13 nm, 35 nm and 55 nm). A cyclic voltage ramp from 0.5 v to 2.0 V was applied with a step of 0.1 V. The current values obtained during the 10^{th} ramp were recorder and employed to calculate the corresponding resistance R_m. Then, for each value of the applied potential, the resistance's percentage variation was calculated according to *Equation 6.12*, where R_{av} is the average value of R_m during the whole potential ramp.

$$\Delta R/R\ (\%) = \frac{100 \times (R_m - R_{av})}{R_{av}} \qquad [Eq.\ 6.12]$$

(b) Dynamic bending regime

Then, CA samples provided with 11 nm-thick Au layers underwent an electrical characterization in dynamic bending conditions, to study how the their ohmic resistance varied accordingly to different curvature angles and mechanical strains. More precisely, CA-Au films (l = 8 mm, w = 4 mm, 75 μm-thick) were fixed in the central region of a larger

cellulose acetate sheets with a total length L = 40 mm, with a 150 m-thick double-sided adhesive tape. The total thickness of the three-layer flexible sheet was th = 300 μm. A custom assembled linear translator (a picture is shown in *Figure 6.2.6*), consisting of a step motor (28BYJ-48, 5V, DC), a rod bar, a moving support and controlled by an Arduino board, was employed in these tests to dynamic bend the flexible samples.

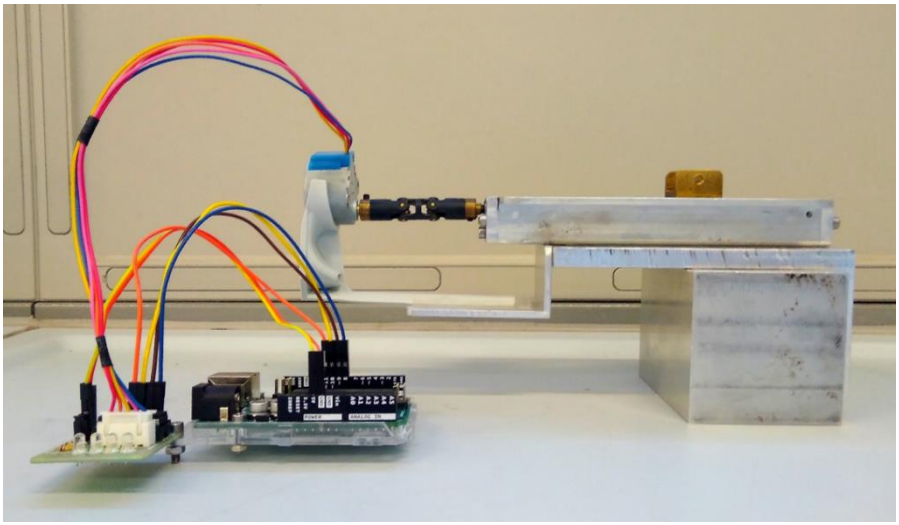

***Figure 6.2.6**. Assembled linear translator controlled with an Arduino board. It was employed to dynamically bend the flexible CA-Au sheets while measuring their ohmic resistance.*

While one end of the sheets was clamped to a fixed part of the translator, the other end was moved towards through a linear displacement ΔL at a speed of 0.1 mm/s. The curvatures induced to the CA samples were approximated as arcs of circumference and their characteristic curvature angle θ (°) and radius r_c were calculated according to *Equation 6.13*, *Equation 6.14*: and *Equation 6.15*:

$$\theta\ (°) = \alpha\ (°)\frac{L\ (mm)}{l\ (mm)} \qquad [Eq.\ 6.13]$$

$$\mathrm{r}_c\ (mm) = \frac{360}{2\pi}\frac{L\ (mm)}{\alpha(°)} \qquad [Eq.\ 6.14]$$

$$\Delta L\ (mm) = L\ (mm) - 2r(mm)sen\frac{\alpha\ (rad)}{2} \qquad [Eq.\ 6.15]$$

where α is the curvature angle induced to the larger acetate sheets on which the CA-Au samples were fixed. With these two relationships, it was possible to associate a θ to different values of ΔL. Since the Au layers were placed on the convex side of the bending CA sheets, they underwent a positive curvature as well as a positive strain ε, calculated according to *Equation 6.16*. Under the constant application of a ΔV = 1 V, the resistance R_m was continuously measured. When ΔL = 0, ε was also 0 and $R_m = R_0$. Under the application of different positive strain values, R_m increased and its relative variation was calculated according to *Equation 6.17*:

$$\varepsilon\ (\%) = \frac{100 \times th\ (mm)}{2r_c\ (mm)} \qquad [Eq.\ 6.16]$$

$$\Delta R/R\ (\%) = \frac{100 \times (R_m - R_0)}{R_0} \qquad [Eq.\ 6.17]$$

Under dynamic bending, R_m and ΔR/R (%) where then plotted against the time t (s), ΔL/L, θ and ε. In the graph ΔR/R (%) Vs ε, a good linear interpolation was achieved and its angular coefficient was calculated and it represented the gauge factor GF_+. ΔR/R (%) was also checked under 100 bending cycles with a maximum strain of +0.46%. The same dynamic characterization was repeated with the Au conductive layer on the concave side of the flexible sheet: in this case, a negative value was assigned to t (s), ΔL/L, θ (°) and ε.

6.2.5 Optical transparency measurements

A UV-Vis spectrophotometer was employed to study and measure the optical transparency of cellulose acetate (CA) sheets provided with cluster-assembled Au layers of different thickness (from 11 to 120 nm). The analysis was conducted in transmittance mode and the wavelength of the incident radiation was varied from 900 to 350 nm. Transmittance spectra were acquired and for each sample T_{av} (%) was calculated as the average transmittance value in the visible range (400-700 nm). The tests were carried out on at least three replicates per each kind of sample, showing a relative variation lower than the 3% in every case.

6.3 IMAGING

6.3.1 Optical microscopy, AFM and SEM

(a) Optical microscopy

An optical microscope (Axio imager pol, Zeiss) was employed to observe the surface of the paper/ionogel/Au hybrid composite materials (*Section 3.2.2*), the PHB-based electromechanical actuators (*Section 3.3.2*) and the ionogels (both metallized or not) based on cellulose derivatives and biodegradable ionic liquids (*Section 4.2.1* and *Section 4.2.5*).

(b) Atomic Force Microscopy (AFM)

A Bioscope Catalyst atomic force microscope (AFM, Bruker) was employed to characterize the morphology of standard paper sheets, the paper/ionogel hybrid composites reported in *Section 3.2.1* and also the layer-by-layer supercapacitors reported in *Section 4.2.5*.

Concerning the paper/ionogel hybrids (*Section 3.2.1*), AFM images were taken using Peak-force Tapping Mode in Large-Amplitude configuration. A silicon tip on nitride cantilevers, with nominal spring 0.4 N/m, was used, the scan rate was set to 1 Hz and the sampling resolution to 512 × 512 points. The scan size ranges from 500 nm to 20 μm, in order to characterize the roughening of the interface at the meso and micro-scale.

Concerning the supercapacitors layer-by-layer deposited on cellulose acetate sheets (*Section 3.2.1*), the morphological examinations were performed in standard AFM tapping mode, using sharp probe with resonant frequency around 399 KHz. The sample was kept in vacuum for 24 hours in order to achieve maximum dehydration. Scan has been made over 50 × 50 and 80 × 80 μm^2 area, with 4096 points per lines and 2048 lines,

resulting in a 20 nm resolution in X direction and 40 nm in Y. Roughness was evaluated as the root mean square of the height of the scan performed. Indentation measurements were also carried out: a custom monolithic borosilicate glass probe was used, consisting in spherical glass bead with radii R of 35 μm, attached to soft silicon, tip-less cantilevers with elastic constant k = 50 N/m, measured using the thermal noise calibration [434]. The probes were fabricated and calibrated, in terms of tip radius, according to an established custom protocol [435,436]. The topographic, mechanical and adhesion maps were obtained, from sets of force vs distance curves (FCs), collected in Point and Shoot (P&S) mode, selecting the regions of interest from optical images, exploiting the accurate alignment of the optical and AFM images obtained using the Miro software module integrated in the AFM software. Each set of FCs consisted in an N × M array of curves spatially separated by approximately 2 μm, each FC containing 4096 points, with ramp length L = 15 μm, maximum load F_{max} = 5 μN, ramp frequency f = 3 Hz. Typical maximum indentation was 200-300 nm. Data processing of the P&S set of curves was carried out measuring the elastic response of the cell can with the Hertzian contact mechanics (*Equation 6.18*)

$$F = \frac{3}{4}\frac{E}{(1-\nu^2)} R^{\frac{1}{2}}\delta^{\frac{3}{2}} \qquad [Eq.\ 6.18]$$

where F is the applied force, ν is the Poisson's ratio, E is the effective Young's modulus, R is the probe's radius and δ is the measured local indentation. From each FC it is possible to calculate both the local height of the cell body, the value of the effective Young's modulus and the adhesion force.

(c) Scanning Electron Microscopy (SEM)

Scanning electron microscopy (SEM) images were acquired with a SEM Zeiss mod. EVO 50' EP to study the morphology of the cellulose nanocrystals (CNCs), the ones embedded inside the matrix of the electroactive hydrogel presented in *Section 2.2.1*. SEM images were also acquired to study the morphology of the paper/ionogel/Au hybrid composites (*Section 3.2.2*) and the metallized PHB-based ionogels (*Section 3.3.2*). This imaging was performed at the MDM laboratories in Agrate Brianza (Milan), using a Zeiss Gemini instrument, equipped with an in-lens detector.

7.

Conclusions and Perspectives

Soft technologies can represent a winning strategy to address many challenging contemporary issues, such as the more and more important need for a safe, efficient and continuous monitoring of the health state for both people and plants. The presented project was focused on the integration of natural-derived and biodegradable polymers and substances with both electronic conductors and ionic electrolytes, in the attempt to design and develop soft eco-friendly nanocomposite materials able to display different useful functionalities (such as actuation, energy storage and delivery, sensing) in the context of soft robotics and electronics. Due to the increasing severity of resource pressure and environmental pollution, in this work a particular attention was paid to avoid or to reduce the use of in exhaustion, pollutant, toxic and non-degradable resources, such as lithium, petroleum derivatives, halogenated compounds and organic solvents. Instead, renewable, natural-derived and biodegradable polymers and substances were mainly used as raw materials and all the carried out processes were mainly water-based or even solvent-free.

Following these principles of environmental sustainability, soft electroactive hydrogels were designed and synthesized with cellulose derivatives and through a water-based process: their underwater electromechanical actuation was studied and characterized, as well as their swelling and mechanical properties. In-air electromechanical actuators were also developed and their design was based on the manufacturing of soft ionogels obtained by the combination of ionic liquids with both office copy paper and a PHB bioplastic. The challenging fabrication of compliant conductive electrodes on the ionogels surface was achieved through a solvent-free supersonic cluster beam deposition (SCBD) technique, that was employed for the realization of cluster-assembled Au electrodes partially interpenetrated into the surface of the soft ionogels, granting a nanostructured interfacial area, a strong adhesion to the substrate and high electronic conductivity. Similar electrodes were also deposited on the surface of thin ionogels obtained with a water-based process by blending together cellulose derivatives and biodegradable ionic liquids: these systems were designed to act as fully biodegradable micro-supercapacitors (EDLC type), strategic functional elements in the field of (renewable) energy storage. In the end, biodegradable cellulose acetate sheets were employed as transparent and flexible substrates for the realization of both transparent conductive films and resistive-type bidirectional strain sensors.

Actuation, sensing, energy delivery and storage were the target features of this work. As it was underlined in the introduction of the manuscript, they are only a portion of the numerous active functions that need to be integrated to develop a full autonomous soft robotic system or device. *Figure 7.1* recalls the one already reported in *Section 1.3*, but some of the “boxes” are now “filled” with the smart materials obtained in this work. Many efforts are still needed to develop a whole class of smart active

materials that can be integrated and interconnected on a same platform or body, toward the realization of autonomous biodegradable soft technologies that can be manufactured and deployed in high number without concerning about their recovery, since they can safely degrade in the environment.

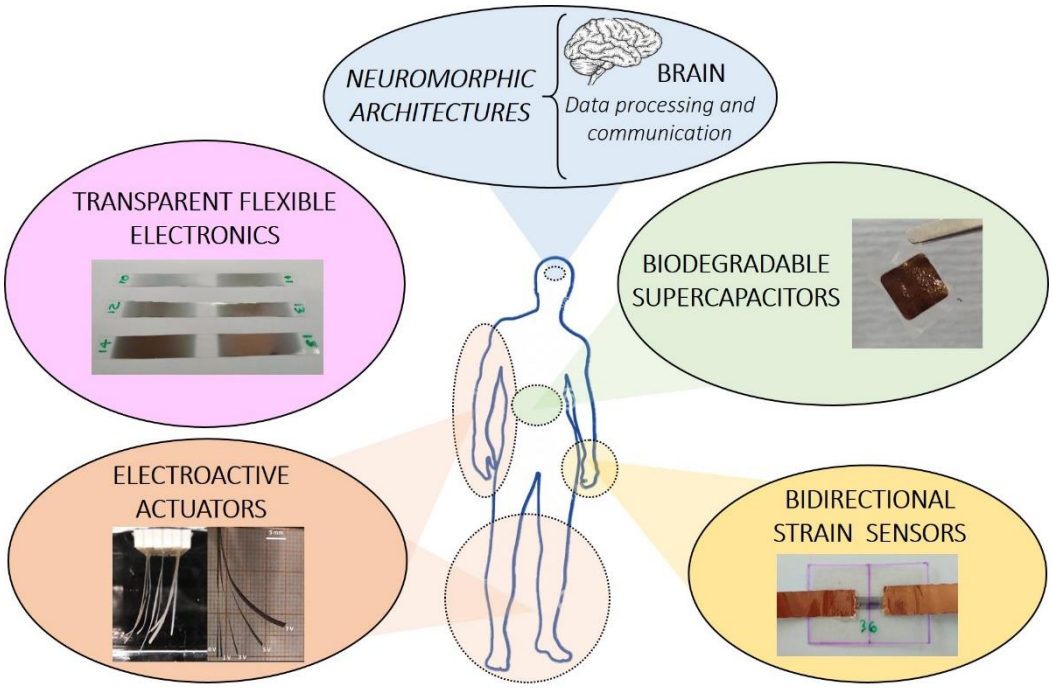

***Figure 7.1**. Graphic representation of the different functionalities needed by a soft autonomous robotic system or device. It is shown how the smart composite materials developed in this work can fulfil some of these desired functions.*

Concerning this work, the current project has not come to an end. In particular, the results concerning the micro-supercapacitors and the strain sensors only constitute a preliminary study of feasibility. The research will continue in the attempt to optimize their formulation and manufacturing process. The realization of other functional devices, such as transistors, neuromorphic architectures, electrochemical batteries and sensors will also be addressed, by keeping the attention on a mutual interconnection and on the use of eco-friendly materials and processes.

APPENDIX A

LIST OF RELATED SCIENTIFIC PUBLICATIONS

Section 2: Cellulose-based electroactive hydrogels (EAHs)

- T. Santaniello, L. Migliorini, E. Locatelli, I. Monaco, Y. Yan, C. Lenardi, M.C. Franchini, P. Milani, Hybrid nanocomposites based on electroactive hydrogels and cellulose nanocrystals for high-sensitivity electro–mechanical underwater actuation, Smart Mater. Struct. 26 (2017).
- L. Migliorini, Y. Yan, F. Pezzotta, F.M.S. Veronesi, C. Lenardi, S. Rondinini, T. Santaniello, P. Milani, Cellulose-based electroactive hydrogels for seaweed mimicking toward hybrid artificial habitats creation, MRS Commun. 8 (2018) 1129–1134.

Section 3: In-air soft actuators from natural polymers

- T. Santaniello, L. Migliorini, F. Borghi, Y. Yan, S. Rondinini, C. Lenardi, P. Milani, Spring-like electroactive actuators based on paper/ionogel/metal nanocomposites, Smart Mater. Struct. 27 (2018).
- T. Santaniello, L. Migliorini, Y. Yan, C. Lenardi, P. Milani, Supersonic cluster beam fabrication of metal – ionogel nanocomposites for soft robotics, J. Nanoparticle Res. 20 (2018).
- L. Migliorini, T. Santaniello, S. Rondinini, P. Saettone, M. Comes Franchini, C. Lenardi, P. Milani, Bioplastic electromechanical actuators based on biodegradable poly(3-hydroxybutyrate) and cluster-assembled gold electrodes, Sensors Actuators, B Chem. 286 (2019) 230–236.

Section 4: Biodegradable micro-supercapacitors *and* ***Section 5: Biodegradable transparent electronics and strain sensors***

- Collection of experimental data still ongoing.

APPENDIX B

GRAFIX PLASTICS - CELLULOSE ACETATE FILMS - DATA SHEET

FILM PROPERTY	VALUE	UNITS	TEST METHOD
Physical Properties			
Specific Gravity	1.32		
Equilibrium moisture content			
23C and 50% RH	circa 2%		
Surface energy	38-42	dyn cm -1	
Areal density	124.45	g/m 2	
Yield	8.04	m 2 /kg	
Dynamic friction coefficient	0.4-0.6		
Tensile Strength	80-100	Nmm -2	ASTM D882
Elongation at break	25-45%	%	ASTM D882
E-Modulus	2000-2500	Nmm -2	ASTM D882
Tear initiation	0.237	N	ASTM D1938
Tear propagation	0.231	N	ASTM D1938
Electrical Properties			
Surface resistivity 50% RH	5.1x10 -13	Ωm -2	
Dielectric breakdown	15	kVmm -1	
Thermal Properties			
Linear Shrinkage 115°C 10 min	1-1.5	%	
Dimensional stability 20 hrs 80°C 95% RH	0.0215	%	
Softening temperature	≈ 120	°C	
Glass transition temperature	≈ 140	°C	

FILM PROPERTY	VALUE	UNITS	TEST METHOD
Optical Properties			
Transparency	90.4	%	ASTM D1476
Gloss			
20°	141.6	%	ASTM D523
60°	148.3	%	BS 2782 520A
85°	123.7	%	
Haze	0.9	%	ASTM D1003
Refractive Index	1.485		BS 2782 521A
Barrier Properties			
Moisture vapour transmission rate M.V.T.R. 25°C & 75% RH	337	gm -2 day -1	
Food contact approved			
Din Certo EN 13432 certified			ASTM D6400
BPI certified			
Vincotte OK Home Compost approved			

BIBLIOGRAPHY

[1] P. Kowal, An Aging World : 2015, (2019).

[2] T. Santaniello, L. Migliorini, Y. Yan, C. Lenardi, P. Milani, Supersonic cluster beam fabrication of metal – ionogel nanocomposites for soft robotics, J. Nanoparticle Res. 20 (2018) 250. doi:10.1007/s11051-018-4352-x.

[3] D. Trivedi, C.D. Rahn, W.M. Kier, I.D. Walker, Soft robotics: Biological inspiration, state of the art, and future research, Appl. Bionics Biomech. (2008). doi:10.1080/11762320802557865.

[4] F. Ilievski, A.D. Mazzeo, R.F. Shepherd, X. Chen, G.M. Whitesides, Soft robotics for chemists, Angew. Chemie - Int. Ed. (2011). doi:10.1002/anie.201006464.

[5] B. Mazzolai, L. Margheri, M. Cianchetti, P. Dario, C. Laschi, Soft-robotic arm inspired by the octopus: II. from artificial requirements to innovative technological solutions, Bioinspiration and Biomimetics. (2012). doi:10.1088/1748-3182/7/2/025005.

[6] R. Pfeifer, M. Lungarella, F. Iida, The challenges ahead for bio-inspired “soft” robotics, Commun. ACM. (2012). doi:10.1145/2366316.2366335.

[7] E. Brown, N. Rodenberg, J. Amend, A. Mozeika, E. Steltz, M.R. Zakin, H. Lipson, H.M. Jaeger, Universal robotic gripper based on the jamming of granular material, Proc. Natl. Acad. Sci. U. S. A. (2010). doi:10.1073/pnas.1003250107.

[8] H.T. Lin, G.G. Leisk, B. Trimmer, GoQBot: A caterpillar-inspired soft-bodied rolling robot, Bioinspiration and Biomimetics. (2011). doi:10.1088/1748-3182/6/2/026007.

[9] A.D. Marchese, R. Tedrake, D. Rus, Dynamics and trajectory optimization for a soft spatial fluidic elastomer manipulator, Int. J. Rob. Res. (2016). doi:10.1177/0278364915587926.

[10] C.D. Onal, D. Rus, Autonomous undulatory serpentine locomotion utilizing body dynamics of a fluidic soft robot, Bioinspiration and Biomimetics. (2013). doi:10.1088/1748-3182/8/2/026003.

[11] M.T. Tolley, R.F. Shepherd, B. Mosadegh, K.C. Galloway, M. Wehner, M. Karpelson, R.J. Wood, G.M. Whitesides, A Resilient, Untethered Soft Robot, Soft Robot. (2014). doi:10.1089/soro.2014.0008.

[12] A.D. Marchese, C.D. Onal, D. Rus, Autonomous Soft Robotic Fish Capable of Escape Maneuvers Using Fluidic Elastomer Actuators, Soft Robot. (2014). doi:10.1089/soro.2013.0009.

[13] I. Must, F. Kaasik, I. Põldsalu, L. Mihkels, U. Johanson, A. Punning, A. Aabloo, Ionic and capacitive artificial muscle for biomimetic soft robotics, Adv. Eng. Mater. (2015). doi:10.1002/adem.201400246.

[14] E.T. Roche, R. Wohlfarth, J.T.B. Overvelde, N. V. Vasilyev, F.A. Pigula, D.J. Mooney, K. Bertoldi, C.J. Walsh, A bioinspired soft actuated material, Adv. Mater. (2014). doi:10.1002/adma.201304018.

[15] P. Polygerinos, Z. Wang, K.C. Galloway, R.J. Wood, C.J. Walsh, Soft robotic glove for combined assistance and at-home rehabilitation, in: Rob. Auton. Syst., 2015. doi:10.1016/j.robot.2014.08.014.

[16] R. Deimel, O. Brock, A novel type of compliant and underactuated robotic hand for dexterous grasping, Int. J. Rob. Res. (2016). doi:10.1177/0278364915592961.

[17] R. V. Martinez, J.L. Branch, C.R. Fish, L. Jin, R.F. Shepherd, R.M.D. Nunes, Z. Suo, G.M. Whitesides, Robotic tentacles with three-dimensional mobility based on flexible elastomers, Adv. Mater. (2013). doi:10.1002/adma.201203002.
[18] R. V. Martinez, C.R. Fish, X. Chen, G.M. Whitesides, Elastomeric origami: Programmable paper-elastomer composites as pneumatic actuators, Adv. Funct. Mater. (2012). doi:10.1002/adfm.201102978.
[19] K. Suzumori, T. Maeda, H. Watanabe, T. Hisada, Fiberless flexible microactuator designed by finite-element method, IEEE/ASME Trans. Mechatronics. (1997). doi:10.1109/3516.653052.
[20] K. Suzumori, S. Endo, T. Kanda, N. Kato, H. Suzuki, A bending pneumatic rubber actuator realizing soft-bodied manta swimming robot, in: Proc. - IEEE Int. Conf. Robot. Autom., 2007. doi:10.1109/ROBOT.2007.364246.
[21] K. Jung, J.C. Koo, J. Do Nam, Y.K. Lee, H.R. Choi, Artificial annelid robot driven by soft actuators, Bioinspiration and Biomimetics. (2007). doi:10.1088/1748-3182/2/2/S05.
[22] E.T. Roche, M.A. Horvath, I. Wamala, A. Alazmani, S.E. Song, W. Whyte, Z. Machaidze, C.J. Payne, J.C. Weaver, G. Fishbein, J. Kuebler, N. V. Vasilyev, D.J. Mooney, F.A. Pigula, C.J. Walsh, Soft robotic sleeve supports heart function, Sci. Transl. Med. 9 (2017) 1–12. doi:10.1126/scitranslmed.aaf3925.
[23] H.K. Yap, B.W.K. Ang, J.H. Lim, J.C.H. Goh, C.H. Yeow, A fabric-regulated soft robotic glove with user intent detection using EMG and RFID for hand assistive application, Proc. - IEEE Int. Conf. Robot. Autom. 2016–June (2016) 3537–3542. doi:10.1109/ICRA.2016.7487535.
[24] P. Polygerinos, K.C. Galloway, E. Savage, M. Herman, K. O'Donnell, C.J. Walsh, Soft robotic glove for hand rehabilitation and task specific training, Proc. - IEEE Int. Conf. Robot. Autom. 2015–June (2015) 2913–2919. doi:10.1109/ICRA.2015.7139597.
[25] P. Polygerinos, K.C. Galloway, S. Sanan, M. Herman, C.J. Walsh, EMG controlled soft robotic glove for assistance during activities of daily living, IEEE Int. Conf. Rehabil. Robot. 2015–September (2015) 55–60. doi:10.1109/ICORR.2015.7281175.
[26] A. Nemiroski, Y.Y. Shevchenko, A.A. Stokes, B. Unal, A. Ainla, S. Albert, G. Compton, E. MacDonald, Y. Schwab, C. Zellhofer, G.M. Whitesides, Arthrobots, Soft Robot. 00 (2017) soro.2016.0043. doi:10.1089/soro.2016.0043.
[27] Mlabrobotics.com, (n.d.).
[28] C. Laschi, M. Cianchetti, Soft Robotics: New Perspectives for Robot Bodyware and Control, Front. Bioeng. Biotechnol. 2 (2014) 1–5. doi:10.3389/fbioe.2014.00003.
[29] S. Seok, C.D. Onal, K.J. Cho, R.J. Wood, D. Rus, S. Kim, Meshworm: A peristaltic soft robot with antagonistic nickel titanium coil actuators, IEEE/ASME Trans. Mechatronics. (2013). doi:10.1109/TMECH.2012.2204070.
[30] R.F. Shepherd, F. Ilievski, W. Choi, S.A. Morin, A.A. Stokes, A.D. Mazzeo, X. Chen, M. Wang, G.M. Whitesides, Multigait soft robot, Proc. Natl. Acad. Sci. U. S. A. (2011). doi:10.1073/pnas.1116564108.
[31] S. Koichi, L. Shoichi, T. Hiroshisa, Applying a Flexible Microactuator to Robotic Mechanisms, IEEE Control Syst. (1992). doi:10.1109/37.120448.
[32] C. Laschi, M. Cianchetti, B. Mazzolai, L. Margheri, M. Follador, P. Dario, Soft robot arm inspired by the octopus, Adv. Robot. (2012). doi:10.1163/156855312X626343.
[33] D. Han, C. Farino, C. Yang, T. Scott, D. Browe, W. Choi, J.W. Freeman, H. Lee, Soft Robotic Manipulation and Locomotion with a 3D Printed Electroactive Hydrogel, ACS

Appl. Mater. Interfaces. 10 (2018) 17512–17518. doi:10.1021/acsami.8b04250.
[34] B. Gorissen, D. Reynaerts, S. Konishi, K. Yoshida, J.W. Kim, M. De Volder, Elastic Inflatable Actuators for Soft Robotic Applications, Adv. Mater. (2017). doi:10.1002/adma.201604977.
[35] D. Ratna, J. Karger-Kocsis, Recent advances in shape memory polymers and composites: A review, J. Mater. Sci. (2008). doi:10.1007/s10853-007-2176-7.
[36] M.A.C. Stuart, W.T.S. Huck, J. Genzer, M. Müller, C. Ober, M. Stamm, G.B. Sukhorukov, I. Szleifer, V. V. Tsukruk, M. Urban, F. Winnik, S. Zauscher, I. Luzinov, S. Minko, Emerging applications of stimuli-responsive polymer materials, Nat. Mater. (2010). doi:10.1038/nmat2614.
[37] Y. Bar-Cohen, K.J. Kim, H.R. Choi, J.D.W. Madden, Electroactive polymer materials, Smart Mater. Struct. (2007). doi:10.1088/0964-1726/16/2/E01.
[38] J. Feher, Quantitative Human Physiology: An introduction, 2016. doi:10.1016/B978-0-12-800883-6.00095-1.
[39] Z. Sonner, E. Wilder, J. Heikenfeld, G. Kasting, F. Beyette, D. Swaile, F. Sherman, J. Joyce, J. Hagen, N. Kelley-Loughnane, R. Naik, The microfluidics of the eccrine sweat gland, including biomarker partitioning, transport, and biosensing implications, Biomicrofluidics. (2015). doi:10.1063/1.4921039.
[40] T.R. Dargaville, B.L. Farrugia, J.A. Broadbent, S. Pace, Z. Upton, N.H. Voelcker, Sensors and imaging for wound healing: A review, Biosens. Bioelectron. (2013). doi:10.1016/j.bios.2012.09.029.
[41] X. Huang, H. Cheng, K. Chen, Y. Zhang, Y. Zhang, Y. Liu, C. Zhu, S.C. Ouyang, G.W. Kong, C. Yu, Y. Huang, J.A. Rogers, Epidermal impedance sensing sheets for precision hydration assessment and spatial mapping, IEEE Trans. Biomed. Eng. (2013). doi:10.1109/TBME.2013.2264879.
[42] G. Schwartz, B.C.K. Tee, J. Mei, A.L. Appleton, D.H. Kim, H. Wang, Z. Bao, Flexible polymer transistors with high pressure sensitivity for application in electronic skin and health monitoring, Nat. Commun. (2013). doi:10.1038/ncomms2832.
[43] W. Gao, S. Emaminejad, H.Y.Y. Nyein, S. Challa, K. Chen, A. Peck, H.M. Fahad, H. Ota, H. Shiraki, D. Kiriya, D.H. Lien, G.A. Brooks, R.W. Davis, A. Javey, Fully integrated wearable sensor arrays for multiplexed in situ perspiration analysis, Nature. (2016). doi:10.1038/nature16521.
[44] Textbook of Cardiovascular Intervention, 2014. doi:10.1007/978-1-4471-4528-8.
[45] D.A. Burns, S.M. Breathnach, N.H. Cox, C.E.M. Griffiths, Rook's Textbook of Dermatology: Eighth Edition, 2010. doi:10.1002/9781444317633.
[46] H. Araki, J. Kim, S. Zhang, A. Banks, K.E. Crawford, X. Sheng, P. Gutruf, Y. Shi, R.M. Pielak, J.A. Rogers, Materials and Device Designs for an Epidermal UV Colorimetric Dosimeter with Near Field Communication Capabilities, Adv. Funct. Mater. (2017). doi:10.1002/adfm.201604465.
[47] S. Knobelspies, A. Daus, G. Cantarella, L. Petti, N. Münzenrieder, G. Tröster, G.A. Salvatore, Flexible a-IGZO Phototransistor for Instantaneous and Cumulative UV-Exposure Monitoring for Skin Health, Adv. Electron. Mater. (2016). doi:10.1002/aelm.201600273.
[48] B.K. Armstrong, A. Kricker, The epidemiology of UV induced skin cancer, J. Photochem. Photobiol. B Biol. (2001). doi:10.1016/S1011-1344(01)00198-1.
[49] E. Apfelstedt-Sylla, E. Zrenner, Electrophysiology, in: Clin. Neuro-Ophthalmology A Pract.

Guid., 2007. doi:10.1007/978-3-540-32708-0_7.
[50] J.G. Webster, Medical Instrumentation-Application and Design, J. Clin. Eng. (1978). doi:10.1097/00004669-197807000-00017.
[51] V.K. Somers, M.E. Dyken, M.P. Clary, F.M. Abboud, Sympathetic neural mechanisms in obstructive sleep apnea, J. Clin. Invest. (1995). doi:10.1172/JCI118235.
[52] M. Modarreszadeh, R.N. Schmidt, Wireless, 32-channel, EEG and epilepsy monitoring system, Annu. Int. Conf. IEEE Eng. Med. Biol. - Proc. (1997). doi:10.1109/iembs.1997.756559.
[53] R.H. Guy, Handbook of non-invasive methods and the skin, J. Control. Release. (1996). doi:10.1016/0168-3659(96)01365-x.
[54] Y. Liu, M. Pharr, G.A. Salvatore, Lab-on-Skin: A Review of Flexible and Stretchable Electronics for Wearable Health Monitoring, ACS Nano. 11 (2017) 9614–9635. doi:10.1021/acsnano.7b04898.
[55] Introduction to Medical Electronics Applications, 1995. doi:10.1016/b978-0-340-61457-0.x5000-1.
[56] P. Lukowicz, T. Kirstein, G. Tröster, Wearable systems for health care applications, Methods Inf. Med. (2004). doi:10.1055/s-0038-1633863.
[57] D.H. Kim, N. Lu, R. Ma, Y.S. Kim, R.H. Kim, S. Wang, J. Wu, S.M. Won, H. Tao, A. Islam, K.J. Yu, T. Il Kim, R. Chowdhury, M. Ying, L. Xu, M. Li, H.J. Chung, H. Keum, M. McCormick, P. Liu, Y.W. Zhang, F.G. Omenetto, Y. Huang, T. Coleman, J.A. Rogers, Epidermal electronics, Science (80-.). (2011). doi:10.1126/science.1206157.
[58] D.-H. Kim, R. Ghaffari, N. Lu, J.A. Rogers, Flexible and Stretchable Electronics for Biointegrated Devices, Annu. Rev. Biomed. Eng. (2012). doi:10.1146/annurev-bioeng-071811-150018.
[59] S. Wang, M. Li, J. Wu, D.H. Kim, N. Lu, Y. Su, Z. Kang, Y. Huang, J.A. Rogers, Mechanics of epidermal electronics, J. Appl. Mech. Trans. ASME. (2012). doi:10.1115/1.4005963.
[60] M.L. Hammock, A. Chortos, B.C.K. Tee, J.B.H. Tok, Z. Bao, 25th anniversary article: The evolution of electronic skin (E-Skin): A brief history, design considerations, and recent progress, Adv. Mater. (2013). doi:10.1002/adma.201302240.
[61] C. Pang, C. Lee, K.Y. Suh, Recent advances in flexible sensors for wearable and implantable devices, J. Appl. Polym. Sci. (2013). doi:10.1002/app.39461.
[62] S. Choi, H. Lee, R. Ghaffari, T. Hyeon, D.H. Kim, Recent Advances in Flexible and Stretchable Bio-Electronic Devices Integrated with Nanomaterials, Adv. Mater. (2016). doi:10.1002/adma.201504150.
[63] M. Kaltenbrunner, T. Sekitani, J. Reeder, T. Yokota, K. Kuribara, T. Tokuhara, M. Drack, R. Schwödiauer, I. Graz, S. Bauer-Gogonea, S. Bauer, T. Someya, An ultra-lightweight design for imperceptible plastic electronics, Nature. (2013). doi:10.1038/nature12314.
[64] B. Xu, A. Akhtar, Y. Liu, H. Chen, W.H. Yeo, S.I.I. Park, B. Boyce, H. Kim, J. Yu, H.Y. Lai, S. Jung, Y. Zhou, J. Kim, S. Cho, Y. Huang, T. Bretl, J.A. Rogers, Flexible Electronics: An Epidermal Stimulation and Sensing Platform for Sensorimotor Prosthetic Control, Management of Lower Back Exertion, and Electrical Muscle Activation (Adv. Mater. 22/2016), Adv. Mater. (2016). doi:10.1002/adma.201670154.
[65] S. Xu, Y. Zhang, J. Cho, J. Lee, X. Huang, L. Jia, J.A. Fan, Y. Su, J. Su, H. Zhang, H. Cheng, B. Lu, C. Yu, C. Chuang, T. Il Kim, T. Song, K. Shigeta, S. Kang, C. Dagdeviren, I. Petrov, P. V. Braun, Y. Huang, U. Paik, J.A. Rogers, Stretchable batteries with self-similar serpentine interconnects and integrated wireless recharging systems, Nat. Commun. (2013).

doi:10.1038/ncomms2553.
[66] W.H. Yeo, Y.S. Kim, J. Lee, A. Ameen, L. Shi, M. Li, S. Wang, R. Ma, S.H. Jin, Z. Kang, Y. Huang, J.A. Rogers, Multifunctional epidermal electronics printed directly onto the skin, Adv. Mater. (2013). doi:10.1002/adma.201204426.
[67] C. Dagdeviren, Y. Su, P. Joe, R. Yona, Y. Liu, Y.S. Kim, Y. Huang, A.R. Damadoran, J. Xia, L.W. Martin, Y. Huang, J.A. Rogers, Conformable amplified lead zirconate titanate sensors with enhanced piezoelectric response for cutaneous pressure monitoring, Nat. Commun. (2014). doi:10.1038/ncomms5496.
[68] J.W. Jeong, M.K. Kim, H. Cheng, W.H. Yeo, X. Huang, Y. Liu, Y. Zhang, Y. Huang, J.A. Rogers, Capacitive epidermal electronics for electrically safe, long-term electrophysiological measurements, Adv. Healthc. Mater. (2014). doi:10.1002/adhm.201300334.
[69] J.W. Lee, R. Xu, S. Lee, K.I. Jang, Y. Yang, A. Banks, K.J. Yu, J. Kim, S. Xu, S. Ma, S.W. Jang, P. Won, Y. Li, B.H. Kim, J.Y. Choe, S. Huh, Y.H. Kwon, Y. Huang, U. Paik, J.A. Rogers, Soft, thin skin-mounted power management systems and their use in wireless thermography, Proc. Natl. Acad. Sci. U. S. A. (2016). doi:10.1073/pnas.1605720113.
[70] S. Il Park, D.S. Brenner, G. Shin, C.D. Morgan, B.A. Copits, H.U. Chung, M.Y. Pullen, K.N. Noh, S. Davidson, S.J. Oh, J. Yoon, K.I. Jang, V.K. Samineni, M. Norman, J.G. Grajales-Reyes, S.K. Vogt, S.S. Sundaram, K.M. Wilson, J.S. Ha, R. Xu, T. Pan, T. Il Kim, Y. Huang, M.C. Montana, J.P. Golden, M.R. Bruchas, R.W. Gereau, J.A. Rogers, Soft, stretchable, fully implantable miniaturized optoelectronic systems for wireless optogenetics, Nat. Biotechnol. (2015). doi:10.1038/nbt.3415.
[71] J. Kim, M. Lee, H.J. Shim, R. Ghaffari, H.R. Cho, D. Son, Y.H. Jung, M. Soh, C. Choi, S. Jung, K. Chu, D. Jeon, S.T. Lee, J.H. Kim, S.H. Choi, T. Hyeon, D.H. Kim, Stretchable silicon nanoribbon electronics for skin prosthesis, Nat. Commun. (2014). doi:10.1038/ncomms6747.
[72] T. Someya, T. Sekitani, S. Iba, Y. Kato, H. Kawaguchi, T. Sakurai, A large-area, flexible pressure sensor matrix with organic field-effect transistors for artificial skin applications, Proc. Natl. Acad. Sci. U. S. A. (2004). doi:10.1073/pnas.0401918101.
[73] Y. Zhang, S. Wang, X. Li, J.A. Fan, S. Xu, Y.M. Song, K.J. Choi, W.H. Yeo, W. Lee, S.N. Nazaar, B. Lu, L. Yin, K.C. Hwang, J.A. Rogers, Y. Huang, Experimental and theoretical studies of serpentine microstructures bonded to prestrained elastomers for stretchable electronics, Adv. Funct. Mater. (2014). doi:10.1002/adfm.201302957.
[74] J. Lee, T.J. Ha, H. Li, K.N. Parrish, M. Holt, A. Dodabalapur, R.S. Ruoff, D. Akinwande, 25 GHz embedded-gate graphene transistors with high-K dielectrics on extremely flexible plastic sheets, ACS Nano. (2013). doi:10.1021/nn403487y.
[75] Y. Wang, R. Yang, Z. Shi, L. Zhang, D. Shi, E. Wang, G. Zhang, Super-elastic graphene ripples for flexible strain sensors, ACS Nano. (2011). doi:10.1021/nn103523t.
[76] B.J. Kim, H. Jang, S.K. Lee, B.H. Hong, J.H. Ahn, J.H. Cho, High-performance flexible graphene field effect transistors with ion gel gate dielectrics, Nano Lett. (2010). doi:10.1021/nl101559n.
[77] M.A. Khan, U.S. Bhansali, H.N. Alshareef, High-performance non-volatile organic ferroelectric memory on banknotes, Adv. Mater. (2012). doi:10.1002/adma.201200626.
[78] Y. Zheng, G.X. Ni, C.T. Toh, M.G. Zeng, S.T. Chen, K. Yao, B. Özyilmaz, Gate-controlled nonvolatile graphene-ferroelectric memory, Appl. Phys. Lett. (2009). doi:10.1063/1.3119215.

[79] L. Petti, N. Münzenrieder, G.A. Salvatore, C. Zysset, T. Kinkeldei, L. Büthe, G. Tröster, Influence of mechanical bending on flexible InGaZnO-based ferroelectric memory TFTs, IEEE Trans. Electron Devices. (2014). doi:10.1109/TED.2014.2304307.

[80] L. Persano, C. Dagdeviren, Y. Su, Y. Zhang, S. Girardo, D. Pisignano, Y. Huang, J.A. Rogers, High performance piezoelectric devices based on aligned arrays of nanofibers of poly(vinylidenefluoride-co-trifluoroethylene), Nat. Commun. (2013). doi:10.1038/ncomms2639.

[81] G. Zhu, R. Yang, S. Wang, Z.L. Wang, Flexible high-output nanogenerator based on lateral ZnO nanowire array, Nano Lett. (2010). doi:10.1021/nl101973h.

[82] Z.L. Wang, ZnO nanowire and nanobelt platform for nanotechnology, Mater. Sci. Eng. R Reports. (2009). doi:10.1016/j.mser.2009.02.001.

[83] S. Xu, Y. Zhang, L. Jia, K.E. Mathewson, K.I. Jang, J. Kim, H. Fu, X. Huang, P. Chava, R. Wang, S. Bhole, L. Wang, Y.J. Na, Y. Guan, M. Flavin, Z. Han, Y. Huang, J.A. Rogers, Soft microfluidic assemblies of sensors, circuits, and radios for the skin, Science (80-.). (2014). doi:10.1126/science.1250169.

[84] A. Larmagnac, S. Eggenberger, H. Janossy, J. Vörös, Stretchable electronics based on Ag-PDMS composites, Sci. Rep. (2014). doi:10.1038/srep07254.

[85] J. Kim, A. Banks, H. Cheng, Z. Xie, S. Xu, K.I. Jang, J.W. Lee, Z. Liu, P. Gutruf, X. Huang, P. Wei, F. Liu, K. Li, M. Dalal, R. Ghaffari, X. Feng, Y. Huang, S. Gupta, U. Paik, J.A. Rogers, Epidermal electronics with advanced capabilities in near-field communication, Small. (2015). doi:10.1002/smll.201402495.

[86] P.D. Mitcheson, E.M. Yeatman, G.K. Rao, A.S. Holmes, T.C. Green, Energy harvesting from human and machine motion for wireless electronic devices, Proc. IEEE. (2008). doi:10.1109/JPROC.2008.927494.

[87] X. Huang, Y. Liu, G.W. Kong, J.H. Seo, Y. Ma, K.I. Jang, J.A. Fan, S. Mao, Q. Chen, D. Li, H. Liu, C. Wang, D. Patnaik, L. Tian, G.A. Salvatore, X. Feng, Z. Ma, Y. Huang, J.A. Rogers, Epidermal radio frequency electronics for wireless power transfer, Microsystems Nanoeng. (2016). doi:10.1038/micronano.2016.52.

[88] K. J., S. G.A., A. H., C. A.M., X. Z., B. A., S. X., L. Y., L. J.W., J. K.-I., H. S.Y., C. K., L. H., Z. B., K. J., Y. L., F. X., X. S., F. M., G. G., H. Y., P. U., R. J.A., Battery-free, stretchable optoelectronic systems for wireless optical characterization of the skin, Sci. Adv. (2016). doi:10.1126/sciadv.1600418 LK - http://rug.on.worldcat.org/atoztitles/link/?sid=EMBASE&issn=23752548&id=doi:10.1126%2Fsciadv.1600418&atitle=Battery-free%2C+stretchable+optoelectronic+systems+for+wireless+optical+characterization+of+the+skin&stitle=Sci+Adv&title=Science+advances&volume=2&issue=8&spage=e1600418&epage=&aulast=Kim&aufirst=Jeonghyun&auinit=J.&aufull=Kim+J.&coden=&isbn=&pages=e1600418-&date=2016&auinit1=J&auinitm=.

[89] Y. Huang, H. Hu, Y. Huang, M. Zhu, W. Meng, C. Liu, Z. Pei, C. Hao, Z. Wang, C. Zhi, From industrially weavable and knittable highly conductive yarns to large wearable energy storage textiles, ACS Nano. (2015). doi:10.1021/acsnano.5b00860.

[90] X. Pu, L. Li, H. Song, C. Du, Z. Zhao, C. Jiang, G. Cao, W. Hu, Z.L. Wang, A self-charging power unit by integration of a textile triboelectric nanogenerator and a flexible lithium-ion battery for wearable electronics, Adv. Mater. (2015). doi:10.1002/adma.201500311.

[91] J. Wang, S. Li, F. Yi, Y. Zi, J. Lin, X. Wang, Y. Xu, Z.L. Wang, Sustainably powering wearable electronics solely by biomechanical energy, Nat. Commun. (2016).

doi:10.1038/ncomms12744.
[92] N.S. Shenck, J.A. Paradiso, Energy scavenging with shoe-mounted piezoelectrics, IEEE Micro. (2001). doi:10.1109/40.928763.
[93] M. Thielen, L. Sigrist, M. Magno, C. Hierold, L. Benini, Human body heat for powering wearable devices: From thermal energy to application, Energy Convers. Manag. (2017). doi:10.1016/j.enconman.2016.11.005.
[94] Z. Yang, J. Deng, X. Sun, H. Li, H. Peng, Stretchable, wearable dye-sensitized solar cells, Adv. Mater. (2014). doi:10.1002/adma.201400152.
[95] F.C. Krebs, S.A. Gevorgyan, J. Alstrup, A roll-to-roll process to flexible polymer solar cells: Model studies, manufacture and operational stability studies, J. Mater. Chem. (2009). doi:10.1039/b823001c.
[96] M. Kaltenbrunner, M.S. White, E.D. Głowacki, T. Sekitani, T. Someya, N.S. Sariciftci, S. Bauer, Ultrathin and lightweight organic solar cells with high flexibility, Nat. Commun. (2012). doi:10.1038/ncomms1772.
[97] S. Berchmans, A.J. Bandodkar, W. Jia, J. Ramírez, Y.S. Meng, J. Wang, An epidermal alkaline rechargeable Ag-Zn printable tattoo battery for wearable electronics, J. Mater. Chem. A. (2014). doi:10.1039/c4ta03256j.
[98] M. Kaltenbrunner, G. Kettlgruber, C. Siket, R. Schwödiauer, S. Bauer, Stretchable Batteries: Arrays of Ultracompliant Electrochemical Dry Gel Cells for Stretchable Electronics (Adv. Mater. 18/2010), Adv. Mater. (2010). doi:10.1002/adma.201090061.
[99] K. Wang, S. Luo, Y. Wu, X. He, F. Zhao, J. Wang, K. Jiang, S. Fan, Super-aligned carbon nanotube films as current collectors for lightweight and flexible lithium ion batteries, Adv. Funct. Mater. (2013). doi:10.1002/adfm.201202412.
[100] L. Hu, H. Wu, F. La Mantia, Y. Yang, Y. Cui, Thin, flexible secondary Li-ion paper batteries, ACS Nano. (2010). doi:10.1021/nn1018158.
[101] A.M. Gaikwad, G.L. Whiting, D.A. Steingart, A.C. Arias, Highly flexible, printed alkaline batteries based on mesh-embedded electrodes, Adv. Mater. (2011). doi:10.1002/adma.201100894.
[102] L. Long, S. Wang, M. Xiao, Y. Meng, Polymer electrolytes for lithium polymer batteries, J. Mater. Chem. A. (2016). doi:10.1039/c6ta02621d.
[103] J. Saunier, F. Alloin, J.Y. Sanchez, G. Caillon, Thin and flexible lithium-ion batteries: Investigation of polymer electrolytes, in: J. Power Sources, 2003. doi:10.1016/S0378-7753(03)00197-6.
[104] X. Peng, L. Peng, C. Wu, Y. Xie, Two dimensional nanomaterials for flexible supercapacitors, Chem. Soc. Rev. (2014). doi:10.1039/c3cs60407a.
[105] Y. Zhu, S. Murali, M. Stoller, K. Ganesh, Carbon-Based Supercapacitors Produced by Activation of Graphene, Science (80-.). (2011).
[106] W.K. Chee, H.N. Lim, Z. Zainal, N.M. Huang, I. Harrison, Y. Andou, Flexible Graphene-Based Supercapacitors: A Review, J. Phys. Chem. C. (2016). doi:10.1021/acs.jpcc.5b10187.
[107] C. Dagdeviren, B.D. Yang, Y. Su, P.L. Tran, P. Joe, E. Anderson, J. Xia, V. Doraiswamy, B. Dehdashti, X. Feng, B. Lu, R. Poston, Z. Khalpey, R. Ghaffari, Y. Huang, M.J. Slepian, J.A. Rogers, Conformal piezoelectric energy harvesting and storage from motions of the heart, lung, and diaphragm, Proc. Natl. Acad. Sci. U. S. A. (2014). doi:10.1073/pnas.1317233111.
[108] W. Jia, X. Wang, S. Imani, A.J. Bandodkar, J. Ramírez, P.P. Mercier, J. Wang, Wearable

textile biofuel cells for powering electronics, J. Mater. Chem. A. (2014). doi:10.1039/c4ta04796f.
[109] W. Jia, G. Valdés-Ramírez, A.J. Bandodkar, J.R. Windmiller, J. Wang, Epidermal biofuel cells: Energy harvesting from human perspiration, Angew. Chemie - Int. Ed. (2013). doi:10.1002/anie.201302922.
[110] A.J. Bandodkar, J.M. You, N.H. Kim, Y. Gu, R. Kumar, A.M.V. Mohan, J. Kurniawan, S. Imani, T. Nakagawa, B. Parish, M. Parthasarathy, P.P. Mercier, S. Xu, J. Wang, Soft, stretchable, high power density electronic skin-based biofuel cells for scavenging energy from human sweat, Energy Environ. Sci. (2017). doi:10.1039/c7ee00865a.
[111] D.J. Lipomi, B.C.K. Tee, M. Vosgueritchian, Z. Bao, Stretchable organic solar cells, Adv. Mater. (2011). doi:10.1002/adma.201004426.
[112] A. King, Technology: The Future of Agriculture, Nature. (2017). doi:10.1038/544S21a.
[113] S. Blackmore, New concepts in agricultural automation, in: Precis. Arab. Farming Curr. Pract. Futur. Potential, 2009.
[114] F. Tobe, Views and forecasts about robotics for the ag industry, Http//Robohub.Org/Viewsand- Forecast. (2017).
[115] S.M. Pedersen, S. Fountas, H. Have, B.S. Blackmore, Agricultural robots - System analysis and economic feasibility, Precis. Agric. (2006). doi:10.1007/s11119-006-9014-9.
[116] J. Maier, Made smarter review. Department for Business, Energy and Industrial Strategy, Http://Hdl.Voced.Edu.Au/10707/444094. (2017).
[117] T. Duckett, S. Pearson, S. Blackmore, B. Grieve, W.-H. Chen, G. Cielniak, J. Cleaversmith, J. Dai, S. Davis, C. Fox, P. From, I. Georgilas, R. Gill, I. Gould, M. Hanheide, A. Hunter, F. Iida, L. Mihalyova, S. Nefti-Meziani, G. Neumann, P. Paoletti, T. Pridmore, D. Ross, M. Smith, M. Stoelen, M. Swainson, S. Wane, P. Wilson, I. Wright, G.-Z. Yang, Agricultural Robotics: The Future of Robotic Agriculture, (2018). http://arxiv.org/abs/1806.06762.
[118] R.N. Jørgensen, C.G. Sørensen, J.M. Pedersen, I. Havn, K. Jensen, H.T. Søgaard, S. L.B., Hortibot: A system design of a robotic tool carrier for high-tech plant nursing, CIGR Ejournal. (2007).
[119] T. Bakker, K. Asselt, J. Bontsema, J. Müller, G. Straten, Systematic design of an autonomous platform for robotic weeding, J. Terramechanics. (2010). doi:10.1016/j.jterra.2009.06.002.
[120] A.K. Mohanty, M. Misra, L.T. Drzal, Sustainable Bio-Composites from renewable resources: Opportunities and challenges in the green materials world, J. Polym. Environ. (2002). doi:10.1023/A:1021013921916.
[121] Rare Earths Elements in High-Tech Industries: Market Analysis and Forecasts amid China's Trade, Res. Mark. (2016).
[122] M.K. Hubbert, Techniques of Prediction as Applied to Production of Oil and Gas, US Dep. Commer. NBS Spec. Publ. (1982).
[123] Tesla Powerwall, Http://Www.Teslamotors.Com/Powerwall. (2016).
[124] Q.A. Schuyler, C. Wilcox, K. Townsend, B.D. Hardesty, N.J. Marshall, Mistaken identity? Visual similarities of marine debris to natural prey items of sea turtles, BMC Ecol. (2014). doi:10.1186/1472-6785-14-14.
[125] M. Wagner, C. Scherer, D. Alvarez-Muñoz, N. Brennholt, X. Bourrain, S. Buchinger, E. Fries, C. Grosbois, J. Klasmeier, T. Marti, S. Rodriguez-Mozaz, R. Urbatzka, A.D. Vethaak, M. Winther-Nielsen, G. Reifferscheid, Microplastics in freshwater ecosystems: what we know and what we need to know, Environ. Sci. Eur. (2014). doi:10.1186/s12302-014-

0012-7.
[126] E. Doelker, Cellulose derivatives, Adv. Polym. Sci. (1993). doi:10.1007/978-3-662-44324-8_2134.
[127] D. Klemm, B. Philipp, T. Heinze, U. Heinze, W. Wagenknecht, Comprehensive Cellulose Chemistry: Volume I: Fundamentals and analytical Methods, 1998. doi:10.1002/3527601929.
[128] F.W. Lichtenthaler, S. Peters, Carbohydrates as green raw materials for the chemical industry, Comptes Rendus Chim. (2004). doi:10.1016/j.crci.2004.02.002.
[129] G. Li, Y. Li, G. Chen, J. He, Y. Han, X. Wang, D.L. Kaplan, Silk-Based Biomaterials in Biomedical Textiles and Fiber-Based Implants, Adv. Healthc. Mater. (2015). doi:10.1002/adhm.201500002.
[130] Ezgi Bezirhan Arikan, Havva Duygu Ozsoy, A Review: Investigation of Bioplastics, J. Civ. Eng. Archit. 9 (2015) 188–192. doi:10.17265/1934-7359/2015.02.007.
[131] S.M. Emadian, T.T. Onay, B. Demirel, Biodegradation of bioplastics in natural environments, Waste Manag. 59 (2017) 526–536. doi:10.1016/j.wasman.2016.10.006.
[132] A.N. Boyandin, S. V. Prudnikova, V.A. Karpov, V.N. Ivonin, N.L. Dỗ, T.H. Nguyễn, T.M.H. Lê, N.L. Filichev, A.L. Levin, M.L. Filipenko, T.G. Volova, I.I. Gitelson, Microbial degradation of polyhydroxyalkanoates in tropical soils, Int. Biodeterior. Biodegrad. 83 (2013) 77–84. doi:10.1016/j.ibiod.2013.04.014.
[133] L.D. Chambers, J. Winfield, I. Ieropoulos, J. Rossiter, Biodegradable and edible gelatine actuators for use as artificial muscles, in: Electroact. Polym. Actuators Devices 2014, 2014. doi:10.1117/12.2045104.
[134] L. Lu, W. Chen, Biocompatible composite actuator: A supramolecular structure consisting of the biopolymer chitosan, carbon nanotubes, and an ionic liquid, Adv. Mater. (2010). doi:10.1002/adma.201001134.
[135] S. Yun, J. Kim, C. Song, Performance of Electro-active paper actuators with thickness variation, Sensors Actuators, A Phys. (2007). doi:10.1016/j.sna.2006.03.007.
[136] K. Mukai, K. Asaka, K. Kiyohara, T. Sugino, I. Takeuchi, T. Fukushima, T. Aida, High performance fully plastic actuator based on ionic-liquid-based bucky gel, Electrochim. Acta. (2008). doi:10.1016/j.electacta.2008.02.113.
[137] J. Winfield, I. Ieropoulos, J. Rossiter, J. Greenman, D. Patton, Biodegradation and proton exchange using natural rubber in microbial fuel cells, Biodegradation. (2013). doi:10.1007/s10532-013-9621-x.
[138] J. Winfield, L.D. Chambers, J. Rossiter, A. Stinchcombe, X.A. Walter, J. Greenman, I. Ieropoulos, Fade to Green: A Biodegradable Stack of Microbial Fuel Cells, ChemSusChem. (2015). doi:10.1002/cssc.201500431.
[139] J. Winfield, L.D. Chambers, J. Rossiter, J. Greenman, I. Ieropoulos, Urine-activated origami microbial fuel cells to signal proof of life, J. Mater. Chem. A. (2015). doi:10.1039/c5ta00687b.
[140] S. Zhang, N. Sun, X. He, X. Lu, X. Zhang, Physical properties of ionic liquids: Database and evaluation, J. Phys. Chem. Ref. Data. 35 (2006) 1475–1517. doi:10.1063/1.2204959.
[141] S. Nemat-Nasser, J.Y. Li, Electromechanical response of ionic polymer-metal composites, J. Appl. Phys. (2000). doi:10.1063/1.372343.
[142] Y. Xia, K. Sun, J. Ouyang, Solution-processed metallic conducting polymer films as transparent electrode of optoelectronic devices, Adv. Mater. (2012). doi:10.1002/adma.201104795.

[143] K.J. Kim, M. Shahinpoor, Ionic polymer metal composites: II. Manufacturing techniques, Smart Mater. Struct. 12 (2003) 65–79. doi:10.1088/0964-1726/12/1/308.
[144] K. Asaka, Soft Actuators, 2012. doi:10.1002/9783527646982.ch13.
[145] S. Sekine, Y. Ido, T. Miyake, K. Nagamine, M. Nishizawa, Conducting polymer electrodes printed on hydrogel, J. Am. Chem. Soc. (2010). doi:10.1021/ja1062357.
[146] F.M. Weiss, T. Töpper, B. Osmani, C. Winterhalter, B. Müller, Impact of electrode preparation on the bending of asymmetric planar electro-active polymer microstructures, in: Electroact. Polym. Actuators Devices 2014, 2014. doi:10.1117/12.2045152.
[147] R.W. Jones, P. Wang, B. Lassen, R. Sarban, Dielectric elastomers and compliant metal electrode technology, in: Proc. Mediterr. Electrotech. Conf. - MELECON, 2010. doi:10.1109/MELCON.2010.5476257.
[148] T.L. Chen, D.S. Ghosh, V. Mkhitaryan, V. Pruneri, Hybrid transparent conductive film on flexible glass formed by hot-pressing graphene on a silver nanowire mesh, ACS Appl. Mater. Interfaces. (2013). doi:10.1021/am403440n.
[149] M.A. Meitl, Y. Zhou, A. Gaur, S. Jeon, M.L. Usrey, M.S. Strano, J.A. Rogers, Solution casting and transfer printing single-walled carbon nanotube films, Nano Lett. (2004). doi:10.1021/nl0491935.
[150] T. Fukushima, T. Aida, Ionic liquids for soft functional materials with carbon nanotubes, Chem. - A Eur. J. (2007). doi:10.1002/chem.200700554.
[151] K.E. Whitener, P.E. Sheehan, Graphene synthesis, Diam. Relat. Mater. 46 (2014) 25–34. doi:10.1016/j.diamond.2014.04.006.
[152] C. Ghisleri, F. Borghi, L. Ravagnan, A. Podestà, C. Melis, L. Colombo, P. Milani, Patterning of gold-polydimethylsiloxane (Au-PDMS) nanocomposites by supersonic cluster beam implantation, J. Phys. D. Appl. Phys. (2014). doi:10.1088/0022-3727/47/1/015301.
[153] F. Borghi, C. Melis, C. Ghisleri, A. Podestà, L. Ravagnan, L. Colombo, P. Milani, Stretchable nanocomposite electrodes with tunable mechanical properties by supersonic cluster beam implantation in elastomers, Appl. Phys. Lett. 106 (2015). doi:10.1063/1.4916350.
[154] K. Wegner, P. Piseri, H.V. Tafreshi, P. Milani, Cluster beam deposition: A tool for nanoscale science and technology, J. Phys. D. Appl. Phys. 39 (2006). doi:10.1088/0022-3727/39/22/R02.
[155] G. Corbelli, Synthesis and Characterization of metal-polymer nanocomposites for stretchable electronics applications, Phd - Thesis Univ. Degli Stud. Di Milano. (2011) 47–57.
[156] P. Piseri, H.V. Tafreshi, P. Milani, Manipulation of nanoparticles in supersonic beams for the production of nanostructured materials, Curr. Opin. Solid State Mater. Sci. (2004). doi:10.1016/j.cossms.2004.08.002.
[157] F. Di Fonzo, A. Gidwani, M.H. Fan, D. Neumann, D.I. Iordanoglou, J.V.R. Heberlein, P.H. McMurry, S.L. Girshick, N. Tymiak, W.W. Gerberich, N.P. Rao, Focused nanoparticle-beam deposition of patterned microstructures, Appl. Phys. Lett. (2000). doi:10.1063/1.1306638.
[158] H.L. Lim, Y. Hwang, M. Kar, S. Varghese, Smart hydrogels as functional biomimetic systems, Biomater. Sci. 2 (2014) 603–618. doi:10.1039/c3bm60288e.
[159] M.L. O'Grady, P.L. Kuo, K.K. Parker, Optimization of electroactive hydrogel actuators, ACS Appl. Mater. Interfaces. 2 (2010) 343–346. doi:10.1021/am900755w.

[160] L. Engel, O. Berkh, K. Adesanya, J. Shklovsky, E. Vanderleyden, P. Dubruel, Y. Shacham-Diamand, S. Krylov, Actuation of a novel Pluronic-based hydrogel: Electromechanical response and the role of applied current, Sensors Actuators, B Chem. 191 (2014) 650–658. doi:10.1016/j.snb.2013.10.031.
[161] T. Jayaramudu, H.U. Ko, H.C. Kim, J.W. Kim, Y. Li, J. Kim, Transparent and semi-interpenetrating network P(vinyl alcohol)- P(Acrylic acid) hydrogels: pH responsive and electroactive application, Int. J. Smart Nano Mater. 8 (2017) 80–94. doi:10.1080/19475411.2017.1335247.
[162] L. Migliorini, T. Santaniello, Y. Yan, C. Lenardi, P. Milani, Low-voltage electrically driven homeostatic hydrogel-based actuators for underwater soft robotics, Sensors Actuators, B Chem. 228 (2016) 758–766. doi:10.1016/j.snb.2016.01.110.
[163] M. Rubinstein, R.H. Colby, Polymer physics, Polym. Int. (2003). doi:10.1002/pi.1472.
[164] O. Okay, General Properties of Hydrogels, in: 2009. doi:10.1007/978-3-540-75645-3_1.
[165] P. Calvert, Electroactive Polymer Gels, Electroact. Polym. Actuators as Artif. Muscles - Reality, Potential Challenges. (2004) 1–16. https://books.google.co.uk/books?id=uxqgkdqE9FIC&dq=%22Paul+Calvert%22+chapter+5&source=gbs_navlinks_s.
[166] S. Han, C. Liu, H. Xu, D. Yao, K. Yan, H. Zheng, H.-J. Chen, X. Gui, S. Chu, C. Liu, Multiscale nanowire-microfluidic hybrid strain sensors with high sensitivity and stretchability, Npj Flex. Electron. 2 (2018). doi:10.1038/s41528-018-0029-x.
[167] N. Rahimi, D.G. Molin, T.J. Cleij, M.A. Van Zandvoort, M.J. Post, Electrosensitive polyacrylic acid/fibrin hydrogel facilitates cell seeding and alignment, Biomacromolecules. (2012). doi:10.1021/bm300161r.
[168] D. Morales, E. Palleau, M.D. Dickey, O.D. Velev, Electro-actuated hydrogel walkers with dual responsive legs, Soft Matter. 10 (2014) 1337–1348. doi:10.1039/c3sm51921j.
[169] J. Feng, S.K. Cho, Mini and micro propulsion for medical swimmers, Micromachines. 5 (2014) 97–113. doi:10.3390/mi5010097.
[170] G.H. Kwon, Y.Y. Choi, J.Y. Park, D.H. Woo, K.B. Lee, J.H. Kim, S.H. Lee, Electrically-driven hydrogel actuators in microfluidic channels: Fabrication, characterization, and biological application, Lab Chip. 10 (2010) 1604–1610. doi:10.1039/b926443d.
[171] S. Jin, J. Gu, Y. Shi, K. Shao, X. Yu, G. Yue, Preparation and electrical sensitive behavior of poly (N-vinylpyrrolidone- co-acrylic acid) hydrogel with flexible chain nature, Eur. Polym. J. 49 (2013) 1871–1880. doi:10.1016/j.eurpolymj.2013.04.022.
[172] F. Fu, L. Shang, Z. Chen, Y. Yu, Y. Zhao, Bioinspired living structural color hydrogels, Sci. Robot. 3 (2018) eaar8580. doi:10.1126/scirobotics.aar8580.
[173] K. Tian, Z. Shao, X. Chen, Natural electroactive hydrogel from soy protein isolation, Biomacromolecules. 11 (2010) 3638–3643. doi:10.1021/bm101094g.
[174] M. Bassil, J. Davenas, M. EL Tahchi, Electrochemical properties and actuation mechanisms of polyacrylamide hydrogel for artificial muscle application, Sensors Actuators, B Chem. (2008). doi:10.1016/j.snb.2008.05.025.
[175] T. Tanaka, I. Nishio, S.T. Sun, S. Ueno-Nishio, Collapse of gels in an electric field, Science (80-.). (1982). doi:10.1126/science.218.4571.467.
[176] J.P. Gong, T. Nitta, Y. Osada, Electrokinetic modeling of the contractile phenomena of polyelectrolyte gels. one-dimensional capillary model, J. Phys. Chem. (1994). doi:10.1021/j100089a036.
[177] M. Doi, M. Matsumoto, Y. Hirose, Deformation of Ionic Polymer Gels by Electric Fields,

Macromolecules. 25 (1992) 5504–5511. doi:10.1021/ma00046a058.
[178] T. Yamaue, H. Mukai, K. Asaka, M. Doi, Electrostress diffusion coupling model for polyelectrolyte gels, Macromolecules. (2005). doi:10.1021/ma047944j.
[179] S.E. Elshaer, W.A. Moussa, Comparative study of chemo-electro-mechanical transport models for an electrically stimulated hydrogel, Smart Mater. Struct. (2014). doi:10.1088/0964-1726/23/7/075022.
[180] M. Bassil, M. Ibrahim, M. El Tahchi, Artificial muscular microfibers: Hydrogel with high speed tunable electroactivity, Soft Matter. (2011). doi:10.1039/c1sm05131h.
[181] M.K. Shin, G.M. Spinks, S.R. Shin, S.I. Kim, S.J. Kim, Nanocomposite hydrogel with high toughness for bioactuators, Adv. Mater. 21 (2009) 1712–1715. doi:10.1002/adma.200802205.
[182] Q. Wang, R. Hou, Y. Cheng, J. Fu, Super-tough double-network hydrogels reinforced by covalently compositing with silica-nanoparticles, Soft Matter. (2012). doi:10.1039/c2sm07233e.
[183] W. Zhao, L. Duan, B. Zhang, X. Ren, G.H. Gao, Tough and ultrastretchable hydrogels reinforced by poly(butyl acrylate-co-acrylonitrile) latex microspheres as crosslinking centers for hydrophobic association, Polymer (Guildf). (2017). doi:10.1016/j.polymer.2017.02.032.
[184] S. Kango, S. Kalia, A. Celli, J. Njuguna, Y. Habibi, R. Kumar, Surface modification of inorganic nanoparticles for development of organic-inorganic nanocomposites - A review, Prog. Polym. Sci. (2013). doi:10.1016/j.progpolymsci.2013.02.003.
[185] Z. Tai, J. Yang, Y. Qi, X. Yan, Q. Xue, Synthesis of a graphene oxide-polyacrylic acid nanocomposite hydrogel and its swelling and electroresponsive properties, RSC Adv. (2013). doi:10.1039/c3ra22335c.
[186] S. Merino, C. Martín, K. Kostarelos, M. Prato, E. Vázquez, Nanocomposite hydrogels: 3D polymer-nanoparticle synergies for on-demand drug delivery, ACS Nano. (2015). doi:10.1021/acsnano.5b01433.
[187] V. Thomas, M. Namdeo, Y.M. Mohan, S.K. Bajpai, M. Bajpai, Review on polymer, hydrogel and microgel metal nanocomposites: A facile nanotechnological approach, J. Macromol. Sci. Part A Pure Appl. Chem. 45 (2008) 107–119. doi:10.1080/10601320701683470.
[188] S. Liu, G. Gao, Y. Xiao, J. Fu, Tough and responsive oppositely charged nanocomposite hydrogels for use as bilayer actuators assembled through interfacial electrostatic attraction, J. Mater. Chem. B. (2016). doi:10.1039/c6tb00583g.
[189] J.H. Kim, B.S. Shim, H.S. Kim, Y.J. Lee, S.K. Min, D. Jang, Z. Abas, J. Kim, Review of nanocellulose for sustainable future materials, Int. J. Precis. Eng. Manuf. - Green Technol. (2015). doi:10.1007/s40684-015-0024-9.
[190] R. Sanna, E. Fortunati, V. Alzari, D. Nuvoli, A. Terenzi, M.F. Casula, J.M. Kenny, A. Mariani, Poly(N-vinylcaprolactam) nanocomposites containing nanocrystalline cellulose: A green approach to thermoresponsive hydrogels, Cellulose. (2013). doi:10.1007/s10570-013-9988-1.
[191] J. Yang, J.J. Zhao, F. Xu, R.C. Sun, Revealing strong nanocomposite hydrogels reinforced by cellulose nanocrystals: Insight into morphologies and interactions, ACS Appl. Mater. Interfaces. (2013). doi:10.1021/am403669n.
[192] K.J. De France, K.J.W. Chan, E.D. Cranston, T. Hoare, Enhanced Mechanical Properties in Cellulose Nanocrystal-Poly(oligoethylene glycol methacrylate) Injectable

Nanocomposite Hydrogels through Control of Physical and Chemical Cross-Linking, Biomacromolecules. (2016). doi:10.1021/acs.biomac.5b01598.
[193] J. Han, T. Lei, Q. Wu, High-water-content mouldable polyvinyl alcohol-borax hydrogels reinforced by well-dispersed cellulose nanoparticles: Dynamic rheological properties and hydrogel formation mechanism, Carbohydr. Polym. (2014). doi:10.1016/j.carbpol.2013.11.045.
[194] T. Santaniello, L. Migliorini, E. Locatelli, I. Monaco, Y. Yan, C. Lenardi, M.C. Franchini, P. Milani, Hybrid nanocomposites based on electroactive hydrogels and cellulose nanocrystals for high-sensitivity electro–mechanical underwater actuation, Smart Mater. Struct. 26 (2017). doi:10.1088/1361-665X/aa7cb6.
[195] C. Chang, L. Zhang, Cellulose-based hydrogels: Present status and application prospects, Carbohydr. Polym. 84 (2011) 40–53. doi:10.1016/j.carbpol.2010.12.023.
[196] C.C. Hydrogel, Electrical Behavior of a Natural Polyelectrolyte Hydrogel :, Society. (2008) 1208–1213. doi:10.1021/bm701204j.
[197] J.P. Maréchal, C. Hellio, Challenges for the development of new non-toxic antifouling solutions, Int. J. Mol. Sci. 10 (2009) 4623–4637. doi:10.3390/ijms10114623.
[198] J. Chapman, C. Hellio, T. Sullivan, R. Brown, S. Russell, E. Kiterringham, L. Le Nor, F. Regan, Bioinspired synthetic macroalgae: Examples from nature for antifouling applications, Int. Biodeterior. Biodegrad. 86 (2014) 6–13. doi:10.1016/j.ibiod.2013.03.036.
[199] H. Tamiya, Mass culture of Algae, Annu. Rev. Plant Physiol. J. (1956). doi:10.1146/annurev.pp.08.060157.001521.
[200] G.J. Edgar, Artificial algae as habitats for mobile epifauna: factors affecting colonization in a Japanese Sargassum bed, Hydrobiologia. 226 (1991) 111–118. doi:10.1007/BF00006812.
[201] S.A. Uymaz, G. Tezel, E. Yel, Artificial algae algorithm (AAA) for nonlinear global optimization, Appl. Soft Comput. J. 31 (2015) 153–171. doi:10.1016/j.asoc.2015.03.003.
[202] E. Ryder, S.G. Nelson, C. McKeon, E.P. Glenn, K. Fitzsimmons, S. Napolean, Effect of water motion on the cultivation of the economic seaweed Gracilaria parvispora (Rhodophyta) on Molokai, Hawaii, Aquaculture. 238 (2004) 207–219. doi:10.1016/j.aquaculture.2004.05.019.
[203] C. Peteiro, Ó. Freire, Effect of water motion on the cultivation of the commercial seaweed Undaria pinnatifida in a coastal bay of Galicia, Northwest Spain, Aquaculture. 314 (2011) 269–276. doi:10.1016/j.aquaculture.2011.02.009.
[204] C.D. Hepburn, J.D. Holborow, S.R. Wing, R.D. Frew, C.L. Hurd, Exposure to waves enhances the growth rate and nitrogen status of the giant kelp Macrocystis pyrifera, Mar. Ecol. Prog. Ser. (2007). doi:10.3354/meps339099.
[205] C.L. Hurd, Water motion, marine macroalgal physiology, and production, J. Phycol. 36 (2000) 453–472. doi:10.1046/j.1529-8817.2000.99139.x.
[206] S.O. Olanrewaju, A. Magee, A.S.A. Kader, K.F. Tee, Simulation of offshore aquaculture system for macro algae (seaweed) oceanic farming, Ships Offshore Struct. (2017). doi:10.1080/17445302.2016.1186861.
[207] E.G. Leigh, R.T. Paine, J.F. Quinn, T.H. Suchanek, Wave energy and intertidal productivity, Proc. Natl. Acad. Sci. 84 (1987) 1314–1318. doi:10.1073/pnas.84.5.1314.
[208] Y. Gonen, E. Kimmel, M. Friedlander, Diffusion boundary layer transport in *Gracilaria conferta* (Rhodophyta), J. Phycol. (1995).

[209] L. Migliorini, Y. Yan, F. Pezzotta, F.M.S. Veronesi, C. Lenardi, S. Rondinini, T. Santaniello, P. Milani, Cellulose-based electroactive hydrogels for seaweed mimicking toward hybrid artificial habitats creation, MRS Commun. 8 (2018) 1129–1134. doi:10.1557/mrc.2018.163.
[210] T. Yasin, S. Ahmed, F. Yoshii, K. Makuuchi, Effect of acrylonitrile content on physical properties of electron beam irradiated acrylonitrile-butadiene rubber, React. Funct. Polym. (2003). doi:10.1016/j.reactfunctpolym.2003.08.004.
[211] L. Migliorini, T. Santaniello, Y. Yan, C. Lenardi, P. Milani, Low-voltage electrically driven homeostatic hydrogel-based actuators for underwater soft robotics, Sensors Actuators, B Chem. 228 (2016). doi:10.1016/j.snb.2016.01.110.
[212] C. Majidi, Soft Robotics: A Perspective—Current Trends and Prospects for the Future, Soft Robot. 1 (2014) 5–11. doi:10.1089/soro.2013.0001.
[213] K.A. Mauritz, R.B. Moore, State of understanding of Nafion, Chem. Rev. 104 (2004) 4535–4585. doi:10.1021/cr0207123.
[214] B.J. Landi, R.P. Raffaelle, M.J. Heben, J.L. Alleman, W. VanDerveer, T. Gennett, Single Wall Carbon Nanotube - Nafion Composite Actuators, Nano Lett. 2 (2002) 1329–1332. doi:10.1021/nl025800h.
[215] J.H. Jung, S. Vadahanambi, I.K. Oh, Electro-active nano-composite actuator based on fullerene-reinforced Nafion, Compos. Sci. Technol. 70 (2010) 584–592. doi:10.1016/j.compscitech.2009.12.007.
[216] B.J. Akle, M.D. Bennett, D.J. Leo, High-strain ionomeric-ionic liquid electroactive actuators, Sensors Actuators, A Phys. 126 (2006) 173–181. doi:10.1016/j.sna.2005.09.006.
[217] J. Lu, F. Yan, J. Texter, Advanced applications of ionic liquids in polymer science, Prog. Polym. Sci. 34 (2009) 431–448. doi:10.1016/j.progpolymsci.2008.12.001.
[218] J. Le Bideau, L. Viau, A. Vioux, Ionogels, ionic liquid based hybrid materials, Chem. Soc. Rev. 40 (2011) 907–925. doi:10.1039/c0cs00059k.
[219] S.H. Ko, H. Pan, C.P. Grigoropoulos, C.K. Luscombe, J.M.J. Fréchet, D. Poulikakos, All-inkjet-printed flexible electronics fabrication on a polymer substrate by low-temperature high-resolution selective laser sintering of metal nanoparticles, Nanotechnology. 18 (2007). doi:10.1088/0957-4484/18/34/345202.
[220] K. Park, M.K. Yoon, S. Lee, J. Choi, M. Thubrikar, Effects of electrode degradation and solvent evaporation on the performance of ionic-polymer-metal composite sensors, Smart Mater. Struct. 19 (2010). doi:10.1088/0964-1726/19/7/075002.
[221] Y. Xu, G. Zhao, L.M. Yang, J.X. Zheng, C.S. Ma, Y.M. Zhu, Research on preparation technique of IPMC artificial muscle, Gongneng Cailiao/Journal Funct. Mater. (2013). doi:10.3969/j.issn.1001-9731.2013.11.029.
[222] S.S. Kim, J.H. Jeon, H. Il Kim, C.D. Kee, I.K. Oh, High-Fidelity Bioelectronic Muscular Actuator Based on Graphene-Mediated and TEMPO-Oxidized Bacterial Cellulose, Adv. Funct. Mater. (2015). doi:10.1002/adfm.201500673.
[223] K. Asaka, K. Mukai, T. Sugino, K. Kiyohara, Ionic electroactive polymer actuators based on nano-carbon electrodes, Polym. Int. (2013). doi:10.1002/pi.4562.
[224] G. Wu, Y. Hu, Y. Liu, J. Zhao, X. Chen, V. Whoehling, C. Plesse, G.T.M. Nguyen, F. Vidal, W. Chen, Graphitic carbon nitride nanosheet electrode-based high-performance ionic actuator, Nat. Commun. (2015). doi:10.1038/ncomms8258.
[225] M. Kotal, J. Kim, K.J. Kim, I.K. Oh, Sulfur and Nitrogen Co-Doped Graphene Electrodes for

High-Performance Ionic Artificial Muscles, Adv. Mater. (2016). doi:10.1002/adma.201505243.
[226] J. Kim, S.-H. Bae, M. Kotal, T. Stalbaum, K.J. Kim, I.-K. Oh, Polymer Actuators: Soft but Powerful Artificial Muscles Based on 3D Graphene-CNT-Ni Heteronanostructures (Small 31/2017), Small. (2017). doi:10.1002/smll.201770167.
[227] H. Okuzaki, S. Takagi, F. Hishiki, R. Tanigawa, Ionic liquid/polyurethane/PEDOT:PSS composites for electro-active polymer actuators, Sensors Actuators, B Chem. (2014). doi:10.1016/j.snb.2013.12.059.
[228] J. Kim, S.D. Deshpande, S. Yun, Q. Li, A comparative study of conductive polypyrrole and polyaniline coatings on electro-active papers, Polym. J. (2006). doi:10.1295/polymj.PJ2005185.
[229] M. Shahinpoor ' ') ', Y. Bar-Cohen@, T. Xue@, J.O. Simpson@, J. Smith, Ionic Polymer - Metal Composites (IPMC) As Biomimetic Sensors and Actuators - Artificial Muscles, (1998) 1–5. doi:10.1021/bk-1999-0726.ch003.
[230] D. Pugal, K. Jung, A. Aabloo, K.J. Kim, Ionic polymer-metal composite mechanoelectrical transduction: Review and perspectives, Polym. Int. 59 (2010) 279–289. doi:10.1002/pi.2759.
[231] S. Nemat-Nasser, Micromechanics of actuation of ionic polymer-metal composites, J. Appl. Phys. 92 (2002) 2899–2915. doi:10.1063/1.1495888.
[232] H. Okazaki, S. Sawada, M. Kimura, H. Tanaka, T. Matsumoto, T. Ohtake, S. Inoue, Soft actuator using ionic polymer-metal composite composed of gold electrodes deposited using vacuum evaporation, IEEE Electron Device Lett. (2012). doi:10.1109/LED.2012.2196970.
[233] A. Kusoglu, A.Z. Weber, Electrochemical/Mechanical Coupling in Ion-Conducting Soft Matter, J. Phys. Chem. Lett. (2015). doi:10.1021/acs.jpclett.5b01639.
[234] C. Paper, S. Anodic, D. Wang, F. Li, J. Zhao, W. Ren, Z. Chen, J. Tan, Z. Wu, I. Gentle, G.Q. Lu, H. Cheng, Fabrication of Graphene / Polyaniline, 3 (2009) 1745–1752.
[235] H. Rasouli, L. Naji, M.G. Hosseini, Electrochemical and electromechanical behavior of Nafion-based soft actuators with PPy/CB/MWCNT nanocomposite electrodes, RSC Adv. 7 (2017) 3190–3203. doi:10.1039/C6RA25771B.
[236] M. Canales, D. Aradilla, C. Alemán, Water absorption in polyaniline emeraldine base, J. Polym. Sci. Part B Polym. Phys. 49 (2011) 1322–1331. doi:10.1002/polb.22300.
[237] W. Gao, The chemistry of graphene oxide, in: Graphene Oxide Reduct. Recipes, Spectrosc. Appl., 2015. doi:10.1007/978-3-319-15500-5_3.
[238] F. Liu, N.A. Hashim, Y. Liu, M.R.M. Abed, K. Li, Progress in the production and modification of PVDF membranes, J. Memb. Sci. 375 (2011) 1–27. doi:10.1016/j.memsci.2011.03.014.
[239] J.C. Dias, A.C. Lopes, B. Magalhães, G. Botelho, M.M. Silva, J.M.S.S. Esperança, S. Lanceros-Mendez, High performance electromechanical actuators based on ionic liquid/poly(vinylidene fluoride), Polym. Test. 48 (2015) 199–205. doi:10.1016/j.polymertesting.2015.10.012.
[240] Y. Tang, Z. Xue, X. Zhou, X. Xie, C.Y. Tang, Novel sulfonated polysulfone ion exchange membranes for ionic polymer-metal composite actuators, Sensors Actuators, B Chem. 202 (2014) 1164–1174. doi:10.1016/j.snb.2014.06.071.
[241] Inamuddin, A. Khan, R.K. Jain, M. Naushad, Development of sulfonated poly(vinyl alcohol)/polpyrrole based ionic polymer metal composite (IPMC) actuator and its

characterization, Smart Mater. Struct. 24 (2015). doi:10.1088/0964-1726/24/9/095003.
[242] Y. Yan, T. Santaniello, L.G. Bettini, C. Minnai, A. Bellacicca, R. Porotti, I. Denti, G. Faraone, M. Merlini, C. Lenardi, P. Milani, Electroactive Ionic Soft Actuators with Monolithically Integrated Gold Nanocomposite Electrodes, Adv. Mater. 29 (2017) 1–9. doi:10.1002/adma.201606109.
[243] T. Kataoka, Y. Ishioka, M. Mizuhata, H. Minami, T. Maruyama, Highly Conductive Ionic-Liquid Gels Prepared with Orthogonal Double Networks of a Low-Molecular-Weight Gelator and Cross-Linked Polymer, ACS Appl. Mater. Interfaces. (2015). doi:10.1021/acsami.5b07981.
[244] A.I. Horowitz, M.J. Panzer, Poly(dimethylsiloxane)-supported ionogels with a high ionic liquid loading, Angew. Chemie - Int. Ed. (2014). doi:10.1002/anie.201405691.
[245] C.R. López-Barrón, P.J. Beltramo, Y. Liu, S.M. Choi, M.J. Lee, Mechanical, dielectric and structural characterization of cross-linked PEG-diacrylate/ethylammonium nitrate ionogels, Polymer (Guildf). (2016). doi:10.1016/j.polymer.2016.02.008.
[246] J. Kim, C.S. Song, S.R. Yun, Cellulose based electro-active papers: Performance and environmental effects, Smart Mater. Struct. 15 (2006) 719–723. doi:10.1088/0964-1726/15/3/007.
[247] Z. Sun, W. Song, G. Zhao, H. Wang, Chitosan-based polymer gel paper actuators coated with multi-wall carbon nanotubes and MnO 2 composite electrode, Cellulose. 24 (2017) 4383–4392. doi:10.1007/s10570-017-1416-5.
[248] D. Nevstrueva, K. Murashko, V. Vunder, A. Aabloo, A. Pihlajamäki, M. Mänttäri, J. Pyrhönen, T. Koiranen, J. Torop, Natural cellulose ionogels for soft artificial muscles, Colloids Surfaces B Biointerfaces. 161 (2018) 244–251. doi:10.1016/j.colsurfb.2017.10.053.
[249] I. Must, V. Vunder, F. Kaasik, I. Põldsalu, U. Johanson, A. Punning, A. Aabloo, Ionic liquid-based actuators working in air: The effect of ambient humidity, Sensors Actuators, B Chem. 202 (2014) 114–122. doi:10.1016/j.snb.2014.05.074.
[250] G. Corbelli, C. Ghisleri, M. Marelli, P. Milani, L. Ravagnan, Highly deformable nanostructured elastomeric electrodes with improving conductivity upon cyclical stretching, Adv. Mater. 23 (2011) 4504–4508. doi:10.1002/adma.201102463.
[251] T. Santaniello, L. Migliorini, F. Borghi, Y. Yan, S. Rondinini, C. Lenardi, P. Milani, Spring-like electroactive actuators based on paper/ionogel/metal nanocomposites, Smart Mater. Struct. 27 (2018). doi:10.1088/1361-665X/aabc32.
[252] A. Bellacicca, T. Santaniello, P. Milani, Embedding electronics in 3D printed structures by combining fused filament fabrication and supersonic cluster beam deposition, Addit. Manuf. 24 (2018) 60–66. doi:10.1016/j.addma.2018.09.010.
[253] D. Klemm, B. Heublein, H.P. Fink, A. Bohn, Cellulose: Fascinating biopolymer and sustainable raw material, Angew. Chemie - Int. Ed. (2005). doi:10.1002/anie.200460587.
[254] P. Ball, Material witness: In praise of wood, Nat. Mater. (2005). doi:10.1038/nmat1425.
[255] H. Liu, H. Qing, Z. Li, Y.L. Han, M. Lin, H. Yang, A. Li, T.J. Lu, F. Li, F. Xu, Paper: A promising material for human-friendly functional wearable electronics, Mater. Sci. Eng. R Reports. (2017). doi:10.1016/j.mser.2017.01.001.
[256] M. Santhiago, C.C. Corrêa, J.S. Bernardes, M.P. Pereira, L.J.M. Oliveira, M. Strauss, C.C.B. Bufon, Flexible and Foldable Fully-Printed Carbon Black Conductive Nanostructures on Paper for High-Performance Electronic, Electrochemical, and Wearable Devices, ACS Appl. Mater. Interfaces. (2017). doi:10.1021/acsami.7b06598.

[257] S. Ge, L. Zhang, Y. Zhang, F. Lan, M. Yan, J. Yu, Nanomaterials-modified cellulose paper as a platform for biosensing applications, Nanoscale. (2017). doi:10.1039/c6nr08846e.
[258] M. Amjadi, M. Sitti, High-Performance Multiresponsive Paper Actuators, ACS Nano. (2016). doi:10.1021/acsnano.6b05545.
[259] H.C. Kim, S. Mun, H.U. Ko, L. Zhai, A. Kafy, J. Kim, Renewable smart materials, Smart Mater. Struct. (2016). doi:10.1088/0964-1726/25/7/073001.
[260] M.M. Hamedi, V.E. Campbell, P. Rothemund, F. Güder, D.C. Christodouleas, J.F. Bloch, G.M. Whitesides, Electrically Activated Paper Actuators, Adv. Funct. Mater. (2016). doi:10.1002/adfm.201505123.
[261] H. Shigemune, S. Maeda, Y. Hara, U. Koike, S. Hashimoto, Kirigami robot: Making paper robot using desktop cutting plotter and inkjet printer, in: IEEE Int. Conf. Intell. Robot. Syst., 2015. doi:10.1109/IROS.2015.7353506.
[262] P.K. Yang, Z.H. Lin, K.C. Pradel, L. Lin, X. Li, X. Wen, J.H. He, Z.L. Wang, Paper-based origami triboelectric nanogenerators and self-powered pressure sensors, ACS Nano. (2015). doi:10.1021/nn506631t.
[263] J. Kim, S. Yun, S.K. Mahadeva, K. Yun, S.Y. Yang, M. Maniruzzaman, Paper actuators made with cellulose and hybrid materials, Sensors. (2010). doi:10.3390/s100301473.
[264] A. Khan, Z. Abas, H.S. Kim, J. Kim, Recent progress on cellulose-based electro-active paper, its hybrid nanocomposites and applications, Sensors (Switzerland). (2016). doi:10.3390/s16081172.
[265] S.K. Mahadeva, C. Yi, J. Kim, Effect of room temperature ionic liquids adsorption on electromechanical behavior of cellulose electro-active paper, Macromol. Res. (2009). doi:10.1007/BF03218664.
[266] S.K. Mahadeva, C. Yi, J. Kim, Electrical and electromechanical properties of 1-butyl-3-methylimidazolium bis(trifluoromethylsulfonyl)imide-blended cellulose, Ionics (Kiel). 17 (2011) 41–47. doi:10.1007/s11581-010-0478-2.
[267] S.K. Mahadeva, J. Kim, Nanocoating of ionic liquid and polypyrrole for durable electro-active paper actuators working under ambient conditions, J. Phys. D. Appl. Phys. 43 (2010). doi:10.1088/0022-3727/43/20/205502.
[268] S. Yun, J. Kim, A bending electro-active paper actuator made by mixing multi-walled carbon nanotubes and cellulose, Smart Mater. Struct. (2007). doi:10.1088/0964-1726/16/4/062.
[269] I. Sen, Y. Seki, M. Sarikanat, L. Cetin, B.O. Gurses, O. Ozdemir, O.C. Yilmaz, K. Sever, E. Akar, O. Mermer, Electroactive behavior of graphene nanoplatelets loaded cellulose composite actuators, Compos. Part B Eng. (2015). doi:10.1016/j.compositesb.2014.10.016.
[270] A. Soroudi, I. Jakubowicz, Recycling of bioplastics, their blends and biocomposites: A review, Eur. Polym. J. 49 (2013) 2839–2858. doi:10.1016/j.eurpolymj.2013.07.025.
[271] P.M. Visakh, Polyhydroxyalkanoates (PHAs), their Blends, Composites and Nanocomposites: State of the Art , New Challenges and Opportunities, Polyhydroxyalkanoate Based Blends, Compos. Nanocomposites. (2014) 1–17. doi:10.1039/9781782622314.
[272] S. Ansari, T. Fatma, Cyanobacterial polyhydroxybutyrate (PHB): Screening, optimization and characterization, PLoS One. 11 (2016) 1–20. doi:10.1371/journal.pone.0158168.
[273] Z. Cai, C. Hou, G. Yang, Characteristics and bending performance of electroactive polymer blend made with cellulose and poly(3-hydroxybutyrate), Carbohydr. Polym. 87

(2012) 650–657. doi:10.1016/j.carbpol.2011.08.038.
[274] L. Migliorini, T. Santaniello, S. Rondinini, P. Saettone, M. Comes Franchini, C. Lenardi, P. Milani, Bioplastic electromechanical actuators based on biodegradable poly(3-hydroxybutyrate) and cluster-assembled gold electrodes, Sensors Actuators, B Chem. 286 (2019) 230–236. doi:10.1016/j.snb.2019.01.141.
[275] M. Du, B. Guo, D. Jia, Newly emerging applications of halloysite nanotubes: A review, Polym. Int. (2010). doi:10.1002/pi.2754.
[276] Y. Yan, T. Santaniello, L.G. Bettini, C. Minnai, A. Bellacicca, R. Porotti, I. Denti, G. Faraone, M. Merlini, C. Lenardi, P. Milani, Electroactive Ionic Soft Actuators with Monolithically Integrated Gold Nanocomposite Electrodes, Adv. Mater. 29 (2017) 1–9. doi:10.1002/adma.201606109.
[277] S.L. Li, W.Y. Kim, T.H. Cheng, I.K. Oh, A helical ionic polymer-metal composite actuator for radius control of biomedical active stents, Smart Mater. Struct. (2011). doi:10.1088/0964-1726/20/3/035008.
[278] G.H. Feng, Z.H. Zhan, A room-temperature processed parylene-patterned helical ionic polymer-metal composite spring actuator with selectable active region, Smart Mater. Struct. (2014). doi:10.1088/0964-1726/23/4/045002.
[279] P. Anbukarasu, D. Sauvageau, A. Elias, Tuning the properties of polyhydroxybutyrate films using acetic acid via solvent casting, Sci. Rep. 5 (2015) 1–14. doi:10.1038/srep17884.
[280] L. Mariani, Fog in the Po valley: Some meteo-climatic aspects, Ital. J. Agrometeorol. 44 (2009) 35–44.
[281] T. Reddy, Linden's Handbook of Batteries, Amazon. (2010). doi:10.1016/0378-7753(86)80059-3.
[282] L. Qi, L. Petersson, T. Liu, Review of Recent Activities on Dielectric Films for Capacitor Applications, J. Int. Counc. Electr. Eng. (2014). doi:10.5370/jicee.2014.4.1.001.
[283] Y. Wang, X. Zhou, Q. Chen, B. Chu, Q. Zhang, Recent development of high energy density polymers for dielectric capacitors, IEEE Trans. Dielectr. Electr. Insul. (2010). doi:10.1109/TDEI.2010.5539672.
[284] M. Vangari, T. Pryor, L. Jiang, Supercapacitors: Review of materials and fabrication methods, J. Energy Eng. (2013). doi:10.1061/(ASCE)EY.1943-7897.0000102.
[285] A. González, E. Goikolea, J.A. Barrena, R. Mysyk, Review on supercapacitors: Technologies and materials, Renew. Sustain. Energy Rev. 58 (2016) 1189–1206. doi:10.1016/j.rser.2015.12.249.
[286] L. Zhang, X. Hu, Z. Wang, F. Sun, D.G. Dorrell, A review of supercapacitor modeling, estimation, and applications: A control/management perspective, Renew. Sustain. Energy Rev. (2018). doi:10.1016/j.rser.2017.05.283.
[287] P. Sharma, T.S. Bhatti, A review on electrochemical double-layer capacitors, Energy Convers. Manag. (2010). doi:10.1016/j.enconman.2010.06.031.
[288] C. Costentin, T.R. Porter, J.M. Savéant, How Do Pseudocapacitors Store Energy? Theoretical Analysis and Experimental Illustration, ACS Appl. Mater. Interfaces. (2017). doi:10.1021/acsami.6b14100.
[289] Q. Lu, J.G. Chen, J.Q. Xiao, Nanostructured electrodes for high-performance pseudocapacitors, Angew. Chemie - Int. Ed. (2013). doi:10.1002/anie.201203201.
[290] A. Muzaffar, M.B. Ahamed, K. Deshmukh, J. Thirumalai, A review on recent advances in hybrid supercapacitors: Design, fabrication and applications, Renew. Sustain. Energy

Rev. (2019). doi:10.1016/j.rser.2018.10.026.
[291] J. Ding, W. Hu, E. Paek, D. Mitlin, Review of Hybrid Ion Capacitors: From Aqueous to Lithium to Sodium, Chem. Rev. (2018). doi:10.1021/acs.chemrev.8b00116.
[292] B.E. Logan, B. Hamelers, R. Rozendal, U. Schröder, J. Keller, S. Freguia, P. Aelterman, W. Verstraete, K. Rabaey, Microbial fuel cells: Methodology and technology, Environ. Sci. Technol. (2006). doi:10.1021/es0605016.
[293] C. Zhu, T. Liu, F. Qian, T.Y.J. Han, E.B. Duoss, J.D. Kuntz, C.M. Spadaccini, M.A. Worsley, Y. Li, Supercapacitors Based on Three-Dimensional Hierarchical Graphene Aerogels with Periodic Macropores, Nano Lett. 16 (2016) 3448–3456. doi:10.1021/acs.nanolett.5b04965.
[294] P.L. Huang, X.F. Luo, Y.Y. Peng, N.W. Pu, M. Der Ger, C.H. Yang, T.Y. Wu, J.K. Chang, Ionic liquid electrolytes with various constituent ions for graphene-based supercapacitors, Electrochim. Acta. 161 (2015) 371–377. doi:10.1016/j.electacta.2015.02.115.
[295] E. Kovalska, C. Kocabas, Organic electrolytes for graphene-based supercapacitor: Liquid, gel or solid, Mater. Today Commun. 7 (2016) 155–160. doi:10.1016/j.mtcomm.2016.04.013.
[296] Z.S. Iro, C. Subramani, S.S. Dash, A brief review on electrode materials for supercapacitor, Int. J. Electrochem. Sci. (2016). doi:10.20964/2016.12.50.
[297] R. Wang, Q.R. Wang, M.J. Yao, K.N. Chen, X.Y. Wang, L.L. Liu, Z.Q. Niu, J. Chen, Flexible ultrathin all-solid-state supercapacitors, Rare Met. 37 (2018) 536–542. doi:10.1007/s12598-018-1034-x.
[298] M. Kaempgen, C.K. Chan, J. Ma, Y. Cui, G. Gruner, Printable thin film supercapacitors using single-walled carbon nanotubes, Nano Lett. 9 (2009) 1872–1876. doi:10.1021/nl8038579.
[299] C. Arbizzani, M. Biso, D. Cericola, M. Lazzari, F. Soavi, M. Mastragostino, Safe, high-energy supercapacitors based on solvent-free ionic liquid electrolytes, J. Power Sources. 185 (2008) 1575–1579. doi:10.1016/j.jpowsour.2008.09.016.
[300] L.G. Bettini, A. Bellacicca, P. Piseri, P. Milani, Supersonic cluster beam printing of carbon microsupercapacitors on paper, Flex. Print. Electron. 2 (2017). doi:10.1088/2058-8585/aa699c.
[301] L.G. Bettini, P. Piseri, F. De Giorgio, C. Arbizzani, P. Milani, F. Soavi, Flexible, ionic liquid-based micro-supercapacitor produced by supersonic cluster beam deposition, Electrochim. Acta. 170 (2015) 57–62. doi:10.1016/j.electacta.2015.04.068.
[302] Z. Niu, L. Zhang, L. Liu, B. Zhu, H. Dong, X. Chen, All-solid-state flexible ultrathin micro-supercapacitors based on graphene, Adv. Mater. 25 (2013) 4035–4042. doi:10.1002/adma.201301332.
[303] X. Pu, M. Liu, L. Li, S. Han, X. Li, C. Jiang, C. Du, J. Luo, W. Hu, Z.L. Wang, Wearable Textile-Based In-Plane Microsupercapacitors, Adv. Energy Mater. 6 (2016). doi:10.1002/aenm.201601254.
[304] G. Wu, P. Tan, D. Wang, Z. Li, L. Peng, Y. Hu, C. Wang, W. Zhu, S. Chen, W. Chen, High-performance Supercapacitors Based on Electrochemical-induced Vertical-aligned Carbon Nanotubes and Polyaniline Nanocomposite Electrodes, Sci. Rep. (2017). doi:10.1038/srep43676.
[305] M. Salanne, Ionic Liquids for Supercapacitor Applications, Top. Curr. Chem. 375 (2017) 1–25. doi:10.1007/s41061-017-0150-7.
[306] J. Xu, S. Gai, F. He, N. Niu, P. Gao, Y. Chen, P. Yang, A sandwich-type three-dimensional

layered double hydroxide nanosheet array/graphene composite: Fabrication and high supercapacitor performance, J. Mater. Chem. A. (2014). doi:10.1039/c3ta14048b.
[307] J. Zhong, L.Q. Fan, X. Wu, J.H. Wu, G.J. Liu, J.M. Lin, M.L. Huang, Y.L. Wei, Improved energy density of quasi-solid-state supercapacitors using sandwich-type redox-active gel polymer electrolytes, Electrochim. Acta. (2015). doi:10.1016/j.electacta.2015.03.114.
[308] H. Hu, Z. Pei, C. Ye, Recent advances in designing and fabrication of planar micro-supercapacitors for on-chip energy storage, Energy Storage Mater. 1 (2015) 82–102. doi:10.1016/j.ensm.2015.08.005.
[309] N.A. Kyeremateng, T. Brousse, D. Pech, Microsupercapacitors as miniaturized energy-storage components for on-chip electronics, Nat. Nanotechnol. 12 (2017) 7–15. doi:10.1038/nnano.2016.196.
[310] Z. Liu, Z.S. Wu, S. Yang, R. Dong, X. Feng, K. Müllen, Ultraflexible In-Plane Micro-Supercapacitors by Direct Printing of Solution-Processable Electrochemically Exfoliated Graphene, Adv. Mater. 28 (2016) 2217–2222. doi:10.1002/adma.201505304.
[311] Z. Peng, R. Ye, J.A. Mann, D. Zakhidov, Y. Li, P.R. Smalley, J. Lin, J.M. Tour, Flexible Boron-Doped Laser-Induced Graphene Microsupercapacitors, ACS Nano. 9 (2015) 5868–5875. doi:10.1021/acsnano.5b00436.
[312] P. Huang, C. Lethien, S. Pinaud, K. Brousse, R. Laloo, V. Turq, M. Respaud, A. Demortière, B. Daffos, P.L. Taberna, B. Chaudret, Y. Gogotsi, P. Simon, On-chip and freestanding elastic carbon films for micro-supercapacitors, Science (80-.). 351 (2016) 691–695. doi:10.1126/science.aad3345.
[313] Y.Z. Zhang, Y. Wang, T. Cheng, W.Y. Lai, H. Pang, W. Huang, Flexible supercapacitors based on paper substrates: a new paradigm for low-cost energy storage, Chem. Soc. Rev. 44 (2015) 5181–5199. doi:10.1039/c5cs00174a.
[314] H. Li, D. Yuan, C. Tang, S. Wang, J. Sun, Z. Li, T. Tang, F. Wang, H. Gong, C. He, Lignin-derived interconnected hierarchical porous carbon monolith with large areal/volumetric capacitances for supercapacitor, Carbon N. Y. 100 (2016) 151–157. doi:10.1016/j.carbon.2015.12.075.
[315] R. Mantravadi, P.R. Chinnam, D.A. Dikin, S.L. Wunder, High Conductivity, High Strength Solid Electrolytes Formed by in Situ Encapsulation of Ionic Liquids in Nanofibrillar Methyl Cellulose Networks, ACS Appl. Mater. Interfaces. 8 (2016) 13426–13436. doi:10.1021/acsami.6b02903.
[316] C. Chen, Y. Zhang, Y. Li, J. Dai, J. Song, Y. Yao, Y. Gong, I. Kierzewski, J. Xie, L. Hu, All-wood, low tortuosity, aqueous, biodegradable supercapacitors with ultra-high capacitance, Energy Environ. Sci. 10 (2017) 538–545. doi:10.1039/c6ee03716j.
[317] Q. Niu, Y. Guo, K. Gao, Z. Shao, Polypyrrole/cellulose nanofiber aerogel as a supercapacitor electrode material, RSC Adv. 6 (2016) 109143–109149. doi:10.1039/c6ra23216g.
[318] W.G. Moon, G.P. Kim, M. Lee, H.D. Song, J. Yi, A biodegradable gel electrolyte for use in high-performance flexible supercapacitors, ACS Appl. Mater. Interfaces. (2015). doi:10.1021/am5070987.
[319] R. Oraon, A. De Adhikari, S.K. Tiwari, G.C. Nayak, Enhanced Specific Capacitance of Self-Assembled Three-Dimensional Carbon Nanotube/Layered Silicate/Polyaniline Hybrid Sandwiched Nanocomposite for Supercapacitor Applications, ACS Sustain. Chem. Eng. 4 (2016) 1392–1403. doi:10.1021/acssuschemeng.5b01389.
[320] G. Lee, S.K. Kang, S.M. Won, P. Gutruf, Y.R. Jeong, J. Koo, S.S. Lee, J.A. Rogers, J.S. Ha,

Fully Biodegradable Microsupercapacitor for Power Storage in Transient Electronics, Adv. Energy Mater. 7 (2017) 1–12. doi:10.1002/aenm.201700157.
[321] M. Petkovic, J.L. Ferguson, H.Q.N. Gunaratne, R. Ferreira, M.C. Leitão, K.R. Seddon, L.P.N. Rebelo, C.S. Pereira, Novel biocompatible cholinium-based ionic liquids - Toxicity and biodegradability, Green Chem. (2010). doi:10.1039/b922247b.
[322] A. Jordan, N. Gathergood, Biodegradation of ionic liquids-a critical review, Chem. Soc. Rev. 44 (2015) 8200–8237. doi:10.1039/c5cs00444f.
[323] D. Mondal, M. Sharma, M. V. Quental, A.P.M. Tavares, K. Prasad, M.G. Freire, Suitability of bio-based ionic liquids for the extraction and purification of IgG antibodies, Green Chem. 18 (2016) 6071–6081. doi:10.1039/c6gc01482h.
[324] M. Isik, R. Gracia, L.C. Kollnus, L.C. Tomé, I.M. Marrucho, D. Mecerreyes, Cholinium-based poly(ionic liquid)s: Synthesis, characterization, and application as biocompatible ion gels and cellulose coatings, ACS Macro Lett. 2 (2013) 975–979. doi:10.1021/mz400451g.
[325] L.H. Xie, Q.D. Ling, X.Y. Hou, W. Huang, An effective Friedel-Crafts postfunctionalization of poly(N-vinylcarbazole) to tune carrier transportation of supramolecular organic semiconductors based on π-stacked polymers for nonvolatile flash memory cell, J. Am. Chem. Soc. (2008). doi:10.1021/ja076720o.
[326] Z. An, C. Zheng, Y. Tao, R. Chen, H. Shi, T. Chen, Z. Wang, H. Li, R. Deng, X. Liu, W. Huang, Stabilizing triplet excited states for ultralong organic phosphorescence, Nat. Mater. (2015). doi:10.1038/nmat4259.
[327] J. Jiang, J. Zhu, W. Ai, X. Wang, Y. Wang, C. Zou, W. Huang, T. Yu, Encapsulation of sulfur with thin-layered nickel-based hydroxides for long-cyclic lithium-sulfur cells, Nat. Commun. (2015). doi:10.1038/ncomms9622.
[328] D. Angmo, T.R. Andersen, J.J. Bentzen, M. Helgesen, R.R. Søndergaard, M. Jørgensen, J.E. Carlé, E. Bundgaard, F.C. Krebs, Roll-to-Roll Printed Silver Nanowire Semitransparent Electrodes for Fully Ambient Solution-Processed Tandem Polymer Solar Cells, Adv. Funct. Mater. (2015). doi:10.1002/adfm.201501887.
[329] Z. Zhong, H. Lee, D. Kang, S. Kwon, Y.M. Choi, I. Kim, K.Y. Kim, Y. Lee, K. Woo, J. Moon, Continuous Patterning of Copper Nanowire-Based Transparent Conducting Electrodes for Use in Flexible Electronic Applications, ACS Nano. (2016). doi:10.1021/acsnano.6b03626.
[330] J. Du, S. Pei, L. Ma, H.M. Cheng, 25th anniversary article: Carbon nanotube- and graphene-based transparent conductive films for optoelectronic devices, Adv. Mater. (2014). doi:10.1002/adma.201304135.
[331] K. Ellmer, Past achievements and future challenges in the development of optically transparent electrodes, Nat. Photonics. (2012). doi:10.1038/nphoton.2012.282.
[332] D.S. Hecht, L. Hu, G. Irvin, Emerging transparent electrodes based on thin films of carbon nanotubes, graphene, and metallic nanostructures, Adv. Mater. (2011). doi:10.1002/adma.201003188.
[333] T. Cheng, Y. Zhang, W.Y. Lai, W. Huang, Stretchable thin-film electrodes for flexible electronics with high deformability and stretchability, Adv. Mater. (2015). doi:10.1002/adma.201405864.
[334] Y.S. Liu, J. Feng, X.L. Ou, H.F. Cui, M. Xu, H.B. Sun, Ultrasmooth, highly conductive and transparent PEDOT:PSS/silver nanowire composite electrode for flexible organic light-emitting devices, Org. Electron. Physics, Mater. Appl. (2016).

doi:10.1016/j.orgel.2016.01.014.
[335] T. Bin Song, Y.S. Rim, F. Liu, B. Bob, S. Ye, Y.T. Hsieh, Y. Yang, Highly Robust Silver Nanowire Network for Transparent Electrode, ACS Appl. Mater. Interfaces. (2015). doi:10.1021/acsami.5b06540.
[336] M.S. Lee, K. Lee, S.Y. Kim, H. Lee, J. Park, K.H. Choi, H.K. Kim, D.G. Kim, D.Y. Lee, S. Nam, J.U. Park, High-performance, transparent, and stretchable electrodes using graphene-metal nanowire hybrid structures, Nano Lett. (2013). doi:10.1021/nl401070p.
[337] M. Montanino, A. De Girolamo Del Mauro, M. Tesoro, R. Ricciardi, R. Diana, P. Morvillo, G. Nobile, A. Imparato, G. Sico, C. Minarini, Gravure-printed PEDOT:PSS on flexible PEN substrate as ITO-free anode for polymer solar cells, in: Polym. Compos., 2015. doi:10.1002/pc.23486.
[338] F. Hoeng, A. Denneulin, N. Reverdy-Bruas, G. Krosnicki, J. Bras, Rheology of cellulose nanofibrils/silver nanowires suspension for the production of transparent and conductive electrodes by screen printing, Appl. Surf. Sci. (2017). doi:10.1016/j.apsusc.2016.10.073.
[339] G.A. Dos Reis Benatto, B. Roth, M. Corazza, R.R. Søndergaard, S.A. Gevorgyan, M. Jørgensen, F.C. Krebs, Roll-to-roll printed silver nanowires for increased stability of flexible ITO-free organic solar cell modules, Nanoscale. (2016). doi:10.1039/c5nr07426f.
[340] Z. Zhong, K. Woo, I. Kim, H. Hwang, S. Kwon, Y.M. Choi, Y. Lee, T.M. Lee, K. Kim, J. Moon, Roll-to-roll-compatible, flexible, transparent electrodes based on self-nanoembedded Cu nanowires using intense pulsed light irradiation, Nanoscale. (2016). doi:10.1039/c6nr00444j.
[341] N. Kim, H. Kang, J.H. Lee, S. Kee, S.H. Lee, K. Lee, Highly conductive all-plastic electrodes fabricated using a novel chemically controlled transfer-printing method, Adv. Mater. (2015). doi:10.1002/adma.201500078.
[342] H.W. Choi, T. Zhou, M. Singh, G.E. Jabbour, Recent developments and directions in printed nanomaterials, Nanoscale. (2015). doi:10.1039/c4nr03915g.
[343] Y. Aleeva, B. Pignataro, Recent advances in upscalable wet methods and ink formulations for printed electronics, J. Mater. Chem. C. (2014). doi:10.1039/c4tc00618f.
[344] D. McCoul, W. Hu, M. Gao, V. Mehta, Q. Pei, Recent Advances in Stretchable and Transparent Electronic Materials, Adv. Electron. Mater. (2016). doi:10.1002/aelm.201500407.
[345] D. Wei, H. Li, D. Han, Q. Zhang, L. Niu, H. Yang, C. Bower, P. Andrew, T. Ryhänen, Properties of graphene inks stabilized by different functional groups, Nanotechnology. (2011). doi:10.1088/0957-4484/22/24/245702.
[346] P. Blake, P.D. Brimicombe, R.R. Nair, T.J. Booth, D. Jiang, F. Schedin, L.A. Ponomarenko, S. V. Morozov, H.F. Gleeson, E.W. Hill, A.K. Geim, K.S. Novoselov, Graphene-based liquid crystal device, Nano Lett. (2008). doi:10.1021/nl080649i.
[347] M. Magliulo, M.Y. Mulla, M. Singh, E. Macchia, A. Tiwari, L. Torsi, K. Manoli, Printable and flexible electronics: From TFTs to bioelectronic devices, J. Mater. Chem. C. (2015). doi:10.1039/c5tc02737c.
[348] D. He, L. Shen, X. Zhang, Y. Wang, N. Bao, H.H. Kung, An efficient and eco-friendly solution-chemical route for preparation of ultrastable reduced graphene oxide suspensions, AIChE J. (2014). doi:10.1002/aic.14499.
[349] W. Bin Liu, S. Pei, J. Du, B. Liu, L. Gao, Y. Su, C. Liu, H.M. Cheng, Additive-free dispersion of single-walled carbon nanotubes and its application for transparent conductive films,

Adv. Funct. Mater. (2011). doi:10.1002/adfm.201002257.
[350] D.S. Hecht, A.M. Heintz, R. Lee, L. Hu, B. Moore, C. Cucksey, S. Risser, High conductivity transparent carbon nanotube films deposited from superacid, Nanotechnology. (2011). doi:10.1088/0957-4484/22/7/075201.
[351] H. Lu, D. Zhang, X. Ren, J. Liu, W.C.H. Choy, Selective growth and integration of silver nanoparticles on silver nanowires at room conditions for transparent nano-network electrode, ACS Nano. (2014). doi:10.1021/nn504969z.
[352] Y. Sun, Y. Xia, Large-scale synthesis of uniform silver nanowires through a soft, self-seeding, polyol process, Adv. Mater. (2002). doi:10.1002/1521-4095(20020605)14:11<833::AID-ADMA833>3.0.CO;2-K.
[353] S. Zhu, Y. Gao, B. Hu, J. Li, J. Su, Z. Fan, J. Zhou, Transferable self-welding silver nanowire network as high performance transparent flexible electrode, Nanotechnology. (2013). doi:10.1088/0957-4484/24/33/335202.
[354] T. Sannicolo, M. Lagrange, A. Cabos, C. Celle, J.P. Simonato, D. Bellet, Metallic Nanowire-Based Transparent Electrodes for Next Generation Flexible Devices: a Review, Small. (2016). doi:10.1002/smll.201602581.
[355] K. Tokarek, J.L. Hueso, P. Kuśtrowski, G. Stochel, A. Kyzioł, Green synthesis of chitosan-stabilized copper nanoparticles, Eur. J. Inorg. Chem. (2013). doi:10.1002/ejic.201300594.
[356] G. Yang, Z. Zhang, S. Zhang, L. Yu, P. Zhang, Y. Hou, Preparation and characterization of copper nanoparticles surface-capped by alkanethiols, Surf. Interface Anal. (2013). doi:10.1002/sia.5309.
[357] P. Alexandridis, Gold Nanoparticle Synthesis, Morphology Control, and Stabilization Facilitated by Functional Polymers, Chem. Eng. Technol. (2011). doi:10.1002/ceat.201000335.
[358] F. Chahdoura, I. Favier, M. Gõmez, Glycerol as suitable solvent for the synthesis of metallic species and catalysis, Chem. - A Eur. J. (2014). doi:10.1002/chem.201403534.
[359] D. Alemu, H.Y. Wei, K.C. Ho, C.W. Chu, Highly conductive PEDOT:PSS electrode by simple film treatment with methanol for ITO-free polymer solar cells, Energy Environ. Sci. (2012). doi:10.1039/c2ee22595f.
[360] N. Minami, Y. Kim, K. Miyashita, S. Kazaoui, B. Nalini, Cellulose derivatives as excellent dispersants for single-wall carbon nanotubes as demonstrated by absorption and photoluminescence spectroscopy, Appl. Phys. Lett. (2006). doi:10.1063/1.2180870.
[361] M. Zheng, A. Jagota, E.D. Semke, B.A. Diner, R.S. McLean, S.R. Lustig, R.E. Richardson, N.G. Tassi, DNA-assisted dispersion and separation of carbon nanotubes, Nat. Mater. (2003). doi:10.1038/nmat877.
[362] W. Xu, Q. Xu, Q. Huang, R. Tan, W. Shen, W. Song, Electrically conductive silver nanowires-filled methylcellulose composite transparent films with high mechanical properties, Mater. Lett. 152 (2015) 173–176. doi:10.1016/j.matlet.2015.03.111.
[363] E.B. Secor, B.Y. Ahn, T.Z. Gao, J.A. Lewis, M.C. Hersam, Rapid and Versatile Photonic Annealing of Graphene Inks for Flexible Printed Electronics, Adv. Mater. (2015). doi:10.1002/adma.201502866.
[364] J.T. Wu, S. Lien-Chung Hsu, M.H. Tsai, Y.F. Liu, W.S. Hwang, Direct ink-jet printing of silver nitrate-silver nanowire hybrid inks to fabricate silver conductive lines, J. Mater. Chem. (2012). doi:10.1039/c2jm31761c.
[365] J. Jang, H. Kang, H.C.N. Chakravarthula, V. Subramanian, Fully Inkjet-Printed Transparent

Oxide Thin Film Transistors Using a Fugitive Wettability Switch, Adv. Electron. Mater. (2015). doi:10.1002/aelm.201500086.
[366] M. Caironi, E. Gili, H. Sirringhaus, Ink-Jet Printing of Downscaled Organic Electronic Devices, in: Org. Electron. II More Mater. Appl., 2012. doi:10.1002/9783527640218.ch9.
[367] F. Ely, C.O. Avellaneda, P. Paredez, V.C. Nogueira, T.E.A. Santos, V.P. Mammana, C. Molina, J. Brug, G. Gibson, L. Zhao, Patterning quality control of inkjet printed PEDOT:PSS films by wetting properties, Synth. Met. (2011). doi:10.1016/j.synthmet.2011.08.014.
[368] A. Chiolerio, P. Rivolo, S. Porro, S. Stassi, S. Ricciardi, P. Mandracci, G. Canavese, K. Bejtka, C.F. Pirri, Inkjet-printed PEDOT:PSS electrodes on plasma-modified PDMS nanocomposites: Quantifying plasma treatment hardness, RSC Adv. (2014). doi:10.1039/c4ra06878e.
[369] M. Reznikov, A. Sharma, T. Hegmann, Ink-jet printed nanoparticle alignment layers: Easy design and fabrication of patterned alignment layers for nematic liquid crystals, Part. Part. Syst. Charact. (2014). doi:10.1002/ppsc.201300248.
[370] W.J. Scheideler, J. Smith, I. Deckman, S. Chung, A.C. Arias, V. Subramanian, A robust, gravure-printed, silver nanowire/metal oxide hybrid electrode for high-throughput patterned transparent conductors, J. Mater. Chem. C. (2016). doi:10.1039/c5tc04364f.
[371] Y.I. Lee, Y.H. Choa, Adhesion enhancement of ink-jet printed conductive copper patterns on a flexible substrate, J. Mater. Chem. (2012). doi:10.1039/c2jm31381b.
[372] T. Cheng, Y.Z. Zhang, W.Y. Lai, Y. Chen, W.J. Zeng, W. Huang, High-performance stretchable transparent electrodes based on silver nanowires synthesized via an eco-friendly halogen-free method, J. Mater. Chem. C. (2014). doi:10.1039/c4tc01959h.
[373] L. Hu, H.S. Kim, J.Y. Lee, P. Peumans, Y. Cui, Scalable coating and properties of transparent, flexible, silver nanowire electrodes, ACS Nano. (2010). doi:10.1021/nn1005232.
[374] J. Kim, Y.S. Nam, M.H. Song, H.W. Park, Large Pulsed Electron Beam Welded Percolation Networks of Silver Nanowires for Transparent and Flexible Electrodes, ACS Appl. Mater. Interfaces. (2016). doi:10.1021/acsami.6b05874.
[375] Y. Lee, W.Y. Jin, K.Y. Cho, J.W. Kang, J. Kim, Thermal pressing of a metal-grid transparent electrode into a plastic substrate for flexible electronic devices, J. Mater. Chem. C. (2016). doi:10.1039/c6tc01234e.
[376] J. Lee, J.Y. Woo, J.T. Kim, B.Y. Lee, C.S. Han, Synergistically enhanced stability of highly flexible silver nanowire/carbon nanotube hybrid transparent electrodes by plasmonic welding, ACS Appl. Mater. Interfaces. (2014). doi:10.1021/am502639n.
[377] W. Honda, S. Harada, T. Arie, S. Akita, K. Takei, Wearable, human-interactive, health-monitoring, wireless devices fabricated by macroscale printing techniques, Adv. Funct. Mater. (2014). doi:10.1002/adfm.201303874.
[378] W. Zeng, L. Shu, Q. Li, S. Chen, F. Wang, X.M. Tao, Fiber-based wearable electronics: A review of materials, fabrication, devices, and applications, Adv. Mater. (2014). doi:10.1002/adma.201400633.
[379] A. Pantelopoulos, N.G. Bourbakis, A survey on wearable sensor-based systems for health monitoring and prognosis, IEEE Trans. Syst. Man Cybern. Part C Appl. Rev. (2010). doi:10.1109/TSMCC.2009.2032660.
[380] P. Bingger, M. Zens, P. Woias, Highly flexible capacitive strain gauge for continuous long-term blood pressure monitoring, Biomed. Microdevices. (2012). doi:10.1007/s10544-

012-9636-9.
[381] M. Amjadi, A. Pichitpajongkit, S. Lee, S. Ryu, I. Park, Highly stretchable and sensitive strain sensor based on silver nanowire-elastomer nanocomposite, ACS Nano. (2014). doi:10.1021/nn501204t.
[382] J.D. Pegan, J. Zhang, M. Chu, T. Nguyen, S.J. Park, A. Paul, J. Kim, M. Bachman, M. Khine, Skin-mountable stretch sensor for wearable health monitoring, Nanoscale. (2016). doi:10.1039/c6nr04467k.
[383] Y. Wang, J. Hao, Z. Huang, G. Zheng, K. Dai, C. Liu, C. Shen, Flexible electrically resistive-type strain sensors based on reduced graphene oxide-decorated electrospun polymer fibrous mats for human motion monitoring, Carbon N. Y. (2018). doi:10.1016/j.carbon.2017.10.034.
[384] Y. Zheng, Y. Li, K. Dai, Y. Wang, G. Zheng, C. Liu, C. Shen, A highly stretchable and stable strain sensor based on hybrid carbon nanofillers/polydimethylsiloxane conductive composites for large human motions monitoring, Compos. Sci. Technol. (2018). doi:10.1016/j.compscitech.2018.01.019.
[385] X.G. Yu, Y.Q. Li, W. Bin Zhu, P. Huang, T.T. Wang, N. Hu, S.Y. Fu, A wearable strain sensor based on a carbonized nano-sponge/silicone composite for human motion detection, Nanoscale. (2017). doi:10.1039/c7nr01011g.
[386] S.J. Park, J. Kim, M. Chu, M. Khine, Highly Flexible Wrinkled Carbon Nanotube Thin Film Strain Sensor to Monitor Human Movement, Adv. Mater. Technol. (2016). doi:10.1002/admt.201600053.
[387] J.W. Zha, W. Huang, S.J. Wang, D.L. Zhang, R.K.Y. Li, Z.M. Dang, Difunctional Graphene-Fe3O4 Hybrid Nanosheet/Polydimethylsiloxane Nanocomposites with High Positive Piezoresistive and Superparamagnetism Properties as Flexible Touch Sensors, Adv. Mater. Interfaces. (2016). doi:10.1002/admi.201500418.
[388] L. Yi, W. Jiao, K. Wu, L. Qian, X. Yu, Q. Xia, K. Mao, S. Yuan, S. Wang, Y. Jiang, Nanoparticle monolayer-based flexible strain gauge with ultrafast dynamic response for acoustic vibration detection, Nano Res. (2015). doi:10.1007/s12274-015-0803-1.
[389] E. Roh, B.U. Hwang, D. Kim, B.Y. Kim, N.E. Lee, Stretchable, Transparent, Ultrasensitive, and Patchable Strain Sensor for Human-Machine Interfaces Comprising a Nanohybrid of Carbon Nanotubes and Conductive Elastomers, ACS Nano. (2015). doi:10.1021/acsnano.5b01613.
[390] S. Gong, D.T.H. Lai, Y. Wang, L.W. Yap, K.J. Si, Q. Shi, N.N. Jason, T. Sridhar, H. Uddin, W. Cheng, Tattoolike Polyaniline Microparticle-Doped Gold Nanowire Patches as Highly Durable Wearable Sensors, ACS Appl. Mater. Interfaces. (2015). doi:10.1021/acsami.5b05001.
[391] A. V. Desai, M.A. Haque, Mechanics of the interface for carbon nanotube-polymer composites, Thin-Walled Struct. (2005). doi:10.1016/j.tws.2005.07.003.
[392] C. Lee, L. Jug, E. Meng, High strain biocompatible polydimethylsiloxane-based conductive graphene and multiwalled carbon nanotube nanocomposite strain sensors, Appl. Phys. Lett. (2013). doi:10.1063/1.4804580.
[393] C. Li, E.T. Thostenson, T.W. Chou, Dominant role of tunneling resistance in the electrical conductivity of carbon nanotube-based composites, Appl. Phys. Lett. (2007). doi:10.1063/1.2819690.
[394] I. Balberg, Tunneling and nonuniversal conductivity in composite materials, Phys. Rev. Lett. (1987). doi:10.1103/PhysRevLett.59.1305.

[395] J. Lee, M. Lim, J. Yoon, M.S. Kim, B. Choi, D.M. Kim, D.H. Kim, I. Park, S.J. Choi, Transparent, Flexible Strain Sensor Based on a Solution-Processed Carbon Nanotube Network, ACS Appl. Mater. Interfaces. (2017). doi:10.1021/acsami.7b03184.
[396] X. Xiao, L. Yuan, J. Zhong, T. Ding, Y. Liu, Z. Cai, Y. Rong, H. Han, J. Zhou, Z.L. Wang, High-strain sensors based on ZnO nanowire/polystyrene hybridized flexible films, Adv. Mater. (2011). doi:10.1002/adma.201103406.
[397] J.J. Park, W.J. Hyun, S.C. Mun, Y.T. Park, O.O. Park, Highly stretchable and wearable graphene strain sensors with controllable sensitivity for human motion monitoring, ACS Appl. Mater. Interfaces. (2015). doi:10.1021/acsami.5b00695.
[398] J.T. Muth, D.M. Vogt, R.L. Truby, Y. Mengüç, D.B. Kolesky, R.J. Wood, J.A. Lewis, Embedded 3D printing of strain sensors within highly stretchable elastomers, Adv. Mater. (2014). doi:10.1002/adma.201400334.
[399] J.H. Kong, N.S. Jang, S.H. Kim, J.M. Kim, Simple and rapid micropatterning of conductive carbon composites and its application to elastic strain sensors, Carbon N. Y. (2014). doi:10.1016/j.carbon.2014.05.022.
[400] S. Tadakaluru, W. Thongsuwan, P. Singjai, Stretchable and flexible high-strain sensors made using carbon nanotubes and graphite films on natural rubber, Sensors (Switzerland). (2014). doi:10.3390/s140100868.
[401] H. Lee, B. Seong, H. Moon, D. Byun, Directly printed stretchable strain sensor based on ring and diamond shaped silver nanowire electrodes, RSC Adv. (2015). doi:10.1039/c5ra01519g.
[402] S. Yao, Y. Zhu, Wearable multifunctional sensors using printed stretchable conductors made of silver nanowires, Nanoscale. (2014). doi:10.1039/c3nr05496a.
[403] D. Kang, P. V. Pikhitsa, Y.W. Choi, C. Lee, S.S. Shin, L. Piao, B. Park, K.Y. Suh, T. Il Kim, M. Choi, Ultrasensitive mechanical crack-based sensor inspired by the spider sensory system, Nature. (2014). doi:10.1038/nature14002.
[404] M. Zheng, W. Li, M. Xu, N. Xu, P. Chen, M. Han, B. Xie, Strain sensors based on chromium nanoparticle arrays, Nanoscale. (2014). doi:10.1039/c3nr04135b.
[405] S. Luo, T. Liu, SWCNT/graphite nanoplatelet hybrid thin films for self-temperature-compensated, highly sensitive, and extensible piezoresistive sensors, Adv. Mater. (2013). doi:10.1002/adma.201301796.
[406] T. Yamada, Y. Hayamizu, Y. Yamamoto, Y. Yomogida, A. Izadi-Najafabadi, D.N. Futaba, K. Hata, A stretchable carbon nanotube strain sensor for human-motion detection, Nat. Nanotechnol. (2011). doi:10.1038/nnano.2011.36.
[407] L. Cai, L. Song, P. Luan, Q. Zhang, N. Zhang, Q. Gao, D. Zhao, X. Zhang, M. Tu, F. Yang, W. Zhou, Q. Fan, J. Luo, W. Zhou, P.M. Ajayan, S. Xie, Super-stretchable, transparent carbon nanotube-based capacitive strain sensors for human motion detection, Sci. Rep. (2013). doi:10.1038/srep03048.
[408] J. Lee, S. Kim, J. Lee, D. Yang, B.C. Park, S. Ryu, I. Park, A stretchable strain sensor based on a metal nanoparticle thin film for human motion detection, Nanoscale. (2014). doi:10.1039/c4nr03295k.
[409] X. Li, R. Zhang, W. Yu, K. Wang, J. Wei, D. Wu, A. Cao, Z. Li, Y. Cheng, Q. Zheng, R.S. Ruoff, H. Zhu, Stretchable and highly sensitive graphene-on-polymer strain sensors, Sci. Rep. (2012). doi:10.1038/srep00870.
[410] S. Luo, T. Liu, Structure-property-processing relationships of single-wall carbon nanotube thin film piezoresistive sensors, Carbon N. Y. (2013).

doi:10.1016/j.carbon.2013.03.024.
[411] M. Hempel, D. Nezich, J. Kong, M. Hofmann, A novel class of strain gauges based on layered percolative films of 2D materials, Nano Lett. (2012). doi:10.1021/nl302959a.
[412] C.S. Boland, U. Khan, C. Backes, A. O'Neill, J. McCauley, S. Duane, R. Shanker, Y. Liu, I. Jurewicz, A.B. Dalton, J.N. Coleman, Sensitive, high-strain, high-rate bodily motion sensors based on graphene-rubber composites, ACS Nano. (2014). doi:10.1021/nn503454h.
[413] W. Obitayo, T. Liu, Effect of orientation on the piezoresistivity of mechanically drawn single walled carbon nanotube (SWCNT) thin films, Carbon N. Y. (2015). doi:10.1016/j.carbon.2014.12.095.
[414] D.J. Cohen, D. Mitra, K. Peterson, M.M. Maharbiz, A highly elastic, capacitive strain gauge based on percolating nanotube networks, Nano Lett. (2012). doi:10.1021/nl204052z.
[415] H. Eom, J. Lee, A. Pichitpajongkit, M. Amjadi, J.H. Jeong, E. Lee, J.Y. Lee, I. Park, Ag@Ni core-shell nanowire network for robust transparent electrodes against oxidation and sulfurization, Small. (2014). doi:10.1002/smll.201400992.
[416] Y. Wang, L. Wang, T. Yang, X. Li, X. Zang, M. Zhu, K. Wang, D. Wu, H. Zhu, Wearable and highly sensitive graphene strain sensors for human motion monitoring, Adv. Funct. Mater. (2014). doi:10.1002/adfm.201400379.
[417] C.X. Liu, J.W. Choi, Analyzing resistance response of embedded PDMS and carbon nanotubes composite under tensile strain, Microelectron. Eng. (2014). doi:10.1016/j.mee.2013.11.013.
[418] W. Hu, X. Niu, R. Zhao, Q. Pei, Elastomeric transparent capacitive sensors based on an interpenetrating composite of silver nanowires and polyurethane, Appl. Phys. Lett. (2013). doi:10.1063/1.4794143.
[419] N. Lu, C. Lu, S. Yang, J. Rogers, Highly sensitive skin-mountable strain gauges based entirely on elastomers, Adv. Funct. Mater. (2012). doi:10.1002/adfm.201200498.
[420] L. Wang, Y. Li, A review for conductive polymer piezoresistive composites and a development of a compliant pressure transducer, IEEE Trans. Instrum. Meas. (2013). doi:10.1109/TIM.2012.2215160.
[421] J. Zhao, C. He, R. Yang, Z. Shi, M. Cheng, W. Yang, G. Xie, D. Wang, D. Shi, G. Zhang, Ultra-sensitive strain sensors based on piezoresistive nanographene films, Appl. Phys. Lett. (2012). doi:10.1063/1.4742331.
[422] J. Zhao, G.Y. Zhang, D.X. Shi, Review of graphene-based strain sensors, Chinese Phys. B. (2013). doi:10.1088/1674-1056/22/5/057701.
[423] M. Amjadi, Y.J. Yoon, I. Park, Ultra-stretchable and skin-mountable strain sensors using carbon nanotubes-Ecoflex nanocomposites, Nanotechnology. (2015). doi:10.1088/0957-4484/26/37/375501.
[424] F.C. Krebs, T. Tromholt, M. Jørgensen, Upscaling of polymer solar cell fabrication using full roll-to-roll processing, Nanoscale. (2010). doi:10.1039/b9nr00430k.
[425] A.J. Morfa, T. Rödlmeier, N. Jürgensen, S. Stolz, G. Hernandez-Sosa, Comparison of biodegradable substrates for printed organic electronic devices, Cellulose. (2016). doi:10.1007/s10570-016-1049-0.
[426] R. Jung, H.S. Kim, Y. Kim, S.M. Kwon, H.S. Lee, H.J. Jin, Electrically conductive transparent papers using multiwalled carbon nanotubes, J. Polym. Sci. Part B Polym. Phys. (2008). doi:10.1002/polb.21457.

[427] R. Xiong, K. Hu, A.M. Grant, R. Ma, W. Xu, C. Lu, X. Zhang, V. V. Tsukruk, Ultrarobust Transparent Cellulose Nanocrystal-Graphene Membranes with High Electrical Conductivity, Adv. Mater. 28 (2016) 1501–1509. doi:10.1002/adma.201504438.
[428] C.M. Boutry, Y. Kaizawa, B.C. Schroeder, A. Chortos, A. Legrand, Z. Wang, J. Chang, P. Fox, Z. Bao, A stretchable and biodegradable strain and pressure sensor for orthopaedic application, Nat. Electron. (2018). doi:10.1038/s41928-018-0071-7.
[429] D. Stauffer, A. Bunde, Introduction to Percolation Theory , Phys. Today. (1987). doi:10.1063/1.2820231.
[430] B. Xie, P. Mao, M. Chen, Z. Li, C. Liu, Y. Qin, L. Yang, M. Wei, M. Liu, X. Wang, D. Han, S. Li, F. Song, M. Han, J.M. Liu, G. Wang, A tunable palladium nanoparticle film-based strain sensor in a Mott variable-range hopping regime, Sensors Actuators, A Phys. 272 (2018) 161–169. doi:10.1016/j.sna.2018.01.058.
[431] S.H. Masood, Intelligent rapid prototyping with fused deposition modelling, Rapid Prototyp. J. (1996). doi:10.1108/13552549610109054.
[432] M.R. Bhambhani, P.A. Cutting, K.S.W. Sing, D.H. Turk, Analysis of nitrogen adsorption isotherms on porous and nonporous silicas by the BET and αs methods, J. Colloid Interface Sci. (1972). doi:10.1016/0021-9797(72)90226-3.
[433] R. Vicentini, L.M. Da Silva, E.P. Cecilio, T.A. Alves, W.G. Nunes, H. Zanin, How to measure and calculate equivalent series resistance of electric double-layer capacitors, Molecules. (2019). doi:10.3390/molecules24081452.
[434] H.-J. Butt, B. Cappella, M. Kappl, Force measurements with the atomic force microscope: Technique, interpretation and applications, Surf. Sci. Rep. 59 (2005) 1–152. doi:10.1016/j.surfrep.2005.08.003.
[435] M. Indrieri, A. Podestà, G. Bongiorno, D. Marchesi, P. Milani, Adhesive-free colloidal probes for nanoscale force measurements: production and characterization, Rev. Sci. Instrum. 82 (2011) 023708. doi:10.1063/1.3553499.
[436] L. Puricelli, M. Galluzzi, C. Schulte, A. Podestà, P. Milani, Nanomechanical and topographical imaging of living cells by atomic force microscopy with colloidal probes, Rev. Sci. Instrum. 86 (2015). doi:10.1063/1.4915896.

ACKNOWLEDGEMENTS AND THANKS

The results obtained in this work and all the thing I learnt in this Ph.D. are not only a personal merit, but they are the fruit of the efforts of many people that cooperated with me and supported me for three long years. Then, I want to warmly and sincerely thank:

Prof. **Sandra Rondinini**, for supervising my project and for the trust she always shown in me;

Prof. **Paolo Milani**, Dr. **Tommaso Santaniello** and Dr. **Yunsong Yan**, for sharing with me their knowledge, for teaching me all I know about polymer-metal composites and for collaborating with me for the realization of the electromechanical actuators reported in this work;

Dr. **Andrea Bellacicca** and Dr. **Chloé Minnai**, for the patient training in the use of the supersonic cluster beam deposition technique;

Dr. **Luca Bettini**, for teaching me how to carry out electrochemical analysis on ionogels;

Francesco Cavaliere, **Daniele Viganò**, **Federico Pezzotta** and **William Merli** from the mechanical workshop of the Physics Department (University of Milan), for giving their time and professional skills to support and improve the quality of the presented work;

Matteo Mirigliano, for helping me in dealing with so many software necessary to carry out the research activity;

the bachelor students **Andrea Vitaloni** and **Marta Di Girolamo**, for collaborating with me in the work regarding biodegradable supercapacitors and for the scientific passion they put in it;

Prof. C. Lenardi, Prof. P. Piseri, Prof. A. Podestà, Sara Moon Villa, **Marco Piazzoni**, **Claudio Piazzoni**, **Matteo Chighizola**, **Francesca Borghi**, **Anita Previdi**, **Valeria Insogna** and all the colleagues that cooperated with me;

my family and my dearest friends for their support and their patience;

I also want to thankfully acknowledge:

the group of Prof. **Mauro Comes Franchini**, Department of Industrial Chemistry, University of Bologna, for providing the cellulose nanocrystals solution;

Bio-on s.p.a., for providing the poly(3-hydroxybutyrrate) powder;

Dr. **Kaija Pohako-Esko**, Institute of Technology, University of Tartu, Estonia, for providing the choline-based biodegradable ionic liquids